Heat Transfer and Pressure Drop During Condensation of Refrigerants in Microchannels

A Dissertation
Presented to
The Academic Faculty

By
Akhil Agarwal

In Partial Fulfillment
Of the Requirements for the Degree
Doctor of Philosophy in the
Mechanical Engineering

Georgia Institute of Technology
December 2006

Heat Transfer and Pressure Drop During Condensation of Refrigerants in Microchannels

Approved By**:**

Dr. Srinivas Garimella, Chairman
G. W. Woodruff School of Mechanical Engineering
Georgia Institute of Technology

Dr. S. Mostafa Ghiaasiaan
G. W. Woodruff School of Mechanical Engineering
Georgia Institute of Technology

Dr. Samuel Graham
G. W. Woodruff School of Mechanical Engineering
Georgia Institute of Technology

Dr. Tom Fuller
School of Chemical and Bio-Molecular Engineering
Georgia Institute of Technology

Dr. Mark G. Allen
School of Electrical and Computer Engineering
Georgia Institute of Technology

Date Approved: 13th November 2006

DEDICATION

To my parents Arvind Kumar Agarwal and Nirmala Kumari Agarwal – for their tireless effort all through their life, that enabled me to achieve such success. To my brother Nikhil Agarwal – for his moral support and for continuously showing me the light at the end of the long tunnel. To my wife Rupali – who trusted my abilities, when I was about to lose faith in myself and brought a renewed sense of joy and confidence to my life. It would not have been possible without her support and dedication to my needs in the final phases of PhD.

ACKNOWLEDGEMENTS

I would like to thank my advisor Dr. Srinivas Garimella for his trust in my abilities and his continuous efforts to bring the best out of me. The improvements that he has brought in me over the years will help me for the rest of my career.

I would like to thank Dr. Todd Christenson at HT Micro Inc. for his guidance and support in the fabrication of the refrigerant channels, which was the stepping stone to start the current study. Discussions with him provided invaluable guidance to me. I would also like to thank HT Micro Inc. for pulling on their other resources, for additional expense due to repeated failures in fabricating the channels.

I would like to thank the members of STSL: Jesse Killion, Ulf Andresen, Biswajit Mitra, Lalit Bohra, Vishwanath Subramanium, Tim Ernst and Matt Determan. They were like a family away from home, which together formed a support structure, without which, I would have never made it through. Jesse Killion was like a co-advisor to me who always found time to look over my analysis on my request and provide much needed ideas, whenever I was stuck.

I would like to thank my PhD Reading Committee for their guidance and encouragement.

TABLE OF CONTENTS

LIST OF TABLES

LIST OF FIGURES

NOMENCLATURE

<u>**Symbols**</u>

A,a	empirical constants, Area (m^2)
AR	aspect ratio
AFF	Annular Flow Factor
Bo	Bond number $= \frac{\rho g L^2}{\sigma}$
b	empirical constants
C	Chisholm parameter
c	empirical constants
Cp	specific heat (J/kg-K)
d	depth of microchannels (m)
D	diameter (m)
exp	function e^x
f	function of, friction factor
Fr	Froude Number $= \frac{V^2}{gL}$
FR	flow rate (m^3/s)
G	mass flux (kg/m^2-s)
g	acceleration due to gravity (m/s^2)
h	enthalpy (kJ/kg), condensation heat transfer coefficient (W/m^2-K), height (m)

ID	inner diameter (m)
J, j	superficial velocity (m/s)
k	conductivity (W/m-K)
$L.l$	length (m)
$M, \dot{m}$	mass flow rate (kg/s)
N	number of parallel channels, number of segments in heat transfer analysis
N_{UC}	number of unit cells
Nu	Nusselt Number = hD/k
OD	outer diameter (m)
P	pressure (kPa)
Pr	Prandtl number = $\mu\, Cp/k$
Q	heat duty (W)
q''	heat flux
R	thermal resistance (K/W), Radius
Re	Reynolds Number = $\rho VD/\mu$
SLR	slug length ratio
T	temperature (ºC, K)
t	thickness (m), time (s)
u	local velocity (m/s)
U	average velocity (m/s)
V	volume (m^3), velocity (m/s)
W,w	width (m)
We	Weber number $=\dfrac{\rho V^2 L}{\sigma}$

x quality, length parameter

z length parameter

X Martinelli Parameter $=\left[\dfrac{(dP/dz)_l}{(dP/dz)_v}\right]^{1/2}$

α thermal diffusivity, = k/ρCp

β homogenous void fraction

γ Expansion/contraction area ratio

δ film thickness (m)

Δ change, difference

π PI = 3.14

λ eigen values, non-dimensional parameter used by Lee and Lee (2001) $=\mu_L^2/(\rho_L\sigma D_h)$

μ dynamic viscosity (kg/m-s)

ρ density (kg/m^3)

ε emissivity

η fin efficiency

ω slug frequency (number of unit cells/length)

τ shear stress (Pa)

ψ Non dimensional parameter $\psi=\dfrac{j\mu_L}{\sigma}$

σ surface tension (N/m)

Subscripts and Superscripts

+	dimensionless turbulent parameter
0	minimum
amb	ambient
ave	average
b	bulk
B	bubble
con	contraction
CL	critical lower
CU	critical upper
Cu	copper
dPdL	pressure gradient
eff	effective
exp	experimental, expansion
f	film, film/bubble section
FM	flow meter
fric	frictional
g,v	gas phase
h,H	hydraulic, heater
H1	pre-heater
H2	post-heater
HE	central heat exchanger section in segmental heat transfer analysis
Hor	horizontal

HT	heat transfer
i	segment/node number
ID	internal diameter
in	inlet
ins	insulation
l,L	liquid, lower, laminar
loss	loss
OD	outer diameter
out	outlet/exit
Qave	heat duty based average
refg	refrigerant
s	slug
sat	saturation
seg	segment
so	soliman
tot	total
TS, ts	test section
U	upper
v	vapor
Ver	vertical
w	water
water	water-side
wall	wall

wb water-block

wf wafer

x differential with respect to x $= \frac{\partial}{\partial x}$

xx second order differential with respect ot x $= \frac{\partial^2}{\partial x^2}$

SUMMARY

Two-phase flow, evaporation, and boiling in microchannels have received considerable attention in the recent past due to the growing interest in the high heat fluxes made possible by these channels. Condensation in such channels has been studied by few investigators, although heat removal and rejection applications can benefit from high heat flux condensation. Most of the studies on small diameter channels have used isothermal air-water mixtures to simulate two-phase flow. However, due to the adiabatic flow in these studies, the results are not directly applicable to phase-change situations. In the current study, small hydraulic diameter ($100 < D_h < 160$ μm) channels were fabricated on a copper substrate by electroforming copper on to a mask patterned by X-ray lithography. The channels were sealed using diffusion bonding, which ensures leak proof flow at saturation pressures as high as 10 MPa. Measurements of local condensation heat transfer coefficients in small quality increments have typically been found to be difficult due to the low heat transfer rates at the small flow rates in these microchannels. In the current study, a novel measurement technique was used to address this issue. Subcooled refrigerant (R134a) was supplied to a precisely controlled electric heater that pre-conditions the refrigerant to the desired quality, followed by condensation in the test section. Further downstream, another precisely controlled electric heater was used to heat the refrigerant to a superheated state. Energy balances on the pre- and post-heaters were used to establish the refrigerant inlet and outlet states at the test section. Cooling of the

refrigerant in the test section was accomplished using water at a high flow rate to ensure that the condensation side presents the governing thermal resistance. The water-side temperature was controlled to obtain the desired incremental condensation rates. This method was used to accurately determine heat transfer coefficients for refrigerant R134a for $200 < G < 800$ kg/m^2-s and $0 < x < 1$ at four different saturation temperatures between 30 and 60^{o}C.

The measured heat transfer coefficients and pressure drops are analyzed and compared with the limited heat transfer and pressure drop models available in the literature for similar flow conditions and explanations for agreements/disagreements with the proposed study are provided. Based on the available flow regime maps in the literature, it was concluded that either the intermittent, or the annular flow regime will predominate for the channels and the flow conditions under consideration. Based on these flow regimes, internally consistent condensation heat transfer and pressure drop models were developed. The proposed pressure drop and heat transfer models predict 95% and 94% of the data within ±25%. The proposed models were then used to analyze the effect of various parameters like mass flux, saturation temperature, aspect ratio and diameter. As the mass flux increases, both the pressure drop and heat transfer increase due to an increase in flow velocities. As the saturation temperature decreases, the void fraction increases due to a decrease in the vapor to liquid density ratio. This increase in void fraction leads to an increase in flow velocities, which in turn leads to an increase in pressure drop and heat transfer. As the aspect ratio increases, both the pressure drop and heat transfer coefficients increase due to an increased occurrence of slugs. As the channel hydraulic diameter decreases, the pressure drop and heat transfer coefficient increase due to a decrease in film thickness and channel diameter.

The results from the current study thus make an important contribution to the understanding of pressure drop and heat transfer mechanisms during condensation in microchannels. The proposed model may be used by engineers for analyzing condensing two-phase flow in microchannels.

CHAPTER 1. INTRODUCTION

With the growing trend towards the decrease in the size of various thermal systems, there is an ever increasing need to understand and develop compact heat exchangers. Microchannels are increasingly being used in the industry to yield compact geometries for heat transfer in a wide variety of applications. Considerable literature exists on single-phase flow, pressure drop, and heat transfer in microchannels, as can be seen in some recent reviews of the literature (Tuckerman and Pease, 1981, 1982; Wu and Little, 1983, 1984; Sobhan and Garimella, 2001; Garimella and Sobhan, 2003; Garimella and Singhal, 2004; Liu and Garimella, 2004). Similarly, *boiling and evaporation* (pool boiling and convective boiling) in microchannels have also been studied due to the interest in heat removal at high heat fluxes in the electronics cooling industry. But limited research has been conducted on flow regimes, and the measurement of pressure drop and heat transfer coefficients during condensation in microchannel geometries, i.e. in the sub-millimeter range of hydraulic diameters. However, condensation is a process that is as important to an overall heat rejection system as boiling or evaporation. The prominence of studies on boiling and evaporation to date can be attributed to the electronics cooling industry's need to remove high heat fluxes through vaporization from compact devices that must be maintained at relatively low temperatures while being not readily accessible or conducive to the installation of large and complex cooling systems. While this is an important endeavor, the ultimate rejection of these large heat duties through compact condensers has not been addressed by the electronics cooling industry. With large heat rejection loads, compact condensers must be an integral part of system design, not an afterthought.

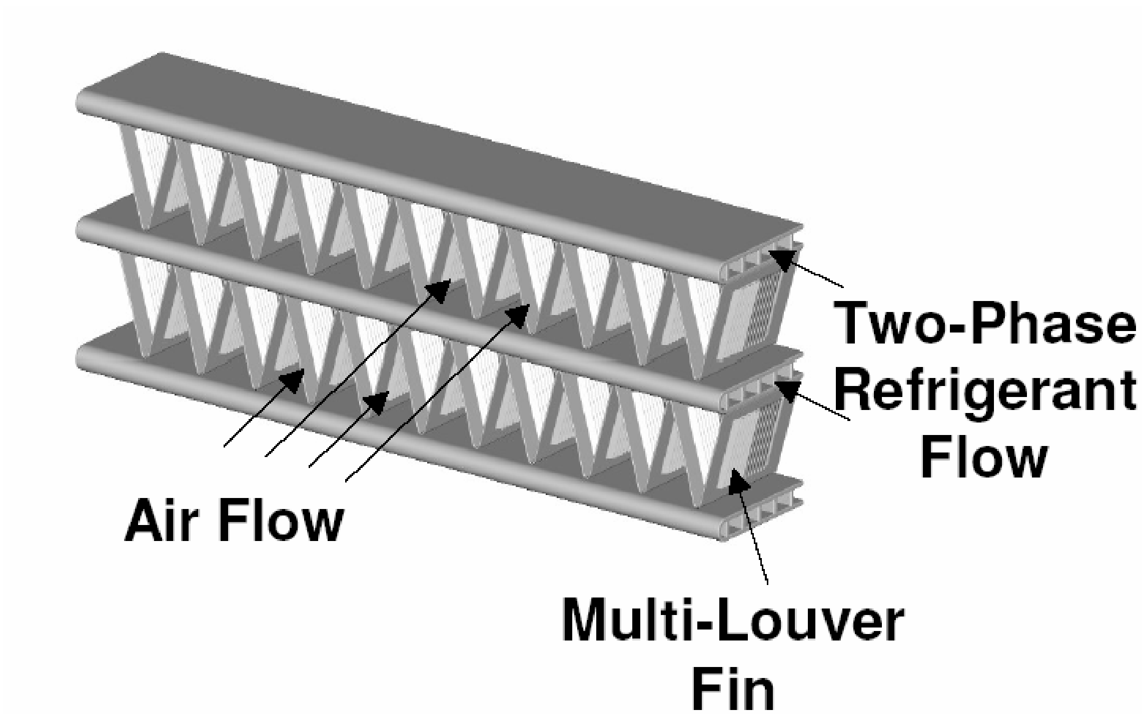

Figure 1.1: Schematic of a Microchannel Tube, Multi-louver Fin Condenser

Compact condensers have been designed and used by the automotive industry, whose air-conditioning condensers consist of rectangular channels with multiple parallel microchannels, often of non-circular cross-sections, cooled by air flowing across multi-louver fins. Figure 1.1 shows the schematic of one such heat exchanger. The microchannels used in these condensers often have hydraulic diameters in the 0.4-0.7 mm range, although an understanding of the fundamental condensation phenomena in these heat exchangers is just beginning to emerge.

The fundamental understanding of condensation at the micro-scales will yield far reaching benefits not only for the above-mentioned industries, but also for other as-yet untapped applications such as portable personal cooling devices, hazardous duty and high ambient air-conditioning, and medical devices, to name a few. It is also clear that the increase in surface area associated with the use of microchannels increases the importance of surface forces over that of body forces, as noted by Serizawa and Feng (2004). Thus, surface phenomena, and in some cases, surface characteristics, become more prominent in these small channels, and the interactions between the fluid and the wall increase in importance. This is another rationale for the commonly noted observation that in microchannels, surface tension and viscous forces dominate over gravitational forces. Neither the same measurement techniques nor the same modeling approaches used for the larger scale channels are adequate for addressing these phenomena that are specific to microchannels. The essential issue and research challenge in microscale condensation is that two-phase flow mechanisms and flow regime transitions in these small channels are considerably different from those found in the more conventional larger diameter tubes. This is because of the significant differences between large round tubes and the smaller non-circular tubes in the relative magnitudes of gravity, shear, and surface tension forces, which determine the flow regime established at a given combination of liquid and vapor-phase velocities. Thus, extrapolation of large round tube correlations to smaller diameters and non-circular geometries could introduce substantial errors into pressure drop and heat transfer predictions. However, heat transfer coefficient and pressure drop calculations for condensation in such geometries have thus far relied on correlations developed for large diameter round tubes (Lockhart and Martinelli, 1949; Chisholm, 1973; Traviss *et al.*, 1973; Shah, 1979). Such extrapolation of large round tube correlations could introduce substantial errors into the pressure drop and heat transfer coefficient predictions, rendering them useless for microscale condensation. In addition, pressure drop and heat transfer are strong functions of local vapor quality. To accurately design these types of heat exchangers for condensation, the variation of the two-phase flow patterns and its effect on pressure drop and heat transfer as the refrigerant changes from vapor to liquid needs to be understood. Simply using the average characteristics at a vapor quality of 50% could result in serious over- or under-predictions of the pressure drop and heat transfer, thus leading to inadequate designs. Hence, accurately representing the local heat transfer and pressure drop characteristics using flow regime based correlations is essential for design.

In the current study, a novel measurement technique was developed to measure heat transfer coefficients and pressure drop during the condensation of R134a in small hydraulic diameter ($100 < D_h < 160$ μm) channels, which are fabricated on a copper substrate by electroforming copper onto a mask patterned by X-ray lithography. This method enables accurate determination of heat transfer coefficients for refrigerant R134a, which in the current study, are measured for $300 < G < 800$ kg/m^2-s for $0 < x < 1$ at four different saturation temperatures 30, 40, 50 and 60^{o}C. The measured heat transfer coefficients and pressure drops were analyzed and compared with the limited heat transfer and pressure drop models available in the literature for similar flow conditions and explanations for agreements/disagreements are discussed. Condensation heat transfer and pressure drop models are developed using these data based on flow regime maps available in the literature.

This dissertation is organized as follows. In chapter two, a review of the literature on condensation pressure drop and heat transfer is presented and the need for the present work is identified. The details of the channel fabrication and the experimental facility are provided in chapter three. The data analysis technique used for determining pressure drops and heat transfer coefficients from the measured experimental parameters is presented in chapter four along with an analysis of the corresponding uncertainties. Chapter five presents the results obtained from the analysis of the data. These experimental results are compared with the commonly cited pressure drop and heat transfer correlations and possible reasons for agreement/disagreement are discussed. In chapter six, new flow regime based pressure drop and heat transfer models are proposed. The effects of variations in various parameters such as mass flux, temperature, channel aspect ratio and diameter are discussed. Chapter seven presents the important conclusions from the current study and suggest areas for further research on condensation in microchannels.

CHAPTER 2. LITERATURE REVIEW

Numerous research efforts have been conducted to understand two-phase flow in microchannels and minichannels. Garimella (Kandlikar *et al.*, 2005) provides one of the recent comprehensive reviews of the current state of the art in the field of condensation in microchannels. Ghiaasiaan and Abdel-Khalik (2001) presented a review of the research work being conducted on two phase flow in microchannels ranging in D_h from 0.1 to 1 mm. They state the need to obtain more data to enable the analysis of the effects of surface tension, surface wettability and liquid viscosity. The existing correlations for predicting pressure drop and heat transfer are still inadequate. The review of the literature presented below is divided into three sections, namely, two-phase flow, pressure drop and heat transfer. Based on this review, the deficiencies in the understanding of condensation in microchannels are discussed.

2.1. Two-Phase Flow

Although research on two-phase flow regimes has been conducted for a long time, much of this work has focused on large diameter tubes in air-water or steam-water mixtures. Early attempts at understanding the influence of decreasing diameters on flow regime transitions include those by Suo and Griffith (1964), Barnea *et al.* (1983), Damianides and Westwater (1988), Fukano *et al.* (1989) and others, who proposed explanations and transition criteria primarily for the intermittent regime in adiabatic air-water flows as departures from the flow regime maps of Mandhane *et al.* (1974) and the theoretical predictions of Taitel and Dukler (1976). Mishima and Hibiki (1996) and Mishima *et al.* (1997; 1998) employed neutron radiography to non-intrusively investigate two-phase flow phenomena in upward flow of air-water mixtures in vertical tubes with $1 < D < 4$ mm, and found reasonable agreement with Mishima and Ishii's (1984) transition criteria. Coleman and Garimella (1999) and Triplett *et al.* (1999b) conducted similar studies on the effect of tube diameter and shape on flow patterns and flow regime transitions for air-water flow in circular, rectangular and semi-triangular tubes in small diameter ($1.1 < D < 5.5$ mm) channels and documented a variety of regimes such as bubble, dispersed, elongated bubble, slug, stratified, churn, slug-annular, wavy, annular-wavy, and annular. Several other adiabatic air-water flows in these smaller channels can also be found in the literature (Barnea *et al.*, 1983; Galbiati and Andreini, 1992; Mishima and Hibiki, 1996; Ide *et al.*, 1997; Zhao and Bi, 2001a). Yang and Shieh (2001) noted that for $1 < D < 3$ mm horizontal tubes, slug-annular transition for R-134a occurs at lower gas velocities, while the intermittent-bubbly transition occurred at higher liquid velocities, both attributed to the lower surface tension of R134a compared to the air-water pair. Tabatabai and Faghri (2001) developed a flow regime map for microchannels based on the relative effects of surface tension, shear, and buoyancy forces. They noted that ripples are generated on the annular layer with an increase in gas-phase velocity which leads to the formation of collars and bridges, with the size and gap between them determining the occurrence of slug, plug and bubble regimes. Wambsganss *et al.* (1991) reported flow patterns and transitions in a single rectangular channel with aspect ratios of 6.0 and 0.167 and D_h = 5.45 mm through flow visualization and dynamic pressure measurements, and later (Wambsganss *et al.*, 1994) extended this work to develop criteria for transition from bubble or plug flow to slug flow based on root-mean-square pressure changes.

Studies on adiabatic two-phase air–water, nitrogen-water and steam-water flow through microchannels with D << 1 mm (25, 50, 100 μm) have also appeared recently (Feng and Serizawa, 1999). Liquid slug, gas core with liquid film, gas core with ring-shaped liquid film, and gas core with deformed interface and various other combinations have been reported, with flow regimes also defined in terms of the probability of occurrence of these mechanisms. Axi-symmetric flow patterns clearly demonstrate the absence of gravitational effects. Similarly, the absence of bubbly flow is attributed to the liquid phase Reynolds number (*Re*) being very low; thus, no bubble breakup induced by liquid phase turbulence occurs. Kawaji *et al.* (Chung and Kawaji, 2004; Chung *et al.*, 2004; Kawahara *et al.*, 2005) have also found that in 50 - 530 μm channels, while for the larger tubes in this range, the flow patterns are similar to those reported for channels of ~1 mm diameter, e.g., Triplett *et al.* (1999b), for the smaller channels, only slug flow is observed. The absence of bubbly, churn, slug–annular and annular flow is attributed to the greater viscous and surface tension effects. They state that with decreasing channel size, the Bond number, the superficial Reynolds numbers, the Weber number, and the capillary number all decrease, which implies that the influence of gravitational and inertia forces decrease, while the importance of surface tension and viscous forces increases. Serizawa *et al.* (2002) also conducted a study similar to that of Kawahara *et al.* (2002) on 20-100 μm circular tubes. Some of these investigators develop particularly imaginative terms that lead to proliferation (and confusion) about the descriptors for the observed flow mechanisms. Some of the terms they use include: dispersed bubbly flow, gas slug flow, liquid ring flow, liquid lump flow, skewed barbecue (Yakitori) shaped flow, annular flow, frothy or wispy annular flow, rivulet flow and liquid droplets flow.

There are only a few relevant studies on vapor-liquid phase-change flows in small diameter channels, as compared to the relatively large number of investigations on adiabatic two-phase flows. Thus, flow maps reported in the early works on refrigerant two-phase flow for large tubes by Traviss and Rohsenow (1973), the modified Taitel-Dukler (1976) maps of Breber *et al.* (1980), Sardesai *et al.* (1981), Tandon *et al.* (1982), Soliman (1982), and others are still used, somewhat inappropriately for smaller channels, due to the unavailability of maps for the small channels for phase-change conditions. These maps primarily focus on the ~5 < D < 25 mm range, and are therefore meant for determining the transitions between gravity-dominated stratified wavy flows and shear-dominated annular flows. In these maps, the von Karman universal velocity profile is often used to describe the film velocity, which is in turn used in conjunction with two-phase multipliers to express the wall shear stress. In many of these maps, the stratified-to-annular transition is represented in terms of a constant value of the Froude number (Fr). Soliman (1986) also developed a correlation for the mist-annular transition using Weber number (We) to represent the balance between the likelihood of entrainment due to the inertia of the vapor phase ($\rho_G V_G^2$) shearing droplets from the surface of the liquid film, and viscous ($\mu_L V_L/\delta$) and surface tension (σ/D) forces stabilizing the liquid film. Dobson and Chato (1998) investigated condensation in small diameter (3.14 < D < 7.04 mm) tubes using several pure refrigerants and blends. The flow progressed through annular-mist, annular, wavy-annular and slug flow depending on the mass flux and quality. As the tube diameter decreased, the transition from wavy flow to wavy-annular flow, and from wavy-annular to annular flow moved to lower qualities. They found good agreement with the Mandhane *et al.* (1974) map after correcting the superficial vapor velocity with the factor $\sqrt{\rho_g / \rho_a}$ to account for gas-phase kinetic energies differences between air and refrigerant vapor. They divided the observed regimes only into gravity dominated and shear-controlled regimes based on *Fr*.

Condensation flow regimes for $3.14 < D < 21$ mm were reported by El Hajal *et al.* (2003), based on their previous work (Kattan *et al.*, 1998a, b, c) on flow boiling by fitting data from several investigators. They represented the void fraction (deduced by relating turbulent annular flow heat transfer data to film thickness) as the logarithmic mean of the Rouhani-Axelsson (1970) drift-flux void fraction and the homogeneous void fraction. Liquid-vapor cross-sectional areas are derived from the void fraction to plot flow regime transitions adapted from the corresponding boiling criteria. While some agreement with the data of various investigators is demonstrated, an unrealistically large intermittent regime, even for an 8 mm tube, is predicted at x as high as about 45% and $G > 1000$ kg/m^2-s. Coleman and Garimella (2000b; 2000a; 2003) and Garimella (2004) conducted flow visualization studies during condensation of refrigerant R134a in nine different tubes of round, square and rectangular cross-sections ($1 < D_h < 4.91$ mm). They developed flow regime maps addressing the effect of diameter and shape for a wide range of mass fluxes ($150 < G < 750$ kg/m^2-s) and qualities ($0 < x < 1$). They reported that as the tube diameter decreases, the area (on a mass-flux vs quality map) under the intermittent and annular flow regime increases, while the wavy flow regime gradually disappears.

Only a few studies have recently appeared on flow patterns during condensation in channels with hydraulic diameters less than 100 μm. Chen and Cheng (2005) reported results of visualizations studies of condensation of steam in trapezoidal silicon microchannels with hydraulic diameters of 75 μm and 80 mm. They observed that droplet condensation took place near the inlet of the microchannels while an intermittent flow of vapor and condensate was observed downstream of the channels. The traditional annular flow, wavy flow and dispersed flow were not observed in microchannels. These findings are in agreement with the findings of Coleman and Garimella (1999; 2003) that the intermittent regime becomes larger as the tube diameter decreases. Wu and Cheng (2005) conducted flow visualization experiments during condensation of steam in a 82.8-μm hydraulic diameter and 30-mm long tube. The experiments were conducted for the mass flux range 193 kg/m^2-s to 475 kg/m^2-s and the pressure range 10^5 Pa to 4.15×10^5 Pa. They reported that at a given inlet pressure and mass flux, the flow pattern depends on the location along the length of the tube and also on time. Different flow patterns can appear at different locations along the tube at the same flow conditions and time. They also discuss a new flow pattern termed vapor injection flow, consisting of a series of bubble growth and detachment events, which appear and disappear periodically and introduce condensation instabilities.

2.2. Pressure Drop

The Lockhart and Martinelli (1949), Chisholm (1973), and Friedel (1979) correlations are widely used to determine pressure drop in conventional channels. These correlations are sometimes also used with modifications to account for the specific geometry or flow conditions under consideration. While these correlations have shown considerable deviations from the data for small channels with phase-change flows, they continue to be the basis for many of the more recent correlations. As in the case of flow regime mapping, most of the work on the small channels has been on adiabatic flows of air-water mixtures. Some investigators (Ungar and Cornwell, 1992; Kureta *et al.*, 1998; Triplett *et al.*, 1999a) have shown that the homogeneous flow model is reasonably successful in predicting pressure drop during adiabatic flow and boiling in channels with $1 < D_h < 6$ mm. The equivalent mass velocity concept of Akers *et al.* (1959) was used by Yang and Webb (1996b) for adiabatic two-phase flows of refrigerant R-12 in rectangular plain and microfin tubes with D_h = 2.64 and 1.56 mm, respectively. The equivalent friction factor is based on an equivalent all-liquid flow that yields the same frictional ΔP as the two-phase flow. Yan and Lin (1999) used the same concept to correlate ΔP for R-134a in a 2 mm circular tube. The two studies yield substantially different results, with Yan and Lin's single-phase friction factors being exceedingly high, which they attributed to the influence of entrance lengths and tube roughness.

Examples of modifications to classical correlations include the work on air-water flows through 1-4 mm tubes of Mishima and Hibiki (1996), who developed the expression $C = 21\left(1 - \exp\left(-0.319 D_h\right)\right)$ for Chisholm's (1967) parameter in the Lockhart-Martinelli (1949) correlation. Wang *et al.* (1997) developed flow-regime-specific values for the C parameter in Chisholm's (1967) equation for the Lockhart-Martinelli (1949) multiplier based on measured ΔP during adiabatic flow of refrigerants R-22, R-134a, and R-407C in a 6.5 mm tube. Based on tests for air-water and R410A in tubes with $D < 10$ mm, Chen *et al.* (2001) modified the homogeneous flow pressure drop model by including the Bond number (Bo) and the Weber number (We) to account for the effects of surface tension and mass flux. They further stated that the Friedel (1979) correlation overemphasizes the effect of gravity through Fr and does not emphasize the effect of surface tension through We as much. They thus modified the Friedel (1979) correlation to properly account for these effects. Zhao and Bi (2001b) similarly modified this parameter for air–water flow through equilateral triangular channels with D_h = 0.866, 1.443 and 2.886 mm. Lee and Lee (2001) also noted that in surface-tension dominated air-water flows through rectangular channels with gaps of 0.4 to 4 mm, the effect of slug Reynolds number (Re_{slug}), the ratio of viscous and surface tension effects ($\psi = \mu_L j/\sigma$) and the parameter $\lambda = \mu_L^2/\left(\rho_L \sigma D_h\right)$ were significant and correlated the Chisholm parameter as $C = A\lambda^q \psi^r \mathrm{Re}_{LO}^s$. This expression accounts for the gap size as well as the phase flow rates, with the flow tending more to plug and slug flow as the gap size decreases, and an increasing effect of surface tension due to the curved gas/liquid interface at the edge of the bubble. Tran *et al.* (2000) attributed the higher ΔP in small tubes to the fact that coalesced bubbles in small channels are confined, elongated, and slide over a thin liquid film, whereas in the case of large tubes, the bubbles may grow and flow unrestricted through the tubes. Therefore, for boiling of refrigerants in circular (2.46 and 2.92 mm) and rectangular (4.06×1.7 mm) channels, they proposed a modified version of the Chisholm (1973) correlation that accounted for the role of surface tension through the confinement number introduced by Cornwell and Kew (1993). Zhang and Webb (2001) measured adiabatic two-phase pressure drops for R-134a, R-22 and R-404A in circular tubes (D = 3.25 and 6.25 mm) and a multi-port extruded aluminum tube (D_h = 2.13 mm). Since the dependence of the Friedel (1979) correlation on We and Fr was weak, they modified it to be a function of reduced pressure (p_r) instead of density and viscosity ratios.

Among regime-specific (intermittent) models, Dukler and Hubbard (1975) developed a model for pressure drop in intermittent flow through 38 mm diameter horizontal tubes using air water mixtures. Their model consists of a slug of liquid with some gas entrained and is based on the observation that a fast moving slug overruns a slow moving liquid film accelerating it to full slug velocity. The bubble/film portion of the flow was assumed to be stratified and cause negligible pressure drop. The authors also developed expressions for the relative slug lengths. Fukano *et al.* (1989) conducted experiments with air-water flow in 1, 2.4 and 4.9 mm tubes and used these data to propose pressure drop correlations for bubbly, slug, plug and annular flow. In slug flow, they represented the relative velocity between the gas bubble and the liquid in the slug as $u_r = 0.2\left(j_G + j_L\right)$ where $j_G + j_L$ is the liquid slug velocity, and also established a relationship for the liquid slug length. Assuming that in slug and plug flows, ΔP occurs in the liquid slug only, while in annular and bubbly regions, it occurs over the entire length of the channel, they developed equations for the two-phase multiplier. They also accounted for expansion losses as the liquid flowed from the annular film surrounding the gas bubble into the liquid slug region. Garimella *et al.* developed ΔP models for condensation of refrigerant R134a in intermittent flow through circular (Garimella *et al.*, 2002) and non-circular (Garimella *et al.*, 2003b) microchannels with $0.4 < D_h < 4.9$ mm. In addition, they developed a model for annular flow (Garimella *et al.*, 2003a), and further extended it to a comprehensive multi-regime ΔP model (Garimella *et al.*, 2005) for microchannels for $150 < G < 750$ kg/m^2-s.

As the channel approaches the smaller dimensions, Kawahara *et al.* (2002), Chung and Kawaji (2004) and others have found that the ΔP for air-water flow through 530 and 250 μm channels and for 100 and 50 μm channels required different mixture viscosity models (Dukler *et al.*, 1964; Beattie and Whalley, 1982) to make homogeneous flow models work. This was attributed to the lower mixing losses due to the weak momentum coupling between the phases in the smaller channels. Like many other investigators, they also proposed a different value for the C parameter (C = 0.24) in the Lockhart-Martinelli (1949) multiplier, and subsequently revised it based on tests with a 96 μm square channel (Chung *et al.*, 2004). Since these models were not able to predict the data for 50 and 100 μm channels adequately, they used the intermittent flow model of Garimella *et al.* (2002) with modifications to calculate pressure drops. Garimella *et al.* (2002) represented the total pressure drop as the summation of the frictional ΔP in the slug and bubble regions and the ΔP associated with the transitions between these regions. Chung and Kawaji (2004) ignored the ΔP associated with the transitions between the slug and bubble regions This model agreed better with the 50 and 100 μm channel data than the homogeneous and two-phase multiplier approaches, but was not recommended for D_h > 100 μm, where the flow is not exclusively intermittent.

2.3. Heat Transfer

Two idealized modes of condensation heat transfer, gravity driven and shear-driven, have received the most attention in the literature, although almost all of it is for channels with D_h > ~7 mm. Gravity driven models are not particularly relevant for the work on microchannels proposed here. A model that has been used widely until recently is the Akers *et al.* (1959) technique of determining an equivalent mass flux that would provide the same shear as the two-phase flow; thus replacing the vapor core with an additional liquid flow rate, and then treating the combined flux as being in single-phase flow. Recent papers have shown that the predictions of these models are not very good, and also that the appropriate friction factors and driving temperature difference are not applied when transforming the two-phase flow to an equivalent single-phase flow. Although corrected versions (Moser *et al.*, 1998) of this model are now available, implementing the corrected versions renders them as involved as the boundary layer analyses, and does not seem to offer any additional ease of use.

Annular flow models, sometimes also refered to as shear-based models, usually relate the interfacial shear stress to the heat transfer across the liquid film. This technique was first introduced by Carpenter and Colburn (1951) and later adapted by several other researchers (Soliman *et al.*, 1968; Traviss *et al.*, 1973) with modifications in the determination of interfacial shear Chen *et al.* (1987) developed a general purpose annular flow correlation starting with asymptotic limits, and blending them through simple combinations of the terms at the respective limits. Several researchers have also used a two-phase multiplier approach similar to that used in the pressure drop models. In the case of the heat transfer models, the two-phase multiplier is applied to the respective single-phase heat transfer coefficient. It should be noted that previously discussed shear based models also use two-phase multipliers to determine the interfacial shear stress, and thus the two approaches are analogous to each other.

Shah (1979) proposed a purely empirical correlation based on the data from multiple researchers. This correlation is commonly used due to its simplicity, the wide range of data that were utilized in its development, and its comparatively good predictions for annular flows. The four-zone map of Breber *et al.* (1980) for $D > 4.8$ mm, based on their transition criteria described above is also widely used. They recommend a convective two-phase multiplier based correlation (annular flow), a Nusselt-type correlation (stratified flow), and due to the lack of appropriate models, annular flow correlations for intermittent and bubbly flows also. Several researchers such as Dobson and Chato (1998), Cavallini *et al.* (2002), and Thome *et al.* (2003) have analyzed data from multiple researchers and developed condensation models spanning a wide range of mass fluxes, diameters, and fluids. Although these correlations in general yield more accurate predictions over a wide range of conditions, they fail to account for the effect of individual flow regimes identified in the previous section of this literature review. Most of these correlations classify the data into stratified/wavy or annular flows. Heat transfer models for intermittent and mist flow regimes have still not been successfully devloped in these studies. Soliman (1986) proposed a quasi-homogeneous model for the mist flow regime.

Only a few researchers have reported heat transfer measurements and models for tubes of $D < 3$ mm. Webb and coworkers (Yang and Webb, 1996b, a, 1997; Webb and Ermis, 2001; Zhang and Webb, 2001) have conducted experiments to determine heat transfer coefficients in extruded aluminum tubes with multiple parallel ports of $D_h < 3$ mm. They have attempted several different approaches to model the heat transfer coefficients including shear stress models and equivalent mass flux models, but a reliable model that predicts and explains the variety of trends seen in these results has however not been developed yet. Yang and Webb (1997) explicitly account for surface tension forces in microchannels (with microfins) by computing the drainage of the liquid film from the microfin tips and the associated heat transfer enhancement when the fin tips are not flooded. Wang *et al.* (Wang and Rose, 2004; Wang *et al.*, 2004) also proposed an analytical treatment for microchannels with D ~1 mm that account for the combined influence of surface tension, shear and gravity in the condensation process.

Baird *et al.* (2003) conducted an experimental investigation to determine the local heat transfer coefficient during condensation in 0.92 mm and 1.95 mm internal diameter tubes. They used thermo-electric coolers to achieve very low mass fluxes. The data showed a strong influence of mass flux and local quality on the heat transfer coefficient and a relatively weaker influence of system pressure. The observed heat transfer coefficient generally increases with the increasing mass flux. Increasing system pressure at constant wall heat flux leads to a decrease in local heat transfer coefficients. To predict the heat transfer coefficients, they proposed an approach similar to that developed by Moser *et al.* (1998) based on a core annular shear-driven gas-liquid flow in which the gas-liquid interface is assumed to be smooth and the liquid film is turbulent, with modifications to the film thickness parameter.

Garimella and Bandhauer (2001) conducted heat transfer experiments using the tubes ($0.4 < D_h < 4.9$ mm) that were used for the ΔP experiments of Garimella *et al.* (2002; 2003a; 2003b; 2005) described previously. They specifically addressed the problems in heat transfer coefficient determination due to the high heat transfer coefficients and low mass flow rates in microchannels by developing a novel thermal amplification technique. Bandhauer *et al.* (2006) reported that during the condensation process, as the refrigerant quality decreases, the flow changes from mist to annular to intermittent flow with large overlaps in these types of flows. They developed an annular flow regime based model, since most of their data were either in the annular flow regime or in transition between the annular flow regime and other regimes. They noted that many of the available shear-driven models, though sound in formulation, led to poor predictions because of the inadequate calculation of shear stresses using pressure drop models that were not applicable to microchannels. Thus, their model is based on boundary layer analyses analogous to the development by Traviss *et al.* (1973), but with the shear stress being calculated from the ΔP models of Garimella *et al.* (2005) developed specifically for microchannels. Their model also indirectly accounts for surface tension through a surface tension parameter in the ΔP used for the shear stress calculation to yield accurate microchannel heat transfer predictions over a wide range of conditions.

Sun *et al.* (2004) recently proposed a heat transfer model for slug flow in a horizontal tube, based on evaporation of refrigerant-12 in a 9 mm tube. To calculate the characteristics of slug flow (slug length, bubble length), they used the model proposed by Dukler and Hubbard (1975) with some modifications. They determined separate heat transfer coefficients for the slug region and bubble/film region, and determined the average heat transfer coefficient by adding the two in the ratio of the slug and bubble lengths, respectively. Both slug and bubble/film heat transfer coefficients were determined as a combination of forced convective and nucleate boiling heat transfer coefficients.

2.4. Deficiencies in Understanding of Microchannel Condensation

The above discussion shows that there are significant gaps in the understanding of two-phase flow mechanisms, pressure drops, and heat transfer during condensation in microchannels. Many of the studies in the literature have investigated channels with much larger D_h than are of interest in the present study. Also, most of the studies on small D_h channels have used isothermal air-water mixtures to simulate two-phase flow. However, due to the adiabatic flow in these studies, the results are not directly applicable to phase-change situations. Often, the large disparity in fluid properties between air-water mixtures and those of refrigerant vapor-liquid phases renders these correlations inapplicable for use in phase change (condensation). Also, the use of air-water mixtures at best provides some knowledge of flow patterns and ΔP, but due to the inherent lack of phase change in air-water studies, no knowledge about condensation heat transfer can be obtained. The limited models of condensation heat transfer at small D_h have typically been only able to predict the specific data for which they were developed with any degree of accuracy, failing to various extents when extrapolated beyond their limited ranges. Often, the match between models developed for one regime and those for an adjacent flow regime even by the same researcher has not been good, leading to large discontinuities in predictions as the flow conditions move across regimes.

Some of this discrepancy in the experimental results reported by several authors can be attributed to experimental uncertainties, especially in the case of microchannels. Sobhan and Garimella (2001) reported that discrepancies in the experimental results can be attributed to entrance and exit effects, differences in surface roughnesses, non uniformity of channel dimensions, the nature of thermal and flow boundary conditions, and uncertainties and errors in instrumentation, measurement, and measurement locations. Celata (2004) has assessed discrepancies in friction factors reported by various authors. The main reason for the discrepancy was proposed to be the experimental uncertainty due to uncertainties in the measurement of channel roughness and dimensions. Liu and Garimella (2004) also reported that errors in the measurement of the microchannel geometry are the greatest contributors to the uncertainty in friction factor. Xu *et al*. (2000) conducted an experimental investigation to determine the effect of using Al or Si channels in the experiments. They suggest that the results of the various researchers who have performed experiments using Al microchannels are inconsistent, while the results of independent investigations conducted using Si microchannels are more consistent. For illustrative purposes, assuming that the surface roughness of Al causes a gap of 0.1 μm between the cover and the Al surface, the authors showed that this can lead to a very significant error in determination of the microchannel cross-section area. On the other hand, the Ions Osmosis process used between the two contact surfaces of silicon wafers and pyrex glass ensures that the two surfaces are sealed without introducing dimensional error in the microchannels. They also stated that in channels with improper joints, leakage from the side of the channels at high pressure has often led to improper calculation of flow velocities.

Thus, there is a strong need for accurate measurement of condensation heat transfer coefficients (h) in microchannel geometries as a function of mass flux, saturation conditions and refrigerant quality, and for developing analytical predictive models based on these data. Some of the main challenges in measuring phase-change heat transfer in microchannels that need to be addressed are limited spaces for measurement probes, small flow rates, heat transfer rates and temperature differences that are difficult to measure accurately. Also the refrigerant channels need to be manufactured and sealed in a manner that introduces minimal dimensional uncertainties and surface roughnesses.

2.5. Objectives of Current Study

It is clear that there are still several unanswered issues that must be addressed to enable a thorough understanding of microscale condensation heat transfer and pressure drop, especially as D_h decreases significantly below 1 mm. Thus, the specific objectives of the current study are as follows:

- Develop and fabricate a test apparatus and a test facility that enables the experimental investigation of condensation h and ΔP in microchannels of $100 < D_h < 200$ μm, for which no reliable data or fundamental understanding is available.
- Analyze the data to deduce h and ΔP, and quantify the uncertainties in the obtained data.
- Develop internally consistent h and ΔP models with particular attention to dominant flow phenomena and transitions that differ from those in conventional geometries.

CHAPTER 3. EXPERIMENTAL APPROACH

The experimental approach used to conduct the tests in this study is described here. The approach and the test section geometry selection are guided by the review of the literature discussed in the previous chapter. Table 3-1 provides details of the geometries tested in the current study.

Table 3-1: Details of the Test Geometries

Width w_{TS} (µm)	Depth d_{TS} (µm)	Hydraulic Diameter D_h (mm)	Aspect Ratio AR	No. of Parallel Channels, N
100	100	0.100	1	20
200	100	0.133	2	18
300	100	0.150	3	15
400	100	0.160	4	15

Tests were conducted for $30 < T_{sat} < 60^{o}C$; $300 < G < 800$ kg/m^2-s, and $\Delta x \leq 40\%$. The primary challenge posed by these test conditions was the measurement of low condensation heat duties. At the lowest saturation temperature case, i.e 30^{o}C, and the highest mass flux 800 kg/m^2-s, the condensation heat duty for a single 200×100 µm channel is just 0.7 W for a change in quality of 25%. Since these low heat duties (even at the highest mass fluxes) are very difficult to measure, multiple parallel channels were used. For example, for eighteen 0.2×0.1 mm channels, the test section heat duties for Δx = 40% vary from ~ 4 W (@ T = 60°C; G = 200 kg/m^2-s) to ~ 20 W (@ T = 30°C; G = 800 kg/m^2-s). The approach described below was specifically developed to address this challenge and yield accurate heat transfer coefficients as a function of quality for the different mass fluxes, saturation temperatures and geometries under consideration. Appendix A supplements this chapter by providing additional pictures of the fabrication and equipment details.

3.1. Test Section Configuration and Fabrication

The test section consists of a refrigerant R134a-to-water heat exchanger, wherein the refrigerant channels are sandwiched between the water channels at the top and bottom as shown in Figure 3.1.

The primary considerations in designing the test section were:

- Multiple channels yield more accurate measurements, because the heat duties are higher than those for single channels.
- The experiments should enable measurement of local heat transfer coefficients, $h = h(x)$.
- Overall UA of the heat exchanger should be such that heat transfer occurs across a measurable temperature difference, which reduces the error in h due to uncertainties in temperature measurement.
- Refrigerant-side thermal resistance should be the dominant resistance.

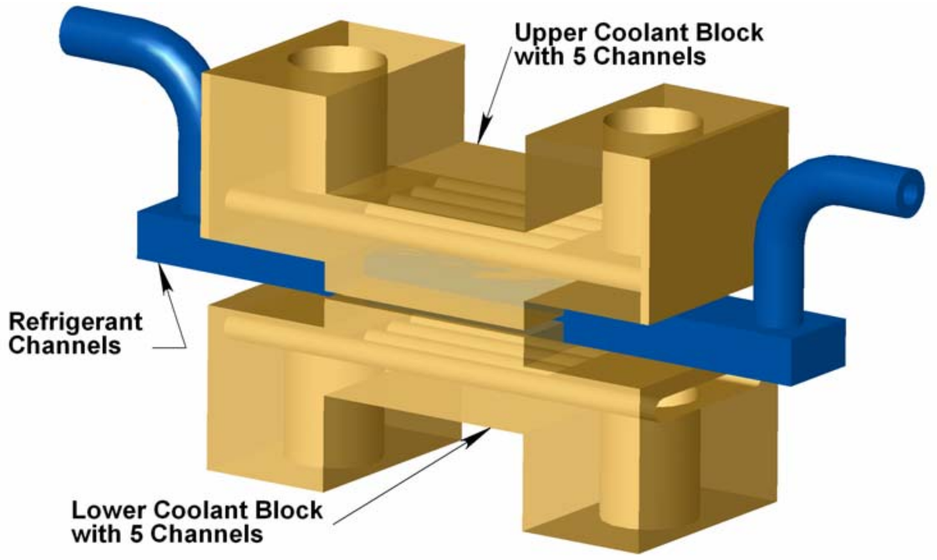

Figure 3.1: Test Section Assembly

3.1.1. Refrigerant Channel Fabrication

Refrigerant channels were fabricated by HT Micro, Inc. (www.htmicro.com) using the process of electroforming. Copper was selected as the material of fabrication due to its high conductivity, its ability to withstand high refrigerant pressures and the applicability of the diffusion bonding process to form the channels. This process starts with the fabrication of an X-ray mask, which is subsequently used to pattern a PMMA (poly-methyl methacrylate) mold over a copper wafer. Figure 3.2 shows the layout of the mask used for X-ray lithography. As shown in the layout, seven different devices (each set of channels, for example 20 0.1×0.1 mm channels, is referred to as device) are obtained from each wafer. All devices have a constant depth of 100 μm, but the varying number of channels and widths yield different channel aspect ratios. The overall lengths of the channels with and without headers are 48 mm and 40 mm respectively.

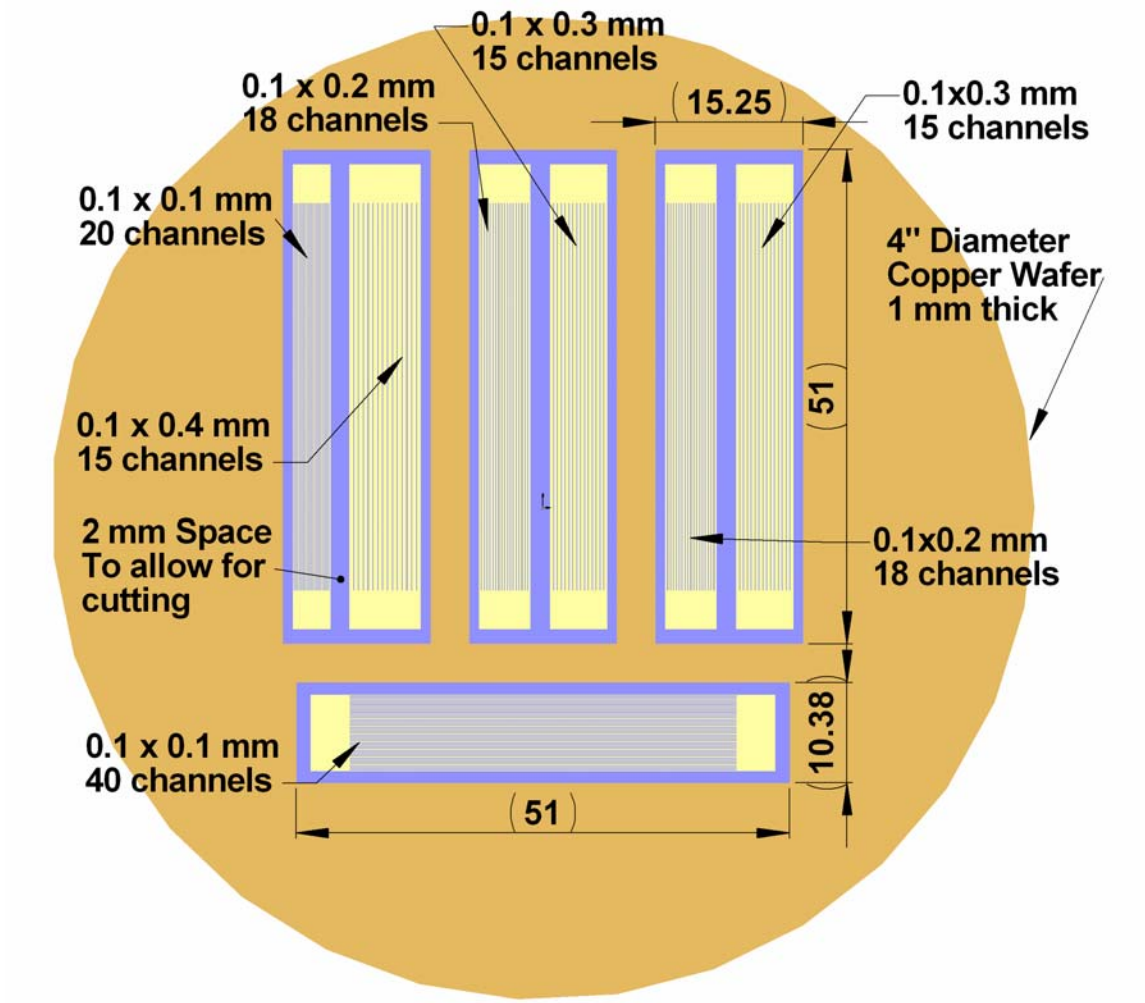

Figure 3.2: Wafer Layout for Electroforming

The corners of the headers and channel wall ends are rounded to reduce the mechanical stress under high pressure operating conditions. The radius of curvature in the header corners is 1 mm and that of the channel wall ends is 100 micrometers. Figures A.1 to A.4 in Appendix A show pictures of the various stages of preparation of the X-ray Mask and the final wafer with PMMA mold.

Copper is then deposited into the mold using the process of electroforming followed by planarization. Holes for refrigerant inlet and exit are then drilled into headers of each of the refrigerant channel sets (devices). Figures A.5 to A.8 in Appendix A show pictures of the wafer during various stages in this process. Figure 3.3 shows a picture of the developed refrigerant channels after the removal of the PMMA mask.

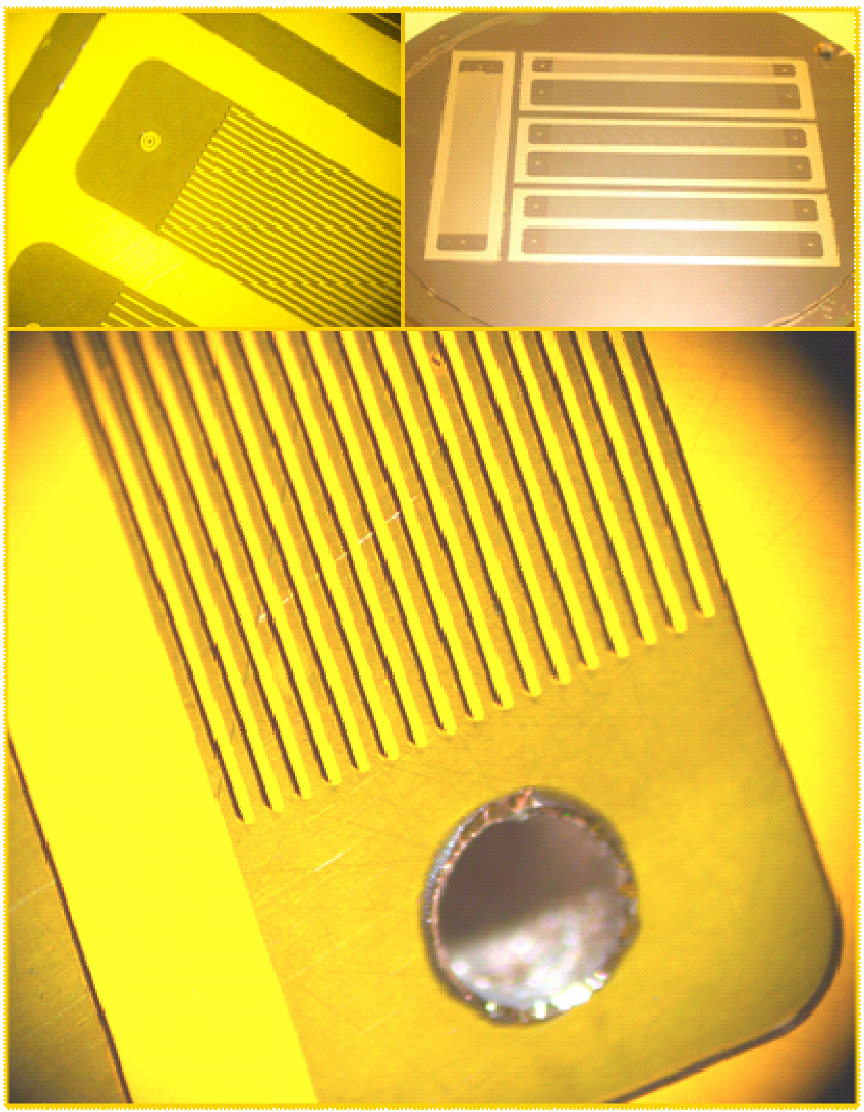

Figure 3.3: Developed Refrigerant Channels before Diffusion Bonding

An open header area and the location of the inlet and exit ports allow for the distribution of refrigerant into the various parallel channels. These channels are then closed using diffusion bonding with another copper wafer (Figure A-9) on the top of the refrigerant channels. No adhesive is used in this process, and bonding is performed in a vacuum oven at 450^{o}C for 3 hours. There is some depression in yield strength resulting from this (from ~ 250 MPa to ~ 175 MPa) (Christenson, 2005). In this process, the bonded joint retains properties close to those of the bulk material, allowing the channels to withstand pressures as high as 10 MPa (Christenson, 2005). After the bonding process, the copper wafers on either side are thinned to the desired thickness of 1 mm from the initial thickness of 6 mm and the individual devices are diced to yield separate refrigerant channels. Copper tubes of 3.175 mm (1/8") OD are then soldered onto the device (with mating holes drilled initially). Appropriate precautions are taken to make sure that no solder material flows into the channels. Figure 3.4 shows a picture of the final assembled device. The dimensional uncertainty of the channels is ± 0.5 μm, with a surface roughness of ~10-15 nm (Christenson, 2005). Figure 3.5 clearly shows the smooth surface profile of the channel walls. The taper in the vertical walls is less than 1^{o}. Figures A.10 to A.12 in Appendix A show additional SEM images illustrating the smooth wall surface and negligible taper in the walls. Figure A.13 and Figure A.14 in Appendix A show a section of the refrigerant channels after the diffusion bonding process, showing a good quality joint. In addition, these copper channels can be easily soldered to the coolant channel copper blocks at the top and bottom as shown in Figure 3.1.

Figure 3.4: Completed Refrigerant Channels (Device)

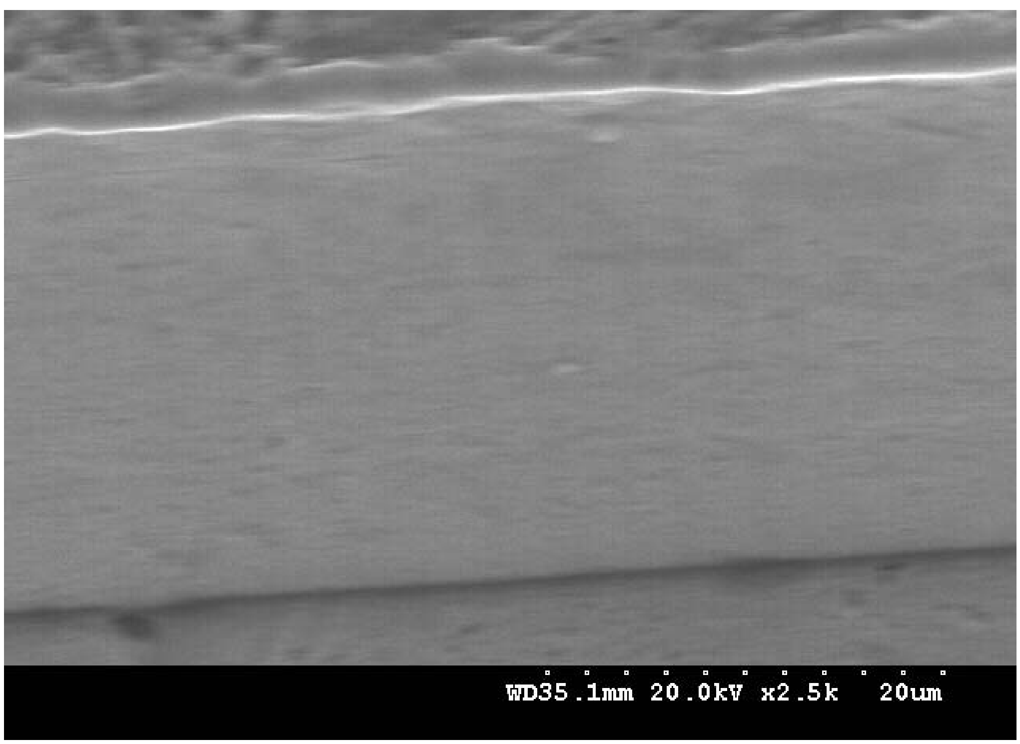

Figure 3.5: SEM Image of Channel Wall Surface Profile

3.1.2. Test Section Assembly

In the present case, the coolant water, flows through channel drilled in copper blocks (Figure 3.6).

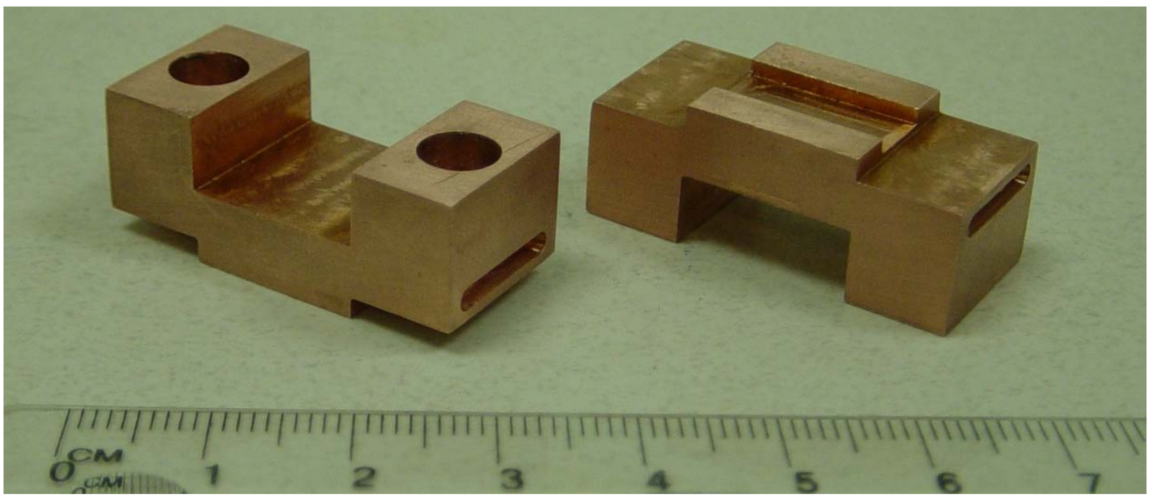

Figure 3.6: Coolant (Water) Channel Blocks

Each water channel block has five 1.5 cm long holes of 0.79 mm (1/32") diameter drilled into the block. Figure 3.7 shows the schematic of the cross-sectional view of the water channel block with five drilled holes. All dimensions in Figure 3.7 are in mm. The ends of the blocks are closed using end caps. Figure A.15 and Figure A.16 in Appendix A show detailed engineering drawings used for the fabrication of the water channel blocks and the corresponding end plates. Considering the intricate geometry of the water channel blocks and the difficulty in machining Copper, a machinable copper alloy (Alloy 145 Machinable Electrically Conductive Copper) was used for these channels. Connections to the coolant block are made using 1/16th NPT fittings. These water channel blocks are soldered to the refrigerant channel blocks as shown previously in Figure 3.1.

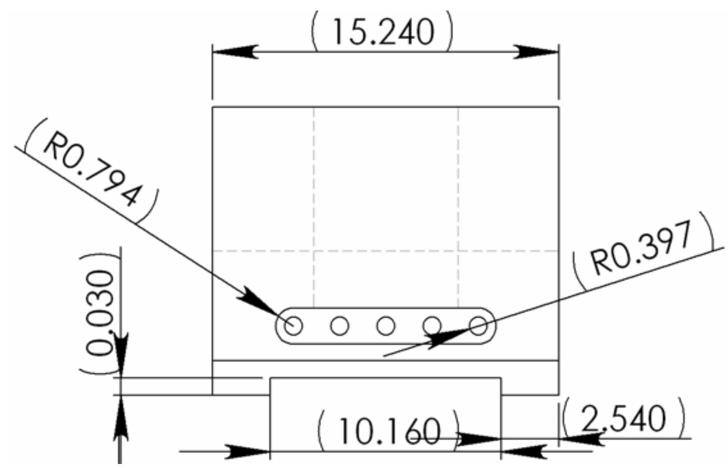

Figure 3.7: Cross-sectional View of Water Channel Blocks

This soldering was conducted at HT Micro Inc. A fixture was used to hold the inlet and exit connecting tubes in place while water channel blocks were soldered. A thin flux-less solder foil was used to solder along the whole surface. The total heat transfer length along which the solder joint exists between the refrigerant channels and the water channel blocks is 1.5 cm. The width of the solder joint is equal to the total channel (device) width, $W_{channels}$. For the 100×100 μm, 200×100 μm, 300×100 μm and 400×100 μm channels, $W_{channels}$ is 5.5, 7.8, 8.5 and 9.8 mm, respectively. Water flows in a direction counter to the refrigerant flow. Figure 3.8 shows a picture of the fully assembled test section.

Figure 3.8: Assembled Test Section with all Connections

3.2. Experimental Facility

A schematic of the test facility used in this study is shown in Figure 3.9. Subcooled refrigerant (state [1]) enters a pre-heater. The bulk temperature and pressure are measured here at the inlet to ensure a subcooled state. This subcooled refrigerant is heated by a resistance cartridge heater to a desired state [2] by precisely controlling the applied electrical heat input. Thus, the heat input is varied based on the G, T_{sat} and x_{in} of interest for a given data point. The test section inlet quality is determined from the pre-heater energy balance, using the pre-heater inlet conditions and the heat input in the heater. The temperature and pressure are measured once again at this location [2], which also constitutes the inlet to the condensing test section. Cooling water flows through the water channel blocks described in the previous section surrounding the refrigerant channel. The coolant flow rate and temperature are varied with each data point to accomplish condensation to the desired exit quality. After exiting the test section (state [3]), the refrigerant enters the post-heater where it is again heated to a superheated state [4] with a measured amount of heat input in the heater. The bulk temperature and pressure are measured at the exit of the heater to confirm the superheated state. The test section exit quality is measured using the heat input in the post-heater and inlet and exit temperatures and pressures. These calculations are illustrated in detail in the next chapter. For fabrication of the refrigerant loop, 6.35 mm (0.25") OD seamless stainless steel tubing is used between the post-heater exit and condenser exit, while 3.2 mm (1/8") OD tubing is used for all other sections of the refrigerant loop.

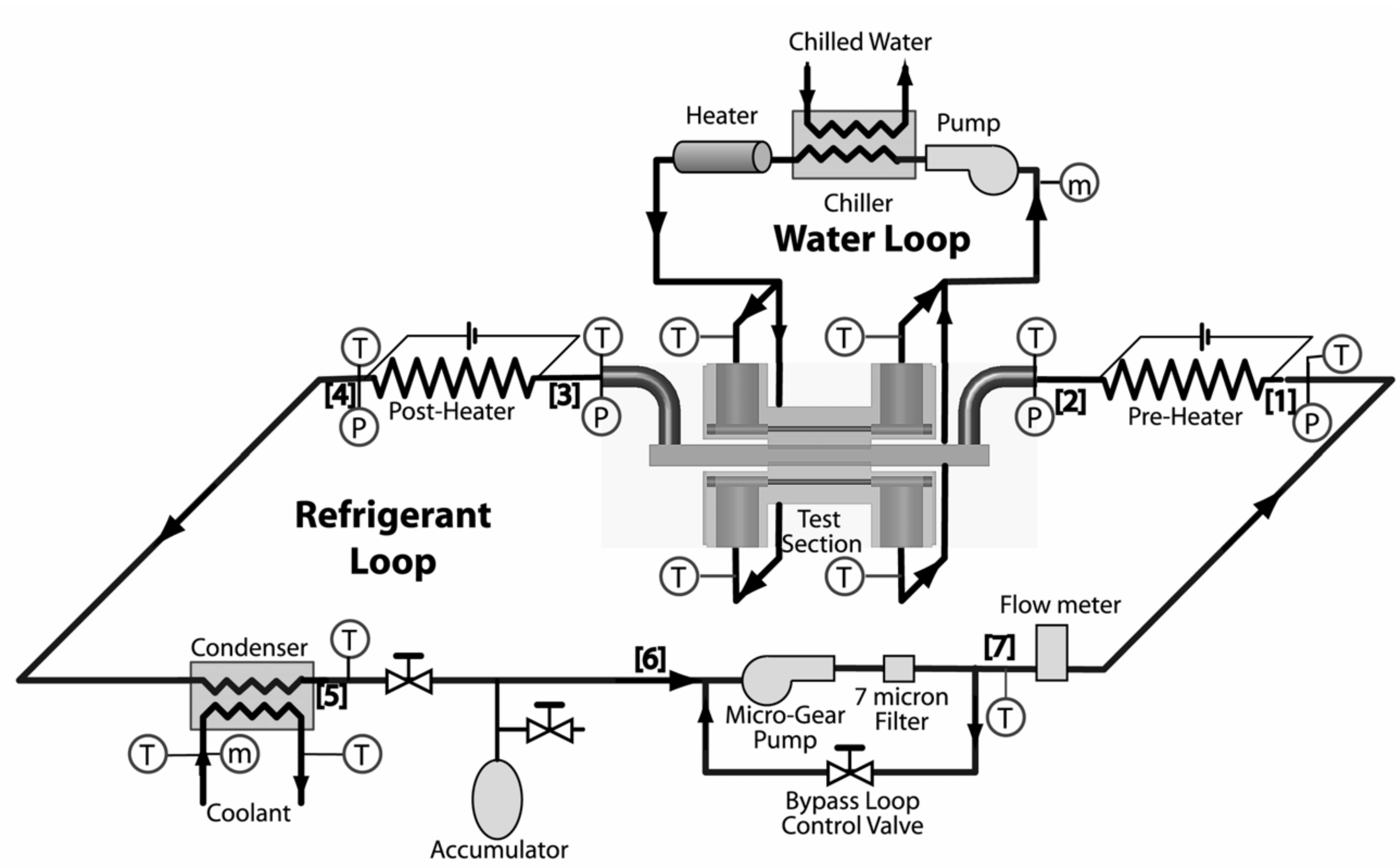

Figure 3.9: Experimental Facility Schematic

The refrigerant pre- and post-heaters are made by fitting a 2" long and ¼" diameter cartridge heater inside a Swagelok Female Run Tee fitting (Part No.: SS-600-3TFT). The Cartridge heater has a ¾" un-heated section in the beginning, so the heated section is surrounded by R134a on all sides. This arrangement minimizes heat losses. Tables A-1 and A-2 in Appendix A provide part numbers for all the fittings used in the heater assembly and the details of the cartridge heater respectively. Table A-3 provides dimensional details of the heater assembly.

Figure 3.10 shows a picture of the actual experimental facility. The refrigerant flows from the post-heater to a condenser, which returns the fluid to a subcooled state [5]. This condenser (Table A-4) is a counter flow tube-in-tube heat exchanger with refrigerant flowing through the inside tube and glycol flowing in the annulus. Upon exiting this condenser, the refrigerant is pumped back to the pre-heater using a Micropump GA 180 gear pump with a 500–4000 rpm DC drive over a ΔP_{max} of 262 kPa (38 psi). A 0 to 30 V DC regulated power supply (B&K Precision Corporation; Model 1627A) is used to supply power to the pump drive and control pump speed. A bypass loop is used to enable the pump to run at high rpm while providing lower flow rates to the test section. Tables A-5 to A-7 in Appendix A provide the complete specifications of the refrigerant pump, drive and power supply. A sight glass (Table A-8) is used to ensure that the refrigerant flowing to the pump is sub-cooled. A filter (Swagelok Stainless Inline Filter SS-2F-7, 7 Micron) is included in the loop downstream of the pump to capture particulates that might block the channels. An accumulator (Accumulators, Inc., AM631003), rated to withstand pressures up to 3000 psi, connected to a nitrogen tank provides independent control of the refrigerant pressure and holds refrigerant charge.

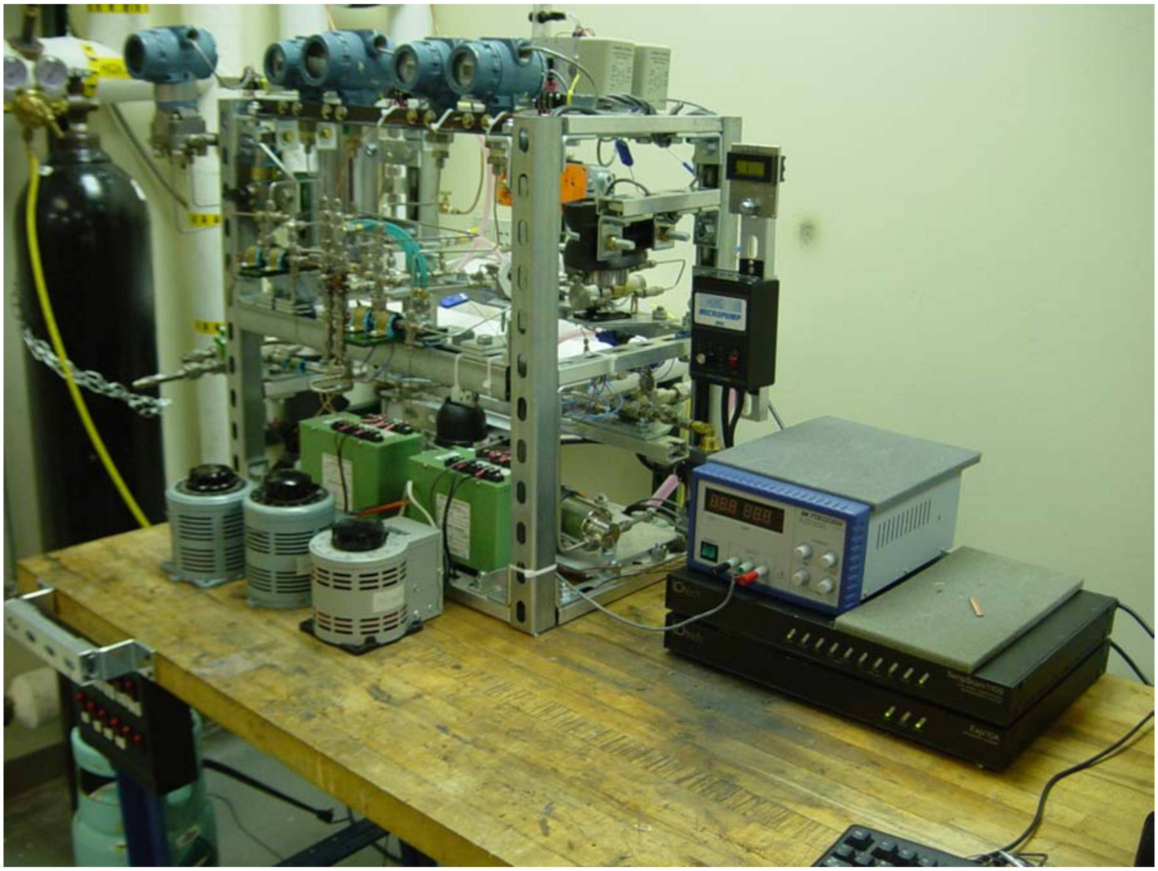

Figure 3.10: Picture of Experimental Facility

The refrigerant mass flow rate is measured using a DEA Microflowmeters (FMTD4) flowmeter in conjunction with the FME2 Display which monitors both flow rate and total flow simultaneously. This nutator flow meter is coupled to a photo emitter/detector device for signal detection, which results in accuracies of ±0.5% (repeatability of ±0.1%) for the range of flow rates 0.9–252 ml/min. Tables A-9 and A-10 provide complete specifications of the refrigerant flow-meter and display. Since this is a volumetric flow meter, the temperature of the refrigerant is measured right before entry into the flow meter for accurate determination of the mass flow rates. (The pressure is assumed to be the same as that measured at the pre-heater inlet.) This refrigerant flow meter gives output as 0-5 V square wave with frequency varying from 0-256 Hz based on the flow rate. The Iotech DAQ used cannot measure frequency input, hence a separate display was purchased from the flow meter manufacturer to display the refrigerant flow rates.

Rosemount absolute pressure transducers with uncertainties of ±0.25% of the span (0 - 2758 kPa) are used to measure pressures of the refrigerant at the inlet and outlet of the pre- and post-heater. Similarly, a Rosemount differential pressure transducer is used for measuring the test section pressure drop with an accuracy of 0.075% of the span (0 - 248 kPa). Microprobes (ThermoWorks, Inc.) with NIST traceable calibration for an accuracy of ±0.1°C ($0 < T < 50^{o}$C) and < 0.3°C ($T < 90^{o}$C) are used for refrigerant temperature measurement at the pre-heater and post-heater inlet and exits, and also at the inlets and exits of both the lower and upper water channels blocks. A standard T type thermocouple (Omega Inc., TMQSS-062(G)-6) with ±0.5°C uncertainty was used at the flow meter inlet. The power input to the pre- and post-heaters is measured using an Ohio Semitronics Inc., GW5-103E watt transducer with an accuracy of 0.2% while the power input to each of the heaters was controlled using separate inline variable transformers. Tables A-11 to A-14 provide complete specifications for the refrigerant loop pressure, temperature and power input measuring devices. Table 3-2 summarizes the important information about various measurement instruments and the Data Acquisition System.

Table 3-2: Summary of Measurement Instruments

<table>
<tr><th>Component</th><th>Manufacturer</th><th>Model</th><th>Range</th><th>Accuracies</th><th>Operating Conditions</th></tr>
<tr><td>Temperature Microprobes</td><td>Physitemp Instrument , Inc</td><td>PT-6</td><td>0 - 90°C</td><td>±0.1°C for 0 to 50°C
& < 0.3°C 50 to 90°C</td><td>-273 to 350°C</td></tr>
<tr><td>Absolute Pressure Transducers</td><td>Rosemount</td><td>2088</td><td>0 – 5515 kPa
(0 - 800 psia)</td><td>±0.25% of the span (400 psi in current facility)</td><td>-40 to 121°C</td></tr>
<tr><td>Differential Pressure Transducers</td><td>Rosemount</td><td>3051</td><td>0 - 284 kPa
(0 – 36 psi)</td><td>0.075% of the span</td><td>-40 to 121°C</td></tr>
<tr><td>Refrigerant Flowmeter</td><td>DEA Engineering</td><td>FMTD4</td><td>0.9 – 252 ml/min</td><td>±0.5%</td><td>-40 to 80°C
0 - 3,000 psig
(0 – 20684 kPa)</td></tr>
<tr><td>AC Watt Transducer</td><td>Ohio Semitronics Inc.</td><td>GW5-103E</td><td>0 – 100 Watts</td><td>0.2% of reading</td><td>-20 to 60°C</td></tr>
<tr><td>Water Flow Meter</td><td>McMaster-Carr</td><td>5079k18</td><td>4.2×10^{-6} –
4.2×10^{-5} m^3/s
(4 – 40 gph)</td><td>4%</td><td>Max. Pressure
689 kPa @ 66°C
(100 psi @ 150°F)</td></tr>
<tr><td rowspan="2">Data Acquisition System</td><td rowspan="2">Iotech, Inc.</td><td rowspan="2">Tempscan/1100</td><td rowspan="2">32 to 992 Channels</td><td colspan="2">Maximum Scan Rate: 960 Channels/s</td></tr>
<tr><td colspan="2">Maximum Single Channel Scan Rate: 60 Hz</td></tr>
</table>

The cooling water for the test section is circulated in a closed loop using a Micropump GB 200 gear pump controlled by a 500 – 9000 rpm AC Drive. Tables A-15 and A-16 in Appendix A provide details of the water loop pump and drive. The maximum flow that can be achieved using this pump-drive combination is limited by the maximum torque rating of the drive and not the maximum pressure rating of the pump. A static head provider (water reservoir at atmospheric pressure, installed at an altitude higher than pump) was introduced upstream of the pump to ensure no cavitation occurred in the pump and for charging the water loop and removing any trapped air. Seamless stainless steel tubing of 6.35 mm (0.25") OD was used for the fabrication of the water loop. Tables A-15 to A-17 give specifications of the water loop pump, drive, and static head provider.

The water loop flow rate was measured using a rotameter. A Polycarbonate Panel Mount Flowmeter (McMaster Part No.: 5079K18; Table A-18) with a range of 4.2×10^{-6} – 4.2×10^{-5} m^3/s (4 - 40 gph) and an accuracy of ±4% was used for this purpose. This water flow rate was used to determine the water flow velocities in the test section heat exchanger, which in turn was used to determine the water-side heat transfer coefficient using correlations available in literature. A conservative 25% uncertainty was assumed in the determined water-side heat transfer coefficient, irrespective of the flow measurement uncertainties, therefore, higer accuracies in this water flow rate measurement are unnecessary. Heat rejected to the coolant in the test-section is rejected ultimately in a pre-conditioning unit consisting of a chiller and heater in series. The desired water temperature was maintained using lab chilled water, with the temperature being fine-tuned by a cartridge heater, depending on the specific operating condition.

The chiller is a counter flow tube-in-tube heat exchanger with refrigerant flowing on the tube side and glycol from the chiller lines flowing on the annulus side. The construction of this heater is very similar to that of the refrigerant heaters, and the power input to the cartridge heater is controlled using the variable AC transformer. Tables A-15 to A-20 provide detailed specifications for each of the components in the water loop.

3.3. Experimental Procedure

The refrigerant-side of the test facility (shown in Figure 3.9) was initially pressurized to 1930 kPa (280 psi) with nitrogen gas and a trace amount of R-134a. An electronic leak detector (Manufacturer: TIF; Model: ZX-1) was used around all of the fittings to verify that the system had no leaks. This was further double checked using soap solution. Once all the leaks were removed, the system pressure was monitored for at least 24 hours to make sure there are no leaks. The test facility was then evacuated to a system pressure of less than 150 microns (20 Pa) using a vacuum pump (DV Industries model DV-85N; 3 cfm; 2 stage; ½ HP). A Supco (Sealed Unit Parts Co., Inc.) digital vacuum gauge (model VG64), with 1 micron resolution for less than 200 micron pressure was used to measure the vacuum pressure. Immediately after evacuation, the system was charged with R-134a. Water was charged in the water loop through the static head provider.

Testing commenced with the refrigerant condenser glycol flow, refrigerant flow, and water flow being turned on in this order. The desired refrigerant mass flow rate was achieved through a combination of needle valves in the bypass loop and a variable speed drive on the pump. The different specific volumes of the refrigerant for different test conditions were accommodated by controlling the Nitrogen side pressure in the accumulator.

Refrigerant pre- and post-heaters were then turned on and the heat input to the heaters was slowly raised in steps of 5 W. Preliminary calculations were first conducted to obtain an estimate of the heat input required at each heater to achieve the desired inlet and exit qualities. The desired system pressure was maintained by controlling the nitrogen pressure in the accumulator. As the heat input to the refrigerant heaters was increased, the chiller and heater in the water loop were adjusted to achieve the desired temperatures in the water loop. It took anywhere from 30 mins to 2 hours to achieve the initial approximate conditions.

Preliminary data points were taken to ensure that the correct conditions were achieved. Based on these preliminary points, the water temperature was adjusted to obtain the desired condensation heat duty, and the power supplied to the heaters was adjusted to get the desired refrigerant inlet/exit qualities. The system pressures, temperatures, and flow rates were constantly monitored during the test. If the calculated values for the preliminary data point corresponded to the desired qualities, the system was run at this condition until steady state was confirmed by ensuring that the results from successive data points were the same. Steady state conditions took between 30 minutes and 2 hours to obtain after initial approximate conditions were established, depending on the specific test condition. After steady state was established, the data point was recorded, with each point representing the average of 121 scans taken over a two-minute interval. Temperatures, pressures and heat inputs were recorded using a TEMPSCAN data acquisition system, which was capable of recording up to 992 channels at speeds of up to 960 channels per second. Details of the data acquisition system used are provided in Table A-21. Refrigerant flow rates and water flow rates were recorded separately from the respective displays. A frequency to voltage convertor was fabricated in the Electronics lab of the School of Mechanical Engineering to convert this frequency output to the 0-5 V voltage output. This 0-5 voltage output was in turn supplied to the DAQ, but the device was not reliable enough to be used in experimental measurements. This device was just used to plot the refrigerant flow rate reading in chart view, to see the trends in the flow rate. The power input to the refrigerant pre- and post-heater was then adjusted to obtain another average test section quality at the same refrigerant flow rate. This process was repeated until several data points, in the range $0.05 < x_{ave} < 0.95$ were taken.

Analysis of these measured data to obtain variables such as mass flux, quality, heat transfer rate, heat transfer coefficient, and frictional pressure drop are described in the following chapter.

CHAPTER 4. DATA ANALYSIS

This chapter explains the procedure used to obtain the refrigerant heat transfer coefficient and pressure drop from the measured quantities in the experiments. As mentioned in the previous chapters, tests were conducted on channels of four different hydraulic diameters and aspect ratio. For each test section, experiments were conducted at four different refrigerant saturation temperatures, T_{refg} = 30, 40, 50 and 60$^{\mathrm{o}}$C and mass fluxes, G = 300, 400, 600 and 800 kg/m^{2}s. For each combination of saturation temperature and mass flux, tests were conducted for a refrigerant vapor quality varying from 0 to 1.

A data point for the 200 x 100 μm channel (18 channels in parallel) with G = 606 kg/m^2-s, T_{sat} = 60.5$^{\mathrm{o}}$C and x_{ave} = 0.39 is used to illustrate the analysis of the data. The equations and step-by-step procedure followed for the analysis of this representative case is also provided in Appendix B. Table B-1 in Appendix B lists all the fixed parameters for the 200 x 100 μm test-section. Table B-2 in Appendix B lists all the measured parameters for this case that are used for data analysis. It also lists the measurement uncertainties for each of the parameters, which are used to derive the uncertainties in the final heat transfer coefficient and other parameters.

The flow meter used to determine the refrigerant flow rate is a volumetric flow meter and hence the density should be determined to obtain the mass flow rate. The measured refrigerant temperature just before entry to the flow meter is 25.9°C. The pressure at the flow-meter is assumed to be the same as that at the pre-heater inlet, i.e. 1727 kPa. Thus, with a volumetric flow rate of 1.8×10^{-7} m^3/s (10.83 ml/min) and density of 1210 kg/m^3, the refrigerant mass flow rate is determined as 2.18×10^{-4} kg/s using equation (4.1).

$$\dot{m} = FR_{refg} \times \rho_{fm,refg} \tag{4.1}$$

The total refrigerant flow area for all the channels in the test section is given by equation (4.2). For a test section with 18 100 μm deep, 200 μm wide channels, the area is 3.6×10^{-7} m^2. Based on this flow area, the refrigerant mass flux is calculated to be (equation 4.3) 606 kg/m^2-s.

$$A_{tot,TS} = d_{TS} \cdot w_{TS} \cdot N \tag{4.2}$$

$$G = \frac{\dot{m}}{A_{tot,TS}} \tag{4.3}$$

4.1. Pre-heater and Post-heater Energy Balance

The refrigerant state can be determined completely by measuring the pressure and temperature in the sub-cooled (state [1] in Figure 3.9) and super-heated (state [4] in Figure 3.9) states. At the pre-heater inlet, the refrigerant is fully sub-cooled, while at the post-heater outlet, it is fully superheated. An energy balance is performed between the two points to determine the test section heat duty.

For each of the heaters, two separate heat losses are considered: from the heater assembly to the ambient and from the Copper tubing between the heaters and the test-section refrigerant channels to the ambient. Appendix B.1 provides details of the procedure used for the heat loss estimation and Table B-3 in Appendix B provides a detailed step-by-step calculation procedure for heat losses in each of the heaters. A brief summary is presented here for the pre-heater and post-heater energy balance. For the representative case being discussed, the refrigerant enters the pre-heater at 1727 kPa and a nominal subcooled temperature of 29.3°C (T_{sat} = 61.1°C, $\Delta T_{subcooling}$ = 31.8°C). A power input of 31.02 W is supplied to the pre-heater to heat the refrigerant to the desired saturation temperature and quality. The heat loss to the ambient from the pre-heater assembly is determined to be 0.80 W. The heat loss in the Copper tubing (OD 3.18 mm, ID 1.55 mm, length 67 mm) from the pre-heater to the test section is 0.27 W (Appendix B.1). This results in an overall heat loss of 1.07 W for the pre-heater and tubing assembly (equation 4.4). For the purpose of calculation of uncertainties discussed later in this chapter, a conservative 50% uncertainty is assumed in the calculated heat losses.

$$Q_{H1,loss} = Q_{H1,heater,loss} + Q_{H1,2,TS,loss} \tag{4.4}$$

With a measured pre-heater electrical input of 31.02 W, and the heat losses calculated above, the net heat supplied to the refrigerant is 29.95 W (equation 4.5).

$$Q_{H1,refg} = Q_{H1} - Q_{H1,loss} \tag{4.5}$$

The enthalpy of the refrigerant entering the pre-heater is determined by measuring the pressure and temperature in the subcooled state (equation 4.6), and the enthalpy of the refrigerant at the test section inlet is determined from a pre-heater energy balance equation (4.7). With an inlet enthalpy of 93 kJ/kg and a refrigerant mass flow rate of 2.18×10^{-4} kg/s, the enthalpy at the test section inlet, $h_{H1,out}$, is determined to be 230 kJ/kg (equation 4.7).

$$h_{H1,in} = f\left(T_{H1,in}, P_{H1,in}\right) \tag{4.6}$$

$$Q_{H1,refg} = \dot{m} \cdot \left(h_{H1,out} - h_{H1,in}\right) \tag{4.7}$$

In the saturated state, the quality of the refrigerant can be determined using the enthalpy calculated above and the saturation pressure. The absolute pressure is measured at the pre-heater assembly exit before entering the refrigerant channels; however, the refrigerant experiences expansion/contraction, bend and frictional losses in the tubing and the headers. Calculation of these pressure losses is discussed in the pressure drop analysis (Section 4.2). For this representative case, the absolute pressure at the pre-heater assembly exit is 1727 kPa and after accounting for the pressure losses, the pressure at the channel inlet is 1724 kPa, which yields an inlet quality of 0.64 (equation 4.8).

$$h_{H1,out} = f\left(P_{in}, x_{in}\right) \tag{4.8}$$

The energy balance for the post-heater is conducted in a similar manner. The pressure measured at the exit of the test section is 1678 kPa, representing a saturation temperature of 59.9°C. The losses include those from the tubing from the refrigerant channels to the post-heater assembly, and those from the post-heater assembly itself. For the post-heater assembly, the heat loss is 0.77 W, and the heat loss from the tubing between the refrigerant channels and the post-heater is 0.26 W, resulting in an overall heat loss of 1.03 W from the post-heater and tubing assembly. Subtracting these heat losses from the electrical input supplied to the post-heater, 28.86 W, the net heat supplied to the refrigerant is 27.83 W. At the post-heater exit, the super-heated refrigerant pressure and temperature are measured to be 1679 kPa and 65.7°C respectively, yielding a refrigerant enthalpy of 286 kJ/kg. Thus, with a mass flow rate of 2.18×10^{-4} kg/s, a post-heater energy balance yields a test section exit enthalpy, $h_{H2,in}$, of 159 kJ/kg. The pressure at the post-heater inlet is measured to be 1678 kPa, and there is a negligible (estimated to be < 0.1 kPa) pressure drop from channel exit to the post-heater assembly due to the low exit quality of the refrigerant. Considering an uncertainty of ±6.9 kPa in the absolute pressure measurement as compared to only a ±0.19 kPa uncertainty in the differential pressure measurement, the test section exit pressure is derived based on a combination of absolute pressure measurements and the measured differential pressure as explained in the next section. Thus, the test section exit pressure is determined to be 1679 kPa, yielding a test section exit quality of 0.14. With a refrigerant mass flow rate of 2.18×10^{-4} kg/s, the test section inlet and exit enthalpies of 230 kJ/kg and 159 kJ/kg, respectively, yield a condensation heat duty of 15.54 W as shown in equation (4.9).

$$Q_{TS} = \dot{m}\left(h_{H1,out} - h_{H2,in}\right) \tag{4.9}$$

Additional details of these calculations are provided in Table B-3 of Appendix B. The above analysis established the test section inlet and exit conditions for the refrigerant. The following sections discuss the test section pressure drop and heat transfer analysis.

4.2. Pressure Drop Analysis

Figure 4.1 shows a schematic of the test section without the water channel blocks. It illustrates the flow path of the refrigerant and indicates various expansion and contraction pressure losses, frictional losses and acceleration/deceleration losses taken into account before determining the final pressure drop in the 40 mm long refrigerant channels. The refrigerant chanels are connected to the rest of the refrigerant loop through

4-way Swagelok union fittings (Part No. SS-200-4) in which pressure and temperature measurements are made as indicated in the schematic (Figure 4.1). Single-phase validation tests were also conducted with the objective of ensuring that all the relevant minor losses in the fluid flow path were accounted for. Section B.4 in Appendix B provides details of the single phase tests and analyses. Two phase pressure drop analysis, the focus of the current study, is discussed below.

The two-phase pressure drop analysis is also described based on the representative case (G = 606 kg/m^2-s, T_{sat} = 60.5°C, x_{ave} = 0.39 for the 18 200×100 μm channels in parallel) used in the previous section. Table B-5 in Appendix-B reports these calculations in step-by-step fashion. A summary of the methodology is presented here. A conservative 50% uncertainty has been assumed in all minor losses for uncertainty estimation.

A contraction pressure drop is encountered at section AA, CC and EE due to reduction in the flow area. The homogenous flow model (equation 4.10) recommended by Hewitt *et al.* (1993) is used to calculate the contraction pressure drop.

$$\Delta P_{con} = \frac{G^2}{2\rho_l}\left[\left(\frac{1}{C_C}-1\right)^2 + 1 - \frac{1}{\gamma_{con}{}^2}\right]\Psi_H \tag{4.10}$$

where

$$\Psi_{H,x_{in}} = \left|1 + x_{in}\left(\frac{\rho_l}{\rho_g}-1\right)\right| \tag{4.11}$$

$$C_C = \frac{1}{0.639\left(1-\dfrac{1}{\gamma_{con}}\right)^{0.5}+1} \tag{4.12}$$

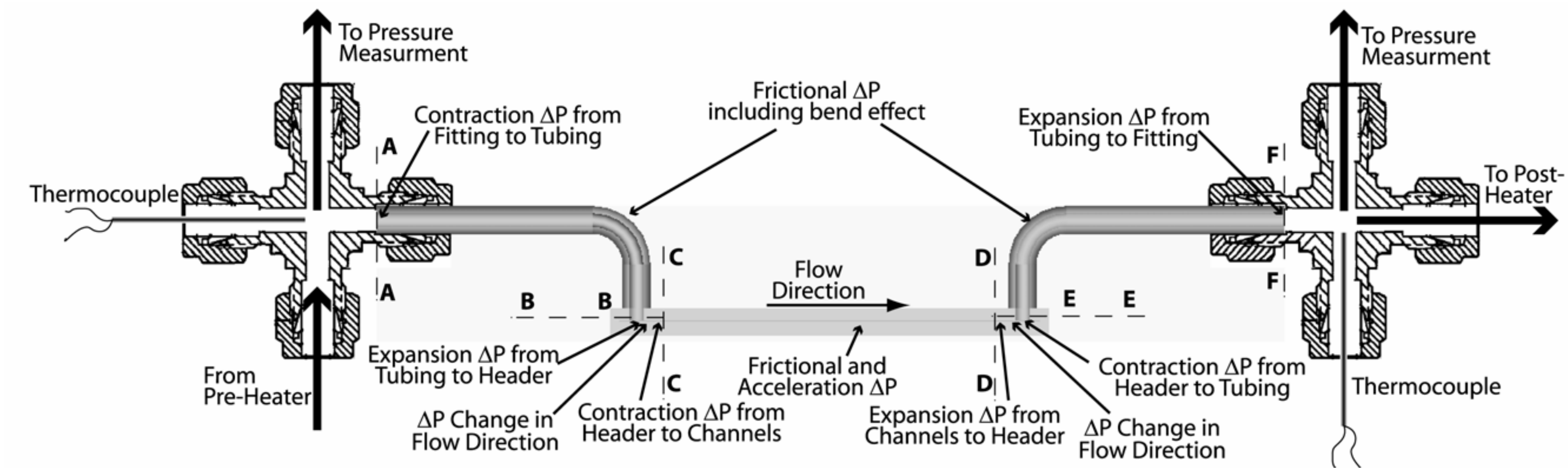

Figure 4.1: Refrigerant Flow Path Schematic for Pressure Drop Analysis

$$\gamma_{con} = \frac{A_{Large}}{A_{Small}} \tag{4.13}$$

At section AA, with a quality of 0.64 at 61.1°C saturation temperature, there is a contraction pressure drop of 51 Pa due to flow from a fitting of flow area 4.10×10^{-6} m^2 to the copper tubing with an internal flow area of 1.89×10^{-6} m^2. The estimated contraction pressure drop at section AA (51 Pa) is very small, because the refrigerant mass flux in the tube is only 116 kg/m^2-s, which is much less than the mass flux of 606 kg/m^2-s in the refrigerant channels. At section CC, the flow goes from the inlet header to the channels at the same inlet quality and temperature. For 18 200×100 μm channels in parallel, the refrigerant flow areas in the header and channels are 5.3×10^{-7} m^2 and 3.6×10^{-7} m^2 respectively, i.e. a contraction ratio of 1.47, yielding a contraction pressure drop of 923 Pa. This contraction loss is much more significant because of the higher mass flux of 606 kg/m^2-s in channels. At section EE on the exit side, with a quality of 0.14 at 59.9°C saturation temperature, the refrigerant flows from a header of flow area 2.12×10^{-5} m^2 (looking along the direction of the vertical tubing) to an internal flow area of copper tubing of 1.89×10^{-6} m^2, yielding a contraction pressure drop of 22 Pa.

At section BB, DD and FF, the refrigerant flows from a smaller flow area to a larger flow area, encountering expansion pressure gain due to reduction in flow velocities. The separated flow model (equation 4.14) recommended by Hewitt *et al.* (1993) is used to determine the expansion pressure gain at these sections.

$$\Delta P_{\exp} = -\frac{G^2\gamma_{\exp}(1-\gamma_{\exp})\Psi_S}{\rho_L} \tag{4.14}$$

where $$\Psi_S = \left[1 + \left(\frac{\rho_l}{\rho_v} - 1 \right) \left(B_B.x(1-x) + x^2 \right) \right] \tag{4.15}$$

$$\gamma_{\exp} = \frac{A_{tot,TS}}{A_{header,TS}} \tag{4.16}$$

At section BB, with an inlet quality of 0.64 at 61.1°C saturation temperature, the refrigerant flows from the internal flow area of copper tubing 1.89×10^{-6} m^2 to a header of flow area 2.12×10^{-5} m^2 (looking along the direction of vertical tubing), yielding an expansion pressure gain of 6 Pa. At section DD on the exit side, with an exit quality of 0.14 at 59.9°C saturation temperature, the refrigerant flows from the refrigerant channels with a total flow area of 3.6×10^{-7} m^2 to a header of flow area 5.3×10^{-7} m^2, i.e. an expansion ratio of 0.68, yielding an expansion pressure gain of 118 Pa due to the large mass flux of 606 kg/m^2-s. At section FF, there is an expansion pressure gain of 5 Pa due to flow from copper tubing with an internal flow area of 1.89×10^{-6} m^2 to a fitting of flow area 4.10×10^{-6} m^2. Again, the estimated expansion pressure gain at this section FF is very small, because the refrigerant mass flux in the tube is only 116 kg/m^2-s.

The pressure drop in the tubing between the heater and the refrigerant channels consists of frictional pressure drop in the horizontal/vertical sections of the tubing and the pressure drop in the bends. The frictional pressure drop in the copper tubing is estimated assuming adiabatic flow (i.e. neglecting acceleration/deceleration pressure drop). The multiple flow regime pressure drop model of Garimella *et al.* (2005) for condensing flows of refrigerant R134a in tubes with $0.5 < D < 4.9$ *mm* was used for this purpose. Although this model consists of separate sub-models for the intermittent flow regime and the annular/mist/disperse flow regimes, in the current study, the annular flow portion is used for all data for ease of implementation. Considering the low pressure drops in the tubing due to low mass fluxes and an assumed 50% uncertainty, this assumption is not expected to have a significant impact on the results. This assumption of using only the annular pressure drop model instead of complete model, which greatly simplifies the calculations, is further discussed in Section B.5 of Appendix B. In the annular flow model, the interfacial friction factor is computed from the corresponding liquid-phase *Re* and friction factor, the Martinelli parameter, and a surface tension-related parameter:

$$\frac{f_i}{f_l} = A \cdot X^a \, \mathrm{Re}_l^{\,b} \, \psi^c \tag{4.17}$$

The friction factors required for the individual-phase pressure drops in the Martinelli parameter were computed using $f = 64/\mathrm{Re}$ for $Re_l < 2100$ and the Blasius expression $f = 0.316 \cdot \mathrm{Re}^{-0.25}$ for $Re_l > 3400$. The Martinelli parameter X is given by:

$$X = \left[\frac{\left(dP/dz \right)_l}{\left(dP/dz \right)_v} \right]^{1/2} \tag{4.18}$$

For this model, the liquid-phase *Re* is defined in terms of the annular flow area occupied by the liquid phase, $\mathrm{Re}_l = \dfrac{GD\left(1-x\right)}{\left(1+\sqrt{\alpha}\right)\mu_l}$, and the gas-phase *Re* is $\mathrm{Re}_v = \dfrac{GxD}{\mu_v \sqrt{\alpha}}$. The surface tension parameter ψ in equation (4.19) (Lee and Lee, 2001) is given by:

$$\psi = \frac{j_l \mu_l}{\sigma} \tag{4.19}$$

where, $j_l = \dfrac{G(1-x)}{\rho_l(1-\alpha)}$ is the liquid superficial velocity. The interfacial friction factor thus determined is related to the pressure drop through the void fraction model (Baroczy, 1965) using the following equation:

$$\frac{\Delta P}{L} = \frac{1}{2} \cdot f_i \frac{G^2 \cdot x^2}{\rho_v \cdot \alpha^{2.5}} \cdot \frac{1}{D} \tag{4.20}$$

As mentioned before, the internal diameter of connecting copper tubes at the inlet and exit of the refrigerant channels is 1.55 mm, yielding the mass flux of 116 kg/m^2-s for this representative case. For the inlet side copper tubing, with a saturation temperature of 61.1° and quality of 0.64, the frictional pressure gradient is 2.1 kPa/m, yielding a pressure drop of 87 Pa in the 42 mm horizontal section and 21 Pa in the 10 mm long vertical section. For the exit side copper tubing, with a saturation temperature of 59.9°C and quality of 0.14, the frictional pressure gradient is 0.85 kPa/m yielding a pressure drop of 36 Pa in the 42 mm horizontal section and 9 Pa in the 10 mm long vertical section. The frictional pressure drop is higher in the inlet copper tubing due to the higher quality.

As seen in Figure 4.1, the refrigerant flows through a 10 mm radius bend in the copper inlet and outlet tubing. In addition, upstream and downstream of the refrigerant channels, there is a change in the direction of flow in both headers, which is treated like flow through a bend. Two phase pressure drops in bends are calculated using the homogenous flow model (equation 4.21) given by Hewitt *et al.* (1993).

$$\Delta P_{Bend} = k_B \cdot \frac{G^2}{2 \cdot \rho_l} \cdot \Psi_H \tag{4.21}$$

where Ψ_H is given by equation (4.11). The value for constant k_B varies with the type of bend and bend radius. The typical value for a circular tube bend such as that in the copper tubing under consideration is 0.15. Using the appropriate input quantities, for the bend in the inlet tubing with a quality of 0.64 at 61.1°C, the pressure drop is 8 Pa. Similarly, on the exit side tubing with quality of 0.14 at 59.9°C, the bend pressure drop is 2 Pa. The bend radius in the header approaches zero, because of the abrupt turn; therefore, for this case, the constant k_B is assumed to be 0.6 based on the plots given by Hewitt (1984). The mass flux required for calculating the pressure drop at the abrupt turn in the header is determined based on the minimum flow area in the header when the refrigerant spreads into the header from the area just under the tube (equation 4.22).

$$G_{header} = \frac{\dot{m}}{\pi \cdot D_{TS,tube,ID} \cdot d_{TS}} \tag{4.22}$$

where, d_{TS} is the depth of the channels, which in turn is equal to the depth of the header. Based on the above equation, G_{header} is determined to be 448 kg/m^2-s, which yields pressure drops in the inlet and exit headers of 452 Pa and 146 Pa based on the respective inlet and exit conditions.

In addition to the above minor pressure losses/gains, the refrigerant also undergoes a deceleration, and therefore, a pressure rise due to the decrease in quality from the inlet to the outlet. The deceleration pressure gain is calculated using the model (equation 4.23) recommended by Carey (1992).

$$\Delta P_{deceleration} = \left[\frac{G^2x^2}{\rho_v\alpha} + \frac{G^2(1-x)^2}{\rho_l(1-\alpha)}\right]_{x=x_{in}} - \left[\frac{G^2x^2}{\rho_v\alpha} + \frac{G^2(1-x)^2}{\rho_l(1-\alpha)}\right]_{x=x_{out}} \tag{4.23}$$

where $$\alpha\big|_x = \left[1+\left(\frac{1-x}{x}\right)^{0.74}\left(\frac{\rho_v}{\rho_l}\right)^{0.65}\left(\frac{\mu_l}{\mu_v}\right)^{0.13}\right]^{-1} \tag{4.24}$$

For this representative case with a mass flux of 606 kg/m^2-s inlet and exit qualities of 0.64 and 0.14 respectively, the pressure gain due to deceleration is estimated to be 1610 Pa. The properties required to calculate α were determined at the respective saturation temperatures at the inlet and exit.

Summing the pressure drops and gains on the inlet and exit sides separately as per equations (4.25) and (4.26), the net pressure drop on the inlet and exit sides are 1.5 kPa and 0.1 kPa, respectively.

$$\begin{aligned}\Delta P_{others,in} &= \Delta P_{con,H1} + \Delta P_{H1,2,TS,Hor} + \Delta P_{H1,2,TS,Ver} + \Delta P_{Tube,Bend,in} \\ &\quad + \Delta P_{\exp,TS,header,in} + \Delta P_{Bend,header,in} + \Delta P_{con,TS,in}\end{aligned} \tag{4.25}$$

$$\Rightarrow \Delta P_{others,in} = 51+87+28+8+(-6)+452+923 = 1.54\times 10^3 \text{ Pa}$$

$$\begin{aligned}\Delta P_{others,out} &= \Delta P_{\exp,TS,out} + \Delta P_{Bend,header,out} + \Delta P_{con,TS,header,out} + \Delta P_{TS,2,H2,Ver} \\ &\quad + \Delta P_{TS,2,H2,Hor} + \Delta P_{Tube,Bend,out} + \Delta P_{\exp,H2}\end{aligned} \tag{4.26}$$

$$\Rightarrow \Delta P_{others,out} = (-118)+146+22+9+36+2+(-5) = 89 \text{ Pa}$$

Finally, the frictional component of the pressure drop occurring in the test section is calculated as follows:

$$\Delta P_{fric,TS} = \Delta P_{measured} - \Delta P_{others,in} - \Delta P_{others,out} + \Delta P_{deccleration} \tag{4.27}$$

$$\Rightarrow \Delta P_{fric,TS} = 47.2 - 1.5 - 0.1 + 1.6 = 47.2 \text{ kPa}$$

From the above analysis, it can be seen that the frictional pressure drop for this case is approximately 100 % of the measured pressure drop as deceleration pressure gain cancels the effect of inlet/exit minor losses. Thus, the deceleration, inlet and outlet pressure drops/gains are 3.4, 3.2, and 0.2 % of the measured pressure drop, respectively for this data point. Thus, the most significant contributor, other than the frictional pressure drop in the channels, is the deceleration pressure gain in the refrigerant channels. Figure 4.2 depicts the contributions of each of the pressure change elements in the refrigerant flow path along the length between the points of differential pressure measurement as indicated in Figure 4.1.

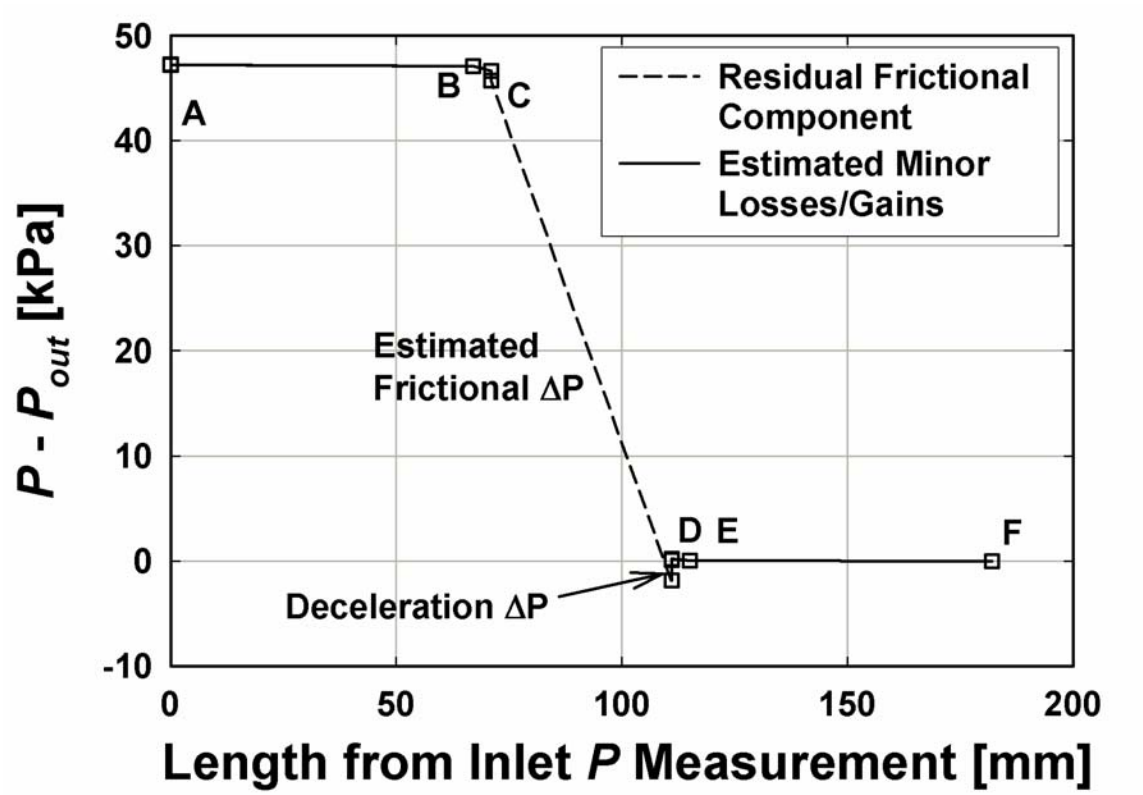

Figure 4.2: Pressure Drop along the Length of Test-Section for Representative Case

The deceleration pressure gain and contraction and expansion losses are proportional to the square of the mass flux, and thus increase or decrease at the same rate with a change in mass flux. The contraction and expansion pressure drop decreases with an increase in channel width because the area contraction or expansion ratio increases. The deceleration pressure drop is proportional to the change in quality across the test section. In the entire test matrix, Δx ranged from 0.28 to 0.90, with an average of 0.52. Section 5.1 provides details regarding contribution of the minor losses and deceleration pressure drops for all the data taken in this study.

The results obtained in the data analysis discussed in the previous section and the heat transfer analysis discussed in the following section are dependent on the inlet and exit pressures at the refrigerant channel inlet and exit. These are determined after subtracting the inlet and exit losses described above from the measured absolute pressures at the test-section inlet and exit. The uncertainties in the measurement of absolute pressures at the heater inlet and exit are ±6.89 kPa, compared to an uncertainty of only ±0.19 kPa in the differential pressure measurement. Thus, in order to minimize the effect of the uncertainty in the absolute pressure measurements, the inlet and exit pressures in the refrigerant channels are estimated by offsetting the minor loss terms from the average of the measured inlet and outlet pressures rather than any one of the measured pressures as shown in equations (4.28) and (4.29). Thus, for the representative case, channel inlet and exit pressures are determined to be 1724±4.9 kPa and 1679±4.9 kPa respectively.

$$P_{in} = \left(\frac{P_{H1,out} + P_{H2,in}}{2} \right) + \frac{\Delta P_{measured}}{2} - \Delta P_{others,in} \tag{4.28}$$

$$P_{out} = \left(\frac{P_{H1,out} + P_{H2,in}}{2} \right) - \frac{\Delta P_{measured}}{2} + \Delta P_{others,out} \tag{4.29}$$

The deceleration pressure gain occurring in the test section is not required in the above calculations as it occurs only along the length of the channels and not before entry or after exit from the channels. It should be noted that the pressure losses/gains calculated in this section are dependent on the inlet/exit qualities calculated in the energy balance section, which in turn are dependent on the channel inlet and exit pressures estimated here. Therefore, these equations are solved iteratively to obtain the pertinent pressures and qualities.

4.3. Heat Transfer Analysis

The calculation of the refrigerant-side heat transfer coefficient from the measured parameters is described here. In establishing the methodology for the heat transfer calculations, two important factors should be considered. Firstly, since the refrigerant channels are fabricated from a Copper wafer, which has a very high thermal conductivity, there is a strong potential for axial conduction through the walls of the refrigerant channels. The total length of the refrigerant channels is 40 mm, out of which the central 15 mm length is in direct contact with the water channel blocks to form the heat exchanger. The remaining 12.5 mm length on either end act as extended surfaces. Secondly, due to high pressure drops through the test section in some cases, refrigerant saturation temperatures may vary from the inlet to the exit of the channels. Due to the simultaneous coupled conduction and convection within the channels and the channel walls, conjugate effects must be addressed. Therefore the heat transfer analysis is conducted by dividing the test section into segments. Table B-6 in Appendix B provides the detailed procedure employed for the heat transfer calculations discussed here. An overview of the analysis is provided here. There are five main steps in the segmental heat transfer analysis:

1. Definition of the segments and nodes.
2. Definition of the boundary conditions (i.e. refrigerant side and water side temperatures).
3. Definition of the thermal resistance for each potential heat flow path
4. An energy balance computation for each node
5. Calculation of additional parameters such as average refrigerant and wall temperatures and resistance ratios.

The following sub-sections describe each of the above steps in the segmental heat transfer analysis.

4.3.1. Definition of Segments and Nodes

Figure 4.3 shows a sample coarse grid structure for the segmental heat transfer analysis. There are three main sections of the complete geometry under consideration, the inlet side extended section of 12.5 mm, the central heat exchanger section of 15 mm and the exit side extended section of 12.5 mm. The inlet and exit sections are subdivided into three segments each ($N_{seg,fin}$), while the central heat exchanger section is divided into four segments ($N_{seg,HE}$). It should be noted that the number of segments for the refrigerant-side and water-side are the same in the central heat exchanger section. It should also be noted that this grid structure is primarily for illustration of the technique. In the actual calculations, a much larger number of segments (10 segments in each of the three sections) are used.

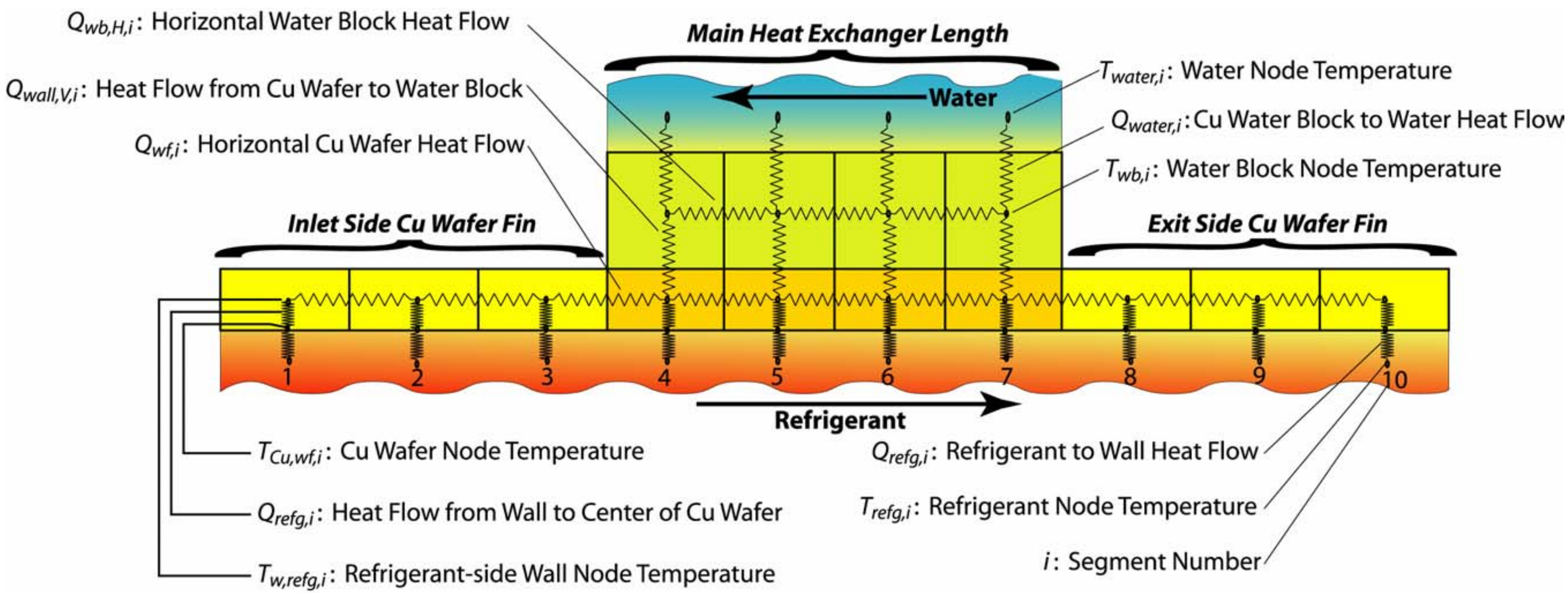

Figure 4.3: Segmental Heat Transfer Analysis Schematic

The effect of the number of the segments on the resulting heat transfer coefficient is discussed later in this section. Thus, for the illustrative case, the total number of segments (equation 4.30) is 10. The segments are numbered from the inlet to the exit as shown in Figure 4.3.

$$N_{seg} = 2 \times N_{seg,fin} + N_{seg,HE} \tag{4.30}$$

Figure 4.3 also shows the thermal resistance network for the segmental heat transfer analysis. This determines the heat flow path from the refrigerant side to water side. The heat transfer from the refrigerant to the water flowing in the counter current direction is considered, along with the axial heat flow along the length of the copper wafer. The details of each of the resistances will be discussed later in this section.

The overall lengths for each of the sections are fixed: 12.5 mm for each of the fins and 15 mm for the central heat exchange section. The length for each of the segments can thus be calculated as follows:

$$L_{seg,i} = \frac{0.0125}{N_{seg,fin}} \quad \begin{cases} 1 \le i \le N_{seg,fin} \\ \left(N_{seg,fin} + N_{seg,HE} + 1\right) \le i \le N_{seg} \end{cases} \tag{4.31}$$

$$L_{seg,i} = \frac{0.015}{N_{seg,HE}} \quad \left\{\left(N_{seg,fin} + 1\right) \le i \le \left(N_{seg,fin} + N_{seg,HE}\right)\right. \tag{4.32}$$

4.3.2. Defining Boundary Conditions

The next step in the analysis is to determine the refrigerant and water-side temperatures. As discussed in the previous chapter, the water-side flow rates are deliberately kept as high as possible to minimize the coolant-side thermal resistance. Thus, there is no measurable change in water temperature between the inlet and the exit.

The uncertainly in temperature measurement is ± 0.1°C, and for all the data points taken in the current study, $\Delta T_{\text{coolant}} < 0.1^{\circ}\text{C}$. The inlet and exit temperature are in turn the average of the measured water temperatures in the upper and lower blocks (equations 4.33 & 4.34).

$$T_{water,in} = \frac{T_{w,U,in} + T_{w,L,in}}{2} \tag{4.33}$$

$$T_{water,out} = \frac{T_{w,U,out} + T_{w,L,out}}{2} \tag{4.34}$$

For the representative case under consideration, the water-side inlet and exit temperatures are 56.3°C and 56.4°C respectively. Thus, water side temperatures are simply determined using a linear interpolation based on the length between the measured water inlet and exit temperatures (equations 4.35 & 4.36).

$$T_{water,N_{seg,fin}+1} = T_{water,out} - \left(\frac{T_{water,out} - T_{water,in}}{15 \times 10^{-3}} \right) \cdot \frac{L_{seg,N_{seg,fin}+1}}{2} \tag{4.35}$$

$$T_{water,i} = T_{water,i-1} - \left(\frac{T_{water,out} - T_{water,in}}{15 \times 10^{-3}} \right) \cdot L_{seg,i} \quad \left\{ N_{seg,fin} + 2 \le \mathrm{i} \le N_{seg,fin} + N_{seg,HE} \right. \tag{4.36}$$

Refrigerant side temperatures are determined based on the refrigerant saturation pressures at each of the nodes in the channels. The pressure drop is a strong function of quality and increases with increasing qualities. Thus if there is a 40% change in the refrigerant quality between the inlet and exit, a constant pressure gradient assumption is not particularly accurate. Figure 4.4 shows sample pressure drop data for the 200×100 μm test section based on the pressure drop analysis discussed above.

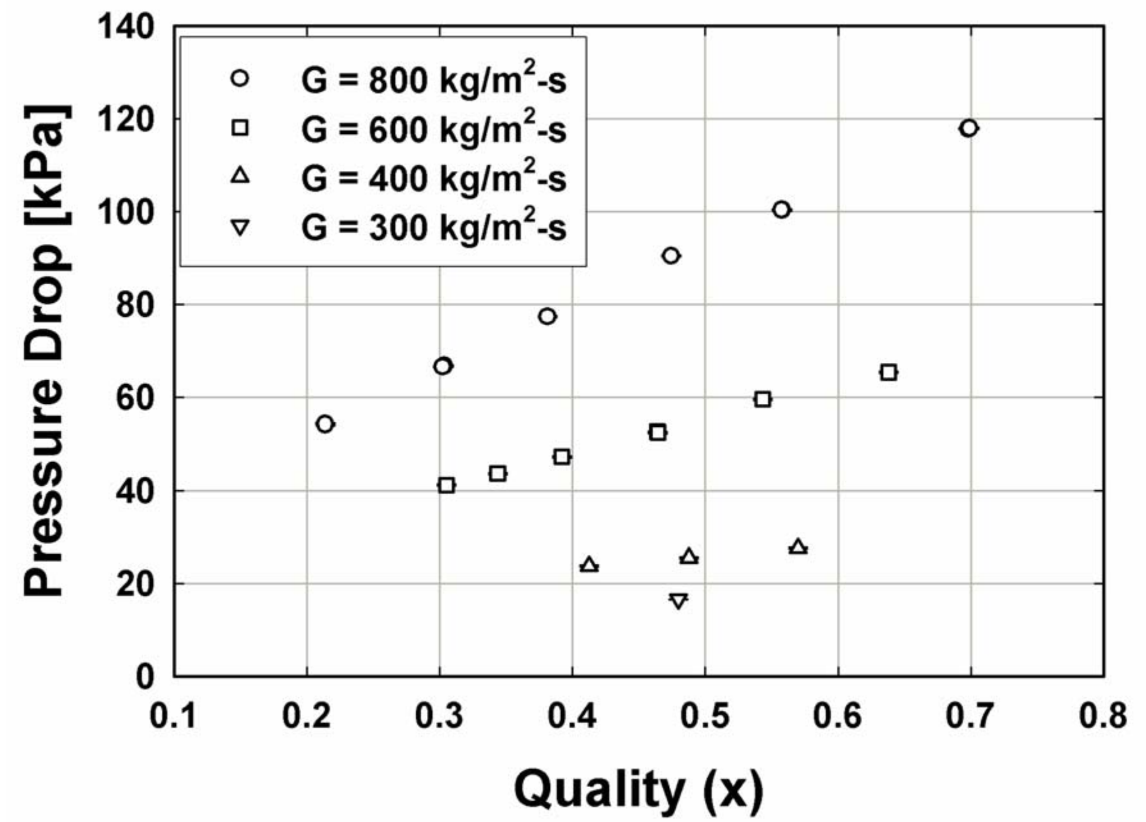

Figure 4.4: Sample Frictional ΔP Data for 200×100 μm Channels at 60°C

It is clearly visible that the pressure drop is a strong function of quality, which suggests that a larger pressure gradient is expected near the channel inlet compared to that towards the channel exit. Therefore, the frictional pressure drop in the channel was calculated as a function of average quality (quadratic or linear expression) for each test section and for each mass flux and temperature combination. For most cases, a linear expression was adequate. For example, for the 200×100 μm, G = 600 kg/m^2-s and T = 60^{o}C data set, the pressure drop in the channel was calculated using equation (4.37) in which the constants a_{dPdL}, b_{dPdL} and c_{dPdL} were determined to be 18063, 75582 and 0 respectively.

$$\Delta P_{TS,fric} = f(x) = a_{dPdL} + b_{dPdL} \cdot x + c_{dPdL} \cdot x^2 \quad (4.37)$$

Appendix B.3 provides values of constants in the above equations for all tubes. Other than the frictional pressure gradient, the deceleration pressure gain for each of the segments will also vary as it is dependent on the quality change, and the quality change may be different in each segment based on the condensation heat duty in the segment. Thus, the empirically determined pressure gradient was used in conjunction with the deceleration pressure gain for each segment to determine the pressure variation along the length of the channel by fixing the channel inlet pressure based on the pressure drop analysis. The deceleration pressure gain (equation 4.23) for each segment was determined using the process described in the pressure drop analysis with the inlet and exit qualities (equation 4.49) for each segment. Equation (4.38) shows the method of calculating the average pressure gradient between the beginning of channels and the first node. Equation (4.39) is then used to determine the pressure at the first node. $\Delta P_{decceleration,0}$ is the deceleration pressure gain between the channel inlet and the first node calculated based on the respective qualities at the two points.

$$\left(\frac{dP}{dL}\right)_0 = \frac{a_{dPdL} + b_{dPdL}\left(\frac{x_{in} + x_1}{2}\right) + c_{dPdL}\left(\frac{x_{in} + x_1}{2}\right)^2}{0.04} \quad (4.38)$$

$$P_{emp,1} = P_{in} - \left(\frac{dP}{dL}\right)_0 \left(\frac{L_{seg,1}}{2}\right) + \Delta P_{decceleration,0} \quad (4.39)$$

where, the subscript '*emp*' refers to empirical. The number 0.04 appears in the denominator because the length of each of the channels was 40 mm and equation (4.37) yields the pressure drop over this length. In equation (4.39), half the segment length is used because first node in only half the segment length away from the channel inlet. For all the downstream nodes, equations (4.40) and (4.41) are used.

$$\left(\frac{dP}{dL}\right)_i = \frac{a_{dPdL} + b_{dPdL}\left(\frac{x_i + x_{i+1}}{2}\right) + c_{dPdL}\left(\frac{x_i + x_{i+1}}{2}\right)^2}{0.04} \quad \left\{1 \le i \le \left(N_{seg} - 1\right)\right. \tag{4.40}$$

$$P_{emp,i} = P_{emp,i-1} - \left(\frac{dP}{dL}\right)_{i-1}\left(\frac{L_{seg,i} + L_{seg,i-1}}{2}\right) + \Delta P_{decceleration,i-1} \quad \left\{2 \le i \le N_{seg}\right. \tag{4.41}$$

In equation (4.41) $\left(\frac{L_{seg,i} + L_{seg,i-1}}{2}\right)$ is used because the lengths of the adjacent segments might differ in certain cases such as in case of segments 3 and 4 in Figure 4.3. The absolute pressure at the end of the channels is then calculated using equations (4.42) and (4.43).

$$\left(\frac{dP}{dL}\right)_{N_{seg}} = \frac{a_{dPdL} + b_{dPdL}\left(\frac{x_i + x_{out}}{2}\right) + c_{dPdL}\left(\frac{x_i + x_{out}}{2}\right)^2}{0.04} \tag{4.42}$$

$$P_{emp,N_{seg}+1} = P_{emp,N_{seg}} - \left(\frac{dP}{dL}\right)_{N_{seg}}\left(\frac{L_{seg,N_{seg}}}{2}\right) + \Delta P_{decceleration,N_{seg}} \tag{4.43}$$

The calculations at the channel inlet and exit had to be addressed differently from all the internal nodes, as they are only half the segment length from the nearest nodes.

Figure 4.5 shows an illustration to explain the determination of these pressures. Plots of the variation of pressure along the channel length are shown. The inlet and exit pressures are the channel inlet and exit pressures determined in the pressure drop analysis.

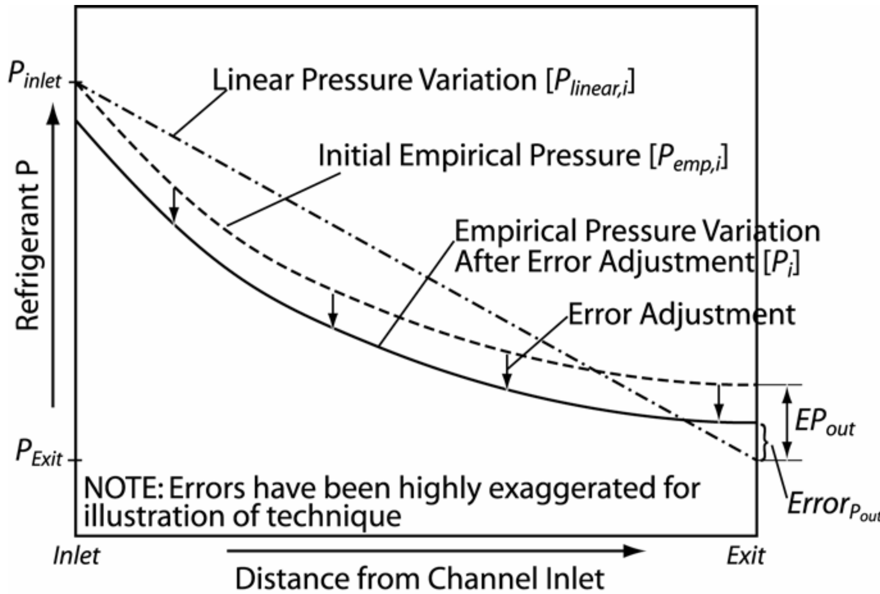

Figure 4.5: Illustration of Empirical Pressure Variation Determination Technique

A graph of the linear pressure drop ($P_{linear,i}$) is also been shown using a dashed and dotted line for comparison. The second dashed line marked 'Initial Empirical Curve' shows the pressure drop variation ($P_{emp,i}$) in the channels determined using the technique explained above. The channel exit pressure determined using this method is then compared with the exit pressure (P_{out}) determined in the pressure drop analysis using equation (4.44), yielding an error term EP_{out}, which is also shown in the plot.

$$EP_{out} = P_{emp,N_{seg}+1} - P_{out} \tag{4.44}$$

This difference in the channel exit pressure is then divided among the inlet and exit pressures by shifting the whole curve by half the above error (equation 4.45) as shown in Figure 4.5.

$$P_i = P_{emp,i} - \frac{EP_{out}}{2} \quad \left\{0 \le i \le \left(N_{seg} + 1\right)\right. \tag{4.45}$$

The solid line in Figure 4.5 shows the final empirical pressure drop variation curve used for further calculations. Using this error adjustment technique to shift the empirical pressure variation reduces the error in absolute pressure. Thus, the net error in the final empirical exit pressure compared to the total pressure drop is:

$$Error_{P_{out}} = \frac{\left(P_{N_{seg}+1} - P_{out}\right)}{\left(P_{in} - P_{out}\right)} \times 100 \tag{4.46}$$

It should be noted that errors shown in Figure 4.5 have been highly exaggerated to illustrate the technique. In most of the cases, the error in the exit pressure was negligible compared to the total pressure drop in the test section. For the representative case being discussed, this error is approximately 0.9% of the total pressure drop. Errors for all the data taken in this study are discussed in chapter 5. Figure 4.6 provides a comparison between the refrigerant pressure and the corresponding temperatures along the length of the channel assuming a linear pressure drop and using the empirically determined pressure drop as a function of quality for the representative case.

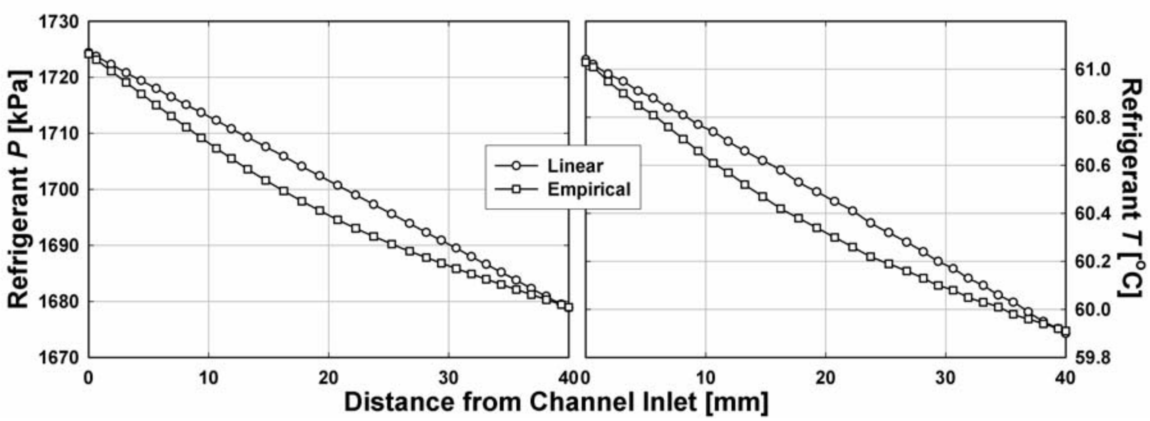

Figure 4.6: Refrigerant *P* and *T* along Channel Length for Representative Case

As seen in Figure 4.6, the pressure gradient in the first half of the channels is larger due to the higher refrigerant quality, but as the flow progresses further downstream, the pressure gradient decreases, and finally, at the exit, the pressure determined is the same as the observed exit pressure. With the pressure gradient varying along the length of the channels as a function of quality, the estimated refrigerant temperatures at the central HE nodes are lower than those predicted by the linear pressure drop profile, decreasing the available temperature gradient between the water side and the refrigerant side for heat transfer. For the representative case, the maximum segment temperature difference between the linear and empirical cases is approximately 0.15^{o}C (Figure 4.6) as compared to a driving temperature difference of 4.1^{o}C (based on empirical, 60.4^{o}C – 56.3^{o}C).

It should be noted that the qualities required for the above pressure calculations are determined based on the refrigerant condensation heat duty in each of the segments, obtained by solving all the equations iteratively. The refrigerant inlet enthalpy is known from the pre-heater energy balance and the enthalpy at the first node is determined using equation (4.47).

$$\frac{Q_{refg,1}}{2} = \dot{m} \cdot \left(h_{in} - h_1 \right) \tag{4.47}$$

where h is the refrigerant enthalpy, $\dot{m}$ is the refrigerant mass flow rate, and Q_{refg} is the condensation heat duty. $Q_{refg,1}$ is the amount of heat that goes from the refrigerant to the heater in the first segment and since the distance between the first node and inlet is half the segment length, only half of $Q_{refg,1}$ is used. This heat duty, when subtracted from the inlet enthalpy yields the enthalpy at the first node. Equation (4.48) is used to determine the enthalpy for each of the nodes downstream along the channel length. Again the difference between the enthalpy of the refrigerant at two adjacent nodes has been equated to the heat transferred to the copper wafer between the adjacent nodes.

$$\frac{\left(Q_{refg,i-1}+Q_{refg,i}\right)}{2}=\dot{m}\cdot\left(h_{i-1}-h_i\right)\quad\left\{2\le i\le N_{seg}\right. \tag{4.48}$$

Refrigerant quality is determined as a function of saturation pressure and enthalpy at the respective node (equation 4.49).

$$x_i=f\left('R134a',P=P_i,h=h_i\right)\quad\left\{1\le i\le N_{seg}\right. \tag{4.49}$$

4.3.3. Defining Thermal Resistances

Once the refrigerant-side and water-side temperatures are fixed, the next step is to define each of the thermal resistances shown in Figure 4.3.

To determine the effective refrigerant-side heat transfer area, the fin effectiveness of the channel walls is required. Figure 4.7 shows the schematic of the channel cross-section with various dimensions. The Copper wall separating the adjacent channels acts as a fin for refrigerant-side convective heat transfer.

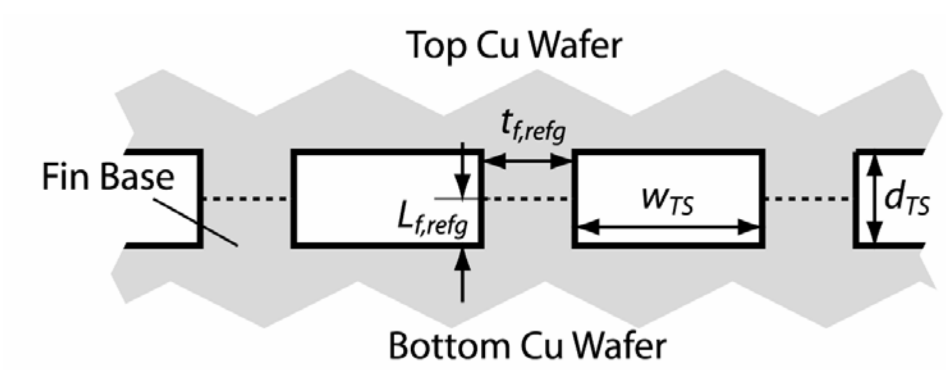

Figure 4.7: Refrigerant-side Effective Area Schematic

This wall is thus treated as a rectangular fin with adiabatic tip and base at the wafer surface. The dashed line in Figure 4.7, is the line of symmetry where the fin ends. Taking the wafer surface as the base of a rectangular fin, the length of the fin, $L_{f,refg}$ (equation 4.50) is half the channel depth, which is a constant 100 μm for all test-sections.

$$L_{f,refg} = \frac{d_{TS}}{2} \tag{4.50}$$

For a rectangular fin with an adiabatic tip, the fin efficiency is determined using equations (4.51) and (4.52), where $t_{f,refg}$ is the refrigerant fin thickness, i.e. 100 μm for all cases, as the wall thickness is 100 μm for all test sections.

$$m_{refg,i} = \sqrt{\frac{h_{refg} \cdot 2}{k_{Cu,i} \cdot t_{f,refg}}} \quad \{1 \le i \le N_{seg} \tag{4.51}$$

$$\eta_{f,refg,i} = \frac{\tanh\left(m_{refg,i} \times L_{f,refg}\right)}{m_{refg,i} \times L_{f,refg}} \quad \{1 \le i \le N_{seg} \tag{4.52}$$

Thus, the effective refrigerant-side area for each of the segments is the sum of effective fin area and the channel surface width (w_{TS}) as follows:

$$A_{eff,refg,i} = L_{seg,i} \times N \times \left(\eta_{f,refg,i} \times L_{f,refg} \times 2 + w_{TS}\right) \times 2 \quad \{1 \le i \le N_{seg} \tag{4.53}$$

In equation (4.53), the trailing factor of two accounts for the heat transfer from the refrigerant channels to both the top and bottom water blocks. Thus, the refrigerant-side condensation heat duty based on convective thermal resistance for each segment is given by equation (4.54).

$$Q_{refg,i} = h_{refg} \cdot A_{eff,refg,i} \cdot \left(T_{refg,i} - T_{w,refg,i}\right) \quad \{1 \le i \le N_{seg} \tag{4.54}$$

where $T_{w,refg,i}$ is the refrigerant-side wall temperature (shown in Figure 4.3), T_{refg} is the refrigerant temperature, and h_{refg} is the refrigerant heat transfer coefficient. It should be noted that the refrigerant-side heat transfer coefficient is assumed to be the same for all the segments. Even though the heat transfer coefficient also depends on quality, the measurements were not taken in enough detail to enable a segment-wise evaluation of the refrigerant heat transfer coefficient. (In Figure 4.3, the heat flow direction is assumed positive from the refrigerant to the water side.)

Figure 4.8 shows one half of the cross-section of the refrigerant channels. The refrigerant flows in the channels shown at the bottom of the block.

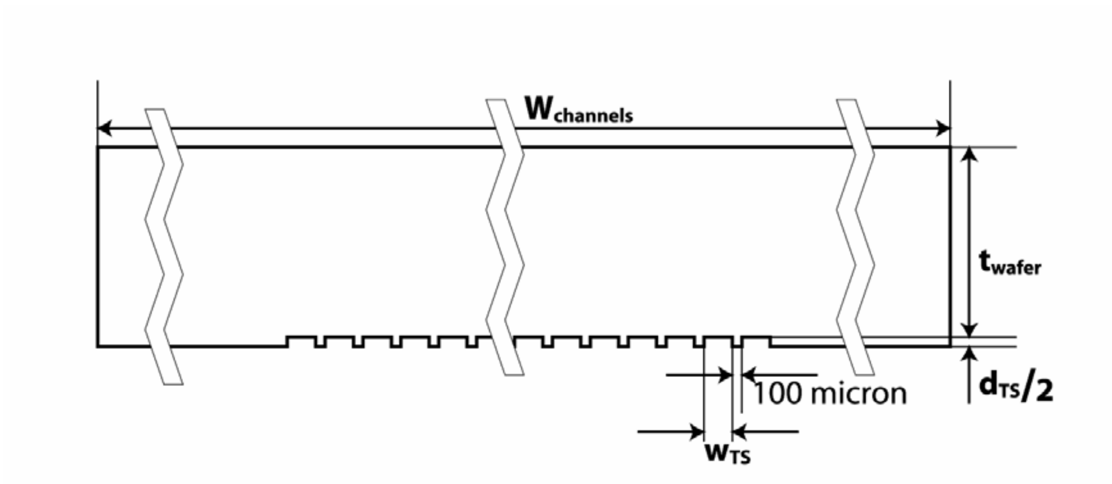

Figure 4.8: Refrigerant Channel Cu Wafer Cross-section Schematic

For heat transfer from the Copper wafer surface to the center of the copper wafer, the net heat transfer area is given by equation (4.55), where the total channel width $W_{channels}$ (shown in Figure 4.8) was measured using a vernier caliper for each test section.

$W_{channels}$ for 100×100 μm, 200×100 μm, 300×100 μm and 400×100 μm are 5.5, 7.8, 8.5 and 9.8 mm respectively. Again, a factor of two is used to account for the two sides.

$$A_{seg,H,i} = W_{channels} \cdot L_{seg,i} \cdot 2 \quad \{1 \le i \le N_{seg} \tag{4.55}$$

The heat flow from the copper wafer surface to the center of the wafer is the same as the heat flow from the refrigerant to the wafer surface for each segment. Thus, the refrigerant condensation heat duty based on the conduction thermal resistance for the heat flow to the center of wafer in each segment is given by equation (4.56).

$$Q_{refg,i} = k_{Cu,wf,i} \cdot \frac{A_{seg,H,i}}{t_{wafer}/2} \cdot \left(T_{w,refg,i} - T_{Cu,wf,i}\right) \quad \{1 \le i \le N_{seg} \tag{4.56}$$

where, $T_{Cu,wf,i}$ is the temperature and the node in center of Copper wafer (shown in Figure 4.3) and the conductivity ($k_{Cu,wf,i}$) is determined at $T_{Cu,wf,i}$. Since the node is located at the center of the wafer (shown in Figure 4.3), only half the wafer length is used in equation (4.56).

Figure 4.8 also shows the area available for the axial heat flow in the copper wafer ($A_{wf,V}$). The thickness of the wafer, t_{wafer} is 1 mm for the 100, 200 and 300 μm wide channels and 1.5 mm for the 400 μm wide channels. As mentioned before, the depth of the channels (d_{TS}) is the same for all test sections, i.e. 100 μm. Thus, the total heat flow area is given by equation (4.57), wherein the trailing factor of two accounts for the top and bottom wafers.

$$A_{wf,V} = \left[W_{channels} \cdot \left(t_{wafer} + \frac{d_{TS}}{2}\right) - N \cdot \frac{d_{TS}}{2} w_{TS}\right] \cdot 2 \quad \{1 \le i \le N_{seg} \tag{4.57}$$

The first term in the above equation is the total cross-sectional area of the wafer and half the channel depth, from which the cross-sectional area of the channels is being subtracted (second term). The conduction thermal resistance for heat flow from one segment to another neighboring segment in the copper wafer can be determined based on the above heat flow area. Thus, the heat flow between the Cu wafer nodes based on conduction thermal resistance along the length of wafer is given by equation (4.58).

$$Q_{wf,i} = k_{Cu,wf,i} \cdot \left(\frac{A_{wf,V}}{\left\{ \left(L_{seg,i} + L_{seg,i+1} \right) \big/ 2 \right\}} \right) \cdot \left(T_{Cu,wf,i} - T_{Cu.wf,i+1} \right) \quad \left\{ 1 \le i \le \left(N_{seg} - 1 \right) \right. \tag{4.58}$$

In certain cases, such as between the corner nodes 3 and 4 at the fin and HE joint in Figure 4.3, the length of the neighboring segments may differ, hence the half length of each segment is added instead of taking just one segment length. The heat flow direction is assumed to be positive from the inlet towards exit. In defining the above two conduction thermal resistances, it was assumed that the conductivity of the electroformed copper is same as that of bulk copper at the temperature of the respective node.

The next thermal resistance in the heat flow path is the conduction thermal resistance for heat flow from copper wafer to the water channel copper block. The vertical heat flow area for the copper wafer and the copper water channel block are different. The vertical heat flow are for each segment in the copper wafer $A_{seg,H,i}$ has already been discussed before (equation 4.55). Figure 4.9 shows the cross-sectional view of the water channel blocks and the refrigerant channels.

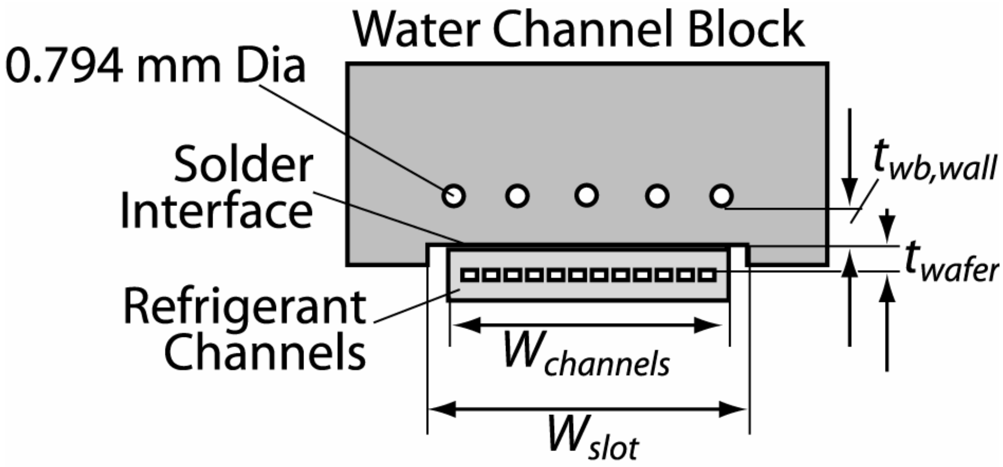

Figure 4.9: Cross-sectional View of Water and Refrigerant Channels

The refrigerant channels are soldered to the water channel block in the center of the 10.16 mm (W_{slot}) slot at the bottom in Figure 4.9. For all cases, the total refrigerant channel width $W_{channels}$ is less than the slot width. Since most of the heat flow takes place through the smallest thermal resistance path, only the slot width (W_{slot}) of 10.16 mm is considered for determining the heat flow area for each segment in the water blocks as shown in equation (4.59).

$$A_{w,seg,i} = W_{slot} \times L_{seg,i} \times 2 \quad \left\{ \left(N_{seg,fin} + 1 \right) \le i \le \left(N_{seg,fin} + N_{seg,HE} \right) \right. \tag{4.59}$$

It should be noted that nodes are located in the center of the Copper wafer and the wall between the water channels and solder interface as shown in Figure 4.3. Thus, the total conduction thermal resistance for heat flow from the center of copper wafer to the center of water block is a combination of two thermal resistances, the conduction resistance from the center of copper wafer to the interface, and the resistance from the interface to the center of the water channel blocks. The heat flow from the Cu wafer nodes to the respective water block nodes based on the total conduction thermal resistance discussed above is given by equation (4.60).

$$Q_{wall,V,i} = \frac{T_{Cu,wf,i} - T_{wb,i}}{\dfrac{t_{wafer}/2}{k_{Cu,wf,i} \cdot A_{seg,H,i}} + \dfrac{t_{wb,wall}/2}{k_{Cu,wb,i} \cdot A_{w,seg,i}}} \quad \left\{ \left(N_{seg,fin} + 1\right) \leq i \leq \left(N_{seg,fin} + N_{seg,HE}\right) \right. \tag{4.60}$$

Equation (4.61) provides the heat flow between the neighboring water block segments based on the conduction thermal resistance between them.

$$Q_{wb,H,i} = k_{Cu,wb,i} \cdot \frac{t_{wb,wall} \times W_{slot} \times 2}{L_{seg,i}} \cdot \left(T_{wb,i} - T_{wb,i+1}\right) \quad \left\{ \left(N_{seg,fin} + 1\right) \leq i \leq \left(N_{seg,fin} + N_{seg,HE} - 1\right) \right. \tag{4.61}$$

where, $T_{wb,i}$ is the temperature at the center of Cu wall separating the water channels and the solder interface (shown in Figure 4.3). In this case, the calculation for the heat flow area has been integrated into the thermal resistance equation as it is fixed for all segments and simple to evaluate. Also, since all segments of the water channel block are always in the central heat exchanger section, the length of each segment is the same. For the water channel blocks also, the positive heat flow direction is assumed to be in the direction of refrigerant flow.

The remaining thermal resistance is for heat flow from the water channel block to the water flowing at high velocity through the 10 channels (total in both the upper and lower blocks), which in turn again consists of the water block conduction thermal resistance and the water-side convective thermal resistance. The conduction thermal resistance from the center of the water channel block to the surface is determined in the same way as that from the interface to the center of the water channel block. The determination of convective thermal resistance is explained below.

The average thickness of the wall separating adjacent water channels is 1.635 mm, with a length of 0.794 mm. For the representative case, the water-side heat transfer coefficient is calculated to be 54.6 kW/m^2-K (demonstrated later), yielding a fin efficiency of 97%. For the complete range of data, based on this approximate calculation, water-side fin efficiencies vary from 96.6% to 97.4%, with an average of 97%. Thus, assuming 100% fin efficiency (to simplify calculations) for copper walls separating the water channels, the effective water-side heat transfer area for each segment is given by equation (4.62).

$$A_{eff,water,i} = 2 \cdot \pi \cdot \frac{D_{h,water}}{2} \times L_{seg,i} \times N_{water} \quad \left\{ \left(N_{seg,fin} + 1 \right) \le i \le \left(N_{seg,fin} + N_{seg,HE} \right) \right. \tag{4.62}$$

For the water-side convective heat transfer coefficient calculation, the water properties were determined based on the average water temperature. Gauge pressure was maintained at approximately 40 psi at the water pump exit for all experiments and the inlet to the pump was at atmospheric pressure. Thus, for property determination, an average pressure of 34 psia was used. The water mass flow rate through the 10 coolant channels with D = 0.794 mm at T_{water} = 56.3°C is calculated using equation (4.63).

$$\dot{m}_w = FR_w \cdot \rho_w \tag{4.63}$$

The flow area for the water channels is given by:

$$A_w = \pi \cdot \frac{D_w^{\ 2}}{4} \cdot N_w \tag{4.64}$$

For the representative case, with $\dot{m}_w$ = 3.73×10^{-2} kg/s and A_w = 4.95×10^{-6} m^2, the water flow velocity in the channels, V_w = 7.65 m/s and the Reynolds number, Re_w = 12.1×10^3 using equation (4.65) and (4.66).

$$V_w = \frac{\dot{m}_w}{\rho_w A_w} \tag{4.65}$$

$$\mathrm{Re}_w = \frac{\rho_w V_w D_w}{\mu_w} \tag{4.66}$$

Using the Dittus-Bolter equation (4.67) for the determination of the water heat transfer coefficient, the Nusselt number is 68, while the water-side heat transfer coefficient (equation 4.68) is 54.6 kW/m^2-K. A conservative 25% uncertainty is assumed in the water-side heat transfer coefficient for the overall uncertainty analysis.

$$Nu_w = 0.023 \cdot \mathrm{Re}_w^{\ 0.8}\, \mathrm{Pr}_w^{\ 0.4} \tag{4.67}$$

$$h_w = Nu_w \frac{k_w}{D_w} \tag{4.68}$$

The water-side convective thermal resistance can be determined based on the heat transfer coefficient from equation (4.68) and the effective area based on equation (4.64). Heat flow from the water block to the water is given by equation (4.69).

$$Q_{water,i} = \frac{T_{wb,i} - T_{water,i}}{\dfrac{t_{wb,wall}/2}{k_{Cu,wb,i} \cdot A_{w,seg,i}} + \dfrac{1}{h_{water} \cdot A_{eff,water,i}}} \quad \left\{ \left(N_{seg,fin} + 1\right) \le i \le \left(N_{seg,fin} + N_{seg,HE}\right) \right. \tag{4.69}$$

All the above determined heat flow rates, along the thermal resistances shown in Figure 4.3, are used as inputs to the energy balance of each of the nodes discussed in the next section. These energy balances are then solved iteratively to obtain all the unknown temperatures, heat flow rates and the refrigerant-side heat transfer coefficients.

4.3.4. Node Energy Balances

After the determination of the thermal resistances for all the heat flow paths as discussed above, an energy balance for each of the segments, and an overall energy balance is performed. The total heat duty for the test-section heat exchanger is determined based on energy balances on the pre-heater and post-heater, as discussed in previous sections. This total heat duty is equal to the total condensation heat removed from the refrigerant in all segments along the length as represented in equation (4.70).

$$\dot{Q}_{TS} = \sum_{i=1}^{N_{seg}} Q_{refg,i} \tag{4.70}$$

The refrigerant channel copper wafer is divided into three sections, one fin section on each side, and the central heat exchanger section. The energy balance for the fin corner nodes (such as node 1 and 10 in Figure 4.3) is shown in Figure 4.10. Equations (4.71) and (4.72) provide the mathematical representation for the energy balance shown in Figure 4.10.

$$Q_{wf,1} = Q_{refg,i} \tag{4.71}$$

$$Q_{refg,N_{seg}} + Q_{wf,N_{seg}-1} = 0 \tag{4.72}$$

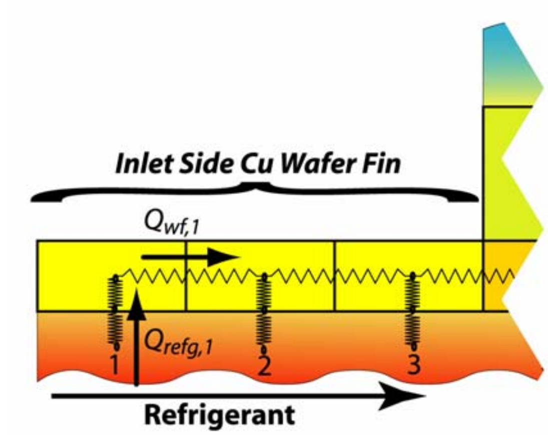

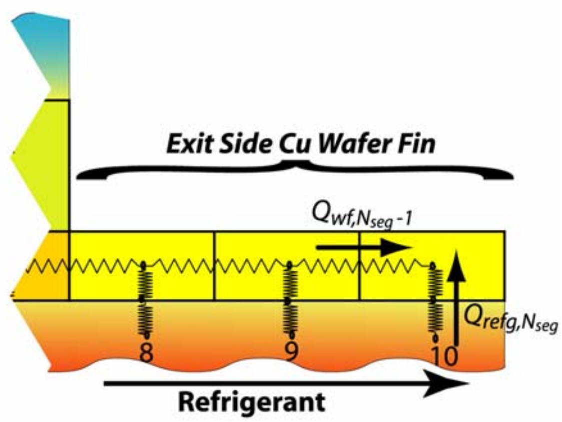

(a) Inlet Side **(b) Exit Side**

Figure 4.10: Fin Corner Nodes Energy Balance

The energy balance for the other nodes along the length of fin (such as nodes 2, 3, 8 and 9 in Figure 4.3) is shown in Figure 4.11 and given by equation (4.73).

$$Q_{wf,i-1} + Q_{refg,i} = Q_{wf,i} \quad \begin{cases} 2 \le i \le N_{seg,fin} \\ \left(N_{seg,fin} + N_{seg,HE} + 1\right) \le i \le \left(N_{seg} - 1\right) \end{cases} \tag{4.73}$$

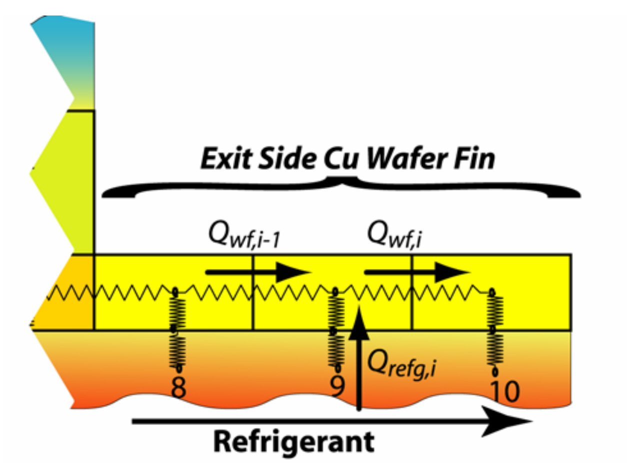

Figure 4.11: Fin Section Middle Node Energy Balance

These energy balances are based on the assumption that heat flow is positive in the direction of flow of the refrigerant and from the refrigerant towards the water-side. The energy balance for the central HE wafer section nodes (such as nodes 4, 5, 6 and 7 in Figure 4.3) is shown in Figure 4.12 and given by equation (4.74).

$$Q_{wf,i-1} + Q_{refg,i} = Q_{wf,i} + Q_{wall,V,i} \quad \left\{ N_{seg,fin} + 1 \le i \le \left(N_{seg,fin} + N_{seg,HE} \right) \right. \tag{4.74}$$

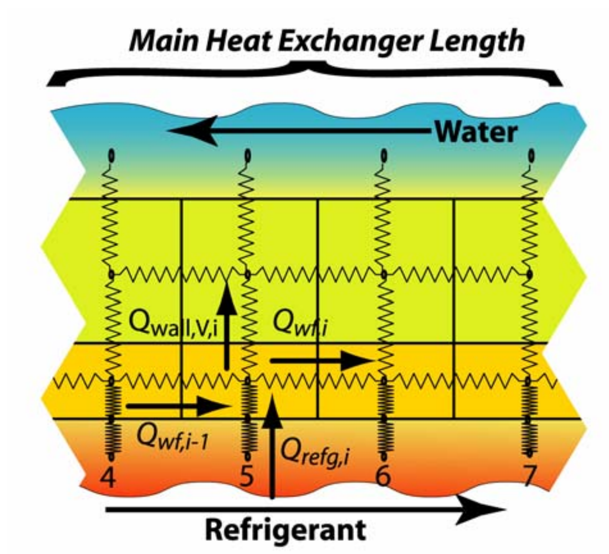

Figure 4.12: Central HE Cu Wafer Node Energy Balance

As in the case of the fin section, for the water block also, the corner nodes must be addressed separately. The energy balances for the two corner nodes in the water block (i.e. nodes 5 and 7 in Figure 4.3) are shown in Figure 4.13 given by equations (4.75) and (4.76).

$$Q_{wall,V,N_{seg,fin}+1} = Q_{wb,H,N_{seg,fin}+1} + Q_{water,N_{seg,fin}+1} \tag{4.75}$$

$$Q_{wall,V,\left(N_{seg,fin}+N_{seg,HE}\right)} + Q_{wb,H,\left(N_{seg,fin}+N_{seg,HE}-1\right)} = Q_{water,\left(N_{seg,fin}+N_{seg,HE}\right)} \tag{4.76}$$

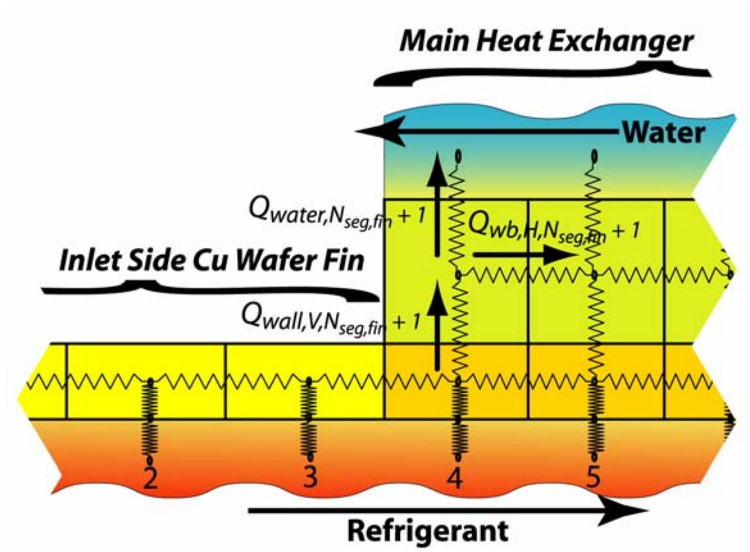

(a) Inlet Side

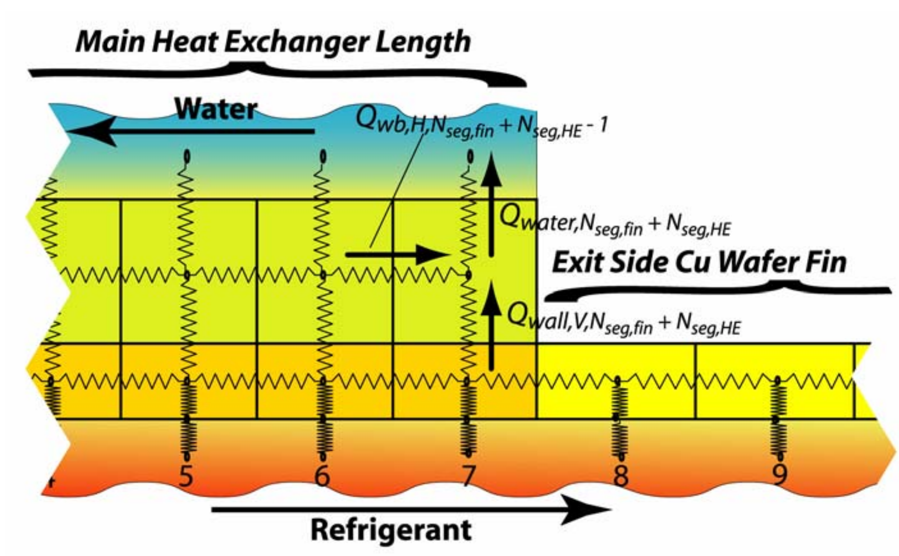

(b) Exit Side

Figure 4.13: Water Block Corner Node Energy Balance

The energy balance for the nodes other than the corner nodes in the water channel blocks (such as nodes 5 and 6 in Figure 4.3) is shown in Figure 4.14 and given by equation (4.77).

$$Q_{wall,V,i} + Q_{wb,H,i-1} = Q_{wb,H,i} + Q_{water,i} \quad \left\{\left(N_{seg,fin} + 2\right) \leq i \leq \left(N_{seg,fin} + N_{seg,HE} - 1\right) \right. \tag{4.77}$$

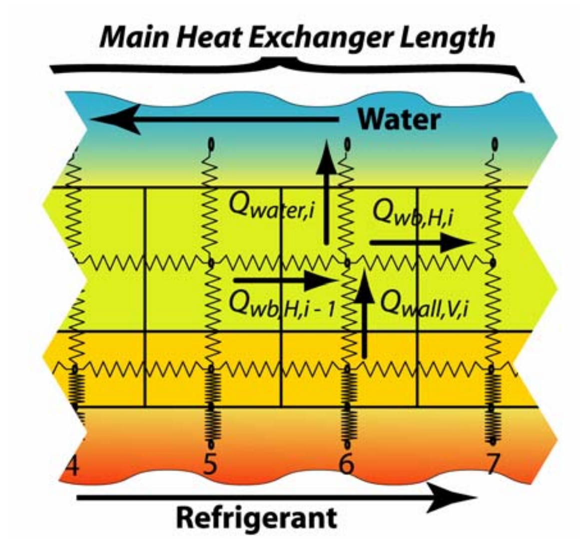

Figure 4.14: Water Block Middle Node Energy Balance

4.3.5. Solution of Segmental Heat Transfer Equations

All the above energy balance equations for each of the nodes, and the equations for each of the resistances are solved simultaneously to determine the refrigerant-side heat transfer coefficients. Figure 4.15 shows the temperature variation in each of the segments based on the heat transfer analysis discussed above.

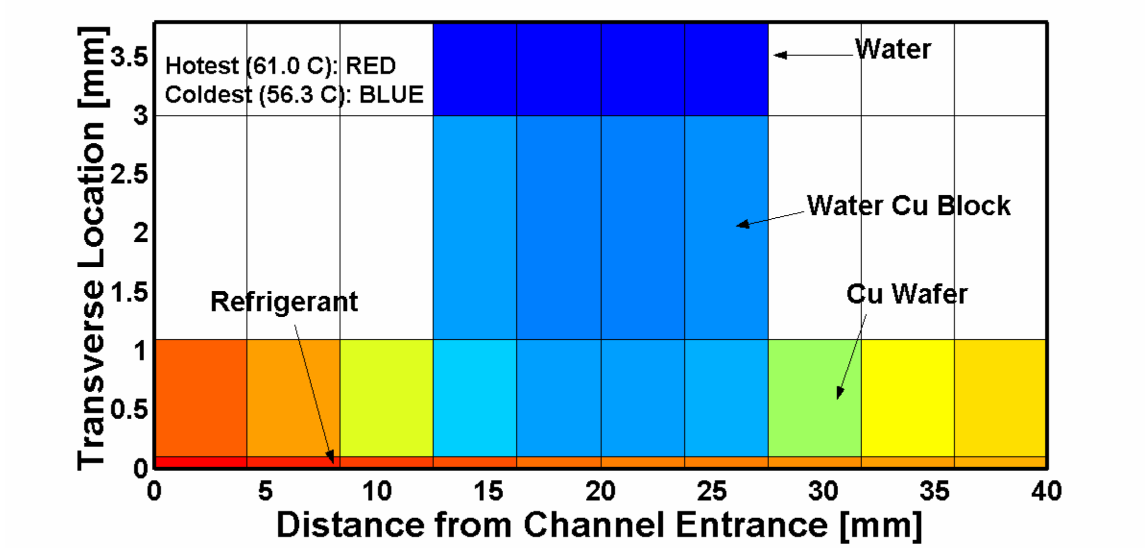

Figure 4.15: Temperature Plot for Representative Case

The temperature of the water is the lowest while the entering refrigerant temperature is the highest. The temperature of the water does not change much due to the high flow rates, while as the refrigerant flows through the refrigerant channels, its saturation temperature decreases more significantly due to the decrease in pressure. The temperature of the Cu wafer nodes first decreases in the inlet fin as we moves towards the center and then again increases in the exit fin, indicating that in both the fins heat is flowing towards the central HE section. Also, in all segments, the Cu Wafer temperature is lower than the corresponding segment refrigerant temperature, indicating that heat flows from the refrigerant to the Cu wafer. The difference between the Cu Wafer temperature and the refrigerant temperature is the highest in the central HE section, indicating that most of the heat is transferred from the refrigerant to the wall in the central HE section. The temperature variation for the Copper wafer nodes is larger on the inlet side fin compared to that in the exit side fin, indicating that more heat is transferred from the refrigerant to the Cu wafer in the inlet side fin as compared to the exit side fin.

The discussion thus far was based on dividing the test section into 10 segments (3 in each of the fins and 4 in the heat exchanger section.) To determine the sensitivity of the results to the grid size, the analysis was repeated using progressively finer grids. Figure 4.16 shows the value of the refrigerant-side heat transfer coefficient estimated using such analysis for a varying number of segments. For this analysis, the number of segments in each of the three sections is same, i.e. if the total number of segments is 30, then there are 10 segments in each of the two fins and 10 segments in the central HE section.

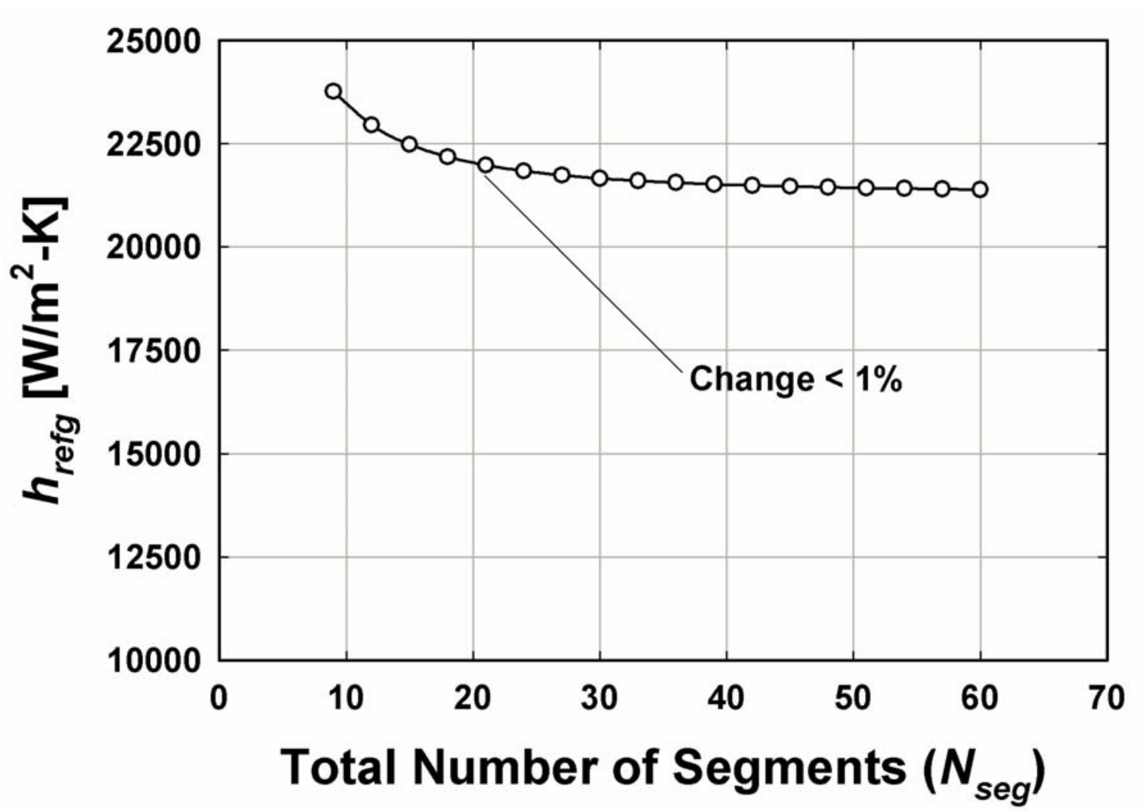

Figure 4.16: Effect of Number of Segments on h_{refg} for Representative Case

As expected, the effect of the number of segments diminishes with an increase in the number of segments. For a total number of segments greater than 20, the change in the estimated refrigerant-side heat transfer coefficient is less than 1%, while the computational time increases considerably with an increasingly finer grid. Based on this analysis, a total of 30 segments were chosen for analyzing the data from this study. The heat transfer coefficient for the representative case based on this analysis is 21.7 kW/m^2-K. An estimation of the uncertainty in the heat transfer coefficient and pressure drop is presented in a subsequent section.

Figure 4.17 shows the variation in the segmental refrigerant condensation heat duty along the length of the channel.

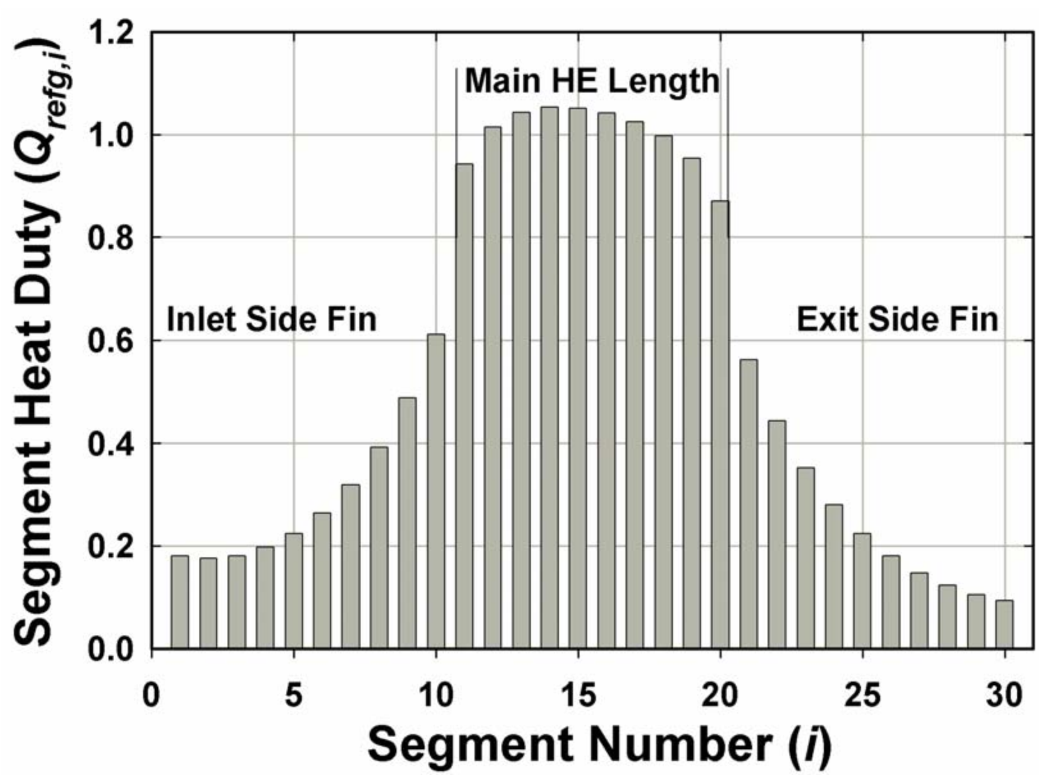

Figure 4.17: Variation in Segment Heat Duty along Channel Length

Since the temperature gradient in the central HE section is the highest, most of the heat is transfered in this section as indicated by the high segmental heat duties. The heat duties in the fin segments decrease as we go further away from the central HE section. The heat duties in the inlet side fin are higher than the exit side fin due to higher refrigerant temperatures. Due to this variation in heat duty along the length of the channel, a simple average of refrigerant or refrigerant-side wall temperature would not be a good representation of the effective refrigerant or refrigerant-side wall temperatures. Similarly, in calculating the refrigerant-side effective heat transfer area (needed to calculate resistance ratios) the difference in the fin effect on the inlet and exit side has to be taken into account. The next section discusses the methodology used to derive these additional parameters based on segmental heat duty considerations.

4.3.6. Calculation of Additional Parameters

In the previous section, the procedure to analyze the data in the current study to obtain the refrigerant-side heat transfer coefficients was explained. But to better understand the results and the uncertainties (discussed in the next section) additional parameters such as the average refrigerant temperature, refrigerant-side wall temperature and resistance ratio must be calculated. This section addresses the determination of these additional parameters.

Both the refrigerant temperature (59.9^{o}C to 61.03^{o}C) and the wall temperature (57.33^{o}C to 60.39^{o}C) vary along the length of the test section. Of the total heat transferred in the test section (15.54 W), 9.99 W, i.e. 64% of the condensation heat duty is extracted out of the refrigerant in the central HE segments (equation 4.78) and the remaining heat duty is transfered in the inlet (3.03) and exit (2.52 W) fin sections (equations 4.79 and 4.80).

$$\dot{Q}_{TS,HE} = \sum_{i=\left(N_{seg,fin}+1\right)}^{\left(N_{seg,fin}+N_{seg,HE}\right)} Q_{refg,i} = 9.99 \text{ W} \tag{4.78}$$

$$\dot{Q}_{TS,Fin,in} = \sum_{i=1}^{N_{seg,fin}} Q_{refg,i} = 3.03 \text{ W} \tag{4.79}$$

$$\dot{Q}_{TS,Fin,out} = \sum_{i=\left(N_{seg,fin}+N_{seg,HE}+1\right)}^{N_{seg}} Q_{refg,i} = 2.52 \text{ W} \tag{4.80}$$

Since a varying amount of heat transfer occurs in the different sections along the length of the refrigerant channels, the average refrigerant and wall temperatures are determined based on a weighted average of the segmental heat duty (equations 4.81 and 4.82).

$$TQ_{refg,i} = Q_{refg,i} \cdot T_{refg,i} \quad \left\{1 \le i \le N_{seg}\right. \tag{4.81}$$

$$T_{refg,Qave} = \frac{\sum_{i=1}^{N_{seg}} TQ_{refg,i}}{\dot{Q}_{TS}} \tag{4.82}$$

In this case, the average refrigerant temperature is determined to be 60.4°C using equations (4.81) and (4.82). Similarly, the average refrigerant wall temperature is determined to be 58.1°C using equations (4.83) and (4.84).

$$TQ_{refg,wall,i} = Q_{refg,i} \cdot T_{w,refg,i} \quad \left\{1 \le i \le N_{seg}\right. \tag{4.83}$$

$$T_{refg,wall,Qave} = \frac{\sum_{i=1}^{N_{seg}} TQ_{refg,wall,i}}{\dot{Q}_{TS}} \tag{4.84}$$

The above determined additional parameters and several other parameters calculated in this section are shown in the schematic shown in Figure 4.18 below.

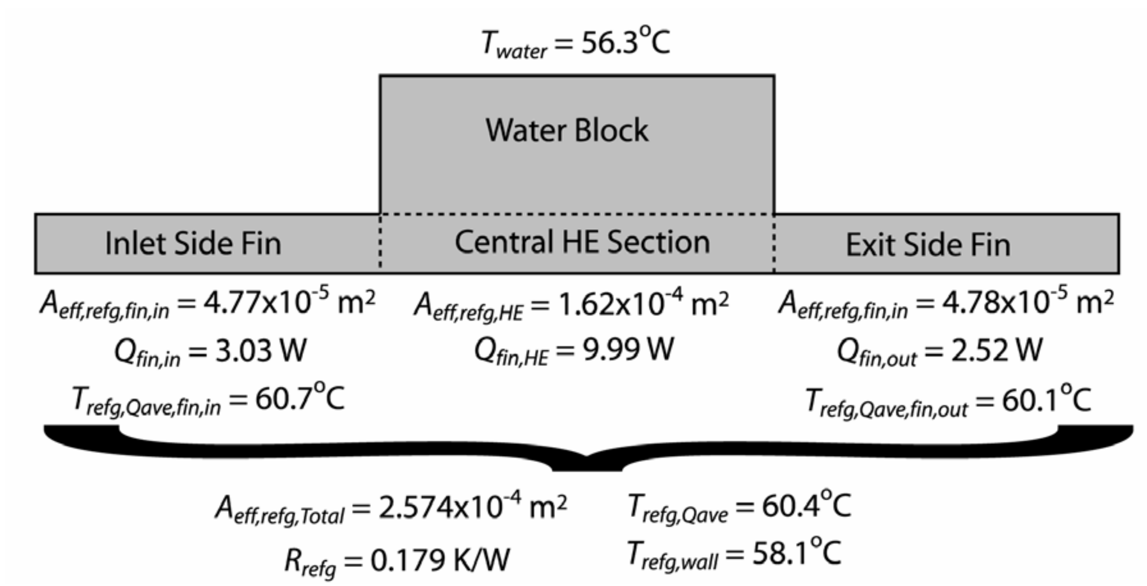

Figure 4.18: Average Refrigerant, Wall and Coolant-Side Parameters

Based on the above refrigerant temperature, and the average water temperature of 56.3°C determined earlier, the total effective resistance of the whole test-section heat exchanger (approximated on a 1-D basis) can be estimated using equation (4.85) to be 0.259 K/W.

$$R_{Total} = \frac{T_{refg,Qave} - T_{water}}{\dot{Q}_{TS}} \tag{4.85}$$

Similarly, for computing the effective refrigerant-side thermal resistance, the effective refrigerant-side area has to be determined. In the central heat exchanger section, the effective refrigerant-side area can be easily determined by simply adding the effective refrigerant areas for each of the segments as in equation (4.86) and is 1.62×10^{-4} m^2.

$$A_{eff,refg,HE} = \sum_{i=N_{seg,fin}+1}^{N_{seg,fin}+N_{seg,HE}} A_{eff,refg,i} \tag{4.86}$$

For determining the effective refrigerant-side area for each of the fin sections, they are treated as simple one dimensional fins, wherein the base temperature is the temperature of the adjacent central HE section corner node (such as nodes 4 and 7 in Figure 4.3). The average refrigerant temperature for the fin section is determined in the same way as for the overall average refrigerant temperature using equations (4.87) and (4.88).

$$T_{refg,Qave,fin,in} = \frac{\sum_{i=1}^{N_{seg,fin}} TQ_{refg,i}}{\dot{Q}_{TS,Fin,in}} \tag{4.87}$$

$$T_{refg,Qave,fin,out} = \frac{\sum_{i=(N_{seg,fin}+N_{seg,HE}+1)}^{N_{seg}} TQ_{refg,i}}{\dot{Q}_{TS,Fin,out}} \tag{4.88}$$

The average refrigerant temperatures for the inlet and exit side fin sections are determined to be 60.7°C and 60.1°C respectively. For a simple one-dimensional fin, the effective area can be determined by dividing the fin heat duty by the convective heat transfer coefficient and the temperature difference between the base and the convective medium. This same methodology is used to determine the effective area for the inlet/exit fin sections using equations (4.89) and (4.90).

$$A_{eff,refg,fin,in} = \frac{\dot{Q}_{Fin,in}}{h_{refg} \cdot \left(T_{refg,Qave,fin,in} - T_{Cu,wf,N_{seg,fin}+1}\right)} \tag{4.89}$$

$$A_{eff,refg,fin,out} = \frac{\dot{Q}_{Fin,out}}{h_{refg} \cdot \left(T_{refg,Qave,fin,out} - T_{Cu,wf,N_{seg,fin}+N_{seg,HE}}\right)} \tag{4.90}$$

The resulting areas for the inlet and exit fin sections are 4.77×10^{-5} m^2 and 4.78×10^{-5} m^2, yielding a total refrigerant side effective area (equation 4.91) of 2.574×10^{-4} m^2.

$$A_{eff,refg,Total} = A_{eff,refg,fin,in} + A_{eff,refg,HE} + A_{eff,refg,fin.out} \tag{4.91}$$

This effective refrigerant-side heat transfer area and the refrigerant heat transfer coefficient yield an effective refrigerant convective resistance of 0.179 K/W (equation 4.92).

$$R_{refg} = \frac{1}{h_{refg} \cdot A_{eff,refg,Total}} \tag{4.92}$$

Thus the resistance ratio between the refrigerant-side thermal resistance and the remaining (composite copper wall and water-side) thermal resistance for the representative case is determined using equation (4.93) to be 2.3.

$$R_{ratio} = \frac{R_{refg}}{R_{Total} - R_{refg}} \tag{4.93}$$

The resistance ratio of 2.3 clearly indicates that the refrigerant-side convective resistance is the dominant resistance. Such high resistance ratios are important to maintain low uncertainties in the determination of the refrigerant heat transfer coefficients. This is further discussed in the next section on uncertainty analysis.

4.4. Uncertainty Analysis

The data analysis discussed above was conducted using Engineering Equation Solver (Klein, 2006) software, which also enables computation of the respective uncertainties based on the approach of Taylor and Kuyatt (1994). If Y is a function of several variables (equation 4.94) X_1, X_2, X_3 etc., then the uncertainty in Y is given by equation (4.95), wherein U_X is the uncertainty in variable X.

$$Y = f\left(X_1, X_2, X_3, ...\right) \tag{4.94}$$

$$U_Y = \sqrt{\sum_i \left(\frac{\partial Y}{\partial X_i}\right)^2 \cdot U_{X_i}^2} \tag{4.95}$$

Table B-9 presents a detailed uncertainty analysis for the representative case. Table B-2 provides the respective uncertainties in each of the measured parameters. With a ±0.5°C uncertainty in the temperature measured at the flow meter entrance and a 6.89 kPa pressure measurement uncertainty, the refrigerant density at the flow meter is estimated to be 1210±2 kg/m^3. This, along with the volumetric flow rate measurement uncertainty of ±0.5% leads to a refrigerant mass flow rate of $2.18\times10^{-4}\pm1.1\times10^{-6}$ kg/s (≈ ±0.52%). The fabrication technique used to make refrigerant channels results in a ±0.5 μm dimensional uncertainty (Christenson, 2005), which in turn yields a total refrigerant flow area of $3.6\times10^{-7}\pm2\times10^{-7}$ m^2 (≈ ±0.56%). This dimensional uncertainty, along with the mass flow rate uncertainty estimated above, yields a refrigerant mass flux in the channels of 606±4.6 kg/m^2-s (≈ ±0.8%).

With the uncertainties in temperature and pressure measurement at the pre-heater inlet, the refrigerant inlet enthalpy is estimated as 93±0.14 kJ/kg. The electrical input in the heater is 31.02 W (±0.2%), while the losses are 1.07 W (where a 50% uncertainty is conservatively assumed for the estimation of heat losses). This yields a heat input to the refrigerant of 29.95±0.54 W (≈ ±1.8%). Combining the measurement uncertainty in mass flow rate and the uncertainty in the refrigerant heat input, the test section inlet enthalpy is calculated to be 230±2.6 kJ/kg, which yields a test section inlet quality of 0.64±0.02. Similar calculations on the post-heater yield a test section outlet quality of 0.14±0.02. These test section inlet and outlet conditions yield a heat duty of 15.54±0.78 W, i.e., an uncertainty of 5%.

The uncertainty in the differential pressure measurement between the test-section inlet and exit is ±0.16 kPa. A conservative 50% uncertainty is assumed in the calculation of the inlet/exit pressure losses and the deceleration pressure gain. Thus, the uncertainty in frictional pressure drop is determined to be 47.2±1.1 kPa, i.e. a 2.3% uncertainty.

Uncertainties in the channel inlet and exit pressures are determined by combining the uncertainty in the measurement of absolute (±6.89 kPa) and differential (±0.19 kPa) pressures at test section inlet/exit. This is because as explained in section 4.2, (Figure 4.1), pressures at the channel inlet and outlet were computed from a combination of a) test section inlet and outlet pressures, b) measured pressure drops, and c) estimates of pressure losses in the inlet and exit sections. For this case, the channel inlet and exit pressures are determined to be 1724±4.9 kPa and 1679±4.9 kPa, respectively.

This channel inlet/exit pressure uncertainty corresponds to an approximately 0.13°C uncertainty in refrigerant inlet and exit temperatures. The uncertainty in the water inlet and exit temperatures is 0.1°C. This temperature measurement uncertainty is different from the temperature measurement uncertainty at the flow meter entrance as two different types of thermocouples were used as discussed in chapter 3. An uncertainty of ±25% is assumed for the calculation of the water-side heat transfer coefficient (and therefore the thermal resistance). The least count of the instrument used in the measurement of the overall width of the channels ($W_{channels}$) was 0.01 mm, thus a conservative 0.1 mm uncertainty is assumed in the overall width of the refrigerant channels. This uncertainty leads to an uncertainty in the thermal resistances associated with the copper wafer. With the above uncertainties and a 5% uncertainty in the test-section condensation heat duty, the heat transfer coefficient is estimated to be 21.7±2.98 kW/m^2-K, i.e., an uncertainty of 14%.

The most important contributor to the uncertainty in h_{refg} is the assumed 25% uncertainty in h_{water} as evidenced by a 5% uncertainty in the condensation heat duty, yielding a 14% uncertainty in the refrigerant heat transfer coefficient. As h_{refg} increases, R_{ratio} decreases, leading to higher uncertainties in h_{refg} due to the increased contribution of the water-side heat transfer coefficient uncertainties. The other major contributors to the uncertainties in the heat transfer coefficients are the uncertainties in the determination of heat losses in the pre-heater and post-heater and uncertainties in the measurement of pressures and temperatures in the test section. For the same test section and saturation temperature, the uncertainty increases as the mass flux decreases, primarily because the test section heat transfer rates are smaller at the lower mass fluxes. This implies that the heat losses in the pre- and post-heaters assume a greater significance at the lower mass fluxes. The other contributors to the uncertainty include uncertainties in water temperature measurement and test section pressure measurement. For the same mass flux, at the lower temperatures, heater losses are insignificant because of the small ΔT with respect to the ambient. However, at the higher saturation temperatures, heat losses increase considerably, becoming the primary determinant of the uncertainty in heat transfer coefficient. The uncertainties in pressure measurement affect the heat transfer coefficient more at the lower temperatures, primarily because at these low temperatures the heat loss contributions are very low. Also, the pressure measurement accuracy decreases at the lower pressures due to its uncertainty being based on the pressure transducer span. This uncertainty in turn affects saturation temperature determination, thereby affecting the uncertainty in refrigerant heat transfer coefficient. A more detailed discussion for the trends observed in the uncertainties for all the data taken in this study is included in chapter 5.

CHAPTER 5. RESULTS AND DISCUSSION

Tests were conducted on channels of four different sizes and shapes as indicated in Figure 5.1. Each of these tubes has a different aspect ratio and hydraulic diameter. Details of these channels were provided in Table 3-1. Thus, from the pressure drop and heat transfer results obtained from experiments on these five tubes, the effects of aspect ratio and hydraulic diameter can be determined. This chapter presents the experimental results for each of the test sections and discusses the trends and uncertainties in the data. In addition, the heat transfer and pressure drop results form this study are compared with the predictions of models available in the literature. These discussions form the basis for the pressure drop and heat transfer models proposed in Chapter 6. This chapter is supplemented by Appendix C, which presents additional detailed tables of the results.

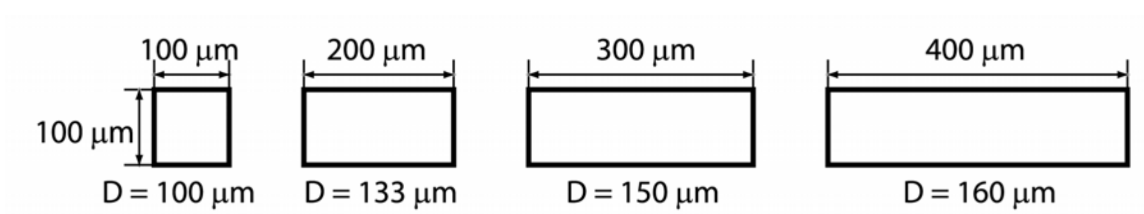

Figure 5.1: Channel Shapes Tested (To Scale Drawing)

For each test section under consideration, tests were conducted at saturation temperatures of 30, 40, 50, and 60^{o}C and mass fluxes of 300, 400, 600 and 800 kg/m^2-s. In the current study, a data set is refers to data at a single temperature and mass flux combination. Thus, a total of 16 data sets were obtained for each test section, and for each data set, several data points were taken at varying average refrigerant qualities. For each data set, the range of quality covered was governed by the minimum quality change that would be achieved across the test section. The uncertainties associated with the mass flux and average quality at each data point are determined using the procedure discussed in the previous chapter. Figures 5.2 to 5.5 show the mass fluxes and average qualities for the data taken for each of the tubes under consideration in the current study. The associated uncertainties in massflux and quality are also shown in the figures. The uncertainties in massflux are relatively insignificant for most of the data points, as the uncertainty in the measurement of volumetric flow rate is only ±0.5%, and the contribution of uncertainties in pressure and temperature measurements and dimensions to the uncertainty in mass flux is almost negligible. Mass-flux uncertainties for the 100×100 μm channels are relatively high as the volumetric flow rates for these channels are very low (5.9 to 8.2 ml/min). Since the dimensional uncertainty in the channels is fixed at ±0.5 μm for all channel walls, their relative contribution in the 100×100 μm channels is the highest. Also, due to the inability to measure and control the lower refrigerant flow rates, and due to high quality changes in the test section at such low flow rates, data for the 300 and 400 kg/m^2-s mass fluxes could not be taken for 100×100 μm channels.

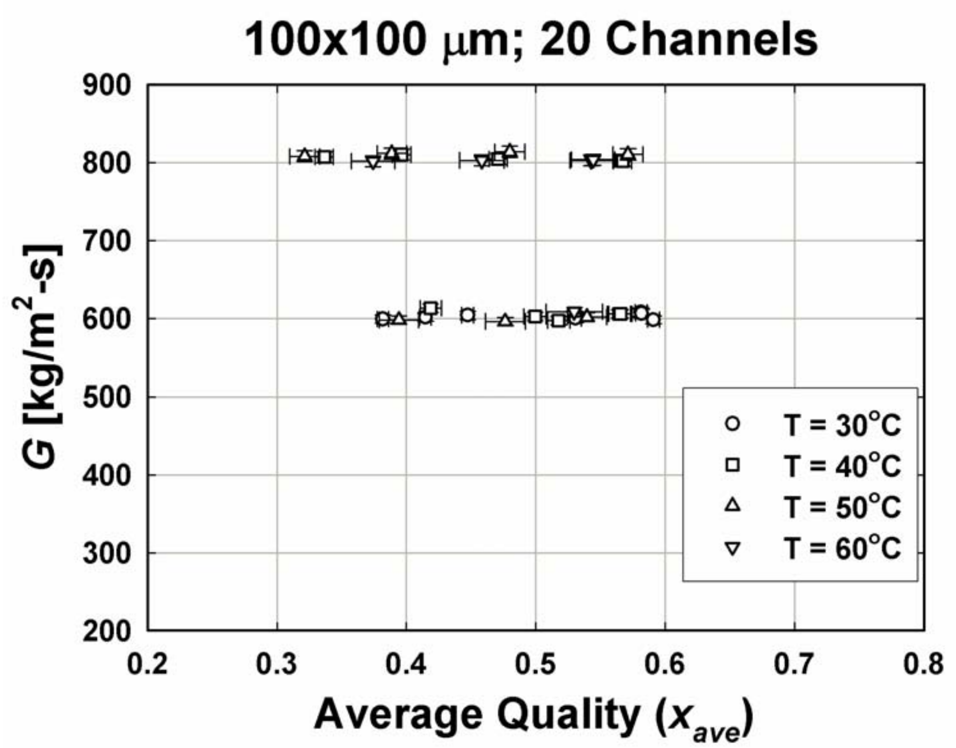

Figure 5.2: Mass Flux and Average Quality Uncertainties for 100×100 μm channels

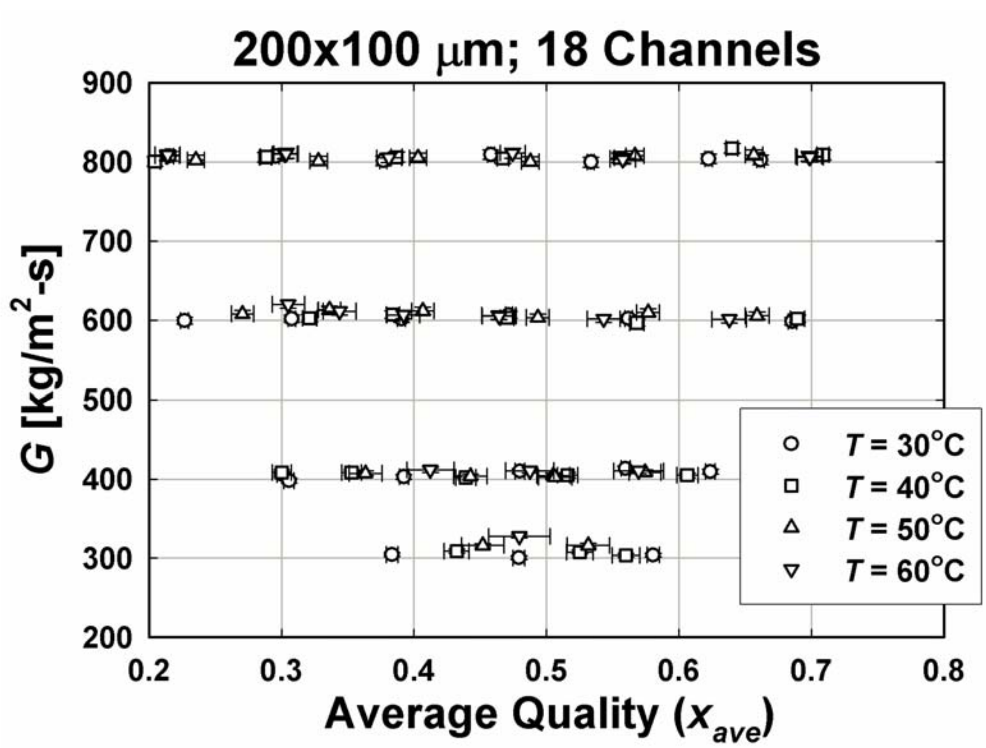

Figure 5.3: Mass Flux and Average Quality Uncertainties for 200×100 μm Channels

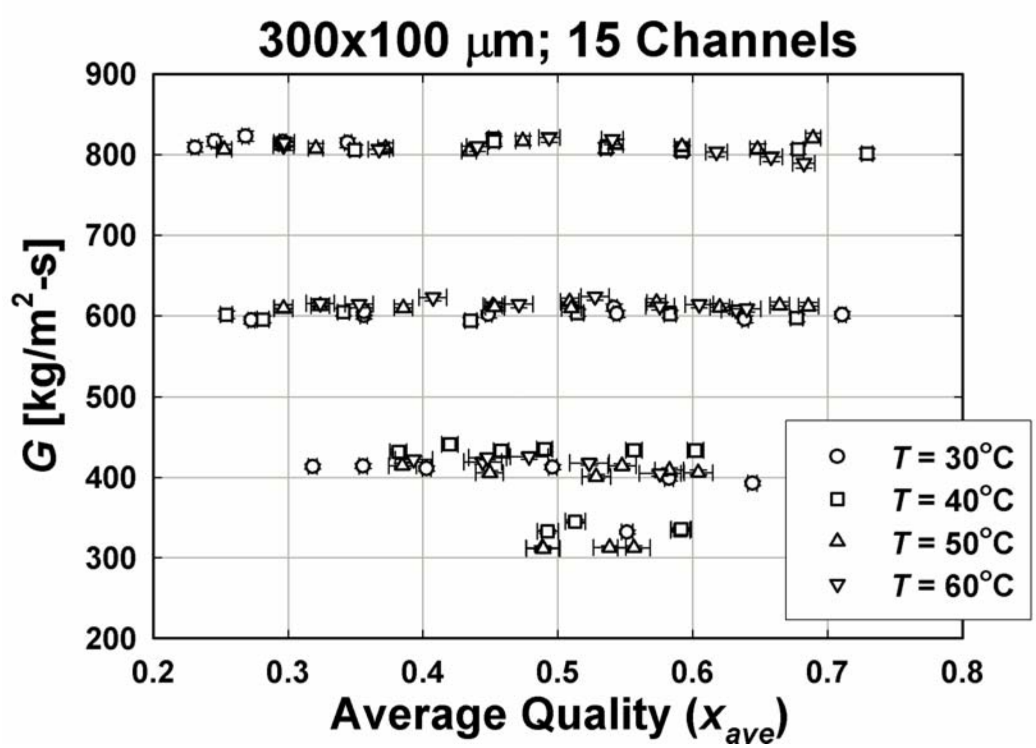

Figure 5.4: Mass Flux and Average Quality Uncertainties for 300×100 μm Channels

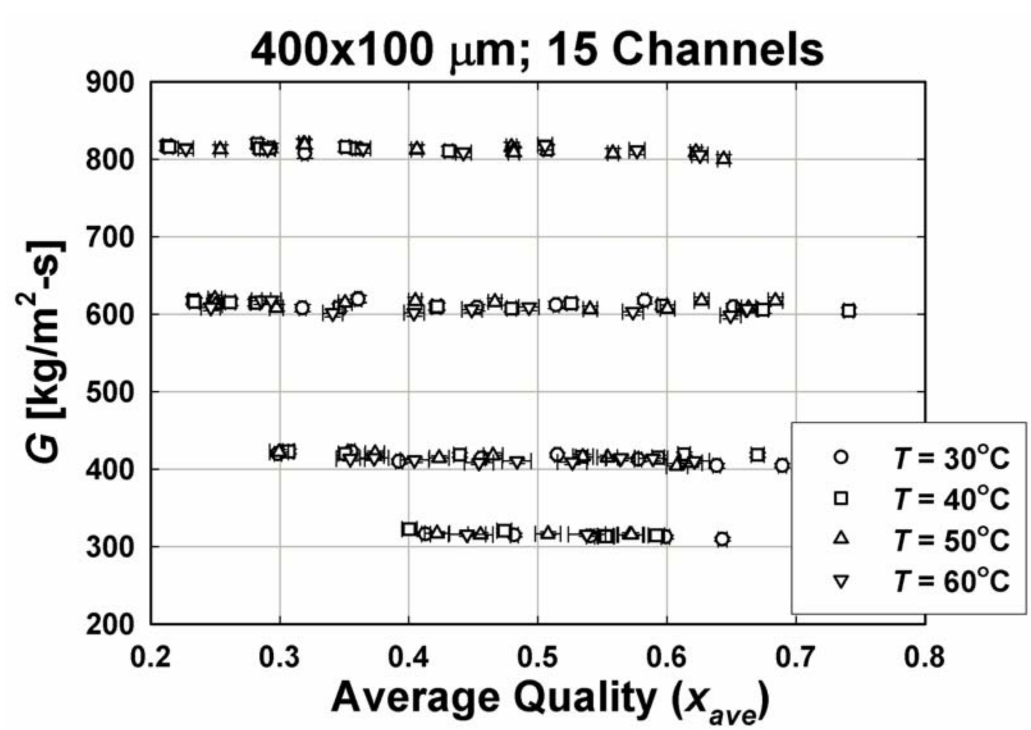

Figure 5.5: Mass Flux and Average Quality Uncertainties for 400×100 μm Channels

The main contributors to the uncertainty in the average quality were the heat losses in the pre- and post-heaters in the refrigerant loop. Heat losses from the pre- and post-heater were higher at higher saturation temperatures, while for these same cases, the latent heat of vaporization is lower (at the higher saturation temperatures). Thus, for the same mass flux and test section, the uncertainty in the determination of inlet/exit qualities is higher at the higher saturation temperatures (for example, for the 200×100 μm channels at a 600 kg/m^2-s mass flux, the average uncertainty in average quality at saturation temperature of 30^{o}C and 60^{o}C is 0.3% and 1.2%, respectively). It should also be noted that the heat losses in the pre- and post-heater are almost the same at all mass fluxes for the same saturation temperature. Due to the relatively large size of the refrigerant pre and post-heaters and very small refrigerant flow rates, the heat losses from the refrigerant to the ambient do not vary appreciably with mass flux. The same amount of heat losses lead to greater uncertainty in quality at lower mass fluxes for the same saturation temperature (for example, for 200×100 μm channels at a saturation temperature of 50^{o}C, the average uncertainty in average quality at mass fluxes of 200 and 800 kg/m^2-s is 1.6% and 0.7%, respectively). Tables C-1 to C-4 provide average uncertainties in quality and mass flux for each of the data sets for each of the tubes tested in the study. For the complete set of data taken in the current study, the uncertainties in mass flux vary from 0.7% to 0.9%, and uncertainties in quality vary from 0.2% to 2.3%. The average uncertainties in mass flux and quality of the whole study are 0.76% and 0.7%, respectively.

The maximum measurable pressure drop across the test section was 248 kPa (36 psi), while the maximum allowable differential pressure drop across the refrigerant pump was 262 kPa (38 psi). In certain cases, for T = 30°C and G = 800 kg/m^2-s (highest pressure drop case for each test section), the total pressure drop across the test section exceeded 220 kPa (32 psi), due to which data could not be taken.

5.1. Pressure Drop Results

The frictional pressure drop in the channels was calculated after subtracting all expansion/contraction, bend and acceleration/deceleration pressure losses from the measured pressure drop as discussed in section 4.2 of chapter 4. Figures 5.6 to 5.9 show the pressure drop results for each of the tubes under consideration in the current study. Each of the plots in these figures show pressure drop results for the same saturation temperature and different mass fluxes. Some of the common trends visible in each of these plots are that as quality increases, the frictional pressure drop at a particular mass flux increases, and as the mass flux increases, the frictional pressure drop increases for the same quality. These trends are similar to those observed by Garimella *et al.* (2005) for channels with $0.5 < D_h < 4.91$ mm.

The average uncertainties in the pressure drop results for 100×100 μm, 200×100 μm, 300×100 μm and 400×100 μm channels are 3.0, 2.8, 3.3 and 2.3%, respectively. These low uncertainties in pressure drop are due to the high accuracy pressure transducers used and the relatively small contribution of the minor losses in the test section. Tables C-1 to C-4 provide average uncertainties in the pressure drop results for each of the data sets and for each of the tubes.

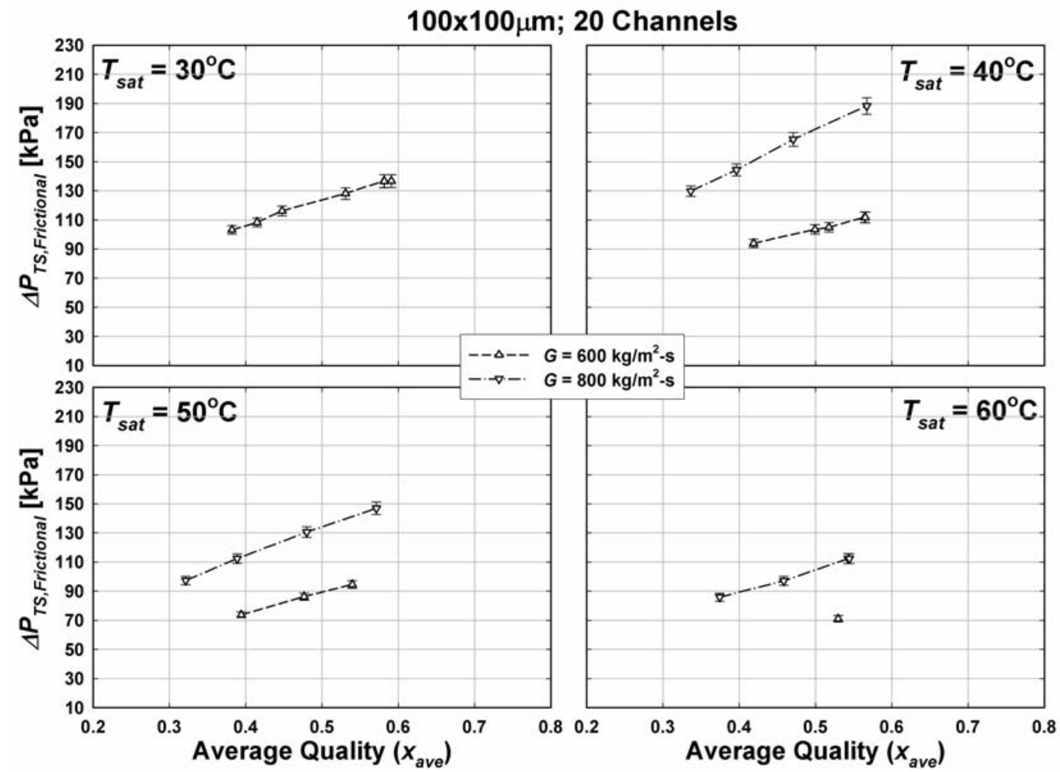

Figure 5.6: Pressure Drop Results for 100×100 μm Channels

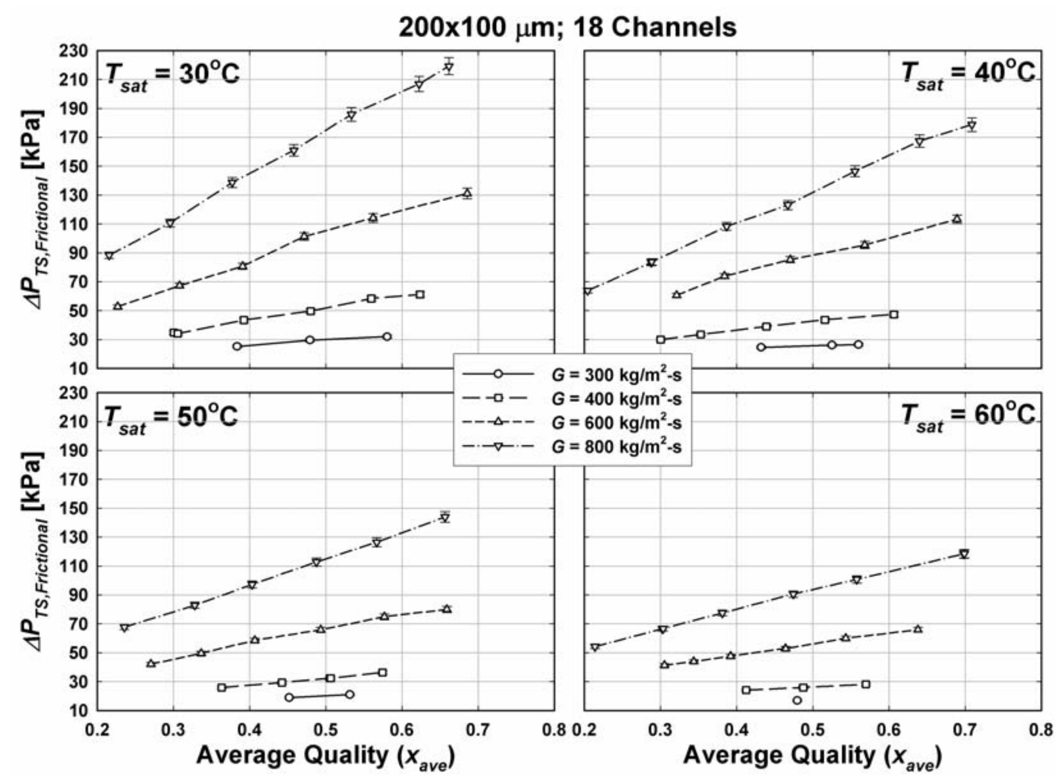

Figure 5.7: Pressure Drop Results for 200×100 μm Channels

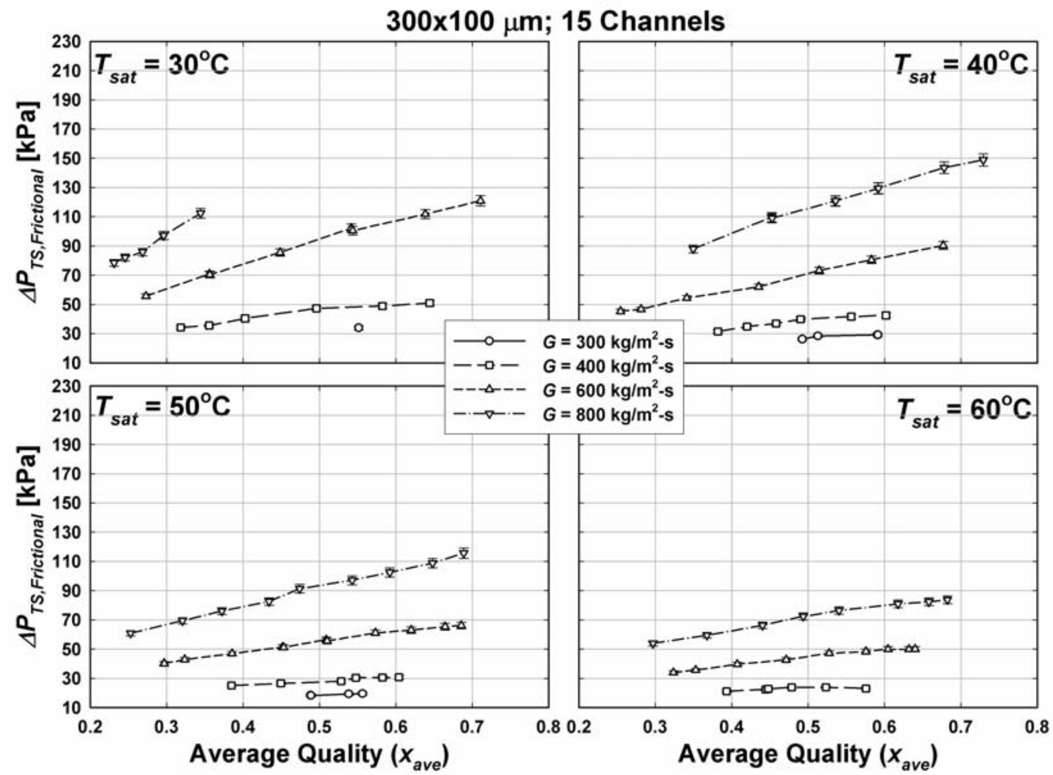

Figure 5.8: Pressure Drop Results for 300×100 μm Channels

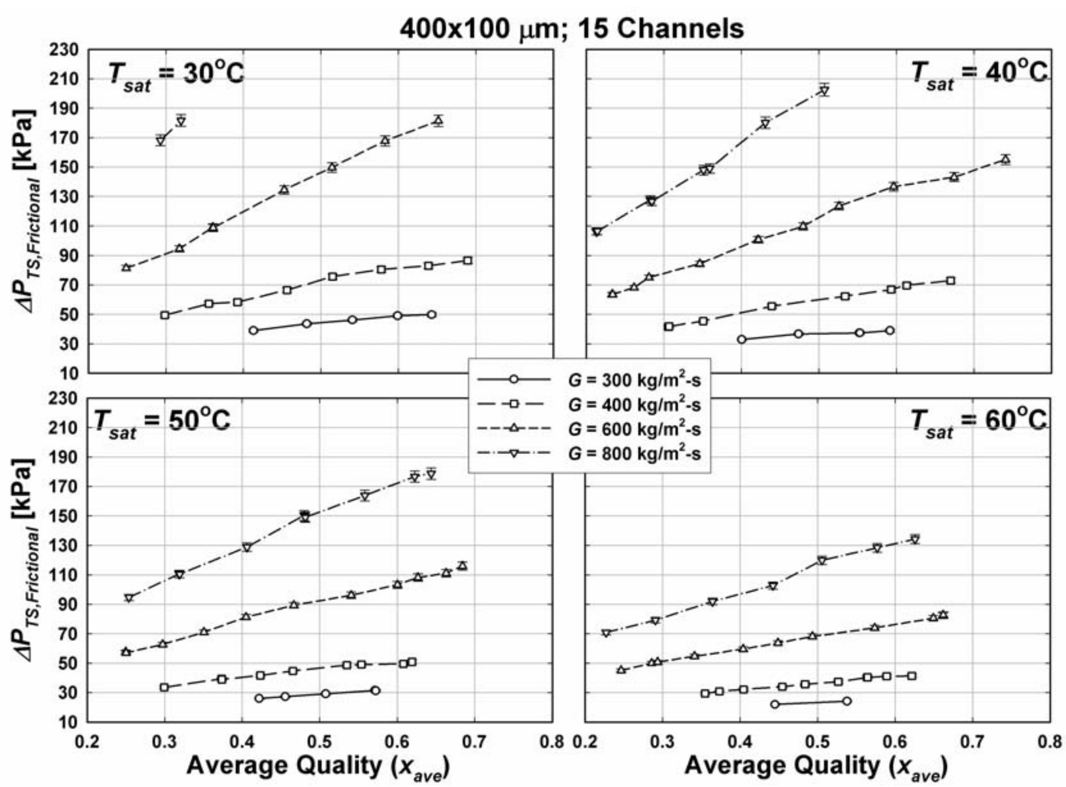

Figure 5.9: Pressure Drop Results for 400×100 μm Channels

The uncertainty in the ΔP data is proportional to the inlet/exit minor losses and the deceleration pressure gain, which in turn are proportional to the square of the flow velocities. Hence, the minor losses for the lower mass flux cases are lower than those for the higher mass flux cases. Thus, the uncertainty bars are only visible for the higher mass flux cases, whereas the magnitude of these uncertainties is too small in lower mass flux cases to be visible in these plots. The average inlet-side minor losses are 3.2%, 3.5% 4.3% and 3.5% of the $\Delta P_{measured}$ for the 100×100 μm, 200×100 μm, 300×100 μm, and 400×100 μm channels, respectively. The average exit-side minor losses are only 0.1%, 0.2% 0.7% and 0.9% of the $\Delta P_{measured}$ for the 100×100 μm, 200×100 μm, 300×100 μm, and 400×100 μm channels, respectively. The inlet-side minor losses are significantly smaller than the exit-side minor losses because the refrigerant exit qualities are much lower than the inlet qualities, and pressure drops are lower at lower qualities. The average deceleration pressure gains are 4.7%, 3.9% 4.3% and 2.5% of the $\Delta P_{measured}$ for the 100×100 μm, 200×100 μm, 300×100 μm, and 400×100 μm channels, respectively. Deceleration pressure gain is also dependent on the Δx across the test-section, which is higher in the case of the smaller channels. Also, the deceleration pressure gain is more significant than the inlet/exit minor losses combined for the 100×100 μm and 200×100 μm channels, thus, the estimated frictional ΔP is 1.2% and 0.2% higher than the $\Delta P_{measured}$. For the same mass flux case, the overall refrigerant flow rates are higher in the header for the 300×100 μm and 400×100 μm channels (for example, at the saturation temperature of 50°C and the mass flux of 600 kg/m^2-s, the average refrigerant flow rates for the 100×100 μm, 200×100 μm, 300×100 μm, and 400×100 μm channels are 5.6, 10.9, 13.7, and 18.2 ml/min, respectively). Thus, for the 300×100 μm and 400×100 μm channels, the inlet/exit minor losses are more significant due to higher flow rates. Thus, the estimated average frictional ΔP is 0.7% and 0.8% lower than the $\Delta P_{measured}$ for 300×100 μm, and 400×100 μm channels, respectively. Tables C-5 to C-8 provide the range and average contributions of the inlet/exit/minor losses and deceleration pressure drops for each of the channels.

Figures 5.10 and 5.11 show the variation in pressure drop for the same mass flux and different saturation temperatures for each of the tubes. It should be noted that these pressure drop results are the same as those presented in Figures 5.6 to 5.9; they are re-plotted here to show the effect of saturation temperature. As the saturation temperature decreases, the pressure drop increases for the same mass flux and average quality due to a decrease in the vapor-to-liquid density ratio. As the temperature decreases from 60°C to 30°C, for example, the vapor density decreases from 87 to 38 kg/m^3 while the liquid density increases from 1053 to 1187 kg/m^3, yielding lower vapor to liquid density ratios at lower saturation temperatures (ρ_v/ρ_l = 0.083 @ 60°C and ρ_v/ρ_l = 0.032 @ 30°C). This decrease in density ratio leads to higher void fractions, yielding higher flow velocities. This increase in flow velocities leads to an increase in pressure drop. It should also be noted that at low ρ_v/ρ_l values, the shear between the vapor and liquid phases is larger, which also leads to higher pressure drops. This phenomenon will be discussed further in Chapter 6.

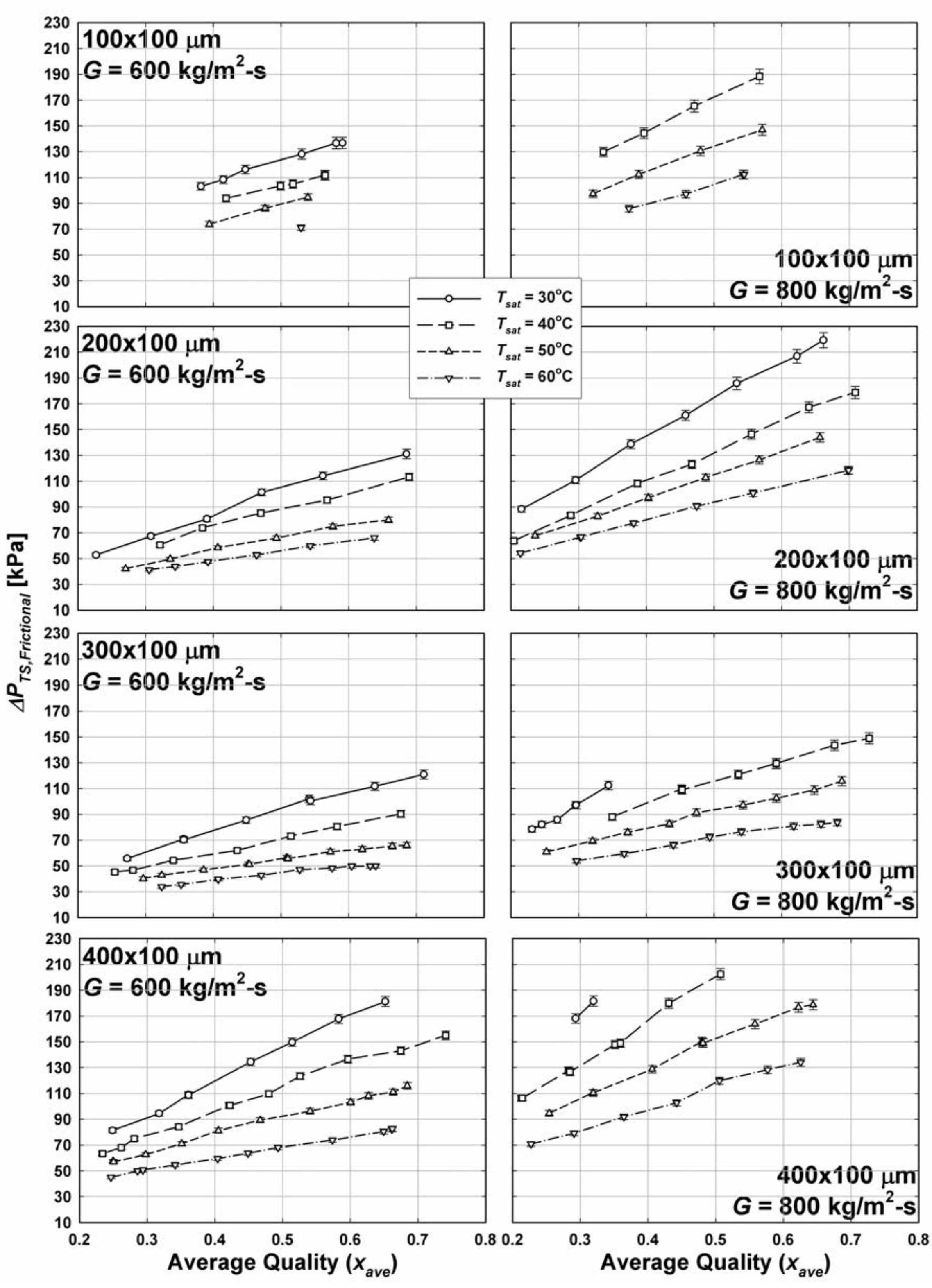

Figure 5.10: ΔP Results for Same G (600 & 800 kg/m^2-s) and Different T

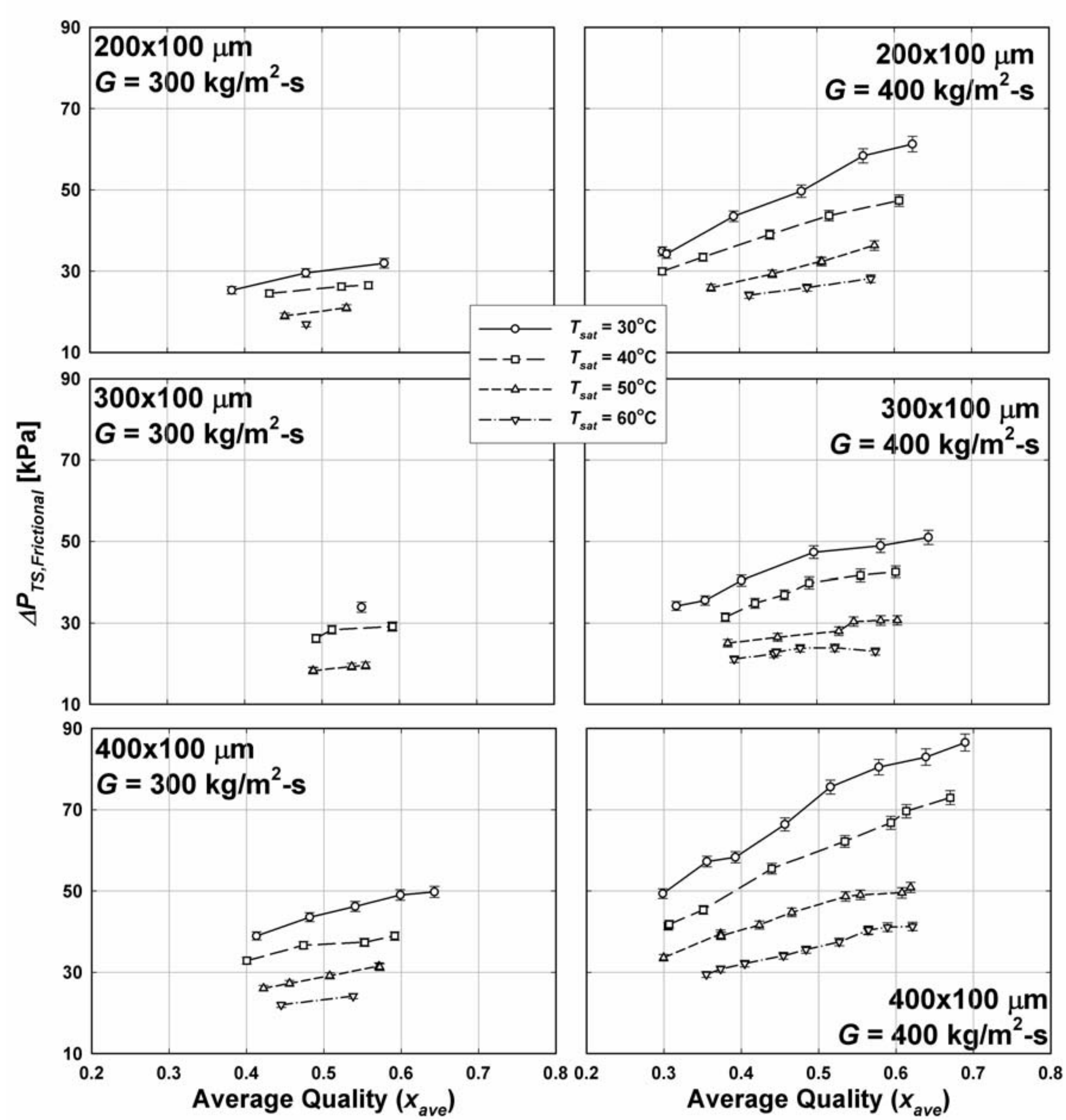

Figure 5.11: ΔP Results for Same G (300 & 400 kg/m^2-s) and Different T

Figure 5.12 shows pressure drop results for selected data sets illustrating the effect of tube shape. For the same test conditions (i.e. for the same temperature, mass-flux and quality), the pressure drop is the highest in the case of the 400×100 μm channels, which are the highest aspect ratio channels. The pressure drop is progressively lower in the 100×100 μm, 200×100 μm and 300×100 μm channels, in that order.

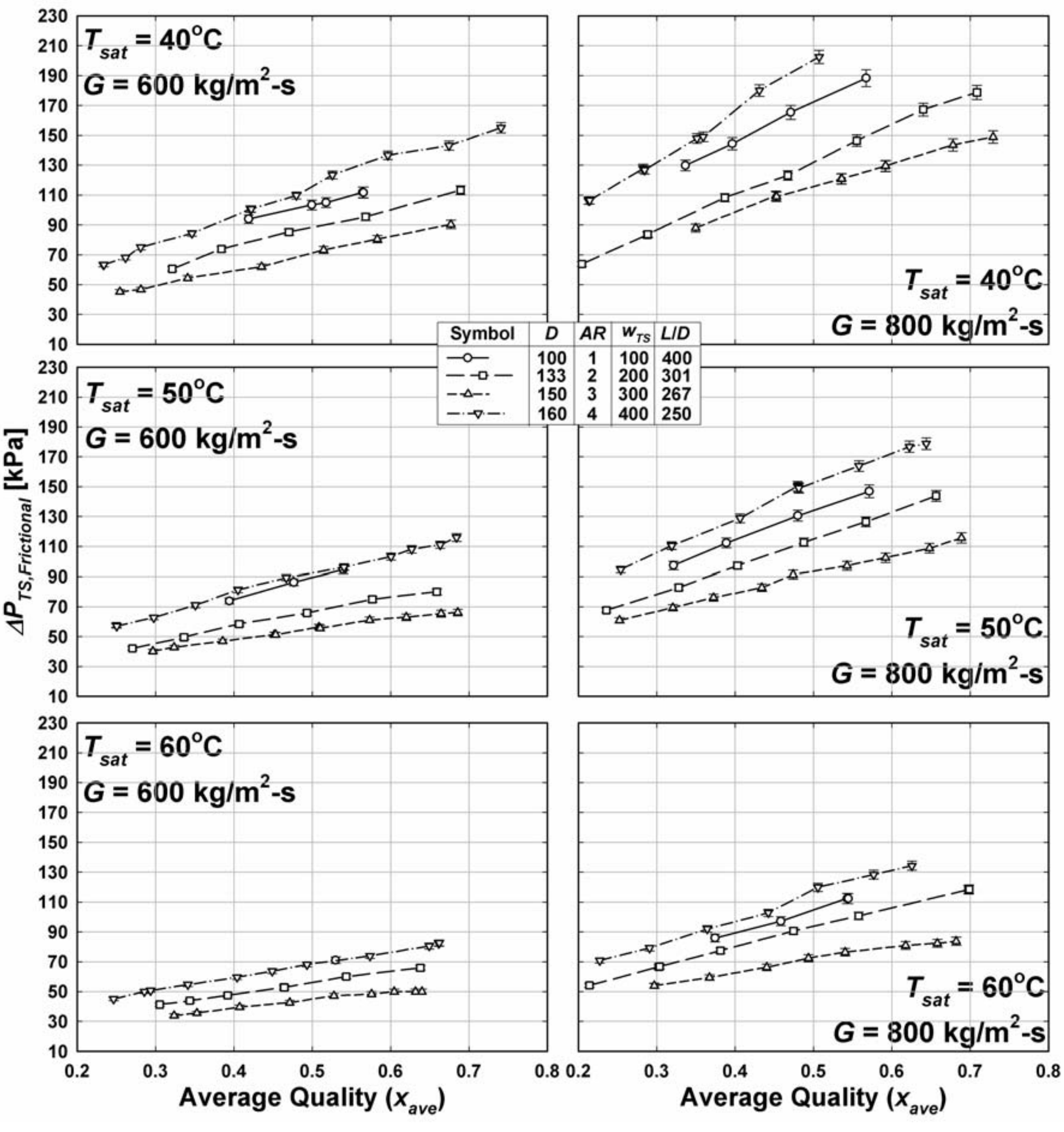

Figure 5.12: Pressure Drop Results at Similar Conditions for Different Tubes

It should be noted that for channels tested in this study, as the aspect ratio increases, the channel hydraulic diameter also increases, which in turn affects the length-to-diameter ratios of the channels. The length of all refrigerant channels was fixed at 40 mm, thus the length-to-diameter ratio decreased as the hydraulic diameter increased. The length-to-diameter ratios for the 100×100 μm, 200×100 μm, 300×100 μm and 400×100 μm channels are 400, 301, 267 and 250 respectively. As the length-to-diameter ratio decreases, it is expected that the frictional pressure drop will decrease for the same flow conditions. Thus, there are several contributing factors influencing the pressure drop results presented here. The pressure drop model developed from these results and presented in the next chapter attempts to account for the effect of all these parameters, i.e., hydraulic diameter, aspect ratio, mass flux, quality, and saturation temperature.

5.2. Heat Transfer Results

Heat transfer coefficients (and corresponding uncertainties) are determined from the measured quantities (and corresponding uncertainties) for each data point as discussed in the previous chapter. Figures 5.13 to 5.16 present the heat transfer results for the each of the tubes. It should be noted that these heat transfer data points correspond to the pressure drop results presented in the previous section, i.e., heat transfer and pressure drop measurements were conducted simultaneously. Thus, many of the trends seen in the pressure drop results are also followed in the heat transfer results. For the same mass flux and saturation temperature, the heat transfer coefficient increases as the quality increases and similarly, for the same quality and saturation temperature, the heat transfer coefficient increases as the mass flux increases.

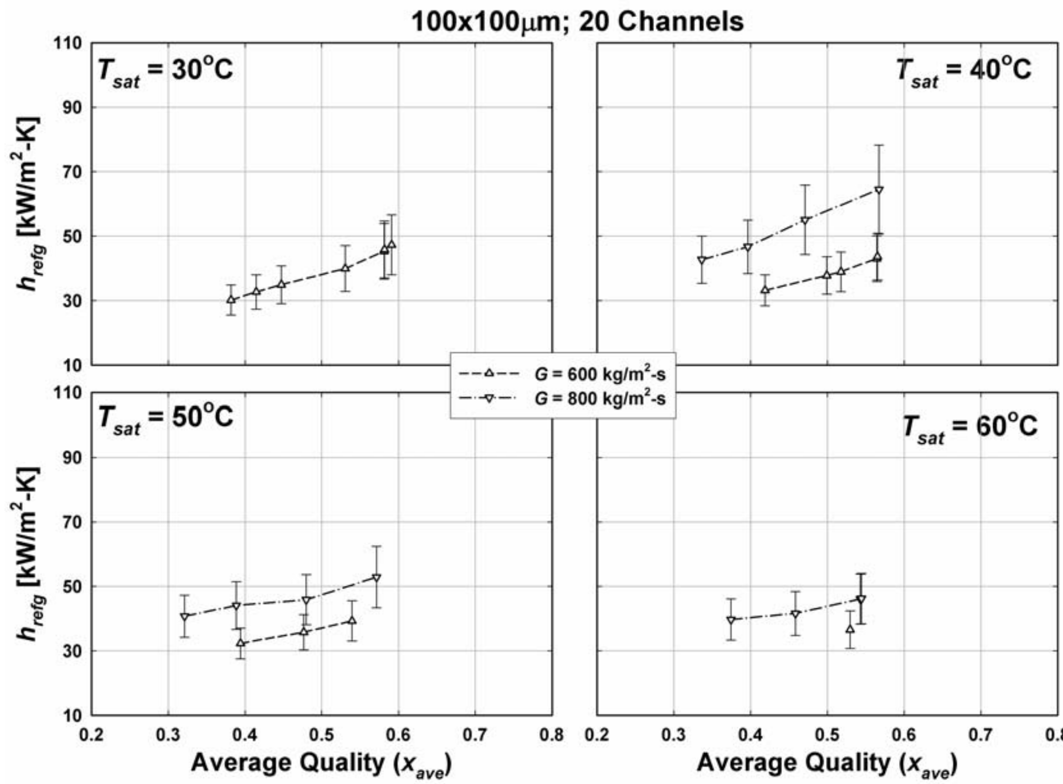

Figure 5.13: Heat Transfer Results for 100×100 μm Channels

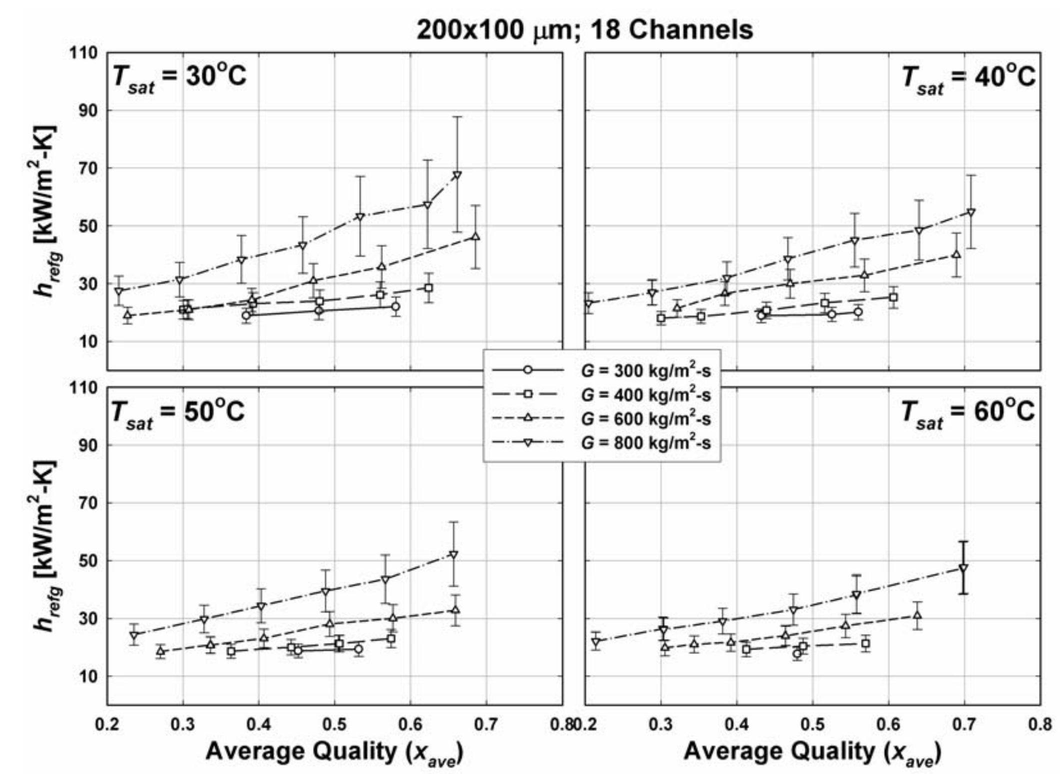

Figure 5.14: Heat Transfer Results for 200×100 μm Channels

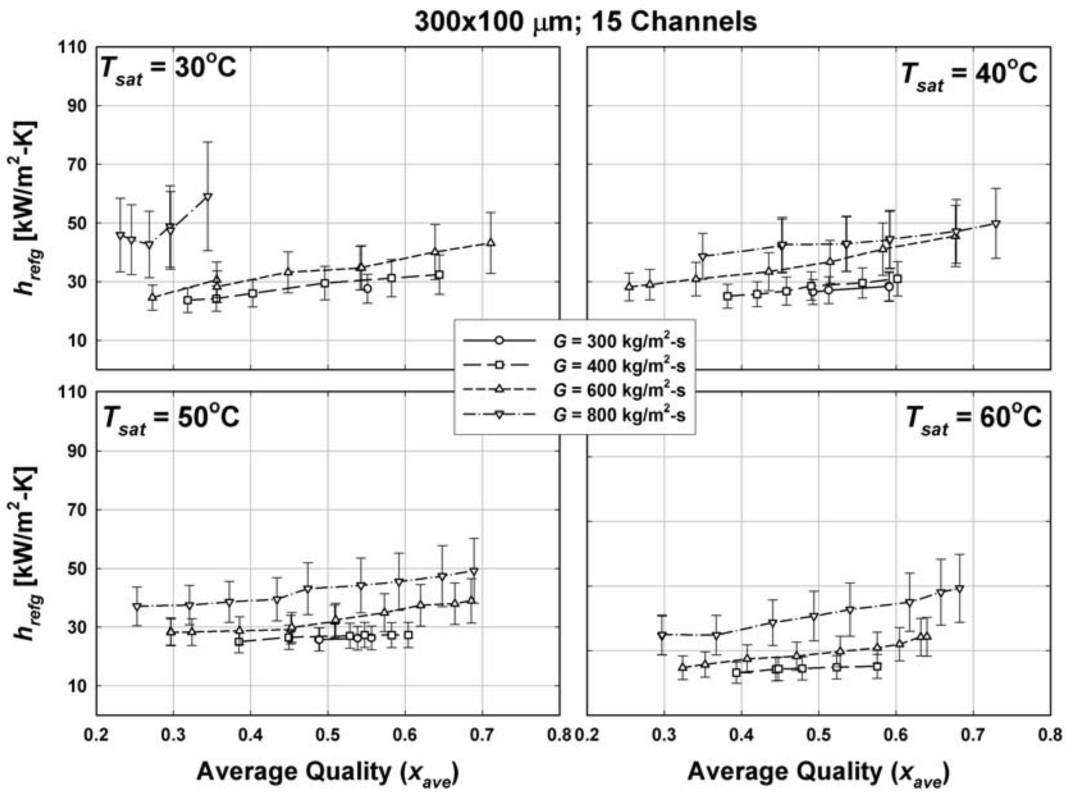

Figure 5.15: Heat Transfer Results for 300×100 μm Channels

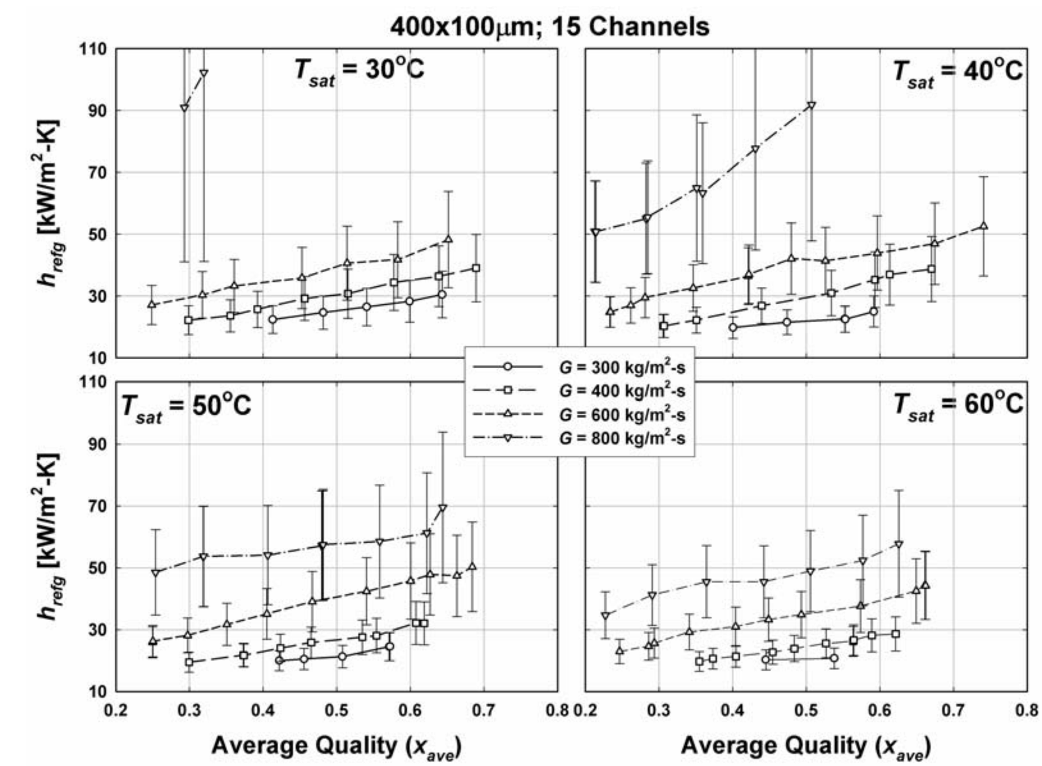

Figure 5.16: Heat Transfer Results for 400×100 μm Channels

Based on the existing flow transition criteria in the literature, it can be concluded that for the channels under consideration, the flow will be either intermittent or annular. The probability of occurancance of annular flow is higher at higher mass fluxes and higher qualities. Heat transfer coefficients are expected to be higher for annular flow, compared to those in slug flow, due to the formation of the thin liquid flim around the wall. Thus, as the quality increases, the flow tends more to annular flow, leading to higher heat transfer coefficients. As the mass flux increases, the flow velocities increase, leading to high heat transfer coefficients. As discussed in the pressure drop results, as the saturation temperature decreases, the vapor-to-liquid density ratio decreases, leading to an increase in the flow velocities and the interfacial shear. This increase in flow velocities again leads to increases in heat transfer coefficients. The increase in interfacial shear has also been related to increases in heat transfer coefficients by several researchers (Carpenter and Colburn, 1951; Traviss *et al.*, 1973; Cavallini *et al.*, 2002; Bandhauer *et al.*, 2006). Due to the coupled effect of the above factors, the heat transfer coeffecents of the lowest saturation temperature (30^{o}C) and the highest mass flux (800 kg/m^2-s) case are extremely high as seen in Figures 5.15 and 5.16. The data set at a saturation temperature of 30^{o}C and mass flux of 800 kg/m^2-s for the 400×100μm channels show unusually high heat transfer coefficients. The driving temperature difference (T - $T_{wall} \approx 1^{o}$C) for these two data points is much lower than for the rest of the data (average T - $T_{wall} \approx 2^{o}$C). At lower driving temperature differences, the thickness of the condensate layer on the tube wall is much less, leading to lower thermal resistances and high heat transfer coefficients. The heat transfer model discussed in chapter 6 captures this effect. However, due to the low resistance ratios in these cases, the uncertainties are very high (>40%), and may not reflect actual heat transfer coefficients accurately.

Figures 5.17 and 5.18 present the same data in a different manner to show the effect of saturation temperature on the heat transfer coefficients.

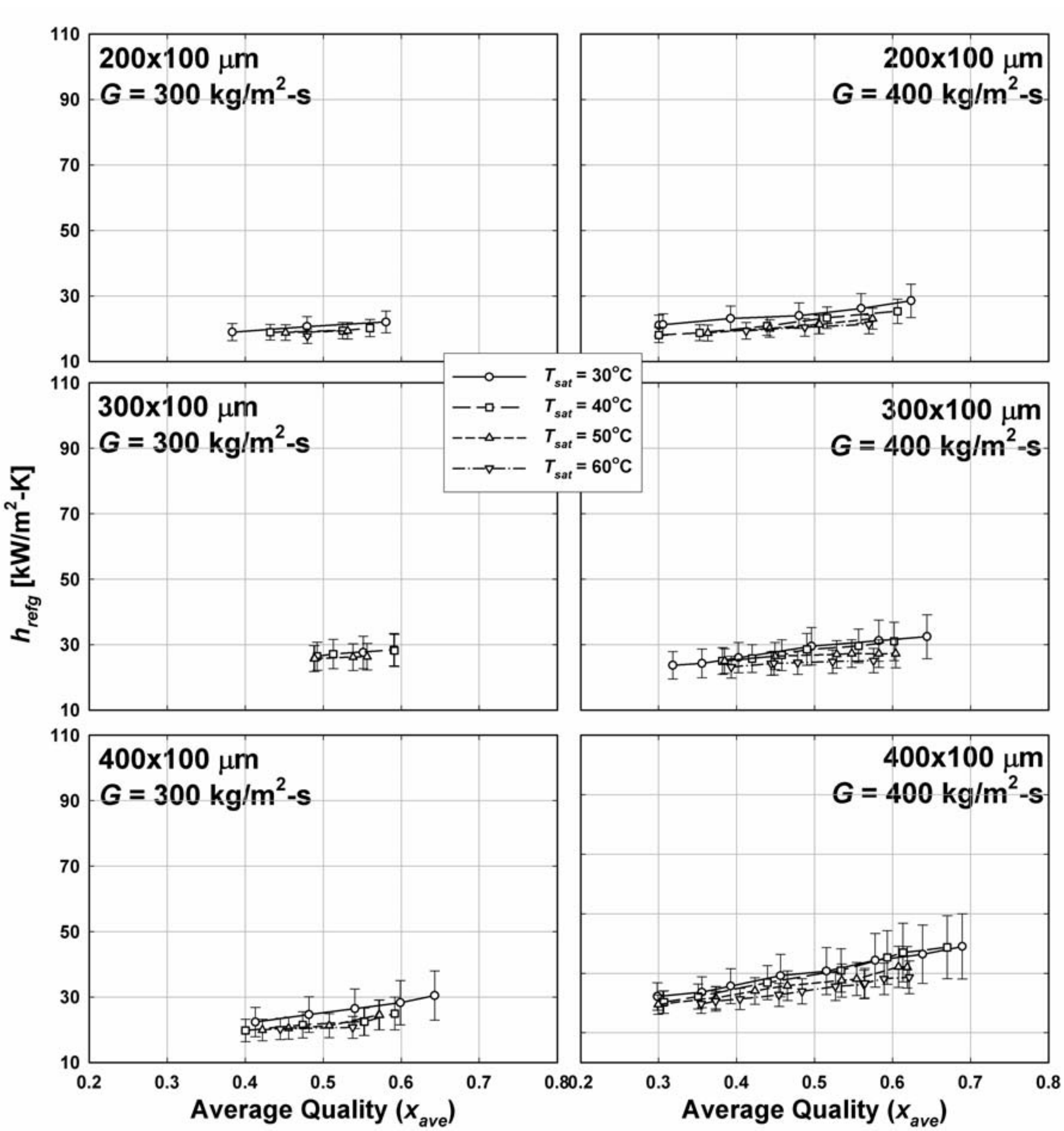

Figure 5.17: Heat Transfer Results for Same *G* (300 & 400 kg/m^2-s) and Different *T*

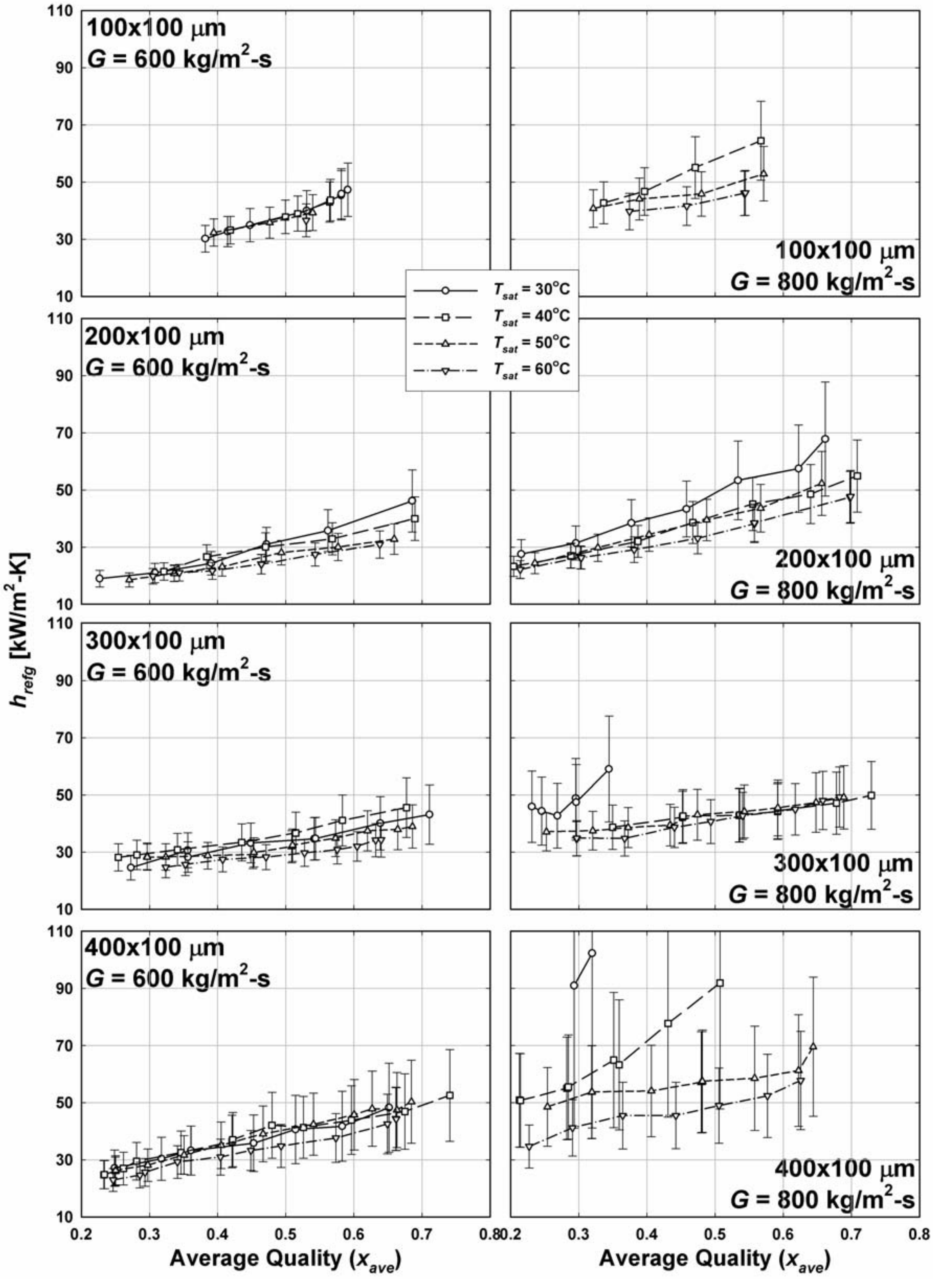

Figure 5.18: Heat Transfer Results for Same G (600 & 800 kg/m^2-s) and Different T

Based on the trends observed in Figure 5.17 and Figure 5.18, most of the differences in the data for the different saturation temperatures at the same mass flux and quality are within the respective uncertainty bonds; thus, it is not possible to derive definitive conclusions. However, it does appear that in most cases, as the saturation temperature decreases, the heat transfer coefficient increases, which is similar to the trend observed in the pressure drop results. As discussed briefly in connection with the pressure drop results, as the saturation temperature decreases, the differences in the velocity of the two phases, and the corresponding vapor-liquid shear increases, leading to this increase in the heat transfer coefficient. Also it should be noted that as the saturation temperature decreases from 60°C to 30°C, the latent heat of evaporation increases from 139 to 173 kJ/kg. This change in h_{fg} also leads to higher h at lower saturation temperatures.

Figure 5.19 presents a comparison of the heat transfer coefficients observed in different tubes under similar flow conditions. Again for most of the cases, the differences in the data for different tubes under similar flow conditions are within the error bands. However, it appears that for most cases, the heat transfer coefficients are the highest for the 400×100 μm channels (which have the highest aspect ratio), followed by the heat transfer coefficients for the 100×100 μm, 200×100 μm and 300×100 μm channels, in that order. These trends are again similar to those observed in the pressure drop results.

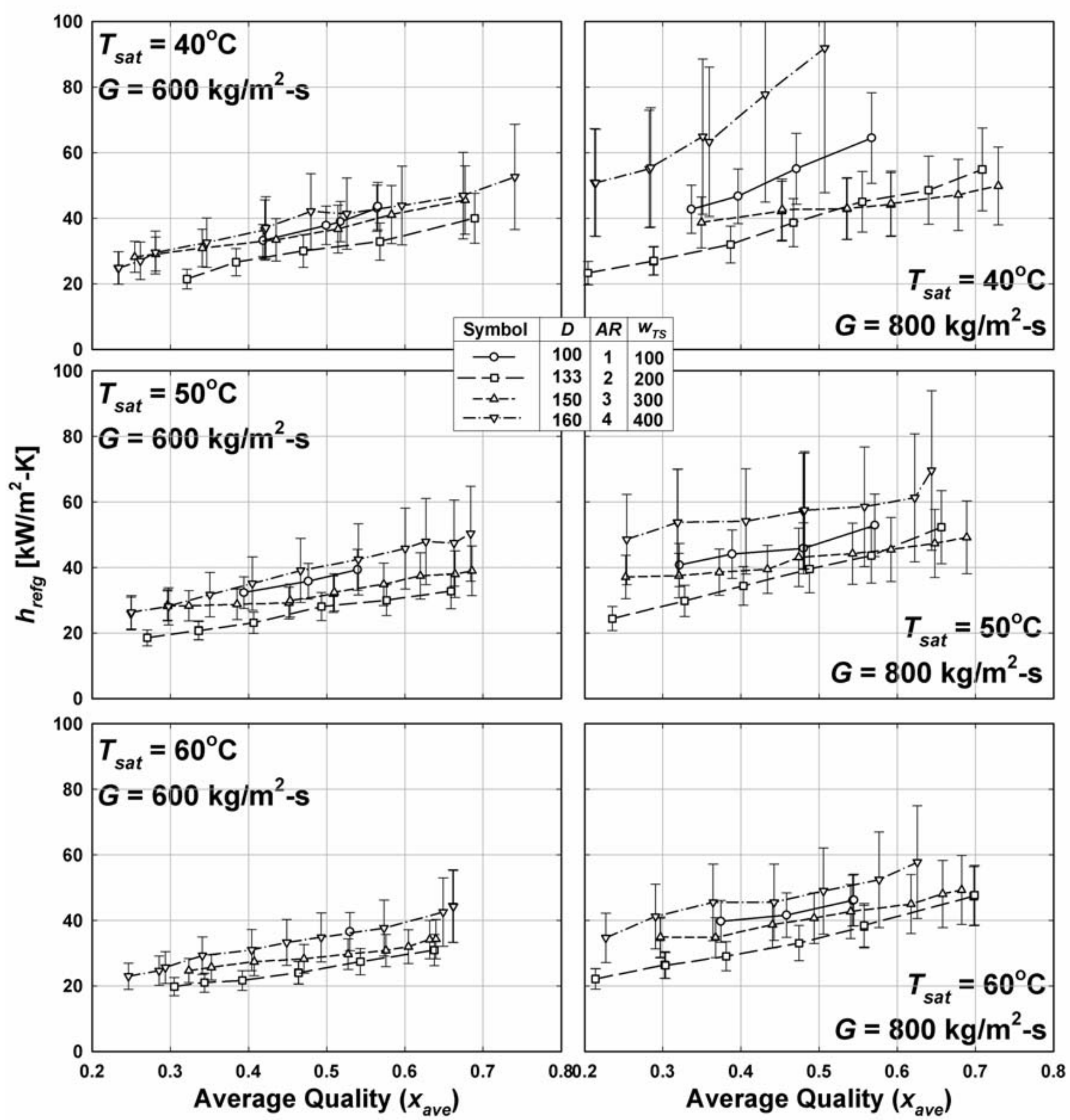

Figure 5.19: Heat Transfer Results for the Same Data Set and Different Tubes

The average uncertainty in the heat transfer coefficients for the 100×100 μm, 200×100 μm, 300×100 μm and 400×100 μm channels are 17, 16, 19 and 25% respectively. Overall, 82% of the data points have uncertainties in the heat transfer coefficients of less than 25%, and 94% of the data have uncertainties less than 30%. Most of the points with uncertainties greater than 25% belong to the 400×100 μm channels. These uncertainty trends can be explained as follows. The most important contributor to the uncertainty in heat transfer coefficients is the assumed 25% uncertainty in the water-side heat transfer coefficients, particularly when the ratio of the refrigerant resistance to remaining resistances is low. The contribution of the water-side heat transfer coefficient uncertainty to the refrigerant-side heat transfer coefficient uncertainty is inversely proportional to the resistance ratios. The water-side flow rate was almost the same for all cases and therefore the variation in water-side thermal resistance is insignificant. Thus, as the mass flux increases, leading to higher refrigerant heat transfer coefficients and low resistance ratios, the uncertainty in heat transfer coefficient increases. Similarly, for the same mass flux, as the quality increases, the refrigerant heat transfer coefficients increase and the resistance ratios decrease, leading to higher uncertainties in the heat transfer coefficients. As the saturation temperature decreases, the heat transfer coefficients increase, leading to lower resistance ratios, thus yielding higher uncertainties in the heat transfer coefficients.

Tables C-1 to C-4 provide the range of resistance ratios for each of the data sets and the corresponding heat transfer coefficient uncertainties. Figure 5.20 shows the resistance ratios for all the data taken in the current study. High resistances ratios help ensure lower uncertainties in the refrigerant-side heat transfer coefficients. The average resistance ratios for the 100×100 μm, 200×100 μm, 300×100 μm and 400×100 μm channels are 1.5, 1.8, 1.4 and 1.0, respectively.

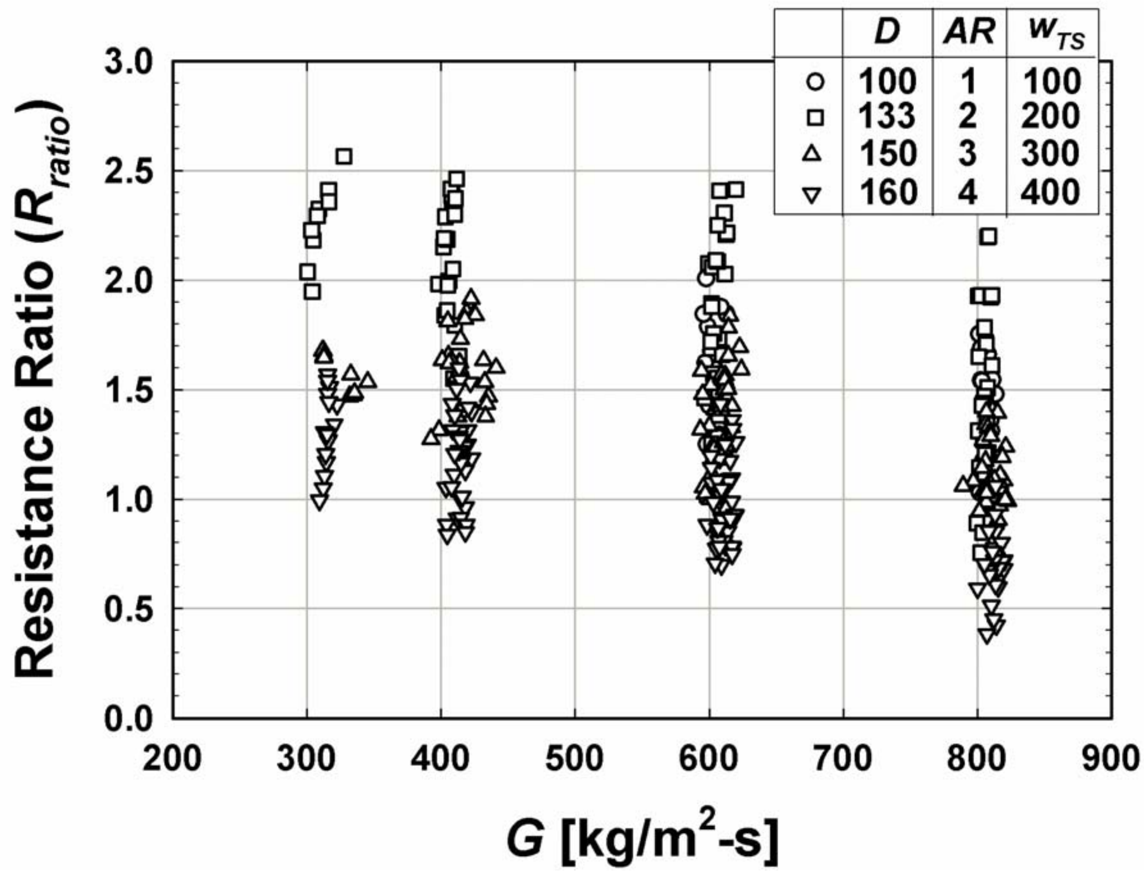

Figure 5.20: Resistance Ratios for Data Taken in Present Study

Figure 5.21 shows the heat transfer coefficient uncertainties corresponding to the resistance ratios presented in Figure 5.20. The uncertainties are particularly high for some of the 800 kg/m^2-s cases due to the low resistance ratios, especially at a saturation temperature of 30^{o}C.

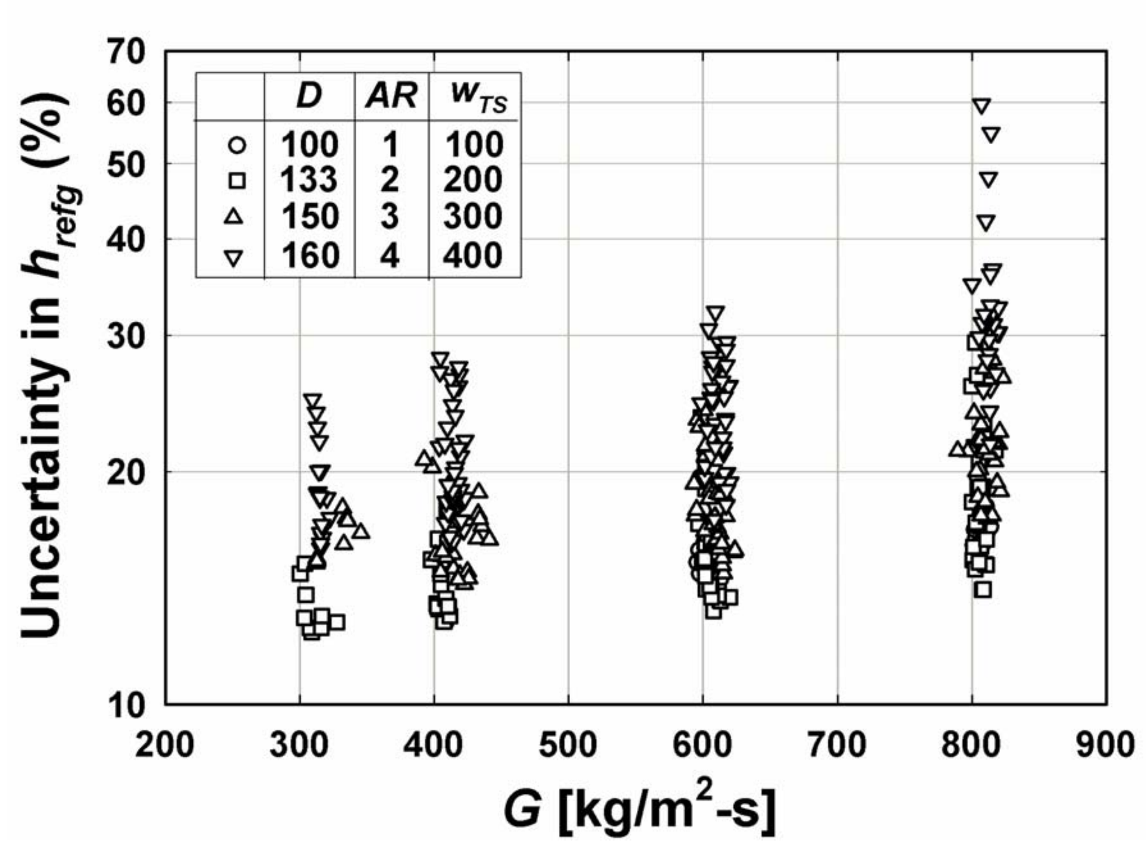

Figure 5.21: Heat Transfer Coefficient Uncertainties

The resistance ratios for the 400×100 μm channels are relatively low leading to higher refrigerant heat transfer coefficient uncertainties. These resistance ratios are lower for the 400×100 μm channels due to several factors. In chapter 6, it is illustrated that in higher aspect ratio channels, the formation of slugs is more frequent due to an unstable annular film. The slug velocity is much higher than the velocity of the fluid in the film and each time the slug passes by, it breaks the liquid film boundary layer leading to higher heat transfer coefficients. Thus, the refrigerant heat transfer coefficients are observed to be relatively high in the case of the 400×100 μm channels, and also the refrigerant-side heat transfer area is the highest for these channels. The combined effect of both these factors leads to low refrigerant-side thermal resistances. As mentioned in Chapter 3, the copper wafer thickness for the 400×100 μm channels was 1.5 mm compared to a thickness of 1 mm for the other channels. Thus, another contributing factor to the low resistance ratio is the somewhat higher conduction resistance in the Copper wafer for the 400×100 μm channels. (It should be noted that the resistance ratio is the ratio of the refrigerant thermal resistance to the total thermal resistance due to the wall and the water side.) Thus, for sevral cases for this test section, the water-side resistance was still less than the refrigerant-side thermal resistance.

Another factor in the uncertainty of the heat transfer coefficient is the T_{sat} used at the inlet and outlet of the channels, which in turn is deduced from the measurements at the test section inlet and outlet and estimates of losses at the inlet and outlet. Furthermore, to conduct the segmental analyses to determine the experimental heat transfer coefficients, empirical correlations were used to estimate the variation in pressure gradient as the quality changes along the length of the test section. Figure 5.22 presents the error in the absolute pressures predicted at the inlet/exit of the channels using these correlations for all data in the present study. The errors are represented as the percentage of the total pressure drop in the test section. It is clear from this figure that the uncertainties in these pressure drop calculations do not contribute appreciably to the uncertainty in heat transfer coefficients.

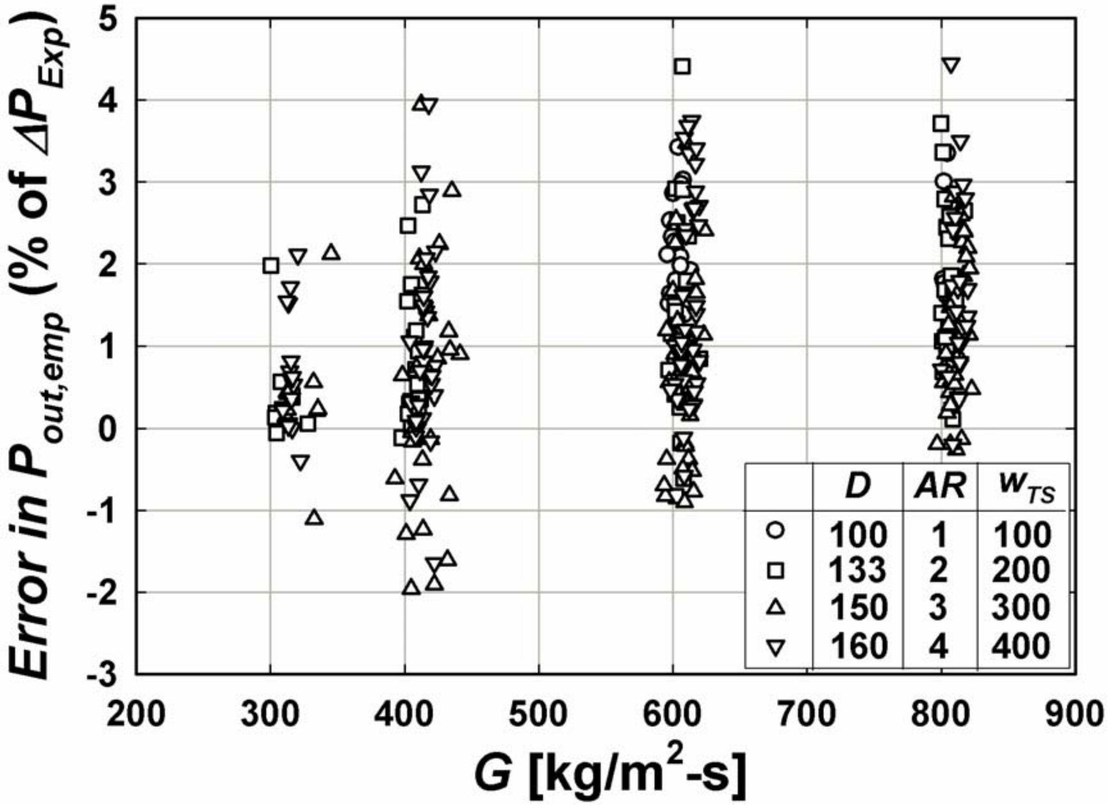

Figure 5.22: Error in Channel Pressure Calculation for T_{sat} Computation

5.3. Comparison of Measured ΔP with Predictions of the Literature

As discussed in the literature review, the pressure drops in conventional channels have long been calculated using three well-known correlations by Lockhart and Martinelli (1949), Chisholm (1973), and Friedel (1979), sometimes with modifications to account for the specific geometry or flow conditions under investigation. This section compares the pressure drop results obtained in the current study with some of the commonly cited models in the literature. For these comparisons, the terms average deviation and absolute average deviation will be used, which are defined as follows:

$$\text{Average Deviation } = \frac{1}{n}\sum_{i=1}^{n}\left(\frac{X_{Model} - X_{Exp.}}{X_{Exp.}} \times 100\right)$$

$$\text{Average Absolute Deviation } = \frac{1}{n}\sum_{i=1}^{n}\left(\frac{\left|X_{Model} - X_{Exp.}\right|}{X_{Exp.}} \times 100\right)$$

It should be noted that lower average deviation does not necessarily mean low scatter in the data. The average deviation indicates whether a particular model under-predicts or over-predicts the data. The average absolute deviation provides an indication of the scatter in the data.

The Lockhart-Martinelli (1949) correlation was based on adiabatic flow of air and benzene, kerosene, water and various oils flowing through 1.5 to 26 mm pipes, and the pressure drops were correlated based on whether the individual liquid and gas phases were considered to be in laminar or turbulent flow. Chisholm (1967) developed the following correlations for the two-phase multipliers of Lockhart and Martinelli:

$$\phi_L^2 = 1 + \frac{C}{X} + \frac{1}{X^2} \tag{5.1}$$

where the Martinelli parameter is given by $X = \left[\frac{\left(dP/dz\right)_l}{\left(dP/dz\right)_v}\right]^{1/2}$ and C depends on the flow regime of the liquid and gas phases. For all the data in the current study Re_L varies from 94 to 815 and Re_V varies from 1147 to 6459; thus, the liquid film is always laminar and the vapor core is considered to be laminar for $Re_V < 2300$ and turbulent otherwise. For a laminar film, Chisholm (1967) proposed the constant C to be 5 or 12 depending on whether the vapor core is laminar or turbulent, respectively. Substituting C = 5 (laminar film and laminar vapor core) for $Re_V < 2300$ leads to significant under prediction of the data, hence, for the comparison here, C = 12 (laminar film and turbulent vapor core) was used for all the data. Figure 5.23 shows the predictions of the Lockhart and Martinelli (1949) model along with predictions of several other models commonly cited in literature. This correlation (with a purely empirical basis) predicts the 100×100 μm, 200×100 μm, 300×100 μm and 400×100 μm data with a 14%, -1%, -4% and -44% average deviation, and with an overall deviation of -16%. The increase in the under-prediction of the pressure drop as the aspect ratio increases indicates that the correlation does not take into account the effect of tube shape and is only dependent on tube diameter. This leads to considerable under-prediction for the higher aspect ratio channels; however, among all the correlations considered in this section, the Lockhart and Martinelli (1949) correlation results in the lowest average deviation.

Mishima and Hibiki (1996) measured frictional pressure drops in air-water flows through 1-4 mm tubes. By comparing their results with the Lockhart-Martinelli (1949) correlation, they noticed that the parameter C in Chisholm's (1967) curve-fit to the multiplier decreased with a decrease in tube diameter. Including the data from other investigators and their own data, they developed the following equation for the parameter C:

$$C = 21\left(1 - \exp\left(-0.319 D_h\right)\right) \tag{5.2}$$

where D_h is in mm. They stated that this equation is applicable for vertical and horizontal round tubes as well as rectangular ducts. But since the above curve fit was based only on 1-4 mm tubes, the above correlation significantly under predicts the parameter C for 0.1 to 0.16 mm hydraulic diameter tubes studied in the current study. Thus, this correlation predicts the overall data with an average deviation of -80%, which is far worse than the prediction of the Lockhart-Martinelli (1949) correlation with Chisholm's (1967) parameter.

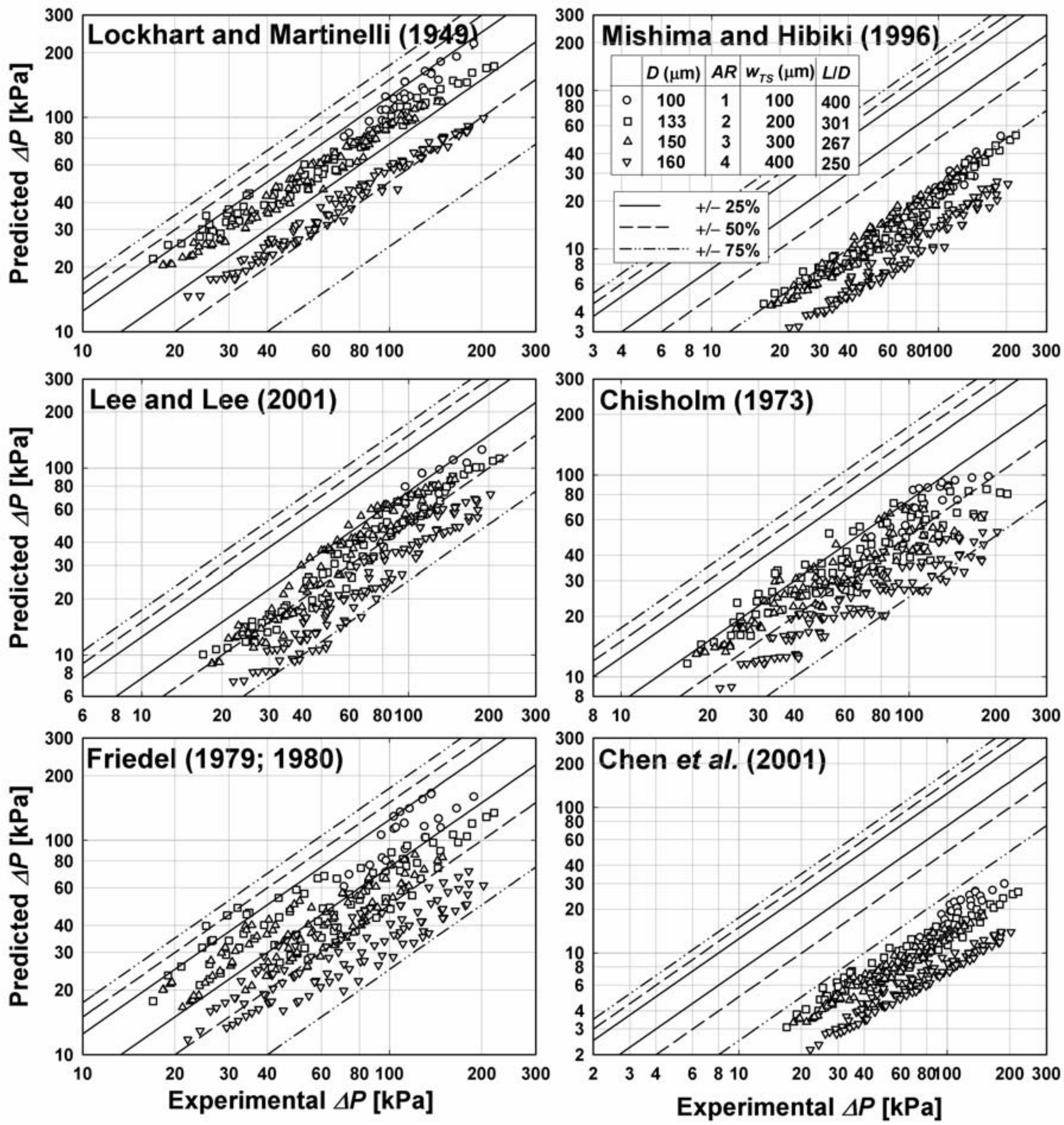

Figure 5.23: Comparison of ΔP Results with Models in Literature

Lee and Lee (2001) investigated pressure drop for air-water flow through 20 mm wide horizontal rectangular channels with gaps of 0.4 to 4 mm. They proposed different values for parameter *C*, accounting for the gap size as well as the phase flow rates. They reasoned that as the gap size decreases, the flow tends more towards plug and slug flow, with an increasing effect of surface tension due to the curved gas/liquid interface at the edge of the bubble. Lee and Lee (2001) used their data to obtain individual values of the constant A and exponents q, r, and s for each combination of liquid and gas flow regimes in the following equation for the parameter C in the two-phase multiplier:

$$C = A\lambda^{q}\psi^{r}\,\mathrm{Re}_{LO}^{s} \tag{5.3}$$

where ψ is the ratio of viscous and surface tension effects, $\psi = \mu_L j/\sigma$, and λ is a combination of parameters independent of the liquid slug velocity, $\lambda = \mu_L^2/\left(\rho_L \sigma D_h\right)$. This correlation is stated to be valid for $175 < Re_{LO} < 17700$ and $0.303 < X < 79.4$. Most of the data in the current study are within this range. But with a laminar film and a turbulent vapor core (which is the case for most data points in the current study) these authors suggested that q and r are zero. Therefore, even though the above model incorporates the effect of surface tension, the dependence is not captured for the current data set. This correlation also significantly under-predicts the data with an average deviation of –50%, which is worse than the prediction of the Lockhart-Martinelli (1949) correlation with Chisholm's (1967) parameter, but better than the Mishima and Hibiki (1996) correlation.

Chisholm (1973) modified the procedure and equations developed by Baroczy (Baroczy and Sanders, 1961; Baroczy, 1966) that account for fluid properties, quality, and mass flux based on steam, water/air, and mercury/nitrogen data to develop the following correlation:

$$\phi_{LO}^2 = 1 + \left(Y^2 - 1\right) B x^{(2-n)/2} \left(1 - x\right)^{(2-n)/2} + x^{2-n} \tag{5.4}$$

where n is the exponent for Reynolds number in the turbulent single-phase friction factor correlation. The parameter Y is the Chisholm parameter:

$$Y = \left[\frac{\left(dP_F/dz\right)_{GO}}{\left(dP_F/dz\right)_{LO}} \right]^{0.5} \tag{5.5}$$

and

$$B = \begin{cases} 55/G^{0.5} & 0 < Y < 9.5 \\ 520/\left(YG^{0.5}\right) & 9.5 < Y < 28 \\ 15000/\left(Y^2 G^{0.5}\right) & 28 < Y \end{cases} \tag{5.6}$$

The Chisholm (1973) correlation predicts the data for the 100×100 μm, 200×100 μm, 300×100 μm and 400×100 μm channels with average deviations of -36%, -39%, -42% and -64%, respectively, and an overall average deviation of -49%. As in the case of the Lockhart and Martinelli (1949) correlation, the increasing under-prediction of pressure drop as the channel aspect ratio increases indicates that the correlation does not take into account the effect of aspect ratio and is only dependent on the tube diameter.

Friedel (1979) developed the following correlation based on a database of 25,000 points for adiabatic flow through channels with D > 1 mm:

$$\phi_{LO}^2 = E + \frac{3.21 FH}{Fr^{0.0454} We^{0.035}} \tag{5.7}$$

where

$$E = \left(1 - x\right)^2 + x^2 \left[\frac{\rho_L f_{GO}}{\rho_G f_{LO}} \right] \tag{5.8}$$

$$F = x^{0.78}(1-x)^{0.224} \quad (5.9)$$

$$H = \left(\frac{\rho_L}{\rho_G}\right)^{0.91}\left(\frac{\mu_G}{\mu_L}\right)^{0.19}\left[1-\frac{\mu_G}{\mu_L}\right]^{0.7} \quad (5.10)$$

Also, $Fr = G^2 / gD\rho_{TP}^2$, $We = G^2 D / \rho_{TP}\sigma$, and f_{LO} and f_{GO} are the single-phase friction factors for the total fluid flow occurring as liquid and gas, respectively. The two-phase mixture density is calculated as $\rho_{TP} = \left[\frac{x}{\rho_G} + \frac{1-x}{\rho_L}\right]^{-1}$. This correlation predicts the data for the 100×100 μm, 200×100 μm, 300×100 μm and 400×100 μm channels with average deviations of -3%, -18%, -27% and -56% respectively, and an overall average deviation of -33%. As in the case of the previously discussed correlations, the increase in the under-prediction of pressure drop as the channel aspect ratio increases indicates that the correlation does not take into account the effect of aspect ratio and is only dependent on tube diameter. The data for the 100×100 μm channels are predicted better by the Friedel (1979) correlation compared to the predictions of the Lockhart and Martinelli (1949) and Chisholm (1973) correlations.

Chen *et al.* (2001) attempted to account for the increased influence of surface tension and the decreased influence of gravity in tubes with D < 10 mm for fluids encompassing a wide range of properties, air-water (in 1.02, 3.17, 5.05, 7.02 mm tubes) and R410A (in 3.17, 5.05, 7.02, 9.0 mm tubes). They modified the Friedel (1979) correlation using the rationale that, when used for small tubes, this correlation does not emphasize surface tension (*We*) enough, and may emphasize gravity (*Fr*) too much. The resulting modification is as follows:

$$\frac{dP}{dz} = \left.\frac{dP}{dz}\right|_{Friedel} \Omega \tag{5.11}$$

$$\Omega = \begin{cases} \dfrac{0.0333\,\mathrm{Re}_{LO}^{0.45}}{\mathrm{Re}_G^{0.09}\left(1+0.4\exp\left(-Bo\right)\right)} & Bo < 2.5 \\ \dfrac{We^{0.2}}{\left(2.5+0.06Bo\right)} & Bo \geq 2.5 \end{cases} \tag{5.12}$$

where Weber number, $We = \dfrac{G^2 D}{\sigma \rho_m}$ and Bond number, $Bo = g\left(\rho_l - \rho_v\right)\left(\dfrac{\left(D/2\right)^2}{\sigma}\right)$. For all the data in the current study, Bo < 2.5; hence, the effect of surface tension (*We*) is still not accounted for, and the correlation predicts the data with an average deviation of -87%, which is far worse than the predictions of the original Friedel (1979) correlation.

Wilson *et al.* (2003) studied the effect of progressively flattening an 8.91 mm round smooth tube and tubes with axial and helical microfin tubes. The pressure drop at a given mass flux and quality increased as the tube approached a rectangular shape. They recommended the circular tube liquid-only two-phase multiplier correlation of Jung and Radermacher (1989):

$$\phi_{LO}^2 = 12.82 X_{tt}^{-1.47}\left(1-x\right)^{1.8} \tag{5.13}$$

Unlike other correlations discussed previously, this correlation significantly over-predicts the frictional pressure drop from the present study with an average deviation of +52%. This correlation predicts the data for the 100×100 μm, 200×100 μm, 300×100 μm and 400×100 μm channels with average deviations of 137%, 83%, 67% and -2% respectively, indicating that the correlation may only be appropriate for very high aspect ratio channels. One possible reason for over prediction by this correlation is that it uses the turbulent liquid film and turbulent vapor core definition of the Martinelli parameter, while in present case, the liquid film is laminar for all data points. Figure 5.24 shows the predictions of this model along with the predictions of other pressure drop models discussed from this point onwards.

Souza *et al.* (1993) proposed the following annular and stratified flow correlation for the two phase multiplier, based on data for R1234a and R12 flowing through a horizontal 10.9 mm tube.

$$\phi_L^2 = 1.376 + C_1 X_{tt}^{-C_2} \tag{5.14}$$

where the values of constants C_1 and C_2 were determined based on Fr_l. For all the data in the current study $Fr_l > 0.7$, thus $C_1 = 7.242$ and $C_2 = 1.655$. The Liquid Froude number $Fr_l = G \big/ \left(\rho_L \sqrt{gD} \right)$ and the corresponding single-phase friction factor were calculated using the Colebrook (1939) equation. This correlation predicts the data for the 100×100 μm, 200×100 μm, 300×100 μm and 400×100 μm channels with average deviations of 19%, -5%, -3% and -45%, respectively, indicating that the correlation does not take into account the effect of aspect ratio. It should be noted that data from the current study are not in stratified flow, although several points are in annular flow. This correlation also, like the Jung and Radermacher (1989) correlation, uses the turbulent liquid film and turbulent vapor core definition of Martinelli parameter, while in the current study, the liquid film is laminar for all data points.

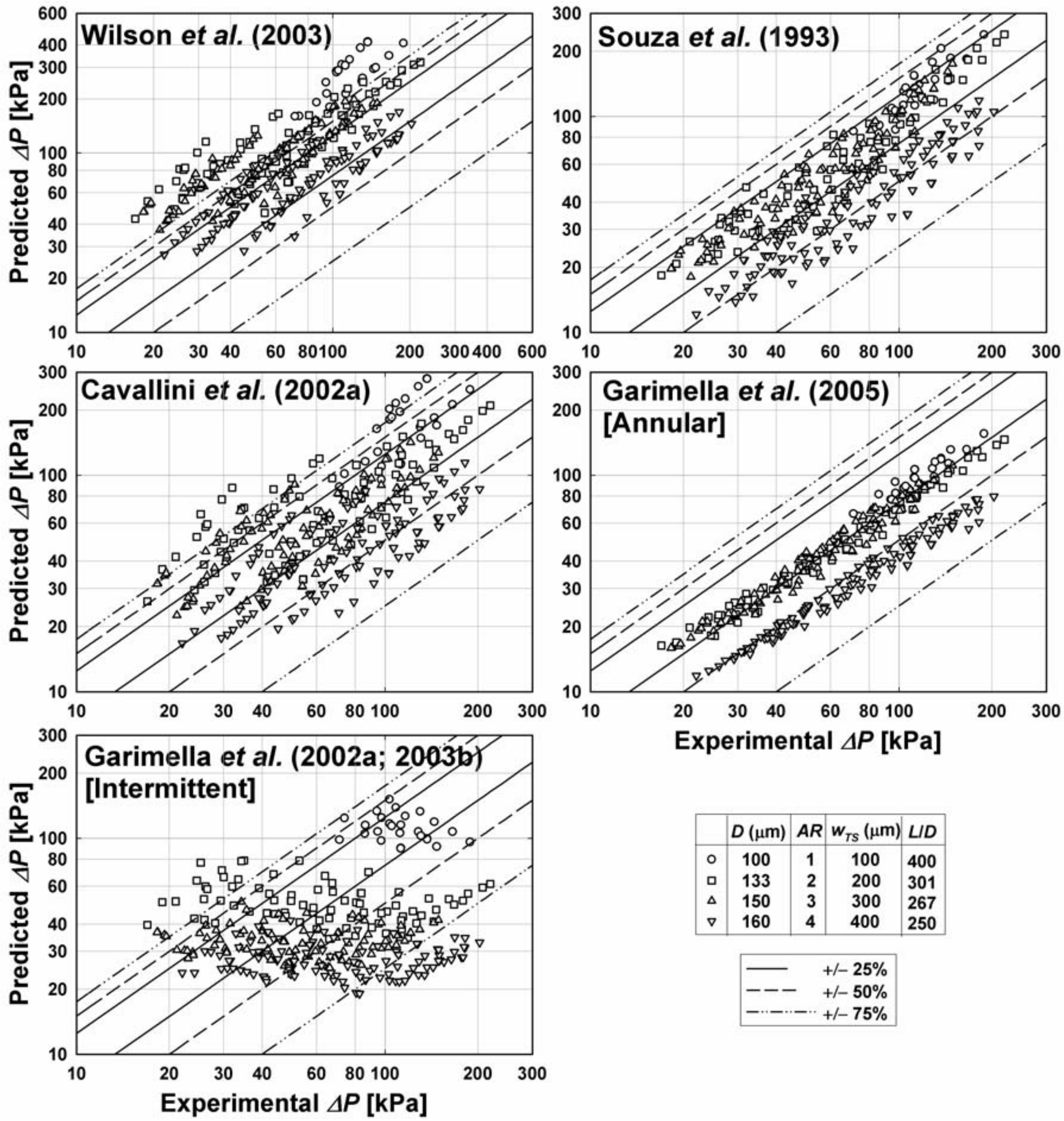

Figure 5.24: Comparison of ΔP Results with Models in Literature

Cavallini *et al.* (2002) gathered condensation data from several researchers for 3 to 21 mm tubes and recommended modifications to the Friedel (1979) correlation. The parameter E is the same as in the Friedel (1979) correlation, while the other parameters are modified as follows:

$$F = x^{0.6978} \tag{5.15}$$

$$H = \left(\frac{\rho_l}{\rho_v}\right)^{0.3278} \cdot \left(\frac{\mu_v}{\mu_l}\right)^{-1.181} \cdot \left(1 - \frac{\mu_v}{\mu_l}\right)^{3.477} \tag{5.16}$$

$$We = \frac{G^2 \cdot D}{\rho_v \cdot \sigma} \tag{5.17}$$

$$\phi_{lo}{}^2 = E + \frac{1.262 \cdot F \cdot H}{We^{0.1458}} \tag{5.18}$$

This correlation predicts the data for the 100×100 μm, 200×100 μm, 300×100 μm and 400×100 μm channels with average deviations of 50%, 22%, 7% and -36%, respectively. This correlation is probably able to capture the effect of diameter because the average deviation is only -1%, but with considerable scatter because the average absolute deviation is 37%.

Garimella *et al.* (2005) developed experimentally validated models for pressure drop during condensation of refrigerant R134a in intermittent flow through circular (Garimella *et al.*, 2002) and noncircular (Garimella *et al.*, 2003b) microchannels with 0.4 < D_h < 4.9 mm. In addition, they developed a model for condensation pressure drop in annular flow (Garimella *et al.*, 2003b), and further extended it to a comprehensive multi-regime pressure drop model (Garimella *et al.*, 2005) for microchannels for the mass flux range 150 < G < 750 kg/m^2-s. Based on the transition criteria suggested by them, most of the data from the present study in the annular flow regime or overlap regions with other regimes. Their flow visualization studies (Coleman and Garimella, 1999; 2003) indicate that the intermittent and annular flow regimes become larger as the tube diameter is decreased, leading to overlap regions between these regimes. Since both flow regimes are of importance in the current study, predictions of each of the models are discussed separately here.

In the annular flow regime model, the interfacial friction factor is computed from the corresponding liquid-phase *Re*, friction factor, the Martinelli parameter, and a surface tension-related parameter:

$$\frac{f_i}{f_l} = A \cdot X^a \, \mathrm{Re}_l^{\,b} \, \psi^c \tag{5.19}$$

The friction factors required for the individual-phase pressure drops in the Martinelli parameter were computed using $f = 64/\mathrm{Re}$ for $Re_l < 2100$ and the Blasius expression $f = 0.316 \cdot \mathrm{Re}^{-0.25}$ for $Re_l > 3400$. The Martinelli parameter X is given by:

$$X = \left[\frac{(dP/dz)_l}{(dP/dz)_v} \right]^{1/2} \tag{5.20}$$

For this model, the liquid-phase *Re* is defined in terms of the annular flow area occupied by the liquid phase as $\mathrm{Re}_l = \dfrac{GD(1-x)}{\left(1+\sqrt{\alpha}\right)\mu_l}$ and similarly, the gas-phase *Re* is calculated as $\mathrm{Re}_v = \dfrac{GxD}{\mu_v\sqrt{\alpha}}$. The surface tension parameter ψ in equation (5.19) (Lee and Lee, 2001) is given by:

$$\psi = \frac{j_l \mu_l}{\sigma} \tag{5.21}$$

where $j_l = \dfrac{G(1-x)}{\rho_l(1-\alpha)}$ is the liquid superficial velocity. The values of constants a, b and c in equation (5.19) are the same for all tubes irrespective of the tube shape and diameter, while the value for constant A is characteristic of the tube shape and diameter. (It should be noted that the values for constants A, a, b, and c are different for laminar and turbulent liquid films, but in the present study, the liquid film is always laminar.) Based on the results of non-circular tubes, in a subsequent study, Agarwal and Garimella (2006) suggested that the constant A is more strongly influenced by tube shape and is not affected appreciably by a change in hydraulic diameter. Here, their model for square channels significantly under-predicted the data for the 100×100 μm channels from the present study. Thus, their model for rectangular channels of hydraulic diameter 0.424 mm is compared with the data for all channels. For this geometry, which is closest to the tubes under consideration in the current study, and $Re_l < 2100$, the values of constants A, a, b and c are 2.576×10^{-3}, 0.4273, 0.9295 and -0.1211 respectively. This correlation predicted the data for the 100×100 μm, 200×100 μm, 300×100 μm and 400×100 μm channels with average deviations of -14%, -25%, -23% and -55% respectively, and an average deviation of -34%. It should be noted that the data used in developing this correlation did not consist of channels with high aspect ratios; therefore, although the predictions for the low aspect ratio channels are acceptable, the predictions for the highest aspect ratio channels are not good.

For modeling intermittent flow in circular (Garimella *et al.*, 2002) and non-circular (Garimella *et al.*, 2003b) channels, Garimella *et al.* approximated intermittent flow as consisting of the vapor-phase traveling as long solitary bubbles surrounded by an annular liquid film and separated by liquid slugs. As the tube size decreases, surface tension forces at the bubble interface begin to dominate the gravitational forces and the bubble tends to a cylindrical shape. In general, the bubble travels faster than the liquid slug, which implies that there is a continual uptake of liquid from the film into the front of the slug. The total pressure drop for this flow pattern includes contributions from the liquid slug, the vapor bubble, and the flow of liquid between the film and slug as follows:

$$\Delta P_{total} = \Delta P_{slug} + \Delta P_{f/b} + \Delta P_{film-slug\ transitions} \tag{5.22}$$

A simple control volume analysis (Garimella *et al.*, 2002, 2003b) similar to that performed by Suo and Griffith (1964) showed that the velocity in the liquid slug can be directly calculated given the overall mass flux and quality. The results of several investigations (Suo and Griffith, 1964; Dukler and Hubbard, 1975; Fukano *et al.*, 1989) suggested that the bubble velocity for these conditions was 1.2 times the slug velocity. With this assumption, the diameter of the bubble, velocity within the film, and relative length of bubble and slug can all be calculated from a system of simultaneous equations including a shear balance at the bubble-film interface. Thus, the Reynolds number in the liquid slug and vapor bubble (based on the relative velocity at the interface between the bubble and the surrounding film) could be directly determined. The Churchill (1977b) correlation was then used to calculate the friction factor and thus the pressure gradient at the respective Reynolds numbers in the liquid slug and bubble/film regions. A relationship from the literature for the pressure loss associated with the mixing that occurs in the uptake of liquid from the film to the slug was used to estimate the pressure loss due to each of these transitions. These components of the total pressure drop are shown below:

$$\frac{\Delta P}{L} = \left(\frac{dP}{dx}\right)_{\substack{film\\bubble}} \left(\frac{L_{bubble}}{L_{\substack{unit\\cell}}}\right) + \left(\frac{dP}{dx}\right)_{slug} \left(\frac{L_{slug}}{L_{\substack{unit\\cell}}}\right) + \Delta P_{\substack{one\\transition}} \left(\frac{N_{\substack{unit\\cells}}}{L}\right) \tag{5.23}$$

For the solution of the above equation, the number of unit cells per unit length is required which was determined from the slug frequency (which yields the unit cell length). The following correlation for slug frequency (non-dimensional unit-cell length, or unit cells/length) based on slug Re and D_h was developed:

$$a\left(\mathrm{Re}_{slug}\right)^{b} = \omega\frac{D_h}{U_{bubble}} = D_h\left(\frac{N_{\substack{unit\\cells}}}{L_{tube}}\right) = \left(\frac{D_h}{L_{\substack{unit\\cell}}}\right) \tag{5.24}$$

where a = 2.437, b = -0.560 for both circular and non-circular (except triangular) channels. This correlation predicted the data for the 100×100 μm, 200×100 μm, 300×100 μm and 400×100 μm channels with average deviations of 2%, 1%, -28% and -54%, respectively, but clearly, as shown in Figure 5.24, the trends in pressure drop are not predicted well. Although the average deviation for the entire data set is only -28%, the average absolute deviation is 50%. Thus, this model is not able to effectively capture the trend of increasing pressure drop with increasing quality at the same mass flux. However, this model has a strong physical basis and is also used as the basis for the model proposed for the data in present study in the next chapter.

Table 5-1 summaries the average deviations for each of the correlations discussed above. Almost all correlations did not capture the effect of aspect ratio and predicted a decreasing pressure drop with an increasing hydraulic diameter. Empirical correlations for large data bases in general yield reasonable predictions for low aspect ratio channels. The Lockhart and Martinelli (1949) correlation has the least average absolute deviation but subsequent modifications (Mishima and Hibiki, 1996; Lee and Lee, 2001) for smaller diameter tubes yield very poor predictions, probably because the original correlation was modified just to fit the data of the specific researchers.

Table 5-1: Average Deviation for Various Pressure Drop Correlations

Correlation \ Channel Width (μm)	Average Deviation (%)					Average Absolute Deviation (%)
	100	200	300	400	All	
Lockhart and Martinelli (1949)	14	-1	-4	-44	-16	22
Mishima and Hibiki (1996)	-77	-78	-77	-86	-81	81
Lee and Lee (2001)	-39	-44	-40	-65	-50	50
Chisholm (1973)	-36	-39	-42	-64	-49	49
Friedel (1979)	-3	-18	-27	-56	-33	38
Chen *et al.* (2001)	-82	-85	-85	-91	-87	87
Wilson *et al.* (2003)	138	83	67	-2	52	62
Souza *et al.* (1993)	19	-5	-3	-45	-17	26
Cavallini *et al.* (2002)	50	22	7	-36	-1	37
Garimella *et al.* (2005) (Annular)	-14	-25	-23	-55	-34	34
Garimella *et al.* (2002; 2003b) (Intermittent)	2	1	-28	-54	-28	50

The Friedel (1979) correlation and its subsequent modification suggested by Cavallini *et al.* (2002), both based on an experimental database from several researchers have the same absolute deviation, but the Cavallini *et al.* (2002) correlation predicts relatively higher pressure drops than the original Friedel (1979) correlation. The Garimella *et al.* (2005) annular flow correlation predicts the data for lower aspect ratio channels well. It will be demonstrated later that the probability for annular flow is higher in lower aspect ratio channels. The Wilson *et al.* (2003) correlation yields better predictions for higher aspect ratio channels because their study included experiments on tubes of aspect ratio up to 13.

5.4. Comparison with Heat Transfer Correlations

This section compares the heat transfer results obtained in the current study with some of the commonly cited correlations in the literature. The Shah (1979) correlation is one of the most widely used general purpose condensation correlations, due to the large database from 21 investigators used for its development, and also its ease of use. Shah reasoned that in the absence of nucleate boiling, condensation heat transfer should be similar to evaporative heat transfer when the tube is completely wet, and extended the correlation developed previously (Shah, 1976) for evaporation to condensation as follows:

$$\frac{h}{h_{lo}} = \left(1-x\right)^{0.8} + \frac{3.8x^{0.76}\left(1-x\right)^{0.04}}{\left(P/P_{crit}\right)^{0.38}} \tag{5.25}$$

$$h_{lo} = 0.023\left(\frac{k_l}{D}\right)\left(\frac{GD}{\mu_l}\right)0.8\,\mathrm{Pr}_l^{0.4} \tag{5.26}$$

The data from the current study are clearly out of the range of applicability of this model, and it was found that this correlation predicted the heat transfer data with an average deviation of -66%. The poor predictions are most probably because this correlation was based on data for tubes with diameter greater than 7 mm. Figure 5.25 shows the predictions of this model along with predictions of other models discussed in this section.

Soliman *et al.* (1968) developed a model for predicting condensation heat transfer coefficients for annular flow. They evaluated the wall shear stress as a combination of friction, momentum and gravity contributions, and used the resulting expression to evaluate the heat transfer coefficient, much like the approach used by Carpenter and Colburn (1951). The following expression for the heat transfer coefficient was developed using data from several investigators:

$$\frac{h\mu_l}{k_l\rho_l^{1/2}} = 0.036\,\mathrm{Pr}_l^{0.65}\,\tau_w^{1/2} \tag{5.27}$$

where, wall shear stress τ_w is a combination of friction, momentum and gravity contributions.

$$\tau_w = \tau_f + \tau_m + \tau_g \tag{5.28}$$

In the case of condensation in horizontal micro-channels, the effect of the axial gravitational field on the wall shear stress can be neglected. The above correlation was developed with data for tube diameters 7.44 < D < 11.66 mm. Extrapolation of the above correlation to the much lower diameters of interest in the current study leads to significant under prediction of heat transfer coefficients, with an average deviation of -77%.

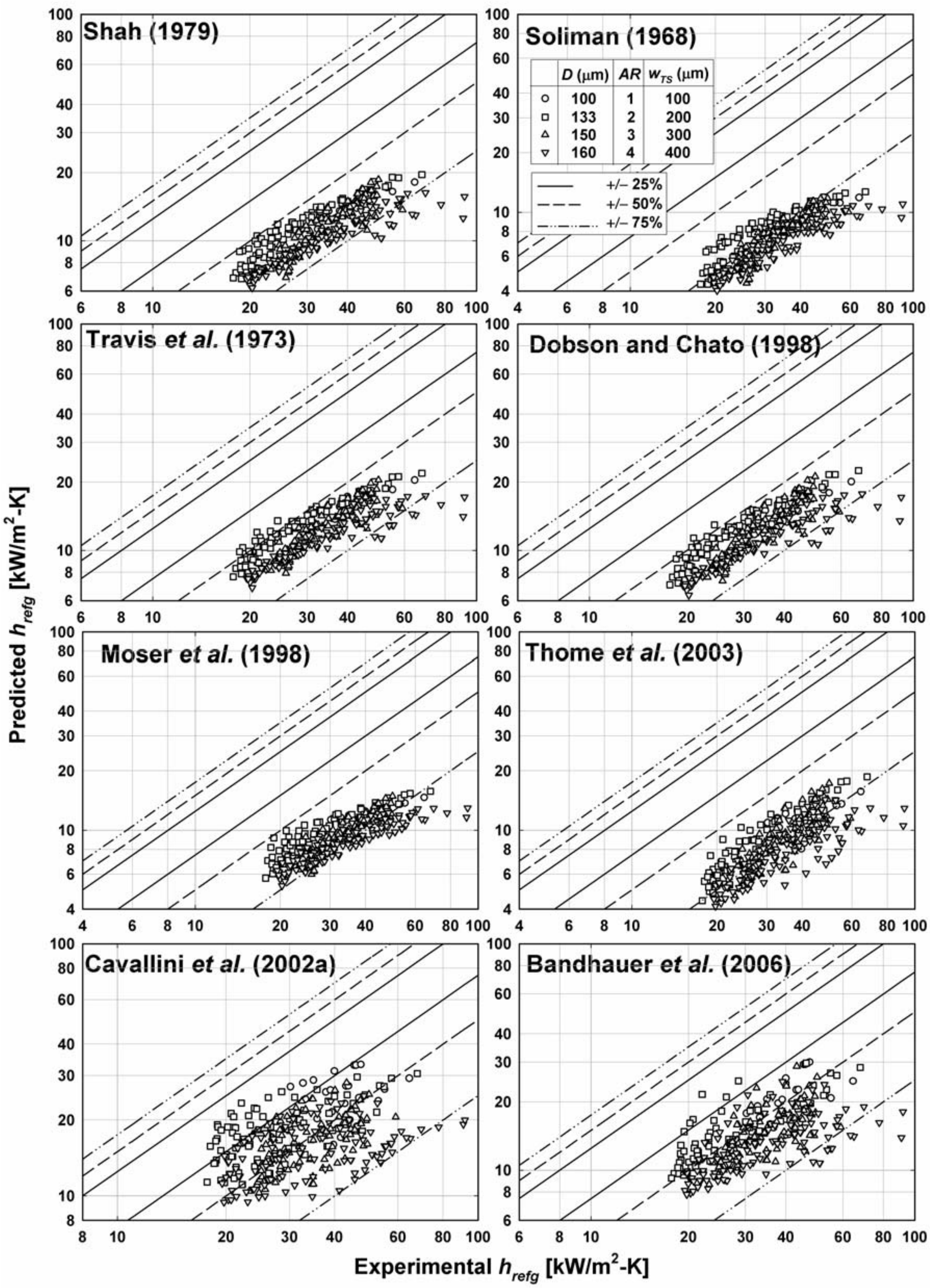

Figure 5.25: Comparison of h_{refg} Results with Models in Literature

Traviss *et al.* (1973) used the heat-momentum analogy and the von Karman universal velocity distribution in the liquid film to develop a correlation for the Nusselt number in annular flow condensation. Using the assumed liquid velocity profile, a relationship for the condensation heat transfer coefficient was determined as a function of the turbulent film thickness. They then derived a relationship for the liquid Reynolds number as a function of this film thickness. By arguing that the interfacial shear to wall shear ratio was approximately unity, a relationship for the condensation heat transfer coefficient was developed as follows:

$$\frac{hD}{k_l} = \frac{0.15\,\mathrm{Pr}_l\,\mathrm{Re}_l^{0.9}}{F_T}\left[\frac{1}{X_{tt}} + \frac{2.85}{X_{tt}^{0.476}}\right] \tag{5.29}$$

where $$F_T = \begin{cases} 5\,\mathrm{Pr}_l + 5\ln\left\{1 + 5\,\mathrm{Pr}_l\right\} + 2.5\ln\left(0.0031\,\mathrm{Re}_l^{0.812}\right) & \mathrm{Re}_l > 1125 \\ 5\,\mathrm{Pr}_l + 5\ln\left[1 + \mathrm{Pr}_l\left(0.0964\,\mathrm{Re}_l^{0.585} - 1\right)\right] & 50 < \mathrm{Re}_l < 1125 \\ 0.707\,\mathrm{Pr}_l\,\mathrm{Re}_l^{0.5} & \mathrm{Re}_l < 50 \end{cases}$$

In the above equations, $\mathrm{Re}_l = \dfrac{G(1-x)D}{\mu_l}$. This correlation predicts the data from the current study with an average deviation of -77%. One possible reason that this model and other models based on the annular flow assumption under-predict the data may be that they are based on shear stresses for large diameter tubes.

Dobson and Chato (1998) noted that the boundary layer analyses used by several investigators, including primarily Traviss *et al.* (1973), could be shown to be similar in basis to the two-phase multiplier approach used by others. Noting also that the primary thermal resistance in annular flow occurs in the laminar and buffer layers (even the presence of waves at the interface or the varying film thickness around the circumference would not significantly affect the near-wall behavior), they did not find it necessary to include a multi-region model of the liquid film resistance. With these considerations, the following annular flow correlation was proposed:

$$Nu_{annular} = 0.023\,\mathrm{Re}_L^{0.80}\,\mathrm{Pr}_L^{0.3}\left(1+\frac{2.22}{X_{tt}^{0.89}}\right) \tag{5.30}$$

They recommended a separate heat transfer model for the wavy flow regime and suggested the following transition criteria to apply the respective models:

$$\begin{aligned} &G \geq 500\,kg/m^2-s: \quad Nu = Nu_{annular} \\ &G < 500\,kg/m^2-s: \quad Nu = Nu_{annular} \text{ for } Fr_{so} > 20; \quad Nu = Nu_{wavy} \text{ for } Fr_{so} < 20 \end{aligned}$$

For all data points in the current study, Fr_{so} > 20, hence only the annular flow correlation was used for comparision. This correlation predicts heat transfer coefficients with an average deviation of -63%. One reason for this poor prediction may be that for the smallest diameter (3.14 mm) tube tested by Dobson and Chato (1998), the data had large uncertainties due to difficulties in measuring small heat transfer rates accurately, which led to relatively larger deviations from the above correlations.

Moser *et al.* (1998) related the friction in the vapor and liquid phases through the two-phase multiplier concept, rather than assuming the friction factors to be equal. This led to the following definition of the equivalent Reynolds number: $\mathrm{Re}_{eq} = \phi_{lo}^{8/7}\,\mathrm{Re}_{lo}$. To evaluate ϕ_{lo}^2, they recommended the use of the Friedel (1979) correlation. The final Nusselt number equation was as follows:

$$Nu = \frac{hD}{k_l} = \frac{0.0994^{C_1}\,\mathrm{Re}_l^{C_2}\,\mathrm{Re}_{eq}^{1+0.875C_1}\,\mathrm{Pr}_l^{0.815}}{\left(1.58\ln\mathrm{Re}_{eq}-3.28\right)\left(2.58\ln\mathrm{Re}_{eq}+13.7\,\mathrm{Pr}_l^{2/3}-19.1\right)} \tag{5.31}$$

where, $C_1 = 0.126\,\mathrm{Pr}_L^{-0.448}$; $C_2 = -0.113\,\mathrm{Pr}_l^{-0.563}$. This correlation predicts heat transfer coefficients with an average deviation of -70%, which is only slightly less than the deviations of the Traviss *et al.* (1973) correlation.

Cavallini *et al.* (2002) proposed separate correlations for the annular and stratified flow regimes. The applicable flow regime was decided based on criteria similar to those proposed by Breber *et al.* (1980), wherein if the dimensionless vapor velocity $J_G^* > 2.5$ and $X_{tt} < 1.6$, the flow is considered to be fully developed annular flow.

$$J_G^{\ *} = \frac{G \cdot x}{\sqrt{D \cdot g \cdot \rho_v \left(\rho_l - \rho_v\right)}} \tag{5.32}$$

This condition is satisfied by all the data points in the current study. For the annular flow regime, they suggested the use of the heat transfer model proposed by Kosky and Staub (1971) with a modified Friedel (1979) correlation for shear stress. The modified Friedel (1979) correlation was discussed in the previous section. The dimensionless film thickness is based on the liquid-phase Reynolds number:

$$\delta^+ = \begin{cases} \left(\dfrac{\mathrm{Re}_l}{2}\right)^{0.5} & \text{for } \mathrm{Re}_l \le 1145 \\ 0.0504\,\mathrm{Re}_l^{7/8} & \text{for } \mathrm{Re}_l > 1145 \end{cases} \tag{5.33}$$

The dimensionless temperature is determined based on the dimensionless film thickness in a manner analogous to Traviss *et al.* (1973). For all the data in the current study, $5 < \delta^+ < 30$; hence T^+ is given by:

$$T^+ = 5\left\{\mathrm{Pr}_l + \ln\left[1 + \mathrm{Pr}_l\left(\frac{\delta^+}{5} - 1\right)\right]\right\} \tag{5.34}$$

Finally, the heat transfer coefficient is calculated as follows:

$$h = \frac{\rho_l C_{pl} \left(\frac{\tau}{\rho_l} \right)^{0.5}}{T^+} \tag{5.35}$$

This model predicts the heat transfer coefficients from the current study with an average deviation of -46%, which is better than the deviations of the other models discussed in this section. However, Cavallini *et al.* (2005) conducted condensation experiments for R134a and R-410A in multiple parallel 1.4 mm channels and indicated that this correlation under predicts their data.

Thome *et al.* (2003) developed a multi-regime heat transfer correlation, in which the regimes identified are handled either as (a) fully annular forced convective, or as (b) consisting of varying combinations of upper gravity driven, and lower forced convective terms. Based on the transition criteria proposed by them in the first part of their study (El Hajal *et al.*, 2003), all the data in the current study belong to either the annular or the intermittent flow regime. They state that intermittent flow is very complex, and therefore assume that is can be predicted approximately by annular flow equations. They proposed the following model for the annular flow regime:

$$h_{refg} = c \cdot \mathrm{Re}_L^n \cdot \mathrm{Pr}_L^m \cdot \frac{k_L}{\delta} \cdot f_i \tag{5.36}$$

where δ is the film thickness determined based on the void fraction model proposed by El Hajal *et al.* (2003) and f_i is determined as follows:

$$f_i = 1 + \left(\frac{u_v}{u_L} \right)^{1/2} \left[\frac{(\rho_L - \rho_v) g \delta^2}{\sigma} \right]^{1/4} \tag{5.37}$$

The constants c, n and m were determined to be 0.003, 0.74 and 0.5 based on a best fit for data for tubes with D_h > 3 mm. This correlation predicts heat transfer coefficients with an average deviation of -74%. The main reason for this disagreement is the extrapolation of correlation to diameters much below the range of applicability of this correlation. Also, this correlation was developed based on the circular tube geometry, while the tubes under consideration in the current study are rectangular.

Bandhauer *et al.* (2006) proposed an annular flow heat transfer model based on the experimental results reported earlier (Garimella and Bandhauer, 2001). They suggested the use of the Traviss *et al.* (1973) boundary layer analysis, but with shear stress computed from models developed specifically for microchannels. The annular flow pressure drop model used by them to determine the shear stress was discussed in the previous section and the dimensionless film thickness was determined using the Baroczy (1965) void fraction model used by them in the pressure drop model.

$$\delta^+ = \frac{\delta \cdot \rho_l \cdot u^*}{\mu_l}; \quad \delta = \left(1-\sqrt{\alpha}\right)\frac{D}{2} \tag{5.38}$$

where $u^* = \sqrt{\frac{\tau_i}{\rho_l}}$. Traviss *et al.* (1973) developed three separate expressions to determine dimensionless Temperature T^+ based on the thickness of three sub-layers, but Bandhauer *et al.* (2006) proposed a classification just based on Re_l. For all data points in the current study, $Re_l < 2100$ and hence the expression used to determine T^+ was the same as equation (5.36). Also, it should be noted that they defined Re_l based on the liquid film flow area as discussed in their pressure drop model. The heat transfer coefficient is given by equation (5.38) in a similar manner with shear stress equal to the interfacial shear stress given by the pressure drop correlation of Garimella *et al.* (2005). This model predicts the heat transfer coefficients with an average deviation of -56%. One possible reason for this under prediction may be the under predictions of their annular flow pressure drop model (-38%), which leads to under-prediction of the shear stresses. These heat transfer predictions are still better than those of most of the other heat transfer models discussed in this section.

Table 5-2 provides a summary of the average deviations for various heat transfer models discussed in this section. Invariably, all models significantly under predict the heat transfer coefficients, further emphasizing the need for a new heat transfer model for microchannels. Unlike the pressure drop models, even the empirical models using large experimental data bases are not able to predict the heat transfer coefficients for the small diameter tubes accurately due to a lack of accurate heat transfer data for small diameter channels. Predictions of the shear flow models based on the boundary layer analysis suggested by Traviss *et al.* (1973) seem to provide better predictions but the results are strongly dependent on the flow models used to determine the film thickness and the applicable shear stress. Improved shear stress predictions would also improve heat transfer predictions. Further, most of the models assume annular flow and do not account for the existence of intermittent flow in the channels. The film thickness determined by using an annular flow assumption could be larger than the actual film thickness in the bubble section of intermittent flow with correspondingly lower heat transfer coefficients.

Table 5-2: Average Deviation for Various Heat Transfer Correlations

Correlation \ Channel Width (μm)	Average Deviation (%)					Average Absolute Deviation (%)
	100	200	300	400	All	
Shah (1979)	-66	-59	-66	-70	-66	66
Soliman (1968)	-77	-73	-77	-79	-77	77
Traviss *et al.* (1973)	-61	-54	-63	-66	-61	61
Dobson and Chato (1998)	-62	-56	-63	-68	-63	63
Moser *et al.* (1998)	-71	-65	-71	-74	-70	70
Thome et al. (2003)	-73	-69	-74	-78	-74	74
Cavallini *et al.* (2002)	-41	-33	-49	-53	-46	46
Bandhauer *et al.* (2006)	-53	-46	-57	-62	-56	56

Based on the above comparisons of the data from the present study with correlations in literature, it can be concluded that most models are not able to predict the pressure drop and heat transfer coefficients satisfactorily. Therefore, an integrated pressure drop and heat transfer model that accounts for the coexistence of the annular and intermittent flow regimes in microchannels is developed in the following chapter.

CHAPTER 6. HEAT TRANSFER AND PRESSURE DROP MODELS

The results and discussion presented in the previous chapter clearly indicate that the existing models in the literature are not able to satisfactorily predict the pressure drop and heat transfer data obtained in the current study. Criteria for transition between flow regimes should also be established so that the appropriate models can be applied. Although it is known that for the small hydraulic diameters under consideration, all of the data from the current study will either be in the intermittent or annular flow regimes, transition between these regimes is not clearly understood.

For their combined pressure drop model, Garimella *et al.* (2005) used transition criteria that included an overlap zone between the annular and intermittent flow regimes. They observed that as the flow transitions from annular to intermittent flow or vice versa, both flow regimes exist at the same time for varying amounts of time. Thus they defined an overlap zone in which interpolation between the two models (annular and intermittent pressure drop) was to be used. In the overlap zone, the probability of existence of annular or intermittent flow regime was dependent on the flow conditions. If the flow conditions are closer to the annular flow regime, annular flow prevails for a larger fraction of time and vice versa. To extend the intermittent flow model to the overlap region, the authors argued that as the flow transitions from intermittent to annular, the number of unit cells in the intermittent flow regime approaches zero.

The flow model developed here is based on a similar approach. Since the hydraulic diameters in the current study are << 1 mm, it is assumed that only annular and intermittent flow regimes exist. In addition, annular flow is assumed to consist of an infinitely long bubble, i.e. intermittent flow with zero slug length. The following sections will discuss the flow models, and pressure drop and heat transfer models based on these models.

6.1. Model for Flow in Microchannels

The proposed model for flow in microchannels is based on the assumption that for the microchannels under consideration, either annular or intermittent flow exists and wavy flow is absent based on the flow visualization studies of Coleman and Garimella (1999; 2003). In addition, as stated above, the annular flow regime is treated as intermittent flow with an infinitely long bubble or with negligible slug length compared to the bubble length.

Figure 6.1 shows the schematic of a unit cell in the intermittent flow regime (Garimella *et al.*, 2002, 2003b). The liquid slugs are assumed to contain no entrained vapor, and similarly in the bubble, it is assumed that there is no entrained liquid. The bubbles are assumed to be surrounded by liquid film on all sides without stratification. Thus, the effect of gravity is neglected. The bubbles are assumed to be uniform and constant throughout the test section. Based on the visual observations of Dukler and Hubbard (1975), a bubble of vapor with annular liquid film surrounding it is assumed to flow somewhat faster than the liquid slugs which bound it on either end. The annular film flows very slowly compared to both the bubble and the slug. Thus, liquid is continuously picked up from film at the front of the slug and shed into the film at the end of the slug.

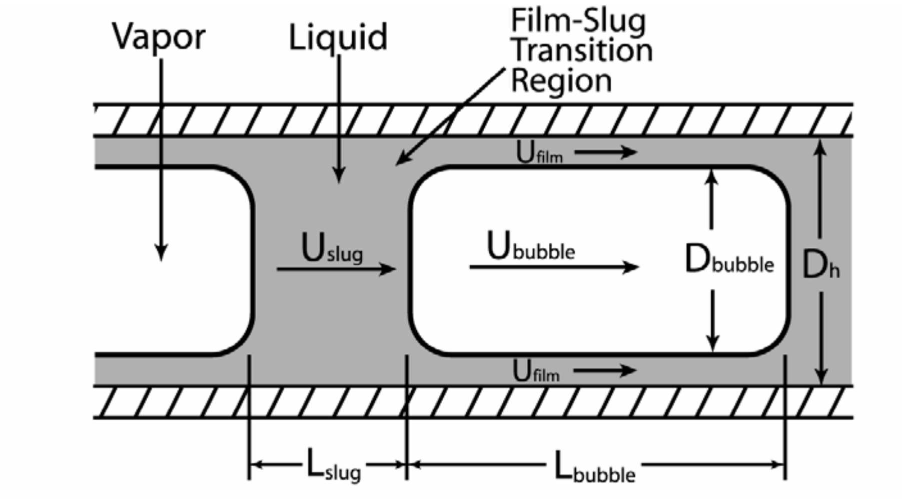

Figure 6.1: Intermittent Flow Unit Cell (Garimella *et al.*, 2002)

In rectangular channels, the actual bubble shape is expected to be elliptical with a thinner liquid film along the longer edge as shown in Figure 6.2. To simplify the analysis, the bubbles are assumed to be rectangular with the same aspect ratio as the tube. This assumption also helps in taking into account the effect of aspect ratio, which is not captured by the use of hydraulic diameter alone.

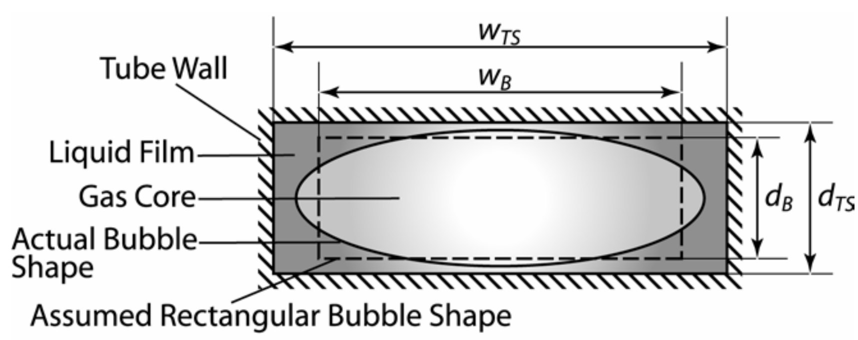

Figure 6.2: Cross-section of Assumed Bubble Shape for Rectangular Channels

In the analysis below, the term "Diameter" refers to "Hydraulic Diameter" calculated as follows:

$$D = \frac{4 \times w_{TS} \times d_{TS}}{2 \cdot \left(w_{TS} + d_{TS}\right)} \tag{6.1}$$

Also, as discussed above, assuming the same aspect ratio for the bubble and the tube, we get:

$$AR = \frac{w_{TS}}{d_{TS}} = \frac{w_B}{d_B} \tag{6.2}$$

To simplify the analysis of the liquid film surrounding the bubble, a length-weighted average film thickness is used, as determined by equation (6.3).

$$\delta_{ave} = \frac{1}{2} \cdot \left[\frac{\left(w_{TS} - w_B\right) \cdot d_{TS} + \left(d_{TS} - d_B\right) \cdot w_{TS}}{w_{TS} + d_{TS}} \right] \tag{6.3}$$

Several authors (Fukano *et al.*, 1989, 1991; Zhao and Bi, 2001b; Serizawa *et al.*, 2002) have indicated that the Armand (1946) correlation predicts the void fraction for intermittent/annular flow in microchannels with sufficient accuracy. This void fraction model is therefore used in the development of the analytical model proposed below. It should be noted that the use of the Armand correlation is equivalent to assuming a slip velocity ratio of 1.2 that was assumed by Garimella *et al.* (2002; 2003b) in the development of their pressure drop model. This can also be proved analytically, as will be shown later in this section. The calculation of void fraction using the Armand (1946) correlation is shown below:

$$\beta = \frac{x \cdot \rho_L}{x \cdot \rho_L + \left(1 - x\right) \cdot \rho_V} \tag{6.4}$$

$$\alpha = 0.833 \times \beta \tag{6.5}$$

$$\alpha = \frac{\text{Bubble Volume}}{\text{Total Unit Cell Volume}} = \frac{l_{bubble} \cdot w_B \cdot d_B}{\left(l_{slug} + l_{bubble}\right) \cdot w_{TS} \cdot d_{TS}}$$

$$\Rightarrow \alpha = \left(1 - \frac{l_{slug}}{l_{slug} + l_{bubble}}\right) \cdot \frac{w_B \cdot d_B}{w_{TS} \cdot d_{TS}} \tag{6.6}$$

Using a mass balance (Suo and Griffith, 1964; Dukler and Hubbard, 1975), the slug velocity is determined to be:

$$U_{slug} = j_L + j_V \tag{6.7}$$

where $j_L = \frac{(1-x)G}{\rho_L}$ and $j_V = \frac{x \cdot G}{\rho_V}$.

The interface velocity is determined by conducting a shear balance at the interface. Detailed derivations of the interface and film velocities are provided in Appendix D.1. A summary is provided here. In a manner similar to Garimella *et al.* (2002; 2003b), it is assumed that vapor flow in the bubble is driven by the pressure gradient in the film-bubble section. The shear stress at the vapor-film interface in bubble section is thus given by the following expression (Garimella *et al.*, 2002, 2003b):

$$\tau_{interface} = -\frac{\left(D_{bubble}/2\right)}{2}\left(\frac{dP}{dx}\right)_{f/b} \tag{6.8}$$

where bubble diameter $D_{Bubble} = \frac{4 \times w_B \cdot d_B}{2 \cdot \left(w_B + d_B\right)}$. This interfacial shear stress should be same as the shear stress at the interface due to the velocity profile in the film. The film velocity profile is determined by treating the liquid flow in the film as a combination of the Couette flow and Poiseuille flow (Garimella *et al.*, 2002, 2003b). The liquid film profile is determined in terms of the interface velocity and pressure gradient as follows:

$$\Rightarrow u_{film} = \frac{1}{2\mu_L}\left(\frac{dP}{dx}\right)_{f/b} y\left(y-\delta_{ave}\right) + U_{interface}\left(1-\frac{y}{\delta_{ave}}\right) \tag{6.9}$$

where y = 0 at the interface and $y = \delta_{ave}$ at the wall. Now, the film shear stress at the interface is given by $\tau_{interface} = \mu_L\left(\frac{du_{film}}{dy}\right)_{y=0}$. Thus,

$$\tau_{interface} = \mu_L\left(-\frac{1}{2\mu}\left(\frac{dP}{dx}\right)_{f/b}\delta_{ave} - \frac{U_{interface}}{\delta_{ave}}\right) \tag{6.10}$$

By equating the interfacial shear stress given by equations (6.8) and (6.10), the interface velocity is determined to be:

$$U_{interface} = \left(\frac{dP}{dx}\right)_{f/b}\left(\frac{D_{bubble}}{2} - \delta_{ave}\right)\frac{\delta_{ave}}{2\cdot\mu_L} \tag{6.11}$$

Substituting the above interface velocity into equation (6.9) and integrating the film velocity over the film thickness, we get the average film velocity to be:

$$U_{film} = \frac{1}{\delta_{ave}}\int_0^{\delta_{ave}} u_{film}dy = \frac{1}{4\mu_L}\left(\frac{dP}{dx}\right)_{f/b}\left[\left(\frac{1}{2}\right)D_{bubble} - \left(\frac{4}{3}\right)\delta_{ave}\right]\delta_{ave} \tag{6.12}$$

This procedure is explained in greater detail in Appendix D.2.

As the bubble moves downstream in the tube, the liquid film surrounding the bubble constantly merges into the slug immediately following the bubble. Thus, the apparent velocity of the bubble is equal to the velocity of the slug plus the rate at which the slug-bubble interface (slug nose) moves forward relative to the slug due to the incoming additional liquid from the film. The rate at which liquid film mass becomes a part of slug is given by equation (6.13).

$$\dot{m}_{transition} = \rho_L \cdot \left(w_{TS} \cdot d_{TS} - w_B \cdot d_B \right) \cdot \left(U_{bubble} - U_{film} \right) \tag{6.13}$$

Bubble Velocity	=	Mean fluid velocity in slug	+	Apparent velocity gained by adding fluid at the slug nose

$$U_{bubble} = U_{slug} + \frac{\dot{m}_{transition}}{\rho_L \cdot w_{TS} \cdot d_{TS}} \tag{6.14}$$

Substituting $\dot{m}_{transition}$ from equation (6.13) into the above equation and re-arranging the terms we get the following relationship between U_{slug}, U_{film} and U_{bubble}:

$$U_{slug} = U_{bubble} \left(\frac{w_B \cdot d_B}{w_{TS} \cdot d_{TS}} \right) + U_{film} \cdot \left(1 - \frac{w_B \cdot d_B}{w_{TS} \cdot d_{TS}} \right) \tag{6.15}$$

Now we have expressions for all velocities and need to determine the length of slug relative to the bubble length. To determine the slug length ratio $\left[\frac{l_{slug}}{l_{slug} + l_{bubble}} \right]$, a mass balance on the liquid entering and exiting the tube is performed. Looking from the perspective of the stationary observer watching the slug flow, the flow would seem to travel with the velocity at which the slug-bubble interface moves. This apparent velocity of the flow is given by U_{bubble}, hence the amount of time taken by a slug and bubble to exit the tube is given by $\frac{l_{slug}}{U_{bubble}}$ and $\frac{l_{bubble}}{U_{bubble}}$, respectively. It should be noted that the apparent velocity (U_{bubble}) is used only for the determination of the time it takes for the bubble or slug to pass a particular point, the actual flow velocities of the fluid inside the slug or film are slower. The amount of liquid mass that exits the tube, when the slug and bubble sections exit is given by equations (6.16) and (6.17) respectively.

$$M_{slug} = U_{slug} \cdot \left(w_{TS} \cdot d_{TS} \right) \cdot \rho_L \cdot \frac{l_{slug}}{U_{bubble}} \tag{6.16}$$

$$M_{film} = U_{film} \cdot \left(w_{TS} \cdot d_{TS} - w_B \cdot d_B \right) \cdot \rho_L \cdot \frac{l_{bubble}}{U_{bubble}} \tag{6.17}$$

In the above equations, the actual flow velocity of the fluid in the slug/film has been multiplied by the flow area, density and the time taken by slug/bubble to pass a particular point. Now, the total liquid mass exiting the tube in time $\left(\frac{l_{slug} + l_{bubble}}{U_{bubble}} \right)$ should be equal to the liquid mass entering the tube in the same amount of time based on the quality and mass flux as shown in equation (6.18), which can be simplified to yield a relationship between the slug length ratio, mass flux, quality and velocities as follows:

$$G \cdot (1 - x) \cdot \left(w_{TS} \cdot d_{TS} \right) = \frac{M_{slug} + M_{film}}{\left(\frac{l_{slug} + l_{bubble}}{U_{bubble}} \right)} \tag{6.18}$$

Substituting M_{slug} and M_{film} from equations (6.16) and (6.17) and rearranging the above equation, we get:

$$\frac{G \cdot (1 - x)}{\rho_L} = U_{slug} \cdot \left(\frac{l_{slug}}{l_{slug} + l_{bubble}} \right) + U_{film} \cdot \left(1 - \frac{w_B \cdot d_B}{w_{TS} \cdot d_{TS}} \right) \cdot \left(1 - \frac{l_{slug}}{l_{slug} + l_{bubble}} \right) \tag{6.19}$$

Using the above relationship and the assumed void fraction model, it can be shown that $\frac{U_{Bubble}}{U_{slug}} = 1.2$ always. The procedure to derive the slip velocity ratio using the above equation is shown in greater detail in Appendix D.3. The objective of the above analysis was to determine the various flow related parameters, such as U_{slug}, U_{Bubble}, U_{film} and $\frac{l_{slug}}{l_{slug} + l_{bubble}}$, which in turn serve as inputs to the pressure drop and heat transfer models. We now have three equations (6.11), (6.15) and (6.19) and four unknowns namely, U_{Bubble}, U_{film}, $\frac{l_{slug}}{l_{slug} + l_{bubble}}$ and $\left(\frac{dP}{dx}\right)_{f/b}$. U_{slug} is already known from equation (6.7). The additional equation required for $\left(\frac{dP}{dx}\right)_{f/b}$ is provided in the next section.

6.2. Pressure Drop Model

The total pressure drop in the channels (after removing the deceleration component) consists of three main contributions, i.e., pressure drop due to friction in the slug, pressure drop due to friction in the film-bubble section and the transitional pressure drop associated with the transfer of liquid from the slow moving film to the fast moving liquid.

The frictional pressure drop in the slug is determined using standard single phase correlations explained below. The channel surface roughness (ε_{tube}) varies from 10 to 15 nm based on the information provided by the manufacturer. Idelchik (1986) suggested that tubes may be considered hydraulically smooth if the following condition is satisfied:

$$\frac{\varepsilon_{tube}}{D} < \frac{181 \cdot \log Re - 16.4}{Re} \approx 17.85 \cdot Re^{-0.875} \tag{6.20}$$

Thus, for ε_{tube} = 15 nm and D = 100 μm, tubes can be considered hydraulically smooth for Reynolds number less than 63.2×10^4. The Reynolds numbers encountered in the current study are much lower than 63.2×10^4 and hence the tubes are considered smooth.

The liquid flow in the slug is treated as single phase liquid flow inside a tube, and Re_{slug} is determined using equation (6.21).

$$\mathrm{Re}_{slug}=\frac{\rho_L\cdot U_{slug}\cdot D}{\mu_L} \tag{6.21}$$

For all the data points in the current study, $2194 < Re_{slug} < 12187$. Based on the findings of several researchers, Shah and Bhatti (1987) recommended the use of the following empirical correlation for the laminar region, i.e., Re < 2000, for the friction factor in rectangular tubes with aspect ratio AR.

$$f\cdot Re=4\times24\left(\begin{array}{r}1-1.3553\cdot\dfrac{1}{AR}+1.9467\cdot\left(\dfrac{1}{AR}\right)^2-1.7012\cdot\left(\dfrac{1}{AR}\right)^3+\\0.9564\cdot\left(\dfrac{1}{AR}\right)^4-0.2537\cdot\left(\dfrac{1}{AR}\right)^5\end{array}\right) \tag{6.22}$$

For the turbulent flow, i.e. Re > 4000, Bhatti and Shah (1987) recommended that the circular tube friction factor for the same hydraulic diameter tube should be multiplied by a factor of $\left[1.0875-0.1125\cdot\left(\dfrac{1}{AR}\right)\right]$. Bhatti and Shah (1987) also mentioned that Blasius correlation (recommended for $4000 < \mathrm{Re} < 10^5$) agrees with the most accurate implicit formula within +2.6% and – 1.3%. Thus, for Re > 4000, the friction factor is calculated using equation (6.23).

$$f=\frac{0.3164}{Re^{0.25}}\cdot\left[1.0875-0.1125\cdot\left(\frac{1}{AR}\right)\right] \tag{6.23}$$

The friction factor for flow with Reynolds number in the transition region, i.e 2000 < *Re* < 4000, is determined by conducting a logarithmic interpolation based on Reynolds number between the values of laminar and turbulent friction factor at critical Reynolds numbers.

$$f = \exp\left[\left(\frac{\ln(\mathrm{Re}) - \ln(\mathrm{Re}_{CL})}{\ln(\mathrm{Re}_{CU}) - \ln(\mathrm{Re}_{CL})}\right) \times \left(\ln\left(f\left(\mathrm{Re}_{CU}\right)\right) - \ln\left(f\left(\mathrm{Re}_{CL}\right)\right)\right) + \ln\left(f\left(\mathrm{Re}_{CL}\right)\right)\right] \quad (6.24)$$

The slug friction pressure gradient is thus determined using equation (6.25), where the slug friction factor is calculated as described above based on Re_{slug}.

$$\left(\frac{dP}{dx}\right)_{slug} = \frac{1}{2} \cdot f_{slug} \cdot \frac{\rho_L \cdot U_{slug}^{\ 2}}{D} \quad (6.25)$$

The Reynolds number for the flow of the vapor in the bubble is calculated based on the bubble hydraulic diameter and the vapor flow velocity relative to the interface velocity as follows:

$$\mathrm{Re}_{Bubble} = \frac{\rho_V \cdot \left(U_{bubble} - U_{interface}\right) \cdot D_{Bubble}}{\mu_V} \quad (6.26)$$

For all the data points in the current study, $1430 < Re_{Bubble} < 6805$. Frictional pressure gradient in film bubble region is thus determined using equation (6.27), where the bubble friction factor is determined from equations (6.22), (6.23) and (6.24) as described above.

$$\left(\frac{dP}{dx}\right)_{f/b} = \frac{1}{2} \cdot f_{bubble} \cdot \frac{\rho_V \cdot \left(U_{bubble} - U_{\mathrm{int}\,erface}\right)^2}{D_{Bubble}} \quad (6.27)$$

Equation (6.27), together with equations (6.11), (6.15) and (6.19) provides the four equations needed to determine the four unknowns namely, U_{Bubble}, U_{film}, $\frac{l_{slug}}{l_{slug}+l_{bubble}}$ and $\left(\frac{dP}{dx}\right)_{f/b}$. The total frictional pressure drop along the test section length can be now determined by adding the pressure drops in the film/bubble section and slug section in proportion to their lengths as shown in the equation below:

$$\Delta P_{fric,only} = L_{tube} \cdot \left[\left(\frac{dp}{dx}\right)_{f/b} \cdot \left(1 - \frac{l_{slug}}{l_{slug}+l_{bubble}}\right) + \left(\frac{dp}{dx}\right)_{slug} \cdot \left(\frac{l_{slug}}{l_{slug}+l_{bubble}}\right) \right] \tag{6.28}$$

where L_{tube} is the total length of the channels. The total pressure drop is the sum of the purely frictional pressure drop in the slug and film/bubble region and the losses associated with the flow transitions between the film and the slug. A pressure drop occurs during transition from the film to the slug due to the acceleration of the liquid in the film to the slug velocity. The pressure drop associated with one such transition is given by equation (6.29).

$$\Delta P_{transition} = \frac{\dot{m}_{transition} \cdot \left(U_{slug} - U_{film}\right)}{w_{TS} \cdot d_{TS}} \tag{6.29}$$

The number of times this transition occurs along the length of the tube is equal to the number of unit cells, N_{UC} (Figure 6.1) along the length of the tube. This quantity is determined from the experimentally measured frictional pressure drop using the following equation:

$$N_{UC} = \frac{\Delta P_{fric,\exp} - \Delta P_{fric,only}}{\Delta P_{transition}} \tag{6.30}$$

Figure 6.3 shows the number of unit cells calculated using the above method for each of the tubes under consideration in the current study. One trend that is clearly visible is that as the quality increases, the number of unit cells decreases, which means that the flow regime tends toward annular flow. Another trend in Figure 6.3 is that for all tubes, the numbers of unit cells are in general larger for the higher refrigerant saturation temperature data sets. As the refrigerant saturation temperature increases, the gas-to-liquid phase density ratio $\left(\rho_g / \rho_l\right)$ increases (ρ_g/ρ_l = 0.083 @ 60°C and ρ_g/ρ_l = 0.032 @ 30°C), leading to a decrease in void fraction (α = 0.74 @ 60°C and α = 0.80 @ 30°C). Due the presence of higher percentage of fluid by volume, there is more frequent formation of slugs, leading to a larger number of unit cells. It should be noted that the number of unit cells shown in the plots correspond to the total number of unit cells in the 40 mm length of each of the tubes. In some cases, the number of unit cells decreases to less than five, which indicates that the flow is almost annular (considering the high *L/D* ratio of the channels under consideration). Also, the number of unit cells does not vary much with the mass flux (for a given saturation temperature and tube) because the asummed void fraction model is not dependent on the mass flux, and the tendency to form more or less unit cells is expected to be related the the ratio of the volume of liquid and vapor present in the tube.

Figure 6.4 shows the data for different tubes on the same plot at the same refrigerant saturation temperatures. Although there is some scatter, in general, the 100×100 μm tubes have the least number of unit cells for similar flow conditions, followed by the 200×100 μm, 300×100 μm and 400×100 μm channels, in that order.

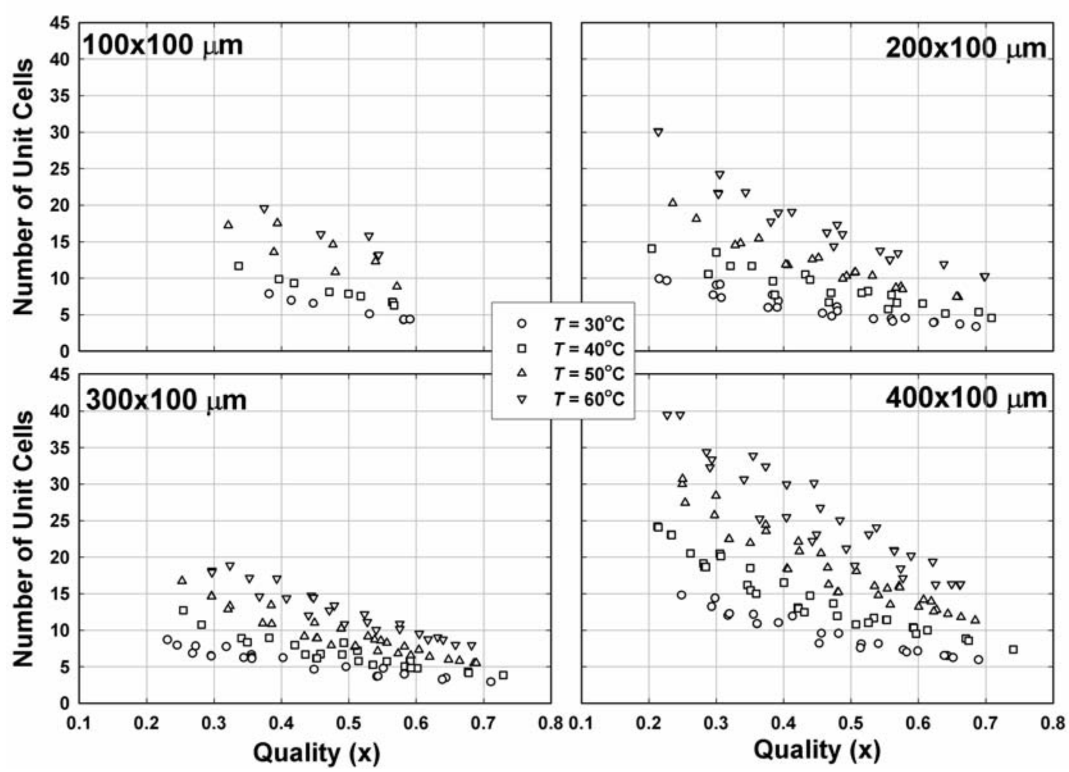

Figure 6.3: Number of Unit Cells Determined from Data for each Tube

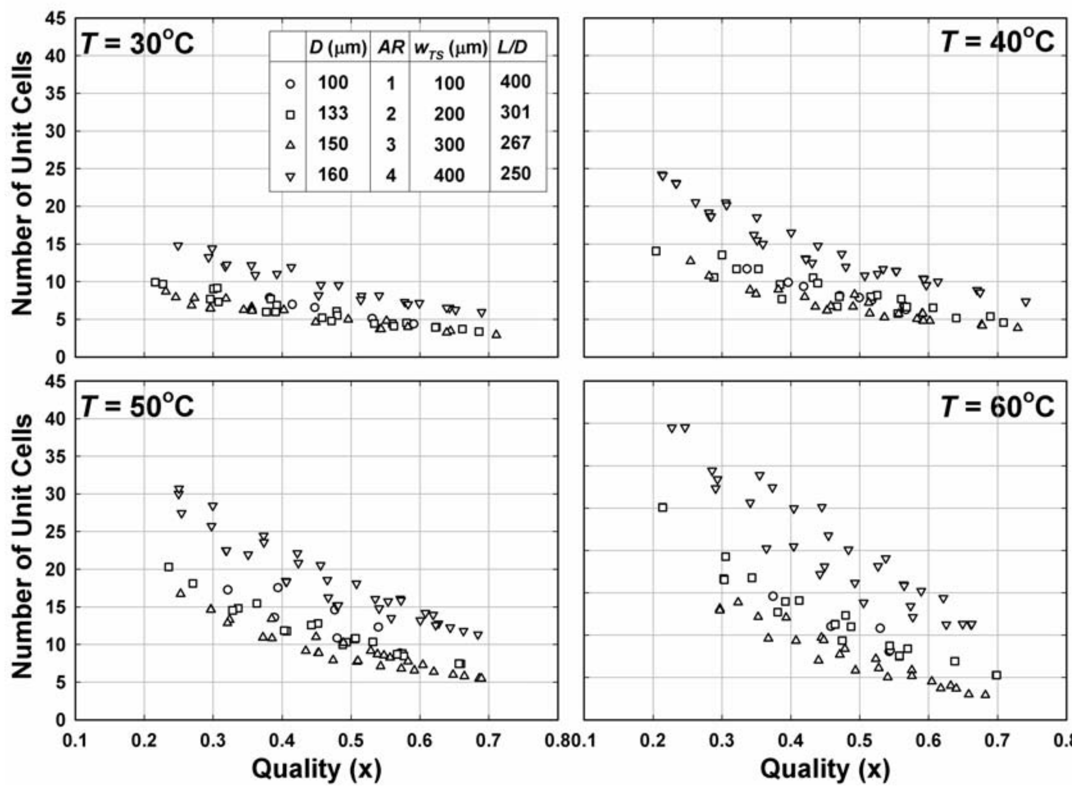

Figure 6.4: N_{UC} for Different Tubes at same Refrigerant Temperature

The 400×100 μm channels have the largest number of unit cells for similar flow conditions indicating that as the aspect ratio increases, the probability of occurrence of the intermittent flow regime increases. This is probably due to the fact that in high aspect ratio channels, the annular film around the bubble is more unstable, leading to frequent formation of slugs. Garimella *et al.* (2002; 2003b) conducted a similar analysis for the intermittent flow pressure drop model proposed by them. They proposed the following correlation for slug frequency (non-dimensional unit-cell length, or unit cells/length) based on Re_{slug} and D for circular and non-circular channels:

$$D_h\left(\frac{N_{\substack{unit\\cells}}}{L_{tube}}\right)=\left(\frac{D_h}{L_{\substack{unit\\cell}}}\right)=2.437\left(\mathrm{Re}_{slug}\right)^{-0.560} \tag{6.31}$$

The data used for the development of the above model were selected based on criteria for transition to intermittent flow given by Coleman and Garimella (1999; 2003). Garimella *et al.* (2005) later extended the above model to include the discrete wave flow regime points based on the same criteria and proposed the following modified correlation for slug frequency:

$$N_{UC}\left(\frac{D_h}{L_{tube}}\right)=\left(\frac{D_h}{L_{UC}}\right)=1.573\left(\mathrm{Re}_{slug}\right)^{-0.507} \tag{6.32}$$

Both the above models predict the number of unit cells only as a function of slug Reynolds number. Figure 6.5 shows the variation of number of unit cells with slug Reynolds number for the data from the current study. The data do show trends similar to those observed by Garimella *et al.* (2002; 2003b), however, there is considerable scatter, indicating that there are other parameters also influencing the number of unit cells. Both the slug frequency models proposed by Garimella *et al.* significantly under-predict the number of unit cells for the data from the current study. Also those pressure drop models do not capture the trends in the present data, as was shown in the previous chapter. One reason for this is that most of the experimental data used by them in the development of these models consisted only of data points with vapor qualities less than 0.2, while for the data in the current study, the average qualities range from 0.2 to 0.8. (It should be noted that in the larger diameter tubes, D_h > 0.4 mm, considered by them, intermittent flow is confined to much lower qualities than would be the case for the channels under consideration here.)

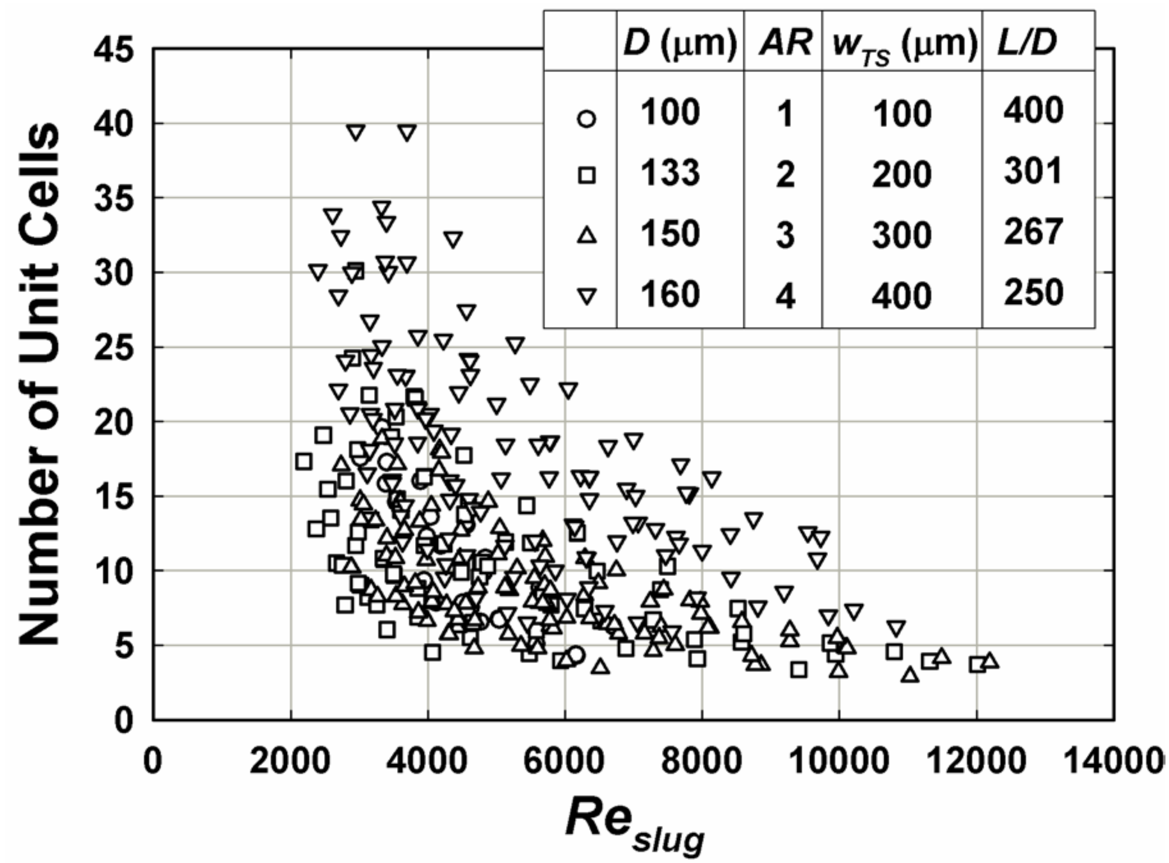

Figure 6.5: Variation in Number of Unit Cells with Slug Reynolds Number

Figure 6.6 shows the variation in the number of unit cells with mass flux for the 300×100 μm channels at a saturation temperature of 50°C. For each data set, as the slug Reynolds number increases, the number of unit cells decreases, but data sets for different mass fluxes clearly do not overlap, indicating that there are other parameters affecting the number of unit cells.

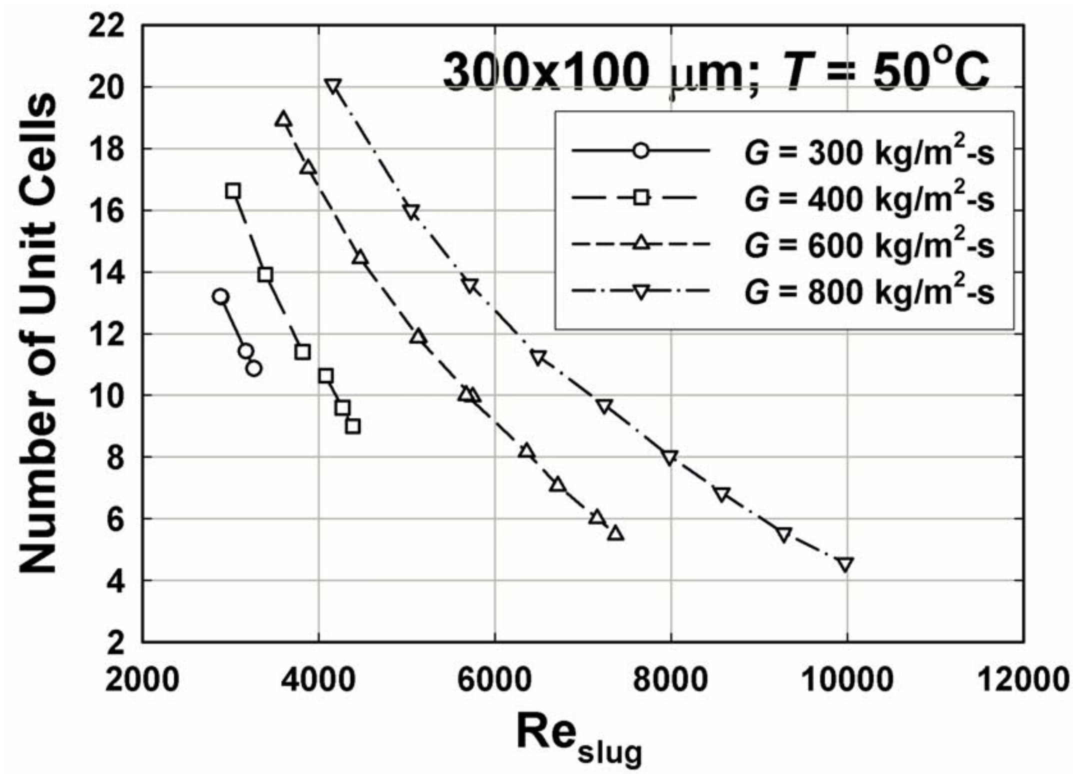

Figure 6.6: Variation of N_{UC} with Re_{slug} for 300×100 μm Channels at 50°C

Based on the above observations, the following correlation was developed for determining the slug frequency:

$$N_{UC} \cdot \frac{D}{L_{tube}} = \left(2.8 \cdot e^{0.4 \cdot AR}\right) \cdot Re_{slug}{}^{-0.35} \cdot \left(\frac{1-x}{x}\right)^{0.46} \cdot \left(\frac{\rho_g}{\rho_l}\right)^{0.868} \tag{6.33}$$

Figure 6.7 shows the number of unit cells for all tubes in the corrent data determined using the data and the above proposed model.

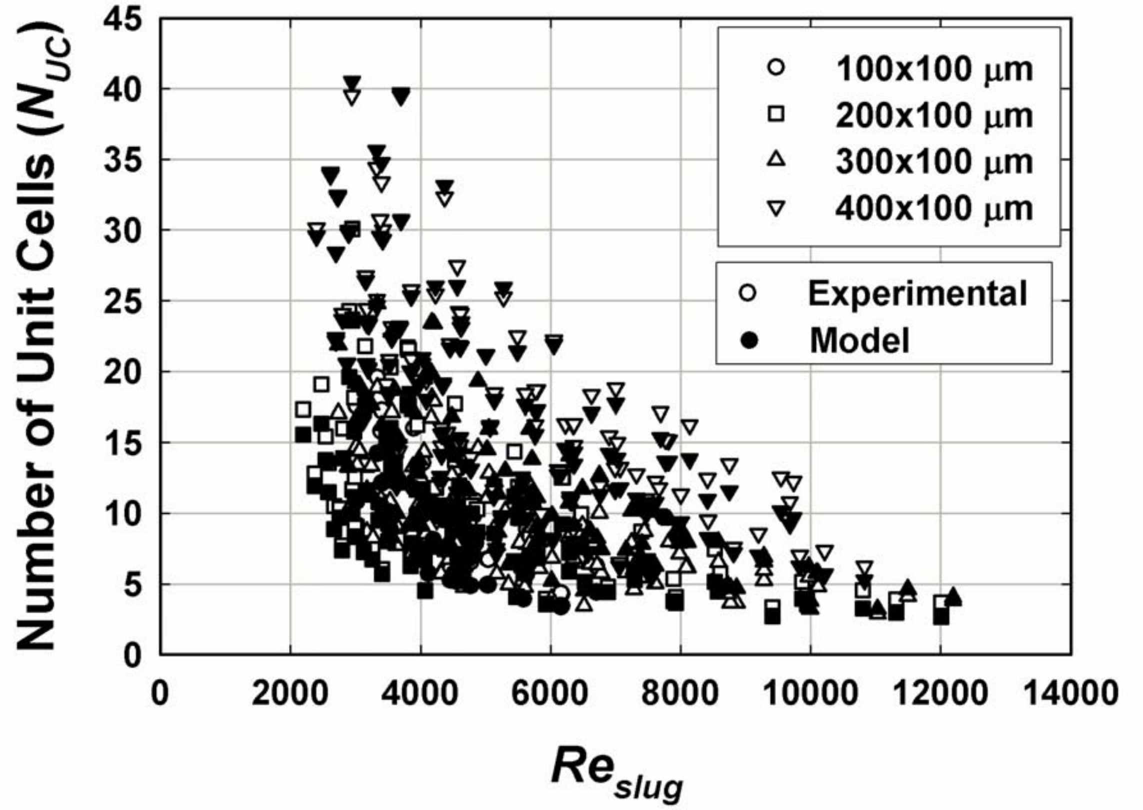

Figure 6.7: N_{UC} Model Predictions and Data

Total ΔP in the test section is then calculated using the following equation:

$$\Delta P_{fric,model} = N_{UC} \cdot \Delta P_{transition} + \Delta P_{fric,only} \tag{6.34}$$

In the above equation, the $\Delta P_{transition}$ and $\Delta P_{fric,only}$ are determined using equations (6.28) and (6.29) respectively, as discussed previously in this section. Appendix D.7 provides the details for the step-by-step implementation of the above model. Figure 6.8 compares the pressure drops predicted using this model and the data from the current study. This pressure drop model predicts the pressure drop for 95% of the data within ±25% of the experimental values.

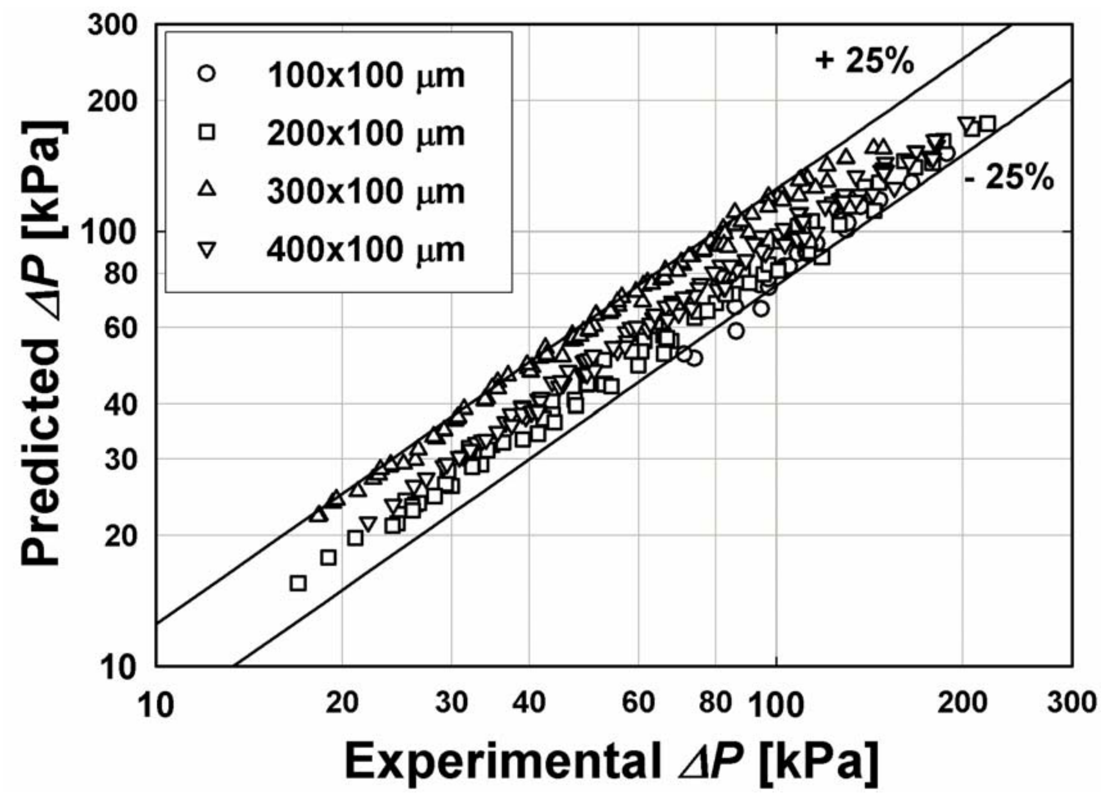

Figure 6.8: Predicted vs Experimental Pressure Drop

Figures 6.9 to 6.12 show the data and the predicted pressure drops for each of the channel shapes individually. It can be seen that the proposed model is able to capture the trends observed in the data well. The average absolute deviation for the 100×100 μm, 200×100 μm, 300×100 μm and 400×100 μm tubes are 21%, 12%, 20% and 5% respectively, with an overall average absolute deviation of 12%. The proposed model slightly under predicts the data for the 100×100 μm and 200×100 μm channels and slightly over-predicts the data for the 300×100 μm channels. The 400×100 μm data are predicted well. Conclusions relating to the effect of diameter, aspect ratio, mass flux and temperature based on the proposed model are discussed together with the trends in the heat transfer predictions in a subsequent section of this chapter.

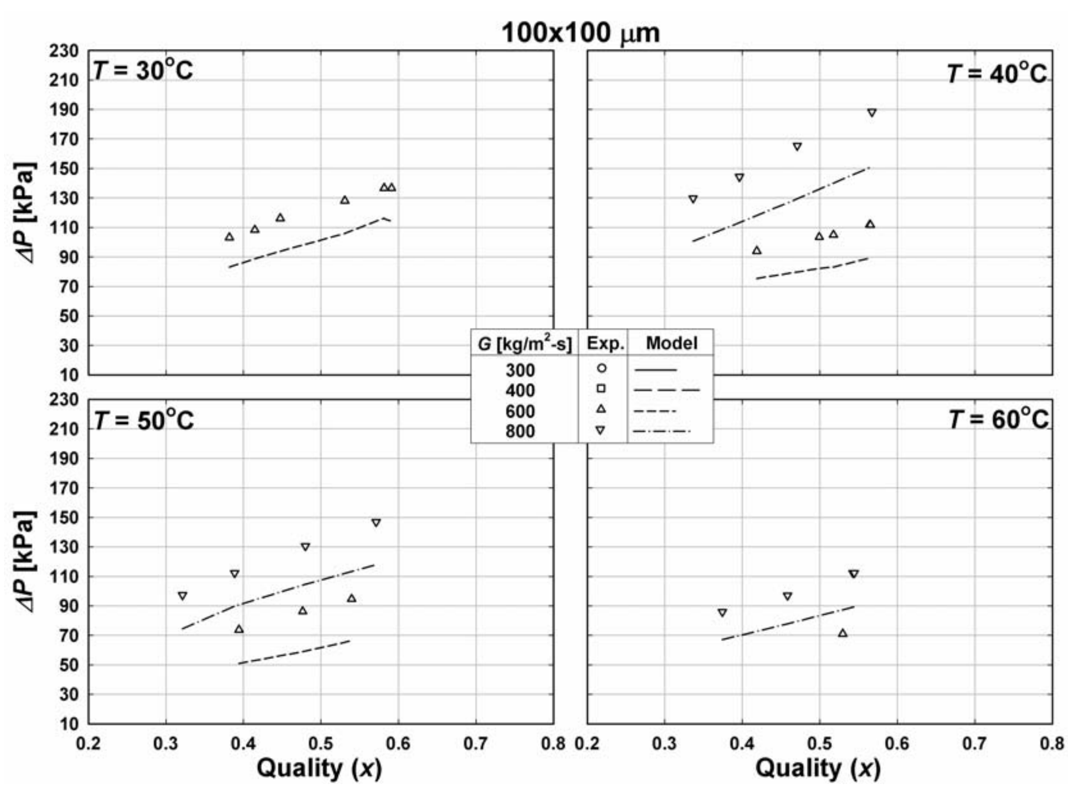

Figure 6.9: ΔP Model and Data for 100×100 μm Channels

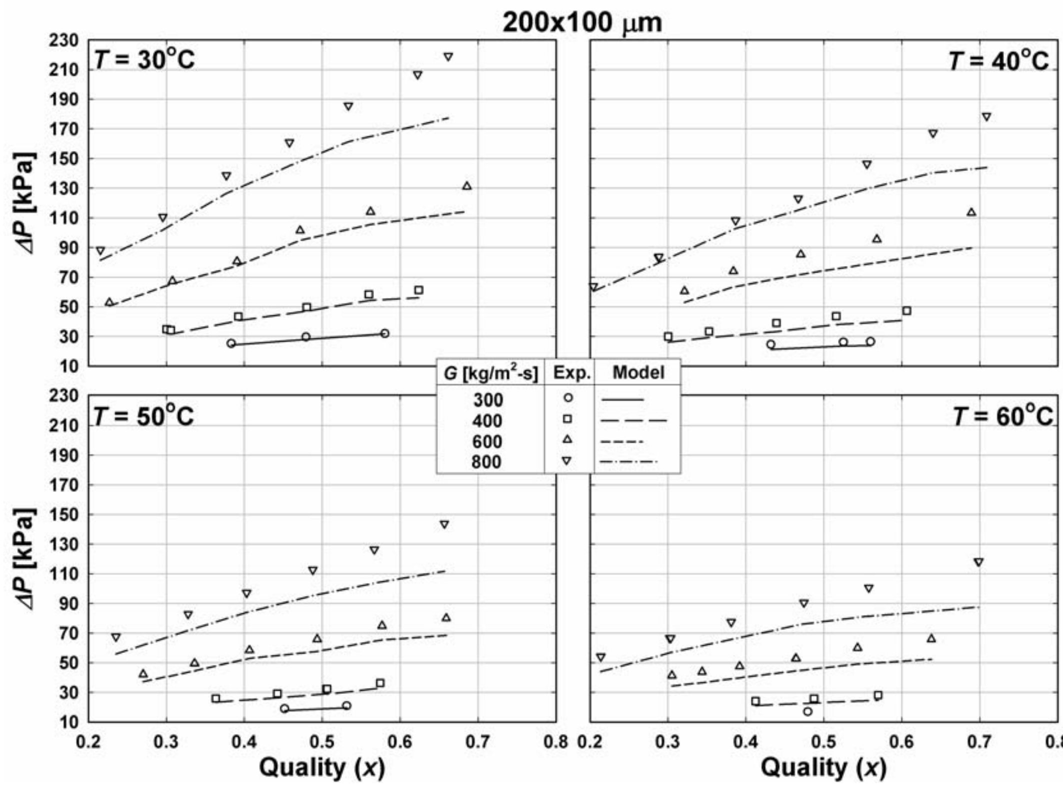

Figure 6.10: ΔP Model and Data for 200×100 μm Channels

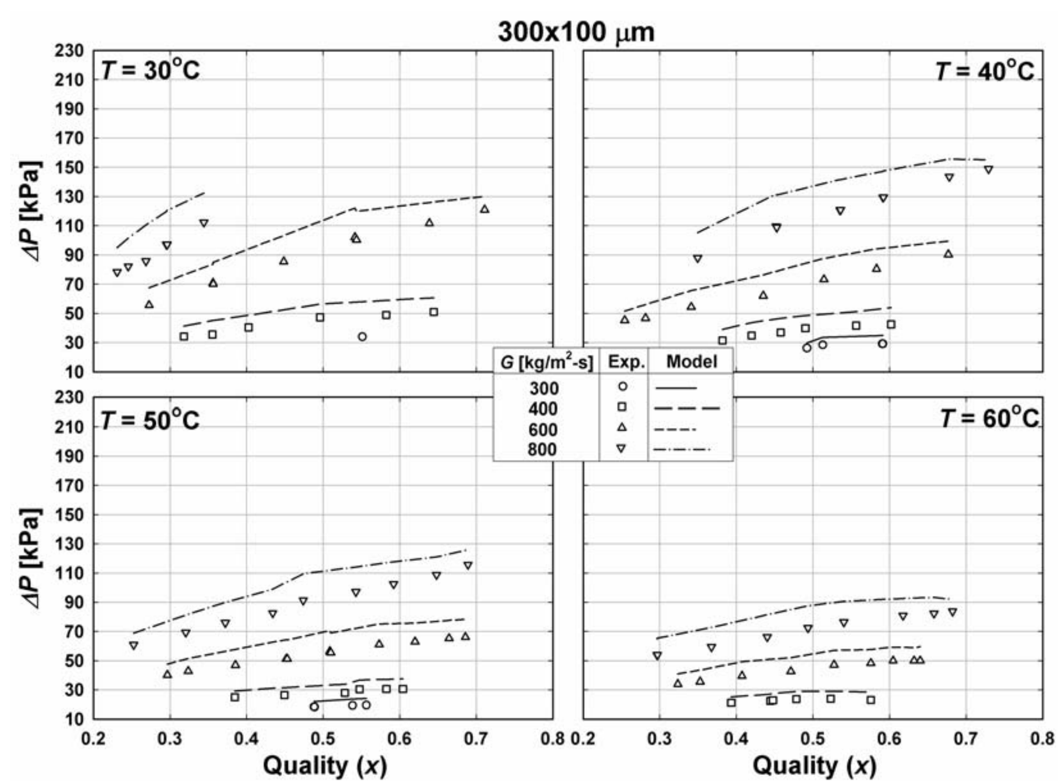

Figure 6.11: ΔP Model and Data for 300×100 μm Channels

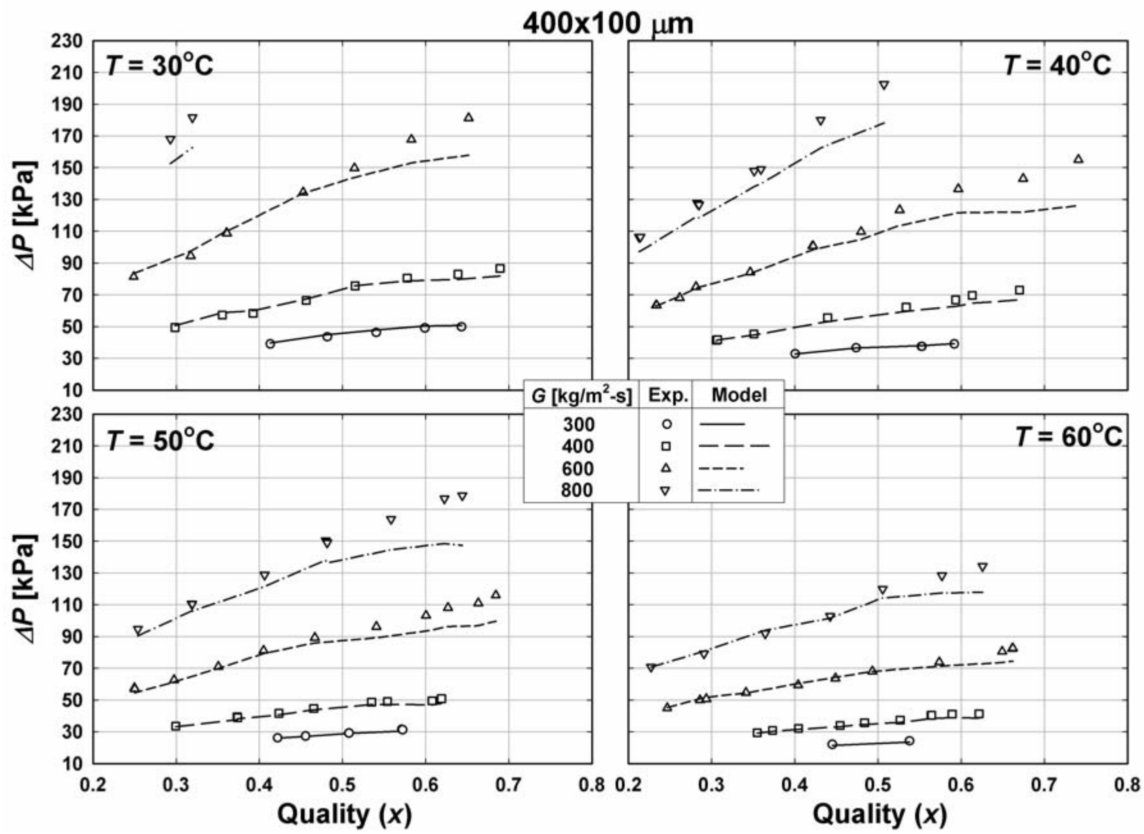

Figure 6.12: ΔP Model and Data for 400×100 μm Channels

6.3. Annular Flow Factor

In this section, based on intermediate parameters used in the pressure drop model discussed above, a criterion for predicting the predominant flow mechanism (intermittent or annular) in the channels for given flow conditions is developed. Thus, in addition to the number of unit cells (N_{UC}) discussed in the previous section, another parameter important in determining whether the flow tends to intermittent or annular flow is the slug length ratio $\dfrac{l_{slug}}{l_{slug}+l_{bubble}}$. Figure 6.13 shows the variation of slug length ratio (*SLR*) with quality for all tubes under consideration. As the quality increases, the slug length ratio decreases, indicating that the flow tends toward annular flow at higher qualities. Also, for all the data points, the slug length ratio is less than 0.25. The *SLR* appears to not depend systematically on tube diameter or aspect ratio, but on saturation temperature as shown in Figure 6.14.

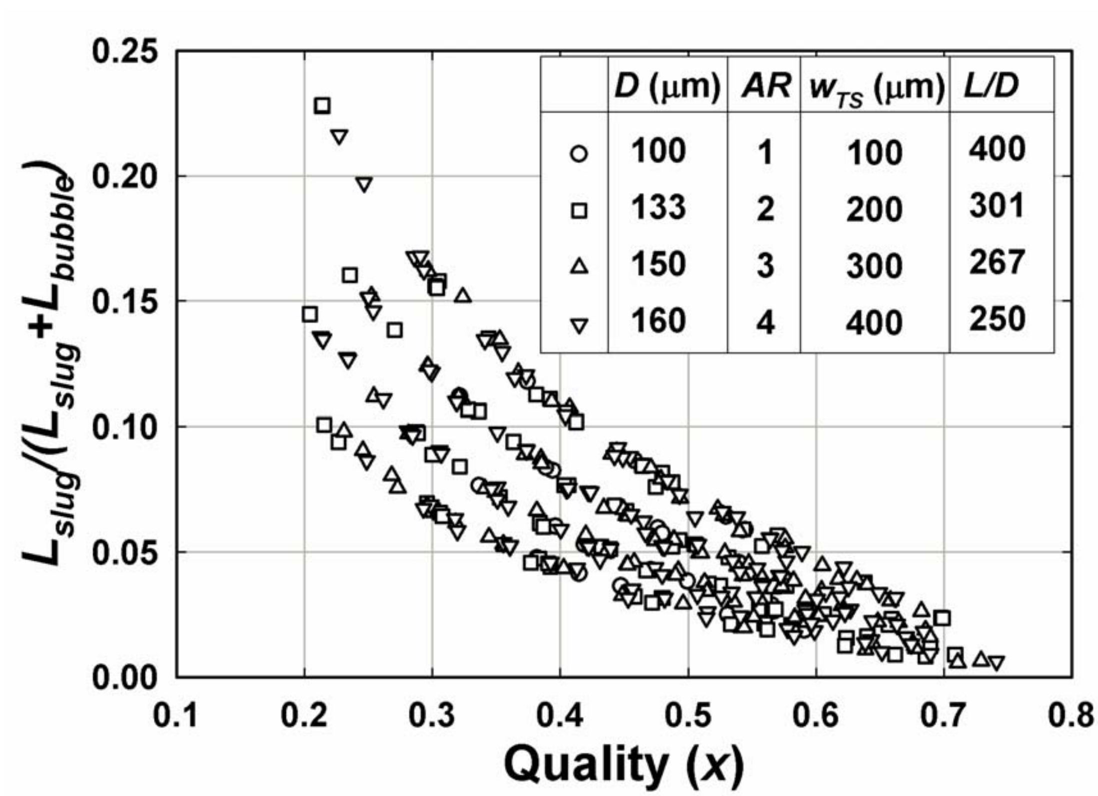

Figure 6.13: Variation of Slug Length Ratio with Quality

Figure 6.14 shows the variation of slug length ratio with quality for the 200×100 μm test section. The slug length ratio is larger at the higher saturation temperatures for the same quality, because the liquid density decreases and the vapor density increases with an increase in the saturation temperature. This phenomenon is also observed for the number of unit cells: the number of unit cells is larger at the higher saturation temperatures (Figure 6.3).

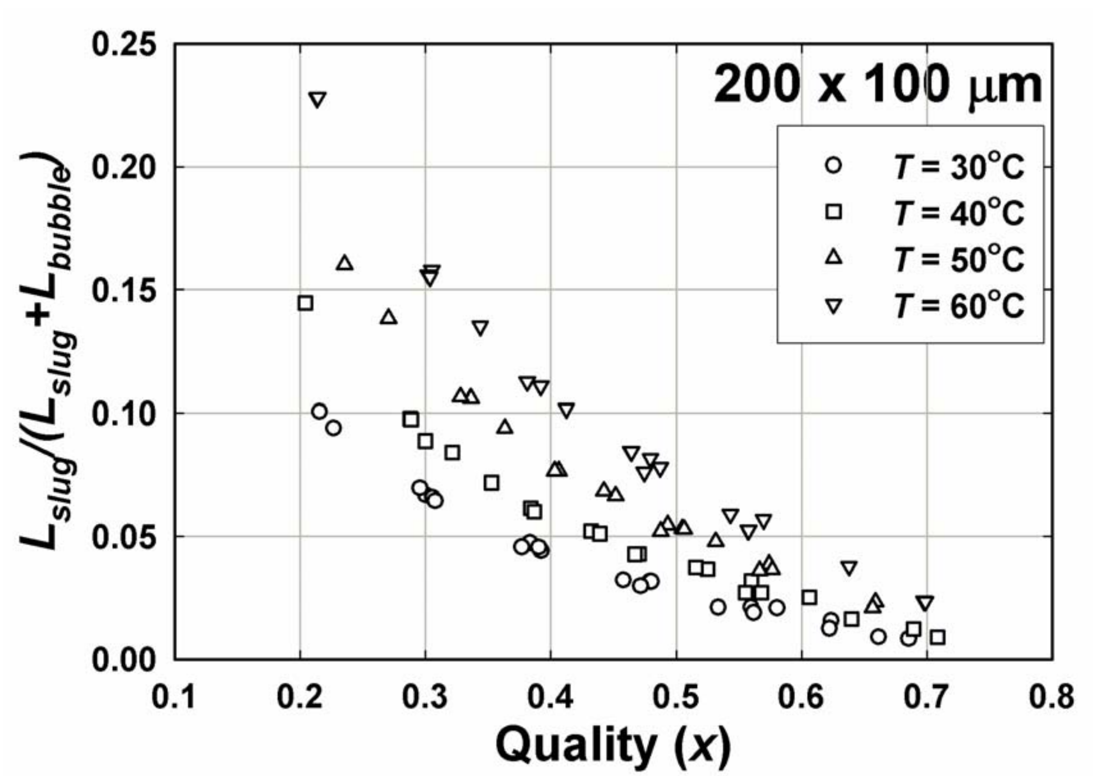

Figure 6.14: Variation of Slug Length Ratio with Quality for 200×100 μm Tubes

From the above discussion, we can conclude that as the quality increases, the number of unit cells decreases and the slug length ratio decreases, leading to annular flow. Similarly, as the refrigerant saturation temperature increases, the number of unit cells and the *s*lug length ratio increase, leading to a predominance of intermittent flow.

The probability of observing annular or intermitten flow in these channels is discussed here. Consider visualization of flow in a 10-mm long section of a 40-mm long tube. If the length of the slug is less than 5% (as in the case of approximately 50% of the points in the current study), the flow observed will predominantly be the film/bubble section of the unit cells. Also, from the discussion above, for cases where the slug length ratio is small, the number of unit cells is also small. Thus, the probability of observing slug flow in the observation section is very low, and the flow will appear to be primarily annular. Several researchers (Kawahara *et al.*, 2002; Serizawa *et al.*, 2002) have observed patterns such as annular ring flow or liquid ring flow during flow visualization studies in microchannels. It is possible that intermittent flow with a negligible slug length ratio (as observed at high vapor qualities) will appear similar to annular ring flow. Similarly at lower qualities, where the slug length ratios are larger (greater than 10% of unit cell length), the number of unit cells are also large and hence the probability of observing slug flow is greater as slugs of longer length pass by the observation location at higher frequencies.

Based on the above discussion, it can be concluded that the probability of observing annular flow is inversely proportional to the number of unit cells and the slug length ratio. An annular flow factor (*AFF*) may be definined as follows:

$$AFF = \sqrt{\left(1 - \frac{l_{slug}}{l_{slug} + l_{bubble}}\right) \cdot \frac{1}{N_{UC}}} \tag{6.35}$$

Thus, Annular Flow Factor (*AFF*) quantifies the predominance of annular flow in the channels: the probability of occurrence of annular flow is higher for larger values of *AFF*.

In equation (6.35), the *SLR* $\left(\frac{l_{slug}}{l_{slug}+l_{bubble}}\right)$ varies from 0 to 1, i.e. $\left(1-\frac{l_{slug}}{l_{slug}+l_{bubble}}\right)$ varies from 1 to 0. $\left(1-\frac{l_{slug}}{l_{slug}+l_{bubble}}\right)$ is 1 when the entire unit cell is occupied by the bubble and 0 when the entire unit cell is occupied by the slug. N_{UC} varies from 1 to $+\infty$, i.e., $\frac{1}{N_{UC}}$ varies from 1 to zero. $\frac{1}{N_{UC}}$ = 1 when there is only one unit cell in the whole tube and 0 when there are infinite number of unit cells. Thus, for fully annular flow, $\left(1-\frac{l_{slug}}{l_{slug}+l_{bubble}}\right)$ = 1 and $\frac{1}{N_{UC}}$=1, which results in *AFF* = 1 and for fully slug flow, $\left(1-\frac{l_{slug}}{l_{slug}+l_{bubble}}\right)$ = 0 and $\frac{1}{N_{UC}}$ = 0, which results in *AFF* = 0. Figure 6.15 shows sample schematics of various possible flow conditions and the corresponding *AFF* for each of them. Figure 6.16 shows constant *AFF* lines for a sample case (D = 130 μm, AR = 3, G = 600 kg/m^2-s; T = 40°C and $T - T_{wall}$ = 2°C). These trends are similar to those observed by Coleman and Garimella (1999; 2003) in their flow visualization studies on channels with $1 < D_h < 4.91$ mm. As the quality and mass flux increase, the probability of observing annular flow increases.

Figures 6.17 to 6.20 show plots of the annular flow factor (*AFF*) for the data for each of the tubes tested in this study. It can be seen that AFF increases with quality and mass flux. For the same the mass flux and quality, the probability of observing annular flow is higher at the lower saturation temperatures. This is due to the decrease in vapor-to-liquid density ratio as the saturation temperature decreases.

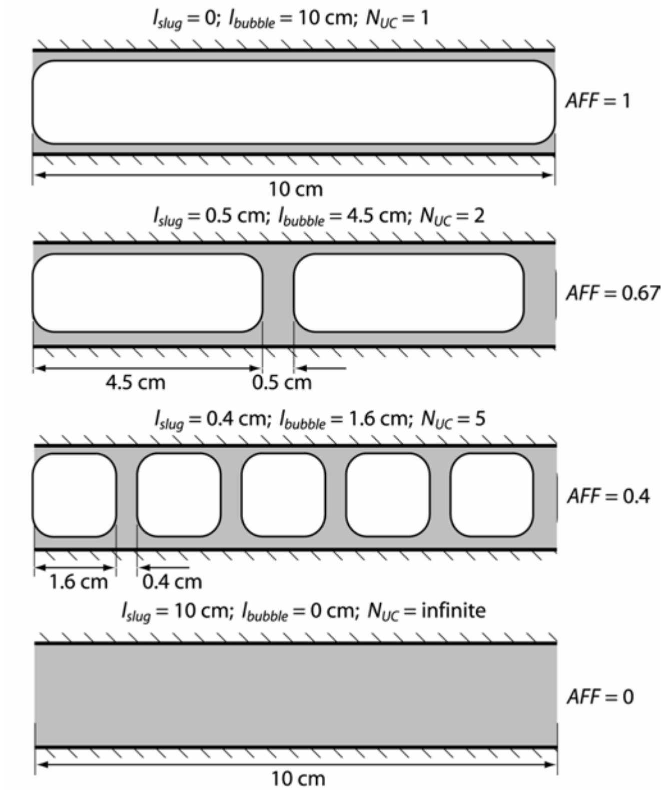

Figure 6.15: Annular Flow Factor Schematic

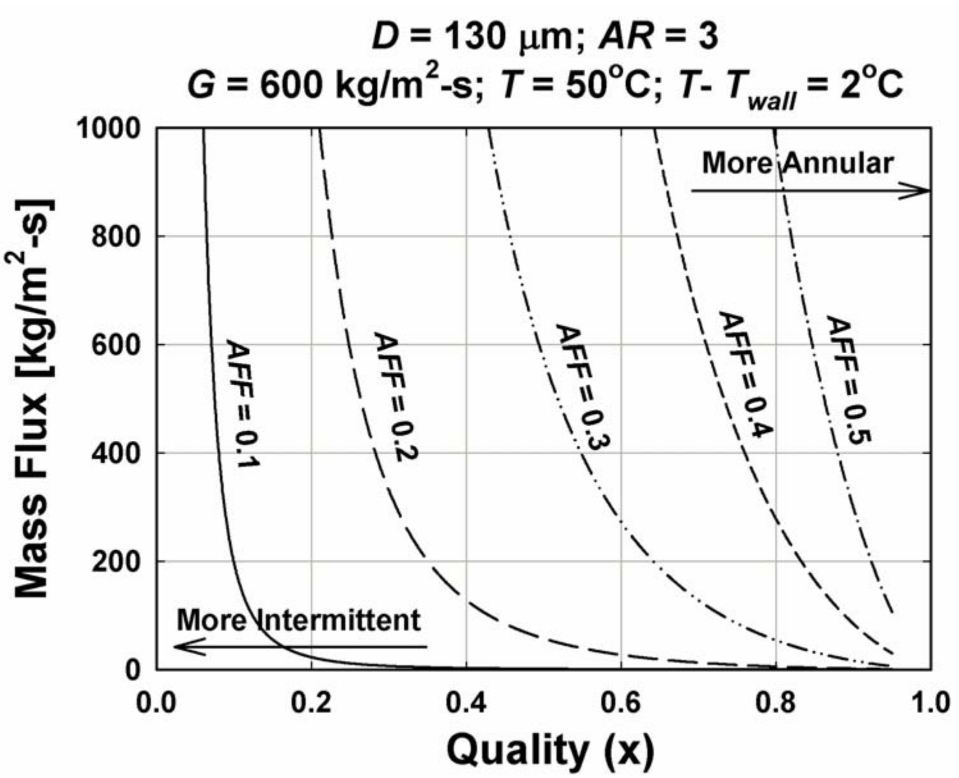

Figure 6.16: Constant AFF Lines for a Sample Flow Condition

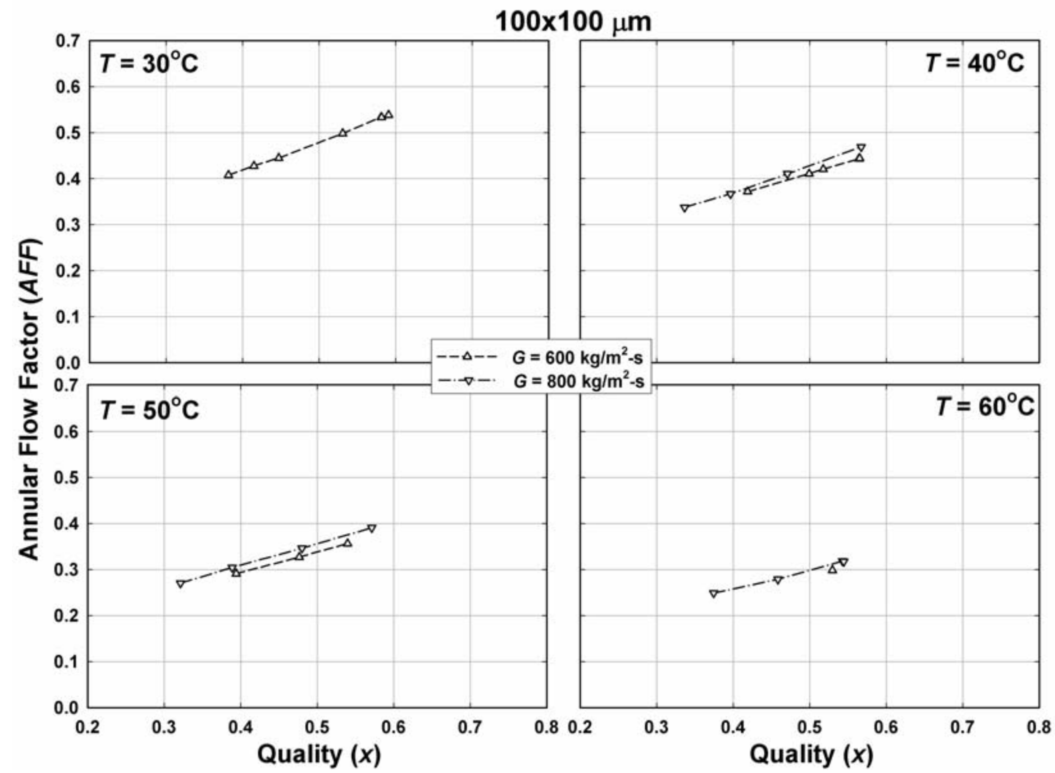

Figure 6.17: Annular Flow Factor for 100×100 μm Channels

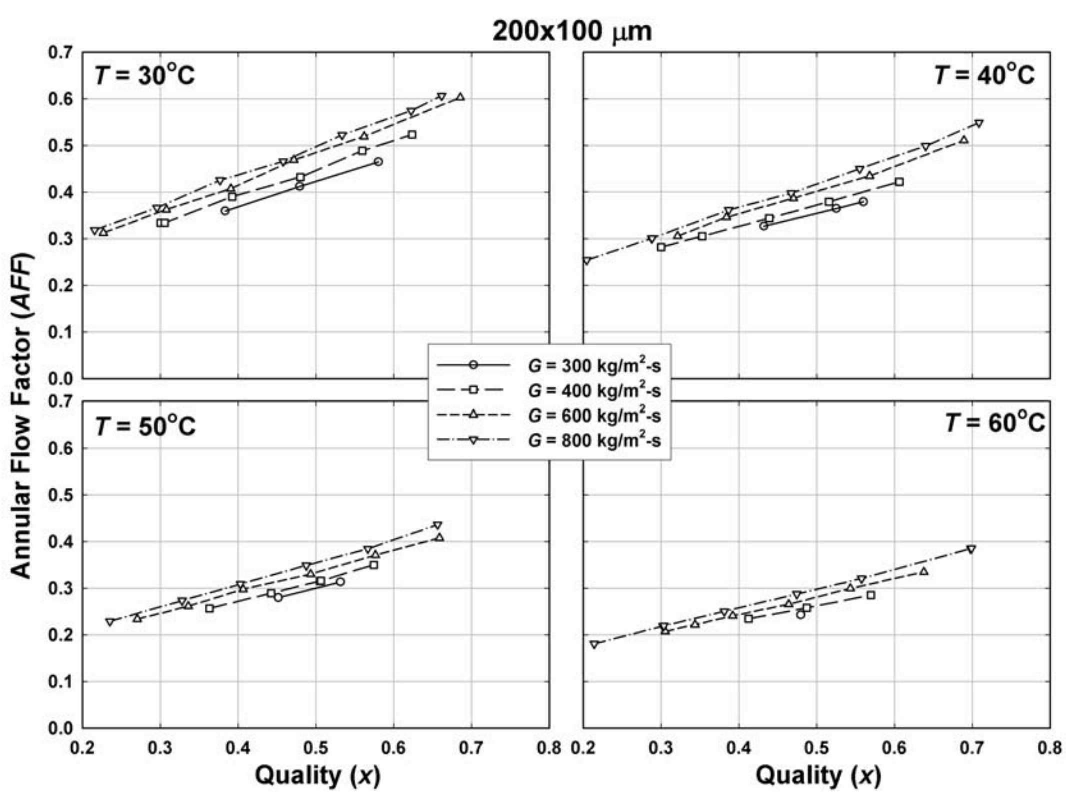

Figure 6.18: Annular Flow Factor for 200×100 μm Channels

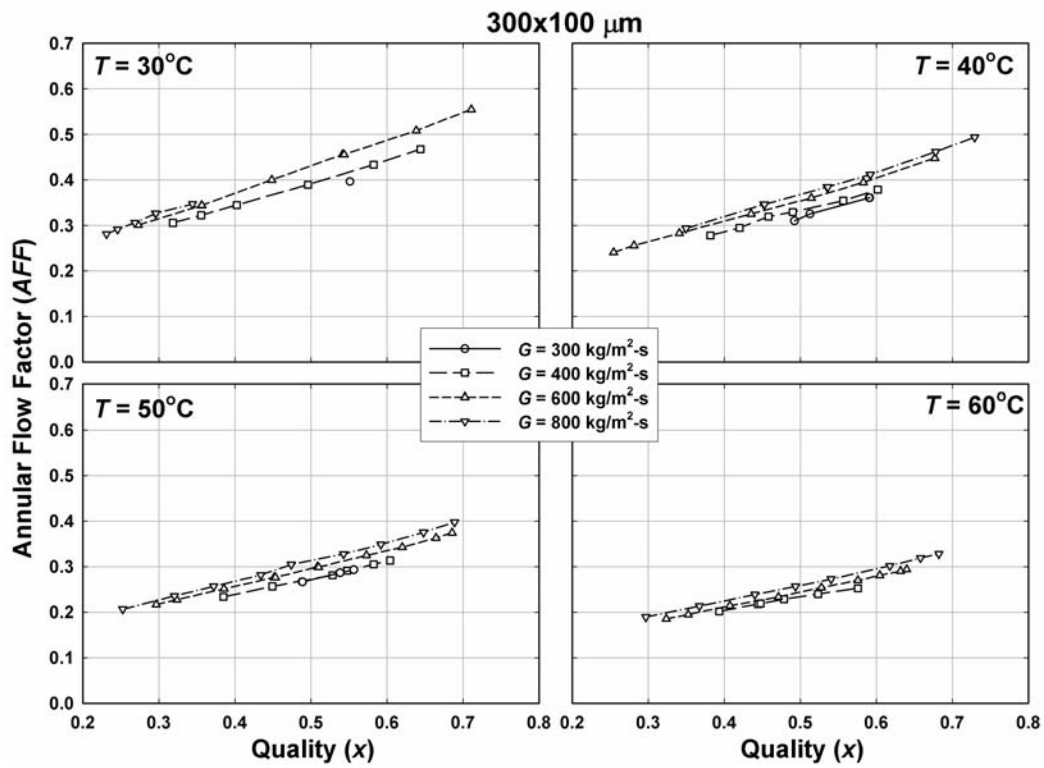

Figure 6.19: Annular Flow Factor for 300×100 μm Channels

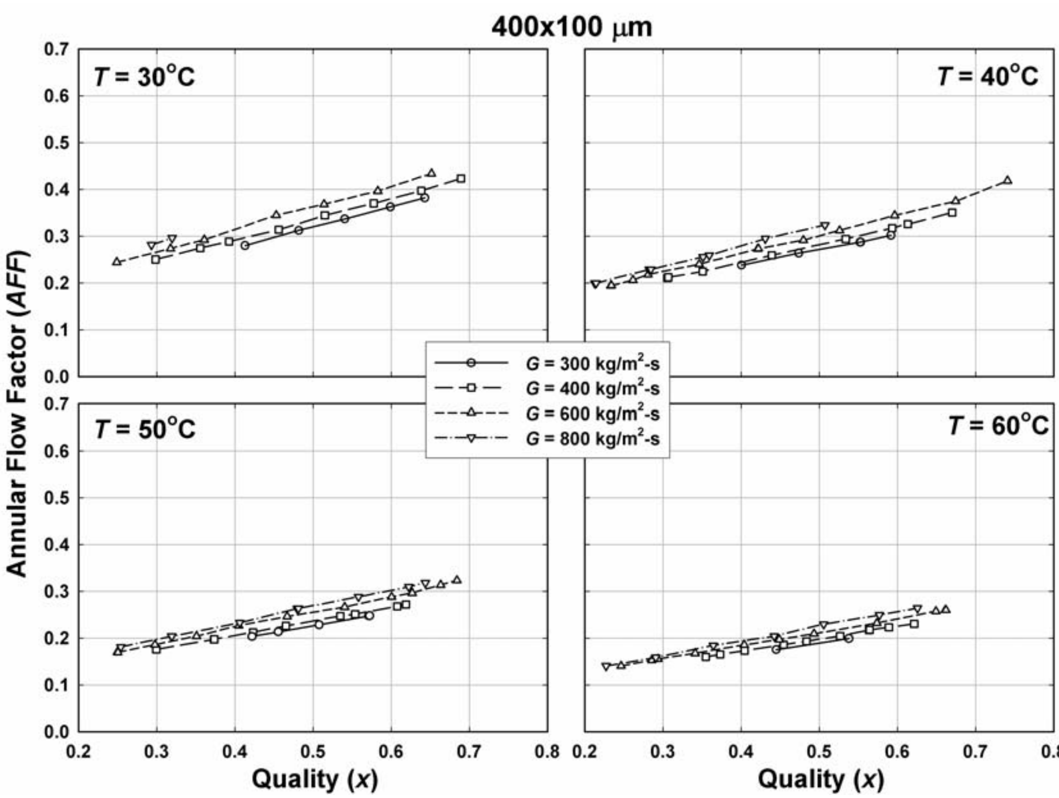

Figure 6.20: Annular Flow Factor for 400×100 μm Channels

Based on the above plots, the *AFF* also appears to depend on the channel aspect ratio. As the aspect ratio (*AR*) increases, the probability for observing annular flow decreases. This is probably due to the instability of the annular liquid film in large aspect ratio channels. The probability of observing annular flow in square channels is larger compared to the corresponding probability in larger aspect ratio channels, perhaps due to a more stable annular liquid film in square channels.

6.4. Heat Transfer Model

During the condensation process, depending on the rate of condensation, as we go downstream along the length of the tube, the vapor quality of the refrigerant decreases. For example, if the fluid enters the tube at a vapor quality of 0.8, then after undergoing condensation in the tube, it exits at the vapor quality of 0.5. As we go downstream along the length of tube, the size of vapor bubbles decreases due to vapor condensation and the size of the slug increases, leading to an overall decrease in the length of the unit cell. According to the proposed pressure drop model discussed above, the number of unit cells per unit length increases as the quality decreases and the slug length ratio increases. At a fixed location along the length of tube, the process proceeds as follows: first a liquid slug passes (without any entrained vapor), leaving behind a thin film of liquid, and then an elongated bubble with a uniform liquid film along its circumference passes. The liquid film around the bubble is formed by the initial film left by the passing slug and the condensing vapor. The process continues upon arrival of the next slug.

Figure 6.21 shows a schematic of the condensation process. As in the case of the pressure drop model, the heat transfer model is also composed of models for the slug section and the film/bubble section. The slug region is treated as single-phase liquid flow, while for the film/bubble section, a condensation heat transfer model is developed. The flow velocities (U_{bubble} and U_{slug}), and the average film thickness (δ_{ave}), are known from the pressure drop model discussed above. The film/bubble section heat transfer coefficient is referred to as the film heat transfer coefficient (h_f) in this section. For heat transfer analysis, it is assumed that h_s and h_f do not vary along the length of slug (l_{slug}) or within the bubble section (l_{bubble}) in a unit cell, respectively.

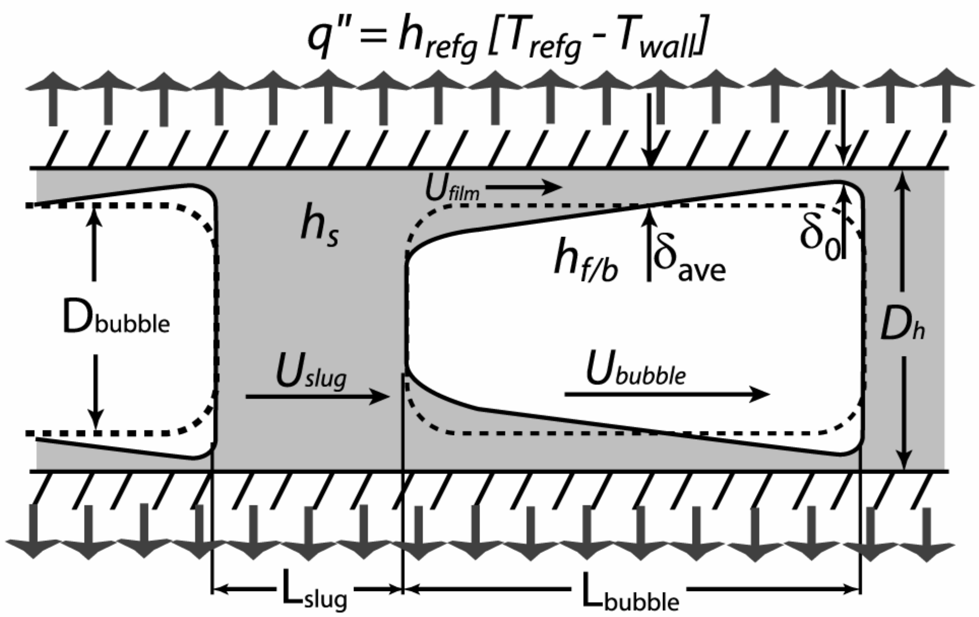

Figure 6.21: Schematic of Condensation Process in Channels

Analysis of the data yields the time-averaged effective refrigerant-side heat transfer coefficient (h_{refg}) as a function of slug and film heat transfer coefficients. The heat flux could vary with time as the slug or the bubble passes by, but the overall average heat flux may be calculated using the time-averaged refrigerant-side heat transfer coefficient. It is assumed that the liquid in the slug or the film is not subcooled; thus, both liquid and vapor are assumed to be at the refrigerant saturation temperature.

The slug Reynolds number (Re_{slug}) for the data under consideration ranges from 2194 to 12187. Churchill (1977a) proposed the following correlation for the determination of Nusselt number (Nu) which is valid for the laminar, transition and turbulent regions:

$$Nu^{10} = Nu_l^{10} + \left[\frac{e^{(2200-\mathrm{Re})/365}}{Nu_{lc}^{\,2}} + \left(Nu_0 + \frac{0.079 \cdot \mathrm{Re} \cdot \sqrt{\dfrac{f}{8}} \cdot \mathrm{Pr}}{\left(1+\mathrm{Pr}^{4/5}\right)^{5/6}} \right)^{-2} \right]^{-5} \tag{6.36}$$

where, Nu_l is the laminar Nusselt number, Nu_{lc} is the laminar Nusselt number at a critical Reynolds number of 2100 where the transition region begins and Nu_0 is the asymptotic value of the laminar Nusselt number as $Pr \rightarrow 0$ and $Re \rightarrow 2100$. Churchill (1977a) suggested that for the uniform heat flux case, $Nu_0 = 6.3$. Shah and Bhatti (1987) recommended that for uniform wall heat flux during laminar flow in rectangular channels, the following correlation based on aspect ratio should be used:

$$Nu_l = 8.235 \left(\begin{aligned} 1 - 2.0421 \cdot \left(\frac{1}{AR}\right) + 3.0853 \cdot \left(\frac{1}{AR}\right)^2 - 2.4765 \cdot \left(\frac{1}{AR}\right)^3 \\ + 1.5078 \cdot \left(\frac{1}{AR}\right)^4 - 0.1861 \cdot \left(\frac{1}{AR}\right)^5 \end{aligned} \right) \tag{6.37}$$

The above correlation is used to determine the laminar Nusselt number based on the hydraulic diameter, and since in laminar region Nu_l remains constant, $Nu_{lc} = Nu_l$. For turbulent Reynolds numbers, Bhatti and Shah (1987) recommended that the circular tube correlation can also be used for the rectangular channels with *Nu* and *Re* defined on the basis of hydraulic diameter. Thus, the Nusselt number (*Nu*) of the slug at any Reynolds number can be determined using equation (6.37). The slug heat transfer coefficient is calculated as follows:

$$h_s = Nu_s \cdot \frac{k_l}{D} \tag{6.38}$$

For the determination of the film heat transfer coefficient, consider the bubble section shown in Figure 6.21. The pressure drop model assumed a uniform film thickness in the film/bubble section as shown by the dashed line in Figure 6.21 and determined an average film thickness (δ_{ave}). As the slug passes by, it leaves a thin liquid film behind, and along the length of the elongated bubble, the film thickness increases due to the condensation process. Consider a small section of length *dz* along the length of the bubble. Now, *dt* is the time taken by this section to pass through a particular point and $d\delta$ is the increase in film thickness during this time. Assuming the heat flux to be $q''_{f/b}$ and equating the amount of heat going out of the tube to the latent heat of evaporation of additional condensed liquid film thickness, we get:

$$q''_{f/b} \cdot 2\pi R \cdot dz \cdot dt = \rho_L \cdot 2\pi \left(R - \delta\right) \cdot d\delta \cdot dz \cdot h_{fg} \tag{6.39}$$

The above equation can be rearranged to obtain the variation in film thickness with time as follows:

$$\Rightarrow d\delta = \frac{q''_{f/b}}{\rho_L \cdot h_{fg}} \frac{R}{\left(R - \delta\right)} \cdot dt \tag{6.40}$$

Assuming that the film thickness is much smaller than the tube radius, i.e. $(R-\delta) \approx R$, and integrating the above equation, we get:

$$\int_{\delta_0}^{\delta} d\delta = \int_{0}^{t} \frac{q''_{f/b}}{\rho_L \cdot h_{fg}} \cdot dt \tag{6.41}$$

$$\Rightarrow \delta = \delta_0 + \frac{q''_{f/b}}{\rho_L \cdot h_{fg}} \cdot t \tag{6.42}$$

Based on the flow model discussed in the previous section, the time $t = \frac{z}{U_{Bubble}}$, where z is the distance along the bubble length from the beginning of the bubble where the film thickness is a minimum.

$$\Rightarrow \delta = \delta_0 + \frac{q''_{f/b}}{\rho_L \cdot h_{fg}} \cdot \frac{z}{U_{bubble}} \tag{6.43}$$

Also, the heat flux in the film/bubble section $q''_{f/b} = h_f\left(T - T_{wall}\right)$, which when substituted in the above equation yields:

$$\Rightarrow \delta = \delta_0 + \frac{h_f\left(T - T_{wall}\right)}{\rho_L \cdot h_{fg}} \cdot \frac{z}{U_{bubble}} \tag{6.44}$$

The above equation provides the film thickness as a function of distance from the nose of bubble. Integrating the above equation over the length of the bubble, l_B, we get the average film thickness as follows:

$$\delta_{ave} = \frac{1}{l_B} \int_{0}^{l_B} \delta \cdot dz \tag{6.45}$$

Additional details are provided in Appendix D.4. The average film thickness can therefore be written as follows:

$$\Rightarrow \delta_{ave} = \delta_0 + \frac{h_f\left(T - T_{wall}\right)}{\rho_L \cdot h_{fg}} \cdot \frac{l_B}{2 \cdot U_{bubble}} \tag{6.46}$$

Rearranging the terms in the above equation, we get the following relation for the film heat transfer coefficient:

$$h_f = \left(\delta_{ave} - \delta_0\right) \cdot \frac{2 \cdot \rho_L \cdot h_{fg} \cdot U_{bubble}}{\left(T - T_{wall}\right) \cdot l_B} \tag{6.47}$$

All the parameters on the right hand side of the above equation are known, except the minimum film thickness (δ_0). Based on the above equation, higher heat transfer coefficients are expected at lower saturation temperatures due to the higher latent heat of vaporization (h_{fg}) at lower saturation temperatures. Similarly, at higher mass fluxes, the heat transfer coefficients are expected to be higher due to increased bubble velocities (U_{bubble}). The effect of aspect ratio is accounted for through the length of bubble, l_B. For higher aspect ratio channels, the numbers of unit cells are higher, leading to lower bubble lengths, which in turn would yield higher heat transfer coefficient. (It should be noted that N_{UC} is the total number of unit cells in a fixed length of tube, so as the N_{UC} increases, the same tube length is divided into more number of segments, thus leading to correspondingly lower slug and bubble lengths.) These trends were also observed in the experimentally obtained refrigerant heat transfer coefficients that were discussed in the previous chapter.

Since both the slug and the bubble are moving with the same apparent velocity U_{Bubble}, the time taken by the film/bubble section to pass by (t_f) and the time taken by the slug to pass by (t_s) are proportional to their lengths.

$$t_f = \frac{l_{bubble}}{U_{Bubble}} \tag{6.48}$$

$$t_s = \frac{l_{slug}}{U_{Bubble}} \tag{6.49}$$

The time-averaged refrigerant heat transfer coefficient can thus be determined by averaging the two heat transfer coefficients weighted by the time taken by the slug and bubble to pass by as shown in equation (6.51).

$$h_{refg}\left(t_f + t_s\right) = h_{slug} \cdot t_s + h_{film} \cdot t_f \tag{6.50}$$

Substituting t_f and t_s from equations (6.49) and (6.50) yields:

$$h_{refg} = h_{slug} \cdot \left(\frac{l_{slug}}{l_{slug} + l_{bubble}} \right) + h_{film} \cdot \left(1 - \frac{l_{slug}}{l_{slug} + l_{bubble}} \right) \tag{6.51}$$

Sun *et al.* (2004) also used a similar approach to determine the effective refrigerant-side heat transfer coefficients in intermittent flow. By determining the time-averaged refrigerant-side heat transfer coefficient in the above manner, transient effects due to the periodically varying convective boundary condition (due to the changing heat transfer coefficient) on the refrigerant side were neglected. This assumption will be justified in the next sub-section.

In the analysis presented above, the only remaining unknown is the minimum film thickness (δ_0), which is required to determine the film heat transfer coefficient, h_f. The data are used to obtain the values of minimum film thickness (δ_0). Substituting the experimental refrigerant heat transfer coefficient (h_{refg}) and the slug heat transfer coefficient (h_s) into equation (6.51), the film heat transfer coefficient, h_f can be obtained. The slug length ratio $\left(\dfrac{l_{slug}}{l_{slug}+l_{bubble}}\right)$ is known from the flow model presented above and h_s is determined using (6.38). These film heat transfer coefficient (h_f) values are then substituted into equation (6.47) to determine the minimum film thickness (δ_0). All other parameters (δ_{ave}, ρ_L, h_{fg}, U_{bubble}, l_B, T, T_{wall}) are known from the pressure drop model and data analysis. Figure 6.22 shows the variation of the ratio of minimum film thickness and the average film thickness for the data obtained in the current study.

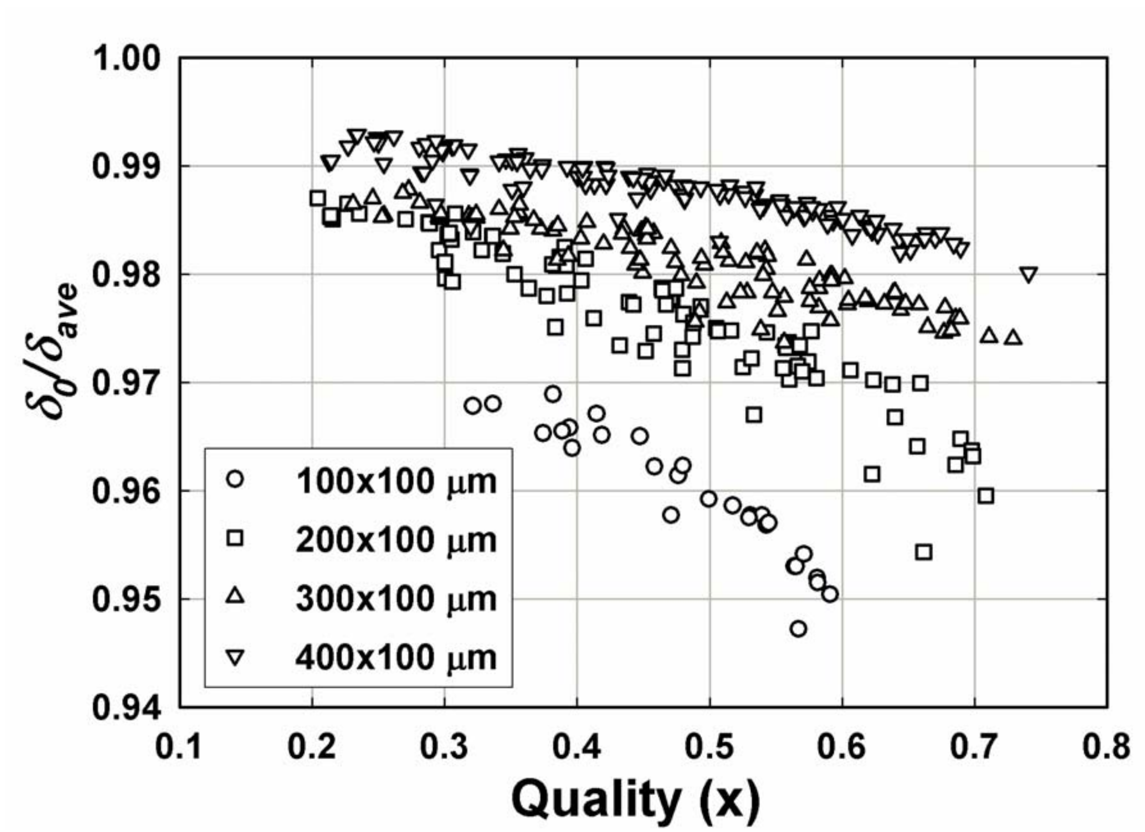

Figure 6.22: Variation of δ_0/δ_{ave} with Quality

As the quality increases and the diameter decreases, the δ_0/δ_{ave} decreases. For all the data points, the film thickness is 4.4 to 4.6% of the channel diameter. As the tube diameter increases, the film thickness increases leading to increased thermal resistance, i.e. decrease in heat transfer coefficients. This decrease in heat transfer coefficients leads to lower condensation rates and hence the difference between the average and minimum film thickness decreases. As the quality increases, the slug length ratio decreases, leading to a decrease in the thickness of the film that it leaves behind. As the diameter increases, the effect of a change in diameter diminishes and the change in δ_0/δ_{ave} with quality decreases. Based on this trend, beyond a certain diameter, an increase in diameter will no longer affect the film thickness ratio. Based on the above observations, the following correlation is proposed for determining δ_0/δ_{ave}:

$$\frac{\delta_0}{\delta_{ave}} = 1 - 0.25 \cdot e^{\left(-2.82 \cdot \frac{D}{D_{ref}}\right)} \cdot \left(\frac{x}{1-x}\right)^{0.424} \tag{6.52}$$

where D_{ref} is the maximum diameter channel investigated here, (D_{ref} = 160 μm). In the above correlation, the first term on the right hand side, is a constant 1, which implies that for a quality of zero, the minimum film thickness and the maximum film thickness are the same and there in no condensation taking place. The second term captures the dependence on quality and diameter. The dependence on diameter was explained above. The dependence on quality is observed because a higher vapor quality implies that there is less amount of fluid in the slug and hence as the slug passes by, it leaves a thinner liquid film behind. Figure 6.23 shows the experimental minimum-to-average film thickenss ratio and those predicted by the above model. Appendix D.7 provides the detailed step-by-step implementation of the above heat transfer model.

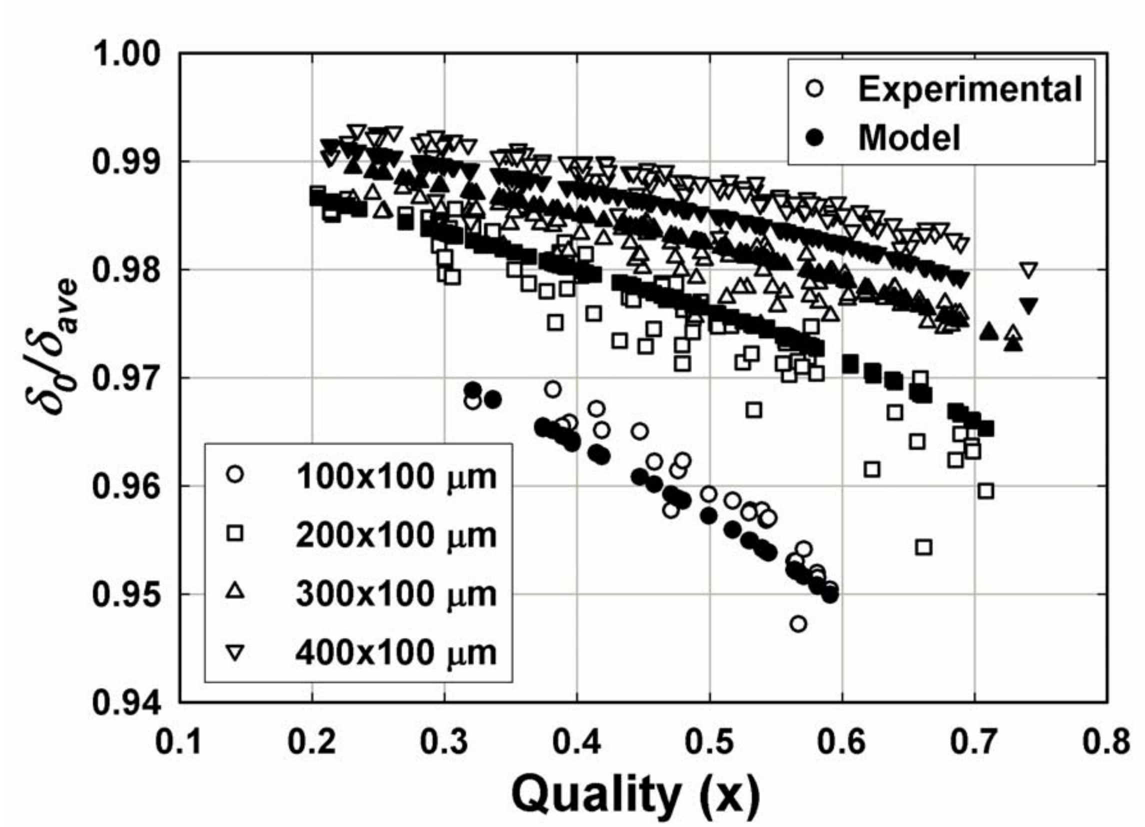

Figure 6.23: Experimental δ_0/δ_{ave} and Model Predictions

Figure 6.24 shows a comparison of the heat transfer coefficients predicted by the above heat transfer model and the experimentally determined values. The proposed heat transfer model predicts refrigerant heat transfer coefficients for 94% of the data within ±25% of the experimental values.

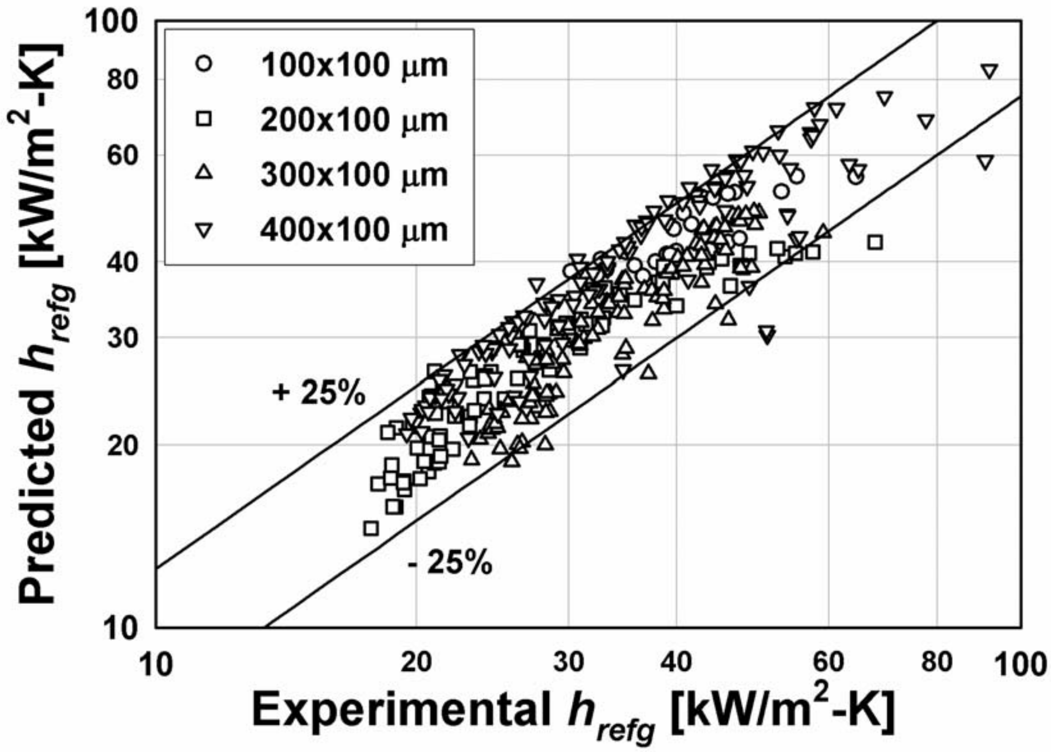

Figure 6.24: Comparison of Experimental and Predicted h_{refg}

Figures 6.25 to 6.28 show the data and the predicted heat transfer coefficients for each of the channels individually. The proposed model is able to capture the trends observed in the experimental data well. The average absolute deviations for the 100×100 μm, 200×100 μm, 300×100 μm and 400×100 μm tubes are 5%, 8%, 9% and 18% respectively, with an overall average absolute deviation of 11%. A discussion of the effect of diameter, aspect ratio, mass flux and temperature on the predicted pressure drops and heat transfer coefficients is presented in a subsequent section.

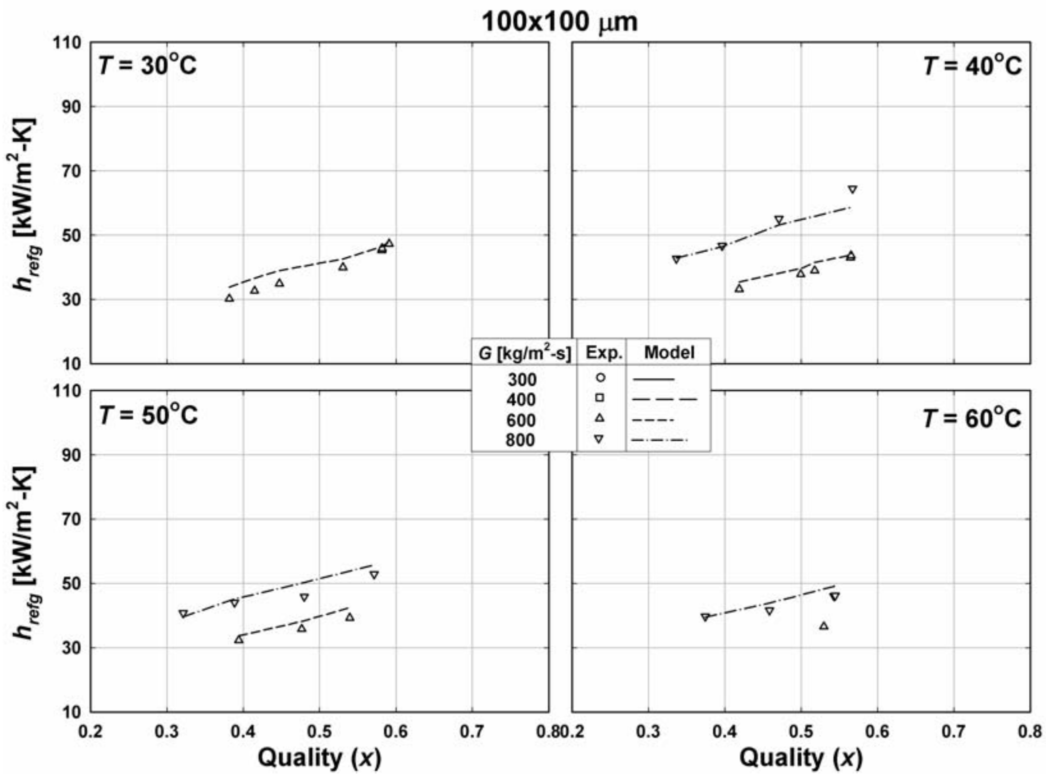

Figure 6.25: Experimental and Predicted h_{refg} for 100×100 μm Channels

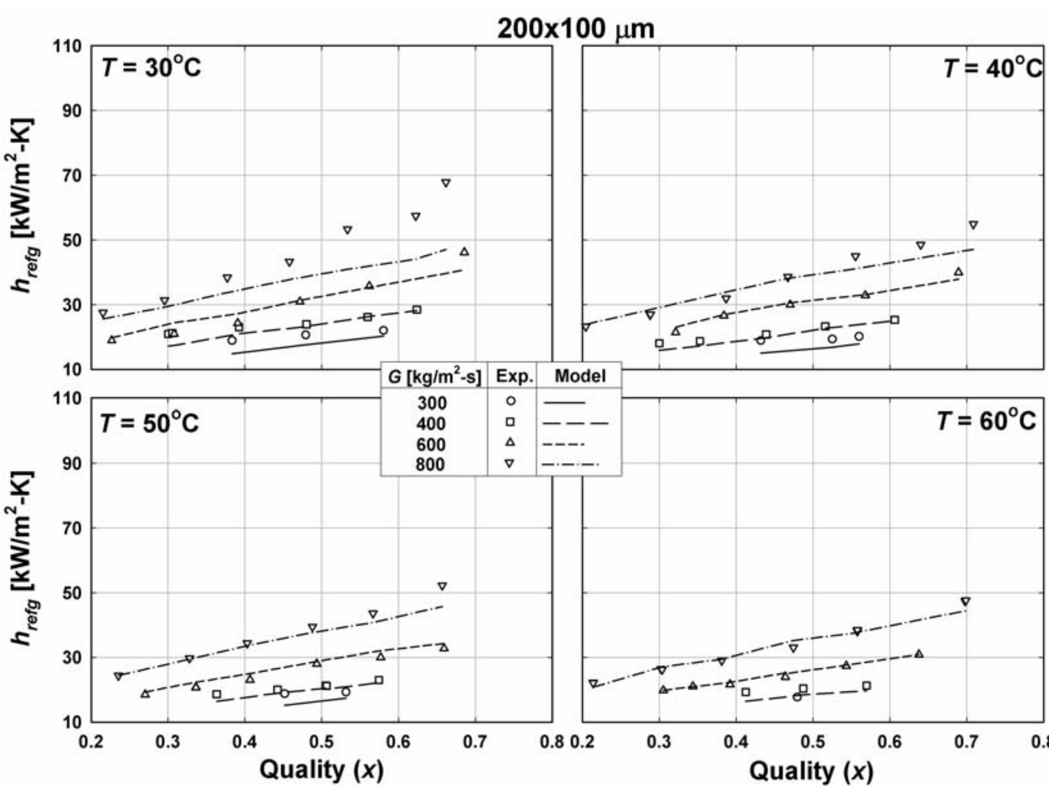

Figure 6.26: Experimental and Predicted h_{refg} for 200×100 μm Channels

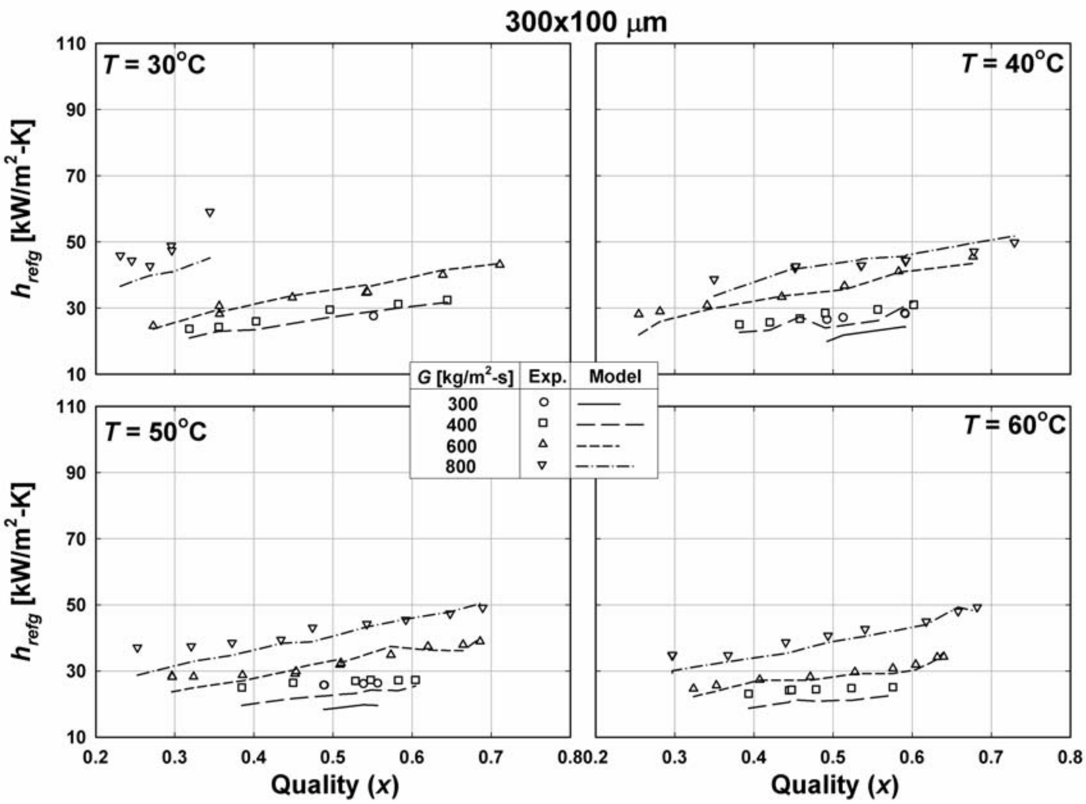

Figure 6.27: Experimental and Predicted h_{refg} for 300×100 μm Channels

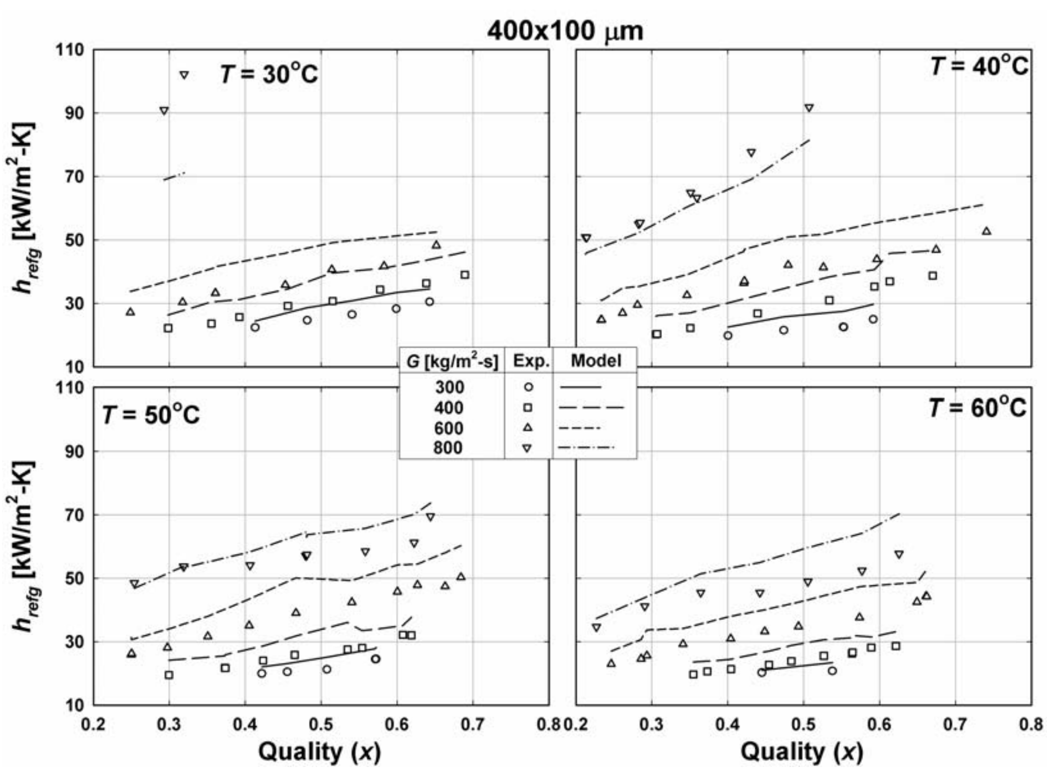

Figure 6.28: Experimental and Predicted h_{refg} for 400×100 μm Channels

6.4.1. Transient Analysis

In the above analysis for determining the effective refrigerant-side heat transfer coefficient, the transient effects due to the periodically varying refrigerant-side heat transfer coefficient were neglected. To verify this assumption, a one-dimensional transient analysis was conducted with a periodically varying convection condition on one side and a constant heat flux boundary condition on the other side as shown in Figure 6.29. In Figure 6.29, $T_X = \frac{\partial T}{\partial x}$ and $T_{XX} = \frac{\partial^2 T}{\partial x^2}$. Appendix D.5 provides the detailed procedure for solving this transient problem.

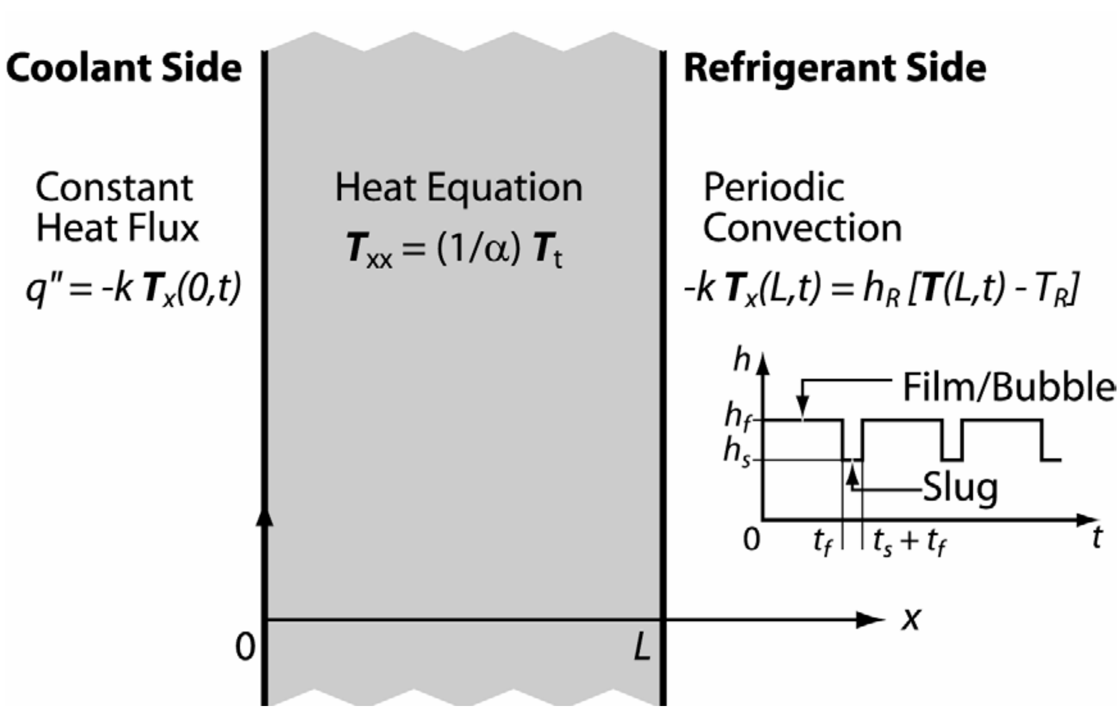

Figure 6.29: Schematic for Wall Transient Problem with Periodic Convection

The temperature profile in the wall is thus given by equation (6.51):

$$T(x,t)=\begin{cases} T_f(x,t) & 0<t<t_f \\ T_s(x,t-t_f) & t_f<t<(t_f+t_s) \end{cases} \tag{6.53}$$

where, $$T_f(x,t)=T_R+q''\left[\frac{1}{k}(L-x)+\frac{1}{h_f}\right]+\sum_{n=1}^{\infty}B_{f,n}\cdot\cos(\lambda_{f,n}x)\cdot\exp(-\lambda_{f,n}^{2}\cdot\alpha\cdot t) \tag{6.54}$$

$$T_s(x,t)=T_R+q''\left[\frac{1}{k}(L-x)+\frac{1}{h_s}\right]+\sum_{n=1}^{\infty}B_{s,n}\cdot\cos(\lambda_{s,n}x)\cdot\exp(-\lambda_{s,n}^{2}\cdot\alpha\cdot t) \tag{6.55}$$

The experimentally obtained refrigerant-side heat transfer coefficients and the theoretically calculated slug heat transfer coefficients are used to obtain values for the film heat transfer coefficient. The thickness of the wall (*L*) was assumed to be equal to 1 mm. In transient analysis, over one complete cycle, the refrigerant-side wall temperature will vary, but the average refrigerant-side wall temperature was assumed to be equal to the wall temperatures determined in the data analysis. The effective film heat transfer coefficient, h_f, determined using the results from this transient analysis were within 1% deviation of the h_f determined using equation (6.49) for 89% of the data, with a maximum deviation of 2.5% for all the data points. Thus the assumption of neglecting the transient effects in the wall and using a simple weighted average of the slug and film/bubble heat transfer coefficients is justified.

Figure 6.30 shows a plot for the wall temperature profile for the same representative case as that used in describing data analysis, i.e 200 x 100 µm, channel (18 channels in parallel) with G = 606 kg/m^2-s, T_{sat} = 60.5°C and x_{ave} = 0.39. For this case, the experimental refrigerant-side heat transfer coefficient (h_{refg}) is 21.7 kW/m^2-K and the refrigerant-side average wall temperature is 58.1°C. The lengths of the bubble and slug are 1.96 and 0.24 mm, respectively. Slug (h_s) and film (h_f) heat transfer coefficients are determined to be 9.2 and 23.2 kW/m^2-K respectively. With a bubble velocity (U_{bubble}) of 3.7 m/s, the time taken by the bubble (t_f) and slug (t_s) to pass a particular point are 535 and 66 μs, respectively. In Figure 6.30, the refrigerant side is shown towards the front (L = 1mm) and the constant heat flux side is shown towards the back (L = 0 mm). Only one time cycle is shown, where from time 0 to t_f, the bubble passes by and from time t_f to (t_f + t_s), the slug passes by.

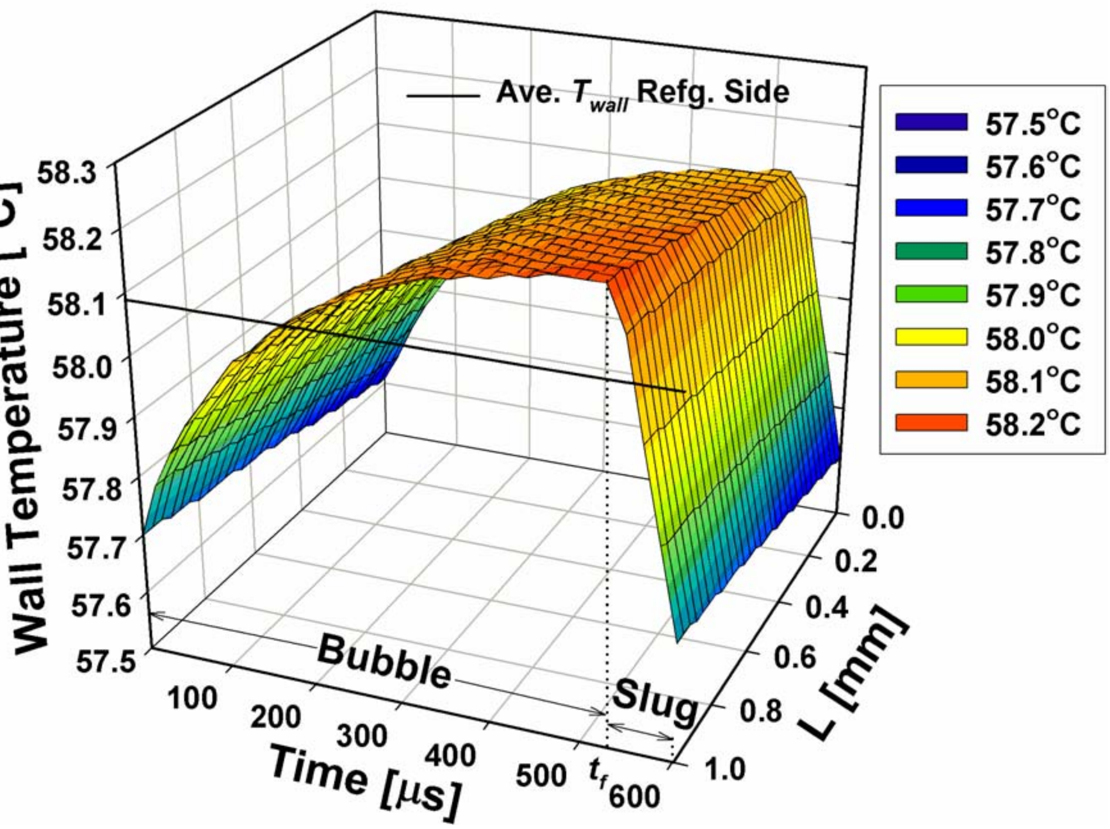

Figure 6.30: Temperature Profile in Wall for Representative Case

The temperature variation along the thickness of the wall is more or less linear due to low Biot numbers (hL/k). For all cases in the current study, the Biot Number was less than 0.3. Since, the film heat transfer coefficients are higher than the slug heat transfer coefficients and heat flux at the other end is assumed to be constant, during the time when bubble passes, more heat is transferred to the wall due to which the temperature of the wall rises and as the slug passes, the wall temperature again rapidly drops. This can be explained further as follows. The rate at which heat is flowing out of the wall to the coolant is fixed due to the constant flux boundary condition on the coolant side. But, the rate at which the heat enters the wall from the refrigerant side is higher when the heat transfer coefficient is higher. Thus, when the bubble passes more heat is transferred into the wall leading to a rise in temperature of the wall due to thermal storage. During the slug phase, the rate of heat transfer into the wall is much less, hence the stored thermal energy in the wall decreases, leading to a decrease in the wall temperature.

Figure 6.31 shows the variation in wall temperature profile with time at various depths (for the same representative case discussed above) and further compares these variations with the overall temperature difference between the refrigerant side and the coolant side. These two plots together show that while the above analysis captures the temperature variations in the wall with time, they are insignificant compared to the overall driving temperature difference between the refrigerant and the coolant. This further justifies the approach of neglecting the transient effects for the determineation of the average refrigerant heat transfer coeffecient.

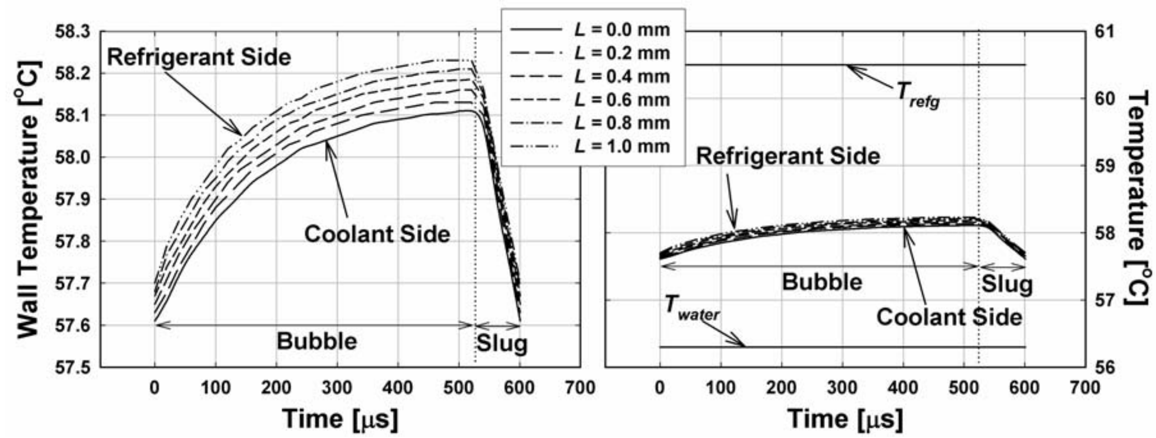

Figure 6.31: Variation in Wall Temperature with Time at Various Depths

Due to the added complexity of the transient analysis without an appreciable difference in the heat transfer coefficients from the simple weighted average approach, the transient effects were neglected.

6.5. Parametric Evaluation and Interpretation

In this section, the flow, pressure drop, and heat transfer models are used to illustrate the effects of various parameters such as hydraulic diameter, aspect ratio, mass flux and temperature. Only one parameter is varied at a time and interpretations for the resulting trends are presented.

Figure 6.32 shows the effect of variation of mass flux for a particular case (D = 130 μm, AR = 3, T = 50°C, T-T_{wall} = 2°C and L/D = 250). The mass flux is varied from 200 to 800 kg/m^2-s.

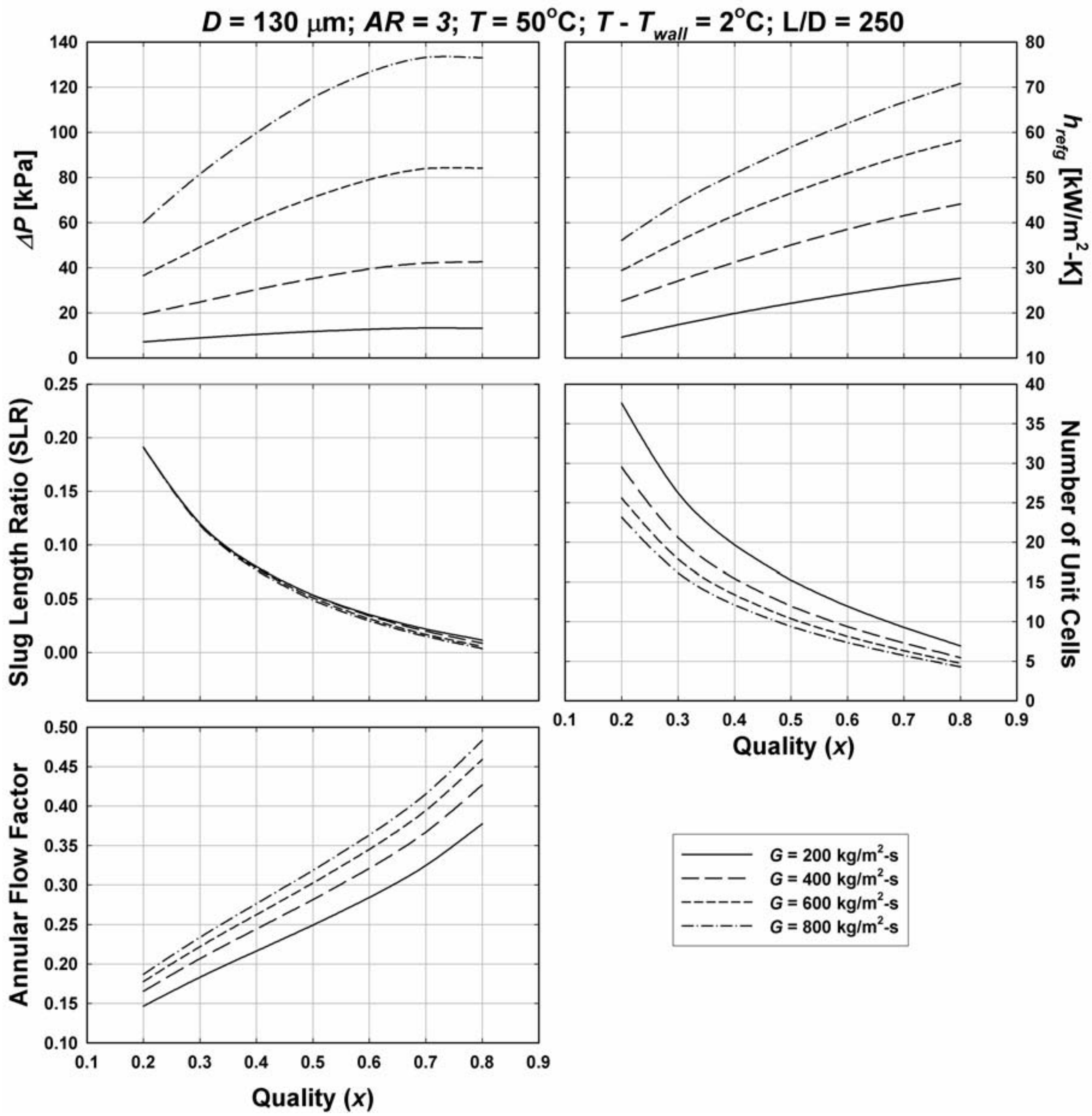

Figure 6.32: Model Predictions: Effect of Mass Flux and Quality

As the mass flux increases, the pressure drop increases due to the increase in the flow velocities. The slug length ratio (*SLR*) shows very little dependence on mass flux, while the number of unit cells decreases with the increasing mass flux, thus yielding a higher annular flow factor at the higher mass fluxes (as shown in the corresponding plot). The probability of observing annular flow at higher qualities is larger at all mass fluxes as the number of unit cells and the slug length ratio decreases with increasing quality. The heat transfer coefficient increases with increasing mass flux due to an increase in the Reynolds number.

Both the pressure drop and the heat transfer coefficient in general increase with increasing quality. The increase in pressure drop with quality plateaus around a quality of 0.7 to 0.8. This trend is similar to that observed by Garimella *et al.* (2005) for channels with $0.4 < D_h < 4.9$ mm. Figure 6.33 shows the variation in slug and film heat transfer ceoffecients with massflux and quality predicted by the model. Film heat transfer coefficients are in general higher than the slug heat transfer coefficients, and as the quality increases, the slug length ratio decreases, leading to a higher contribution of the film heat transfer coefficient towards the time-averaged heat transfer coefficients. Also, as the quality increases, the flow velocities increase due to an increase in vapor velocity, which in turn leads to a corresponding increase in slug velocity. Thus, the slug heat transfer coefficients increase as the quality increases. For the lowest mass flux case, the slug heat transfer coefficient remains almost constant due laminar Re_{slug}. In the laminar region, Nu is constant for single-phase flow. Also, as the quality increases, the minimum-to-average film thickness ratio decreases leading to an increase in film heat transfer coefficients. Thus, as the quality increases, the heat transfer coefficients increase, due to an increase in both h_{slug} and h_f.

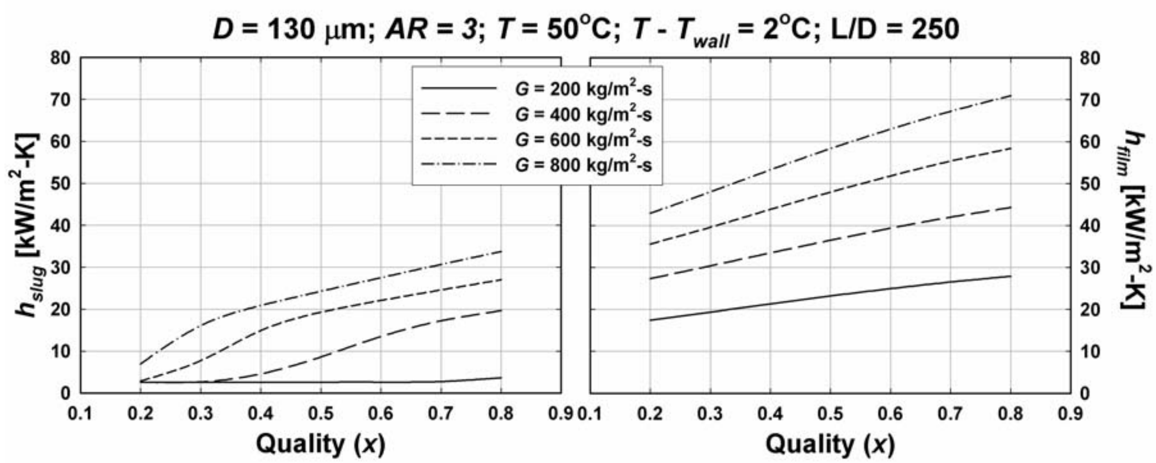

Figure 6.33: Variation in h_{slug} and h_{film} with Mass Flux and Quality

Figure 6.34 shows the effect of variation of refrigerant saturation temperature on the pressure drop, heat transfer coefficient, slug flow probability and the number of unit cells for D = 130 μm, AR = 3, G = 600 kg/m^2-s, T-T_{wall} = 2^{o}C and L/D = 250. The refrigerant saturation temperature varies from 30 to 60^{o}C. As the refrigerant saturation temperature decreases, the gas-to-liquid phase density ratio $\left(\rho_g/\rho_l\right)$ decreases (ρ_g/ρ_l = 0.083 @ 60^{o}C and ρ_g/ρ_l = 0.032 @ 30^{o}C), leading to an increase in void fraction (α = 0.74 @ 60^{o}C and α = 0.80 @ 30^{o}C). This increase in void fraction is also associated with an increase in flow velocities, which in turn yield higher pressure drops. This increase in void fraction also leads to lower slug length ratios $\left(\dfrac{l_{slug}}{l_{slug}+l_{bubble}}\right)$ and fewer unit cells at low refrigerant saturation temperatures. Due to this coupled effect, the annular flow factor is higher at lower saturation temperatures and vice versa at higher saturation temperatures.

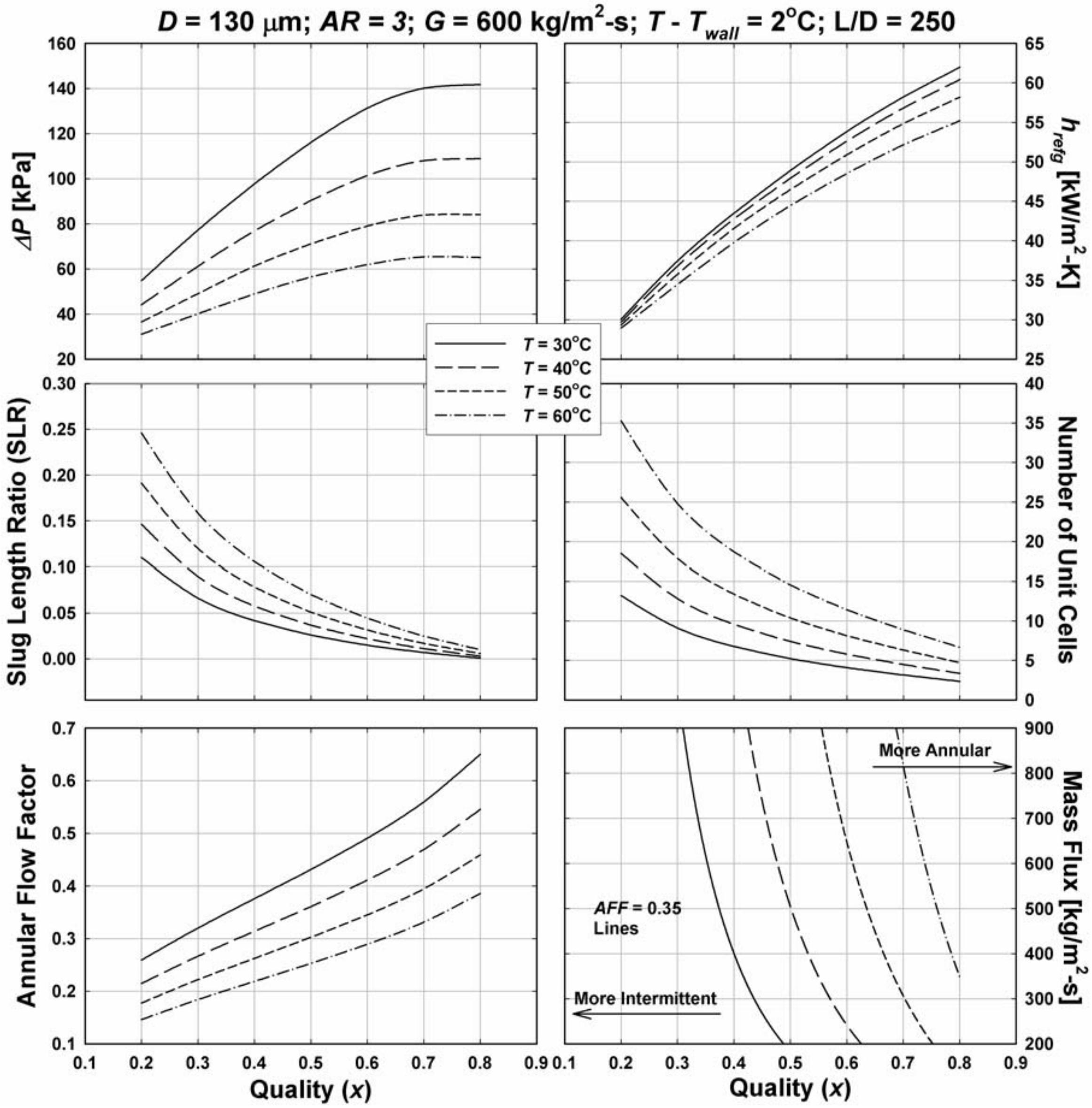

Figure 6.34: Model Predictions: Effect of Temperature

The plot in the lower right corner of Figure 6.34 shows constant annular flow factor lines for each saturation temperature. If this annular flow factor is used as a transition criteria, then for the same annular flow factor, the annular flow zone will be larger at lower saturation temperatures. As the saturation temperature decreases, the refrigerant heat transfer coefficient increases due to two factors. Firstly, as mentioned above, at lower saturation temperatures, the flow velocities are higher leading to an increase in the heat transfer coefficient. Also, as the saturation temperature decreases, the slug length ratio decreases; thus, the contribution of the film heat transfer coefficient toward the time-averaged refrigerant heat transfer coefficient is higher at lower saturation temperatures.

Figure 6.35 shows the effect of a variation in channel aspect ratio on the pressure drop, heat transfer coefficient, slug length ratio, number of unit cells and annular flow factor for D = 130 μm, G = 600 kg/m^2-s, T = 50°C, T-T_{wall} = 2°C and L/D = 250. The aspect ratio was varied from 1 to 4, without varying the hydraulic diameter. It should be noted that unlike the actual channels tested in current study, here the hydraulic diameter is kept constant and only at the aspect ratio varies. Thus as the aspect ratio increases, the channel depth decreases and the width increases. In the discussion of slug frequency presented earlier in this chapter, based on the observed trends, it was concluded that aspect ratio has a significant influence on slug frequency. As the aspect ratio (*AR*) increases, the probability of observing slug flow increases, perhaps due to the instability of the annular liquid film in high aspect ratio channels. Thus, the annular flow factor (*AFF*) in square channels is much higher than that in higher aspect ratio channels. Due to this reason, the constant *AFF* lines shift towards lower quality with a decrease in aspect ratio, i.e. in channels with smaller aspect ratios, the annular flow regime is expected to occur at much lower qualities and mass fluxes. The larger the number of unit cells, the greater is the associated pressure drop in transitions between the slug and the bubbles. Thus, as the aspect ratio increases, the pressure drop increases.

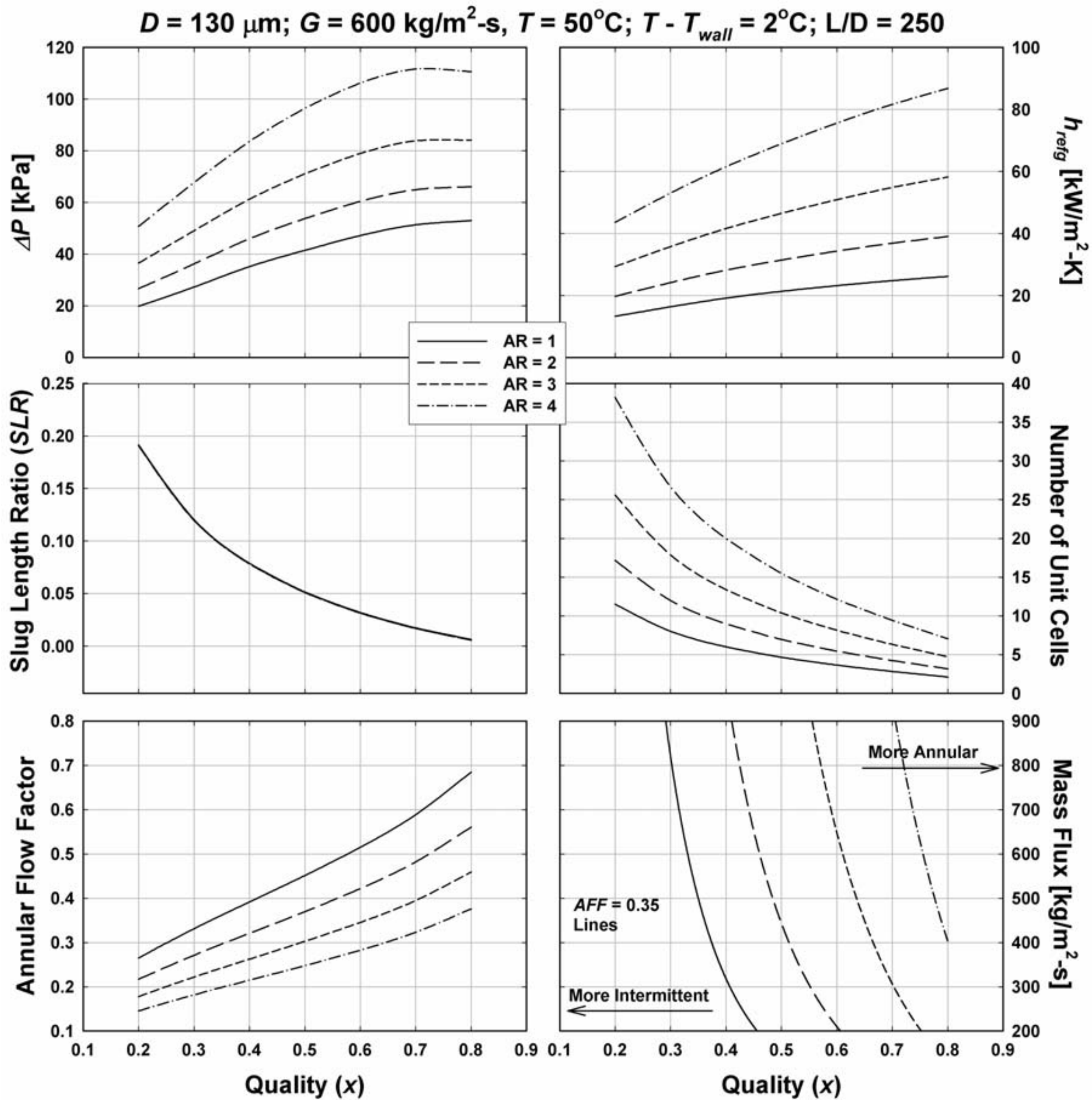

Figure 6.35: Model Predictions: Effect of Channel Aspect Ratio

The slug heat transfer coefficients are higher for higher aspect ratio channels if the slug flow is laminar. Also, according to model for film heat transfer coefficient (equation 6.47), h_f is inversely proportional to the bubble length. Larger number of unit cells at higher aspect ratios lead to shorter bubble lengths, yielding higher film heat transfer coefficients. Thus, as the aspect ratio increases, the heat transfer coefficient increases. Physically this can be understood as follows. Each time the slug passes by, it breaks the liquid film boundary layer and due to fluid passing from film to slug and then from slug to film, there is more mixing of the fluid leading to higher heat transfer coefficients. The higher the number of unit cells, the more frequent is this turbulent mixing due to the passing slugs at turbulent velocities, leading to higher heat transfer coefficients in high aspect ratio channels.

Figure 6.36 shows the effect of variation of channel hydraulic diameter on the pressure drop, heat transfer coefficient, slug flow probability and the number of unit cells for AR = 3, G = 600 kg/m^2-s, T = 50^{o}C, T-T_{wall} = 2^{o}C and L/D = 250. The hydraulic diameter varies from 100 μm to 160 μm. Again, it should be noted that the unlike the actual channels tested in the current study, the aspect ratio is kept constant and only the hydraulic diameter is varied. The slug length ratio (SLR) and the number of unit cells do not show much dependence on the channel hydraulic diameter. As the diameter increases, there is slight decrease in the number of unit cells due to an increase in Reynolds number. This decrease in the number of unit cells causes the corresponding increase in annular flow factor. It should be noted that as the hydraulic diameter decreases, the pressure drop increases even though the length to diameter ratio is constant. Garimella *et al.* (2005) also observed a similar trend in the pressure drop for 0.5 < D_h < 4.9 mm. As the diameter decreases, the film thickness decreases, leading to lower interface velocities. Thus, even if the bubble velocity is the same for tubes of different diameter at the same mass flux, the bubble velocity (U_{bubble} = 5.765 m/s @ x = 0.5 for all D) relative to the interface ($U_{interface}$ = 0.45 m/s for D = 160 μm; $U_{interface}$ = 0.26

m/s for D = 100 μm @ x = 0.5) is increasing with decreasing diameter. Also, the number of unit cells increases slightly with decreasing diameter, leading to an increase in the pressure drop in the transitions between the slug and bubble regions. Both the above factors lead to an increase in pressure drop with decreasing diameter.

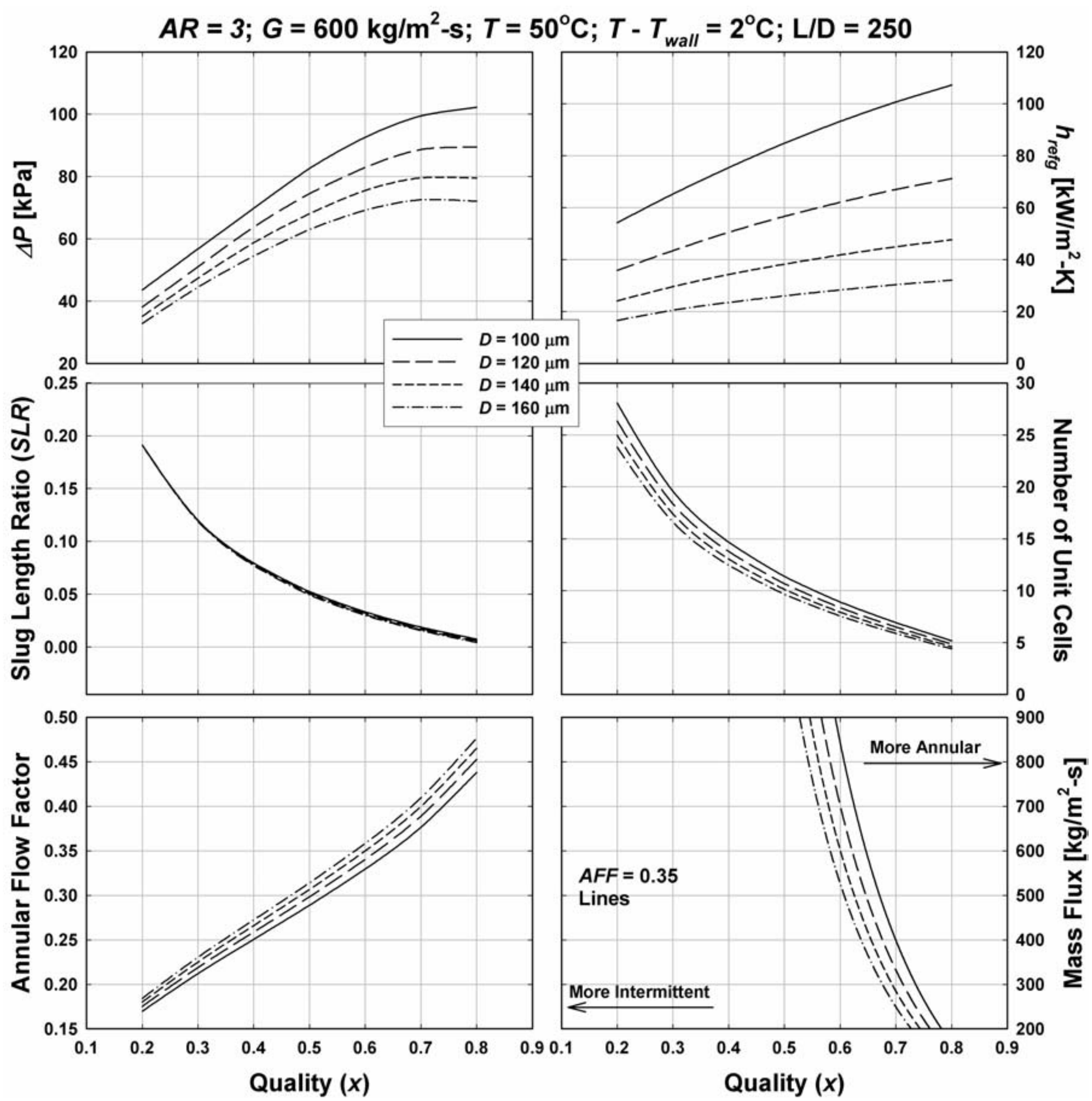

Figure 6.36: Variation with Diameter Predicted by Model

The heat transfer coefficient also increases with a decrease in diameter due to the increase in the film heat transfer coefficients with decreasing diameters. The film heat transfer coefficients increase due to a decrease in film thickness, with the decrease in tube diameter.

In the above discussions about the effect of the aspect ratio and the diameter, it was concluded that both the heat transfer and the pressure drop increase with increasing aspect ratio and decreasing diameter. But the same is not explicitly observed in the data from this study discussed earlier. This is because for the tubes considered in the current study, as the hydraulic diameter increases, the aspect ratio also increases. Figure 6.37 shows the variation in pressure drop and the heat transfer coefficient, under similar flow conditions, for the actual channels tested in the current study. In these plots, a continuously increasing or decreasing trend with change in hydraulic diameter or aspect ratio is not seen due to combined influence of these two parameters.

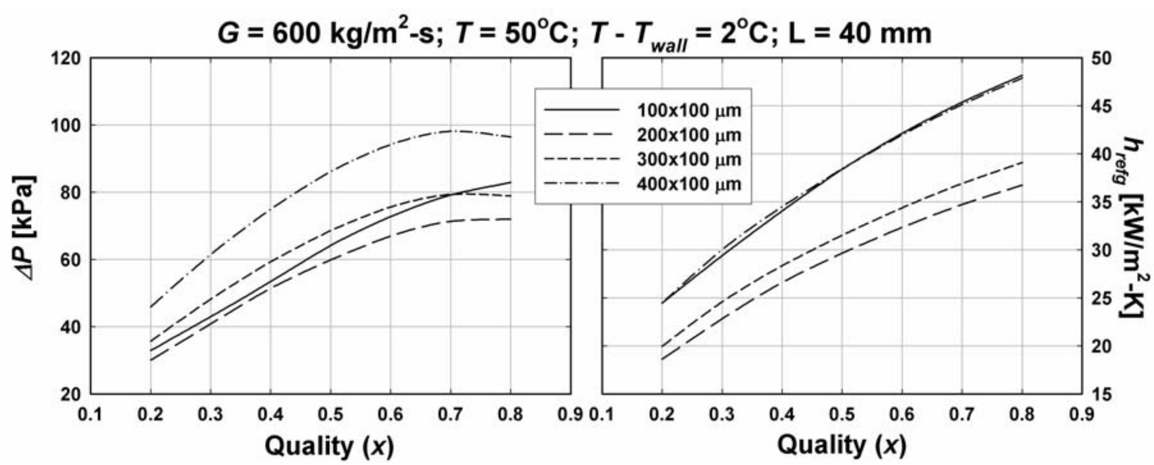

Figure 6.37: Variation in ΔP and h_{refg} for Tested Channels

Figure 6.38 shows the effect of driving temperature difference on the refrigerant heat transfer coefficients for AR = 3, G = 600 kg/m^2-s, T = 50^{o}C, x_{ave} = 0.5, T-T_{wall} = 2^{o}C and L/D = 250. As the driving temperature difference decreases, the rate of condensation decreases, leading to a thinner liquid film on the channel walls, which in turn yields higher heat transfer coefficients. The effect of a change in driving temperature difference diminishes with increasing driving temperature difference. The data for the heat transfer coefficients in some cases shows a steeply increasing trend with increase in vapor quality, while the plots presented in current section (Figure 6.32 to Figure 6.36) do not show this steep increase in heat transfer coefficients.

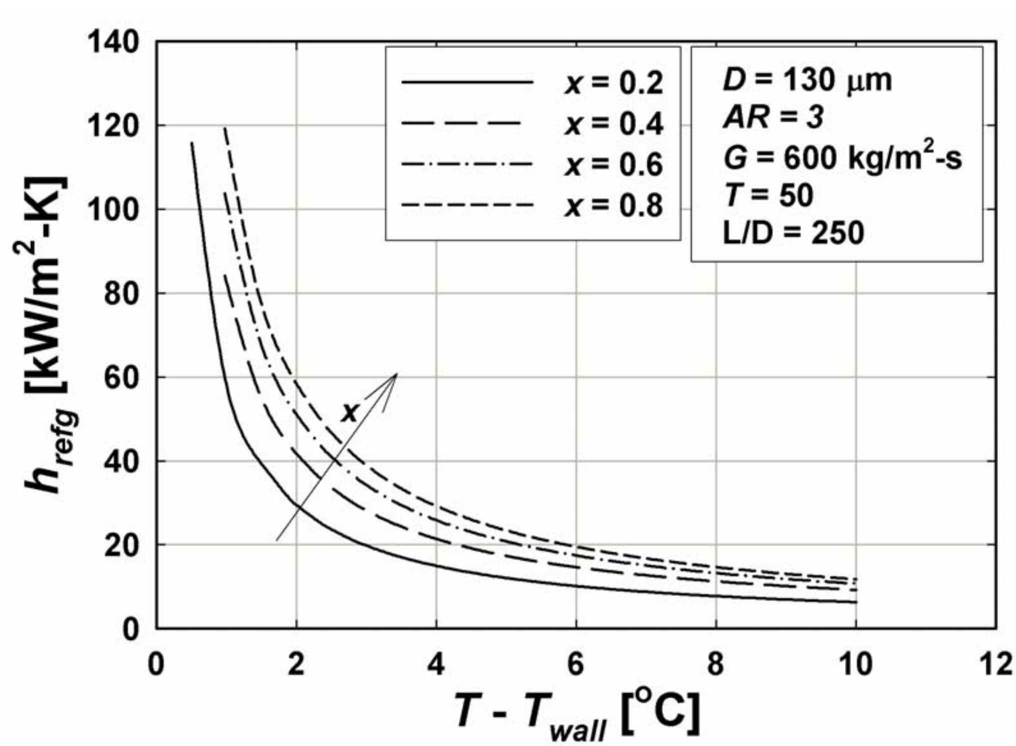

Figure 6.38: Variation with Driving Temperature Difference Predicted by Model

In the data, as the quality increases, the refrigerant heat transfer coefficient increases leading to a decrease in the refrigerant-side thermal resistance, which in turn leads to a lower driving temperature difference. For the results presented in the current section, the driving temperature difference ($T - T_{wall}$) was fixed to a particular value.

The average vapor quality for the data obtained in the current study varies between 0.2 and 0.8. Figure 6.39 shows the pressure drop and heat transfer coefficient predictions if the proposed model is extrapolated to vapor qualities varying from 0.05 to 0.95 for a particular case (D = 130 μm, AR = 3, G = 600 kg/m^2-s, T = 50^{o}C, T-T_{wall} = 2^{o}C and L/D = 250). The single phase liquid only and vapor only pressure drop (ΔP_{LO} = 5.6 kPa and ΔP_{VO} = 31.1 kPa) and heat transfer coefficient ($h_{refg,LO}$ = 2.2 kW/m^2-K and $h_{refg,VO}$ = 3.1 kW/m^2-K) are also shown for this particular case. As the quality decreases to less than 0.2 and approaches 0, the void fraction also approaches zero. Correspondingly, the slug length ratio increases to 1. Thus, as the quality approaches 0, no matter how many number of unit cells are there, the total pressure drop is just equal to the slug pressure drop calculated using the single-phase correlations.

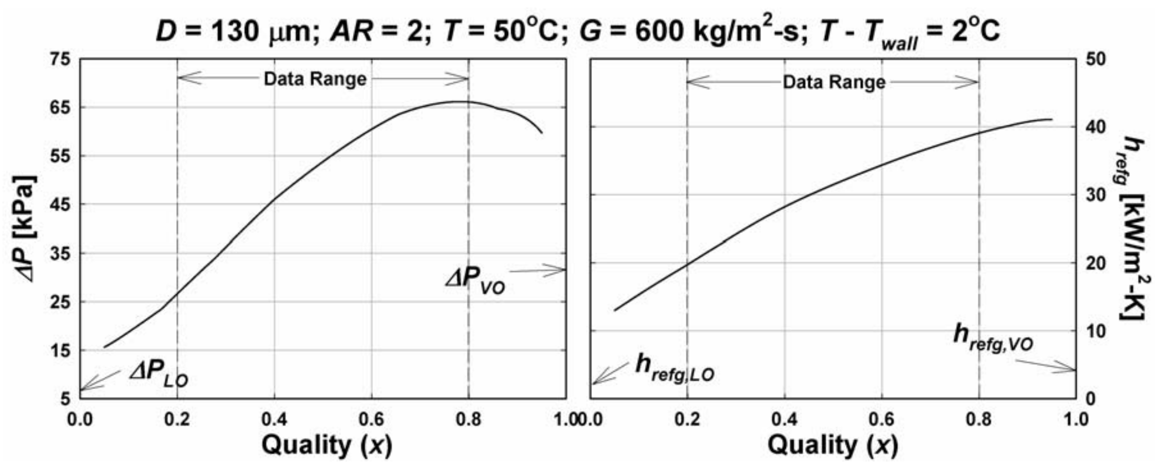

Figure 6.39: Extrapolation of Proposed Model

Similarly, as the quality approaches zero, the heat transfer coefficient also approaches the single-phase heat transfer coefficient. As the quality approaches zero, the contribution of slug heat transfer coefficient in the time-averaged heat transfer coefficient increases, which leads to the approach to the single phase liquid value. As the vapor quality increases, the number of unit cells decreases. Since the viscosity of the film/bubble section is much less than the slug viscosity, the pressure drop tends to decrease as the slugs disappear. The heat transfer coefficient continues to increase as the quality approaches one due to a progressively thinner liquid film. (The model does not account for inlet superheat as might be the situation in an actual condenser)

6.6. Other Considerations

The model proposed here is able to predict the trends in the pressure drop and heat transfer data based on a physical basis. The effect of surface tension is not explicitly captured, even though it might play an important role in microchannels. The behavior at very low ($x < 0.2$) and very high ($x > 0.8$) quality is also not addressed in great detail, because of the lack of data in these regions. The effect of fluid property variation is also not addressed; this would require additional data with different refrigerants. The model proposed here also assumes uniform distribution of flow in all channels and steady state conditions. The model does not account for the maldistribution of flow and flow instabilities arising from the same. This would require repeating similar experiments with several header designs.

CHAPTER 7. CONCLUSIONS AND RECOMMENDATIONS

A comprehensive study of condensation heat transfer and pressure drop in microchannels was conducted. An innovative measurement technique to accurately measure heat transfer coefficients and pressure drops in microchannels ($100 < D_h < 160$ μm) was developed. Refrigerant microchannels were fabricated from copper using X-ray lithography and electroforming processes, which provide excellent dimensional accuracy and minimal surface roughness. The channels were fabricated using diffusion bonding, which ensures that there is no residue remaining in channels that might block them. Heat transfer and pressure drop experiments were conducted on 40-mm long rectangular channels of 100×100 μm, 200×100 μm, 300×100 μm and 400×100 μm for the condensation of refrigerant R134a over a range of mass fluxes, $300 < G < 800$ kg/m^2-s, qualities, $0 < x < 1$, and saturation temperatures, 30, 40, 50 and 60°C. Energy balances on pre- and post-heaters were used to determine the inlet/exit qualities and test section heat duties. Frictional pressure drops were obtained from the measured pressure drops by accounting for expansion and contraction terms, and acceleration or deceleration pressure changes, as applicable. Heat transfer in the channels was analyzed using a detailed segmental analysis of the conjugate conduction and convection processes in the test section. Careful attention was paid to the effect of pressure drop within the channels on saturation temperatures and the resulting driving temperature differences between the refrigerant and coolant. In addition, the effect of the variation of heat transfer coefficient in intermittent flows from the slug to bubble regions was investigated in detail using a transient analysis of the thermal storage within the channel walls. Uncertainties in pressure drops and heat transfer coefficients were conducted using a rigorous propagation of errors approach.

It was found that both pressure drop and heat transfer increased with increasing vapor quality, increasing mass flux and decreasing saturation temperature. Both pressure drop and heat transfer coefficients were the highest for the 400×100 μm channels, followed by 100×100 μm, 200×100 μm, 300×100 μm channels, in the order. Comparisons with commonly cited pressure drop models revealed that most correlations did not adequately predict the data from the present study, primarily because these models in the literature were developed for adiabatic flows of air-water mixtures through larger tubes of circular cross-sections, or only for channels with aspect ratios close to one. It was also found that most of the models from the literature significantly under-predicted the heat transfer data from the present study.

Based on the existing flow regime maps in the literature, it was assumed that condensation would occur in either the intermittent or the annular flow regime for all the test conditions investigated, due to the small hydraulic diameter channels under consideration. An intermittent flow regime-based flow model was used, with assumption that annular flow is equivalent to an infinitely long bubble with vanishing slugs. Assuming Armand's void fraction correlation (Armand, 1946) to be valid, the flow velocities are determined in a manner analogous to Garimella *et al.* (2002; 2003b). The probability of occurrence of slug flow and annular flow under various flow conditions was quantified by defining an Annular Flow Factor (*AFF*). The pressure drop due to single-phase liquid flow in the slug, and due to shear at the bubble-vapor interface were first computed and summed in proportion to the ratio of their lengths. In addition, transitional pressure losses due to the transfer of fluid between the film and slug regions were determined. A new correlation was proposed to predict the slug frequency based on the data from the present study.

The flow velocities and other parameters determined for the pressure drop model are used as inputs for the heat transfer models. The slug and bubble regions were again analyzed separately to determine the slug and film heat transfer coefficients. A time-averaged refrigerant heat transfer coefficient was determined by combining the slug and film heat transfer coefficients according to their transit times through the channel. The proposed pressure drop and heat transfer models predict 95%, and 94% of the data, respectively, within ±25%.

The proposed models were also used to analyze the effect of various parameters such as mass flux, saturation temperature, hydraulic diameter, and aspect ratio. As the mass flux increases, both the pressure drop and heat transfer increase due to an increase in flow velocities. As the saturation temperature decreases, the void fraction increases due to a decrease in the vapor-to-liquid density ratio, which increases velocities and interfacial shear, and in turn, leads to an increase in pressure drop and heat transfer. As the channel hydraulic diameter decreases, the pressure drop and heat transfer coefficient increase due to a decrease in film thickness and channel diameter. As the aspect ratio increases, the pressure drop and heat transfer coefficients increase due to an increased occurrence of slugs.

The results from the current study thus make an important contribution to the understanding of phase-change pressure drop and heat transfer in microchannels. The proposed model may be used by engineers for analyzing condensing two-phase flow in microchannel geometries.

7.1. Recommendations for Future Work

While the present study has led to a considerable advance in the understanding of condensing flows in microchannels, there are several key issues that demand further investigation to further validate the models developed here and extend their applicability. Among the most important investigations that could be performed are:

- Flow visualization studies during the condensation process in channels of similar hydraulic diameters and aspect ratios so that the considerations used here to predict the occurrence of annular and intermittent flows can be confirmed. This will in turn lead to improved accuracies and reliabilities in the predictions of heat transfer and pressure drops over a wide range of conditions.
- Similar experiments with refrigerants other than R134a, which would enable more explicit treatment of the effect of properties such as surface tension, and the properties such as density, viscosity, specific heat and thermal conductivity of the individual phases. Such investigations would definitely make this work relevant to a much wider range of important applications.
- Development of techniques for the measurement of condensation heat transfer and pressure drop in individual microchannels, where the key challenge is the measurements of heat transfer rates of the order of a few micro- and milli- watts over surface areas of < 1 mm^2 under operating temperature differences of tenths of ^oC. If

such experimental techniques are developed, issues such as flow mal-distribution and flow instabilities introduced due to flow through multiple parallel channels can be minimized.

.

APPENDIX-A. EXPERIMENTAL FACILITY DETAILS

A.1. Refrigerant Channel Fabrication Stages

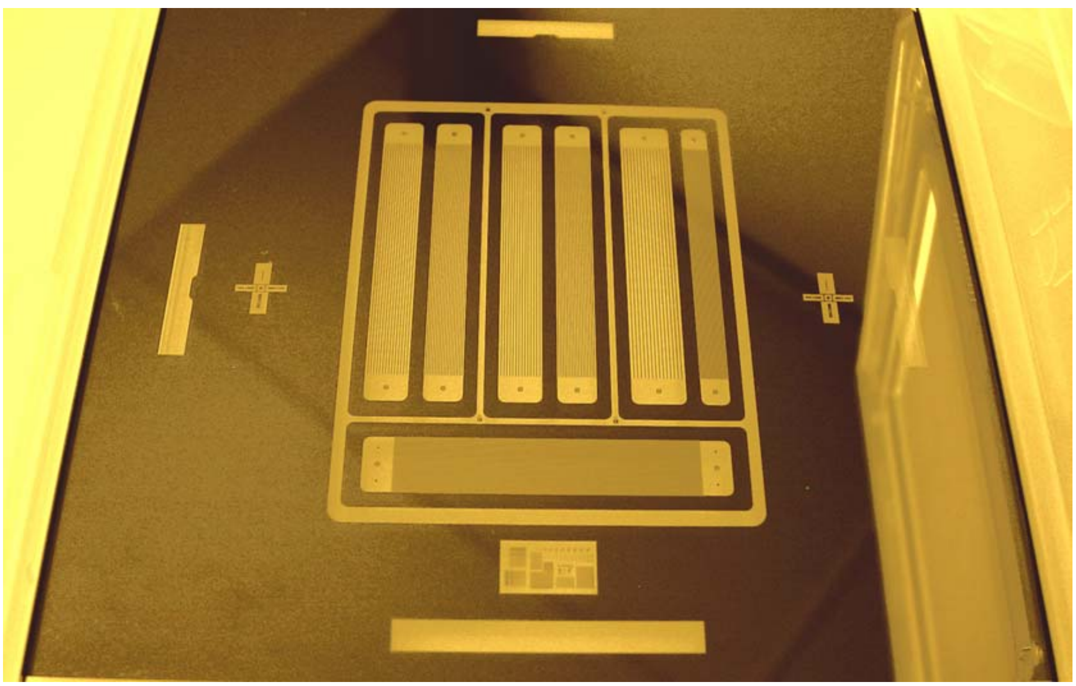

Figure A.1: Nickel Chrome Plate used to make X-ray Mask

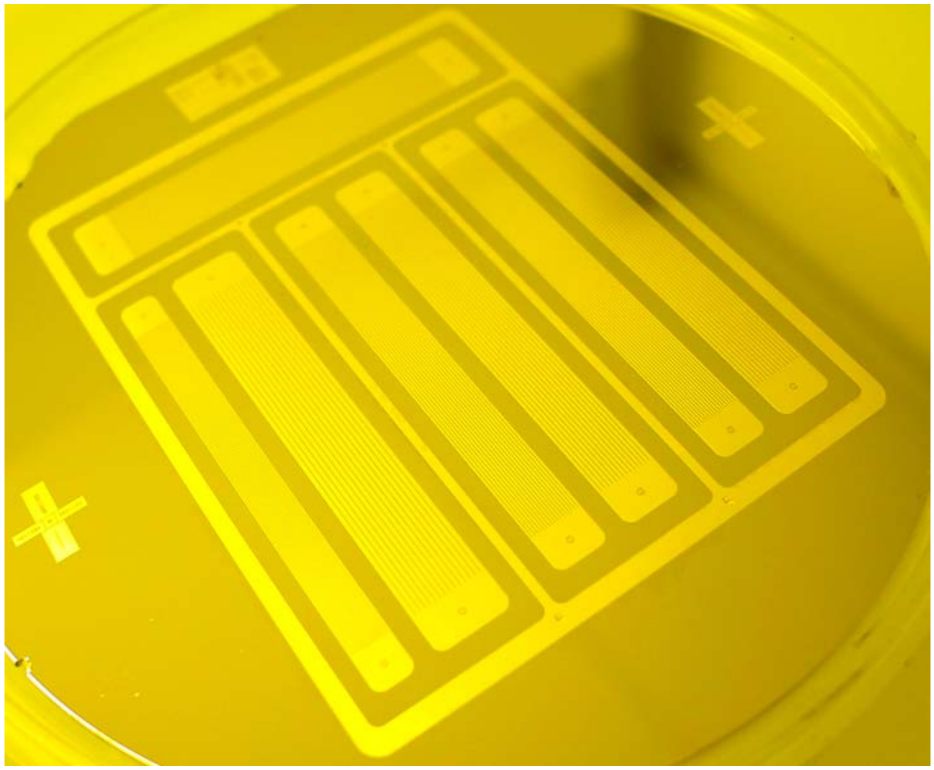

Figure A.2: Completed X-ray Mask

Figure A.3: Close-up of Developed X-ray Mask

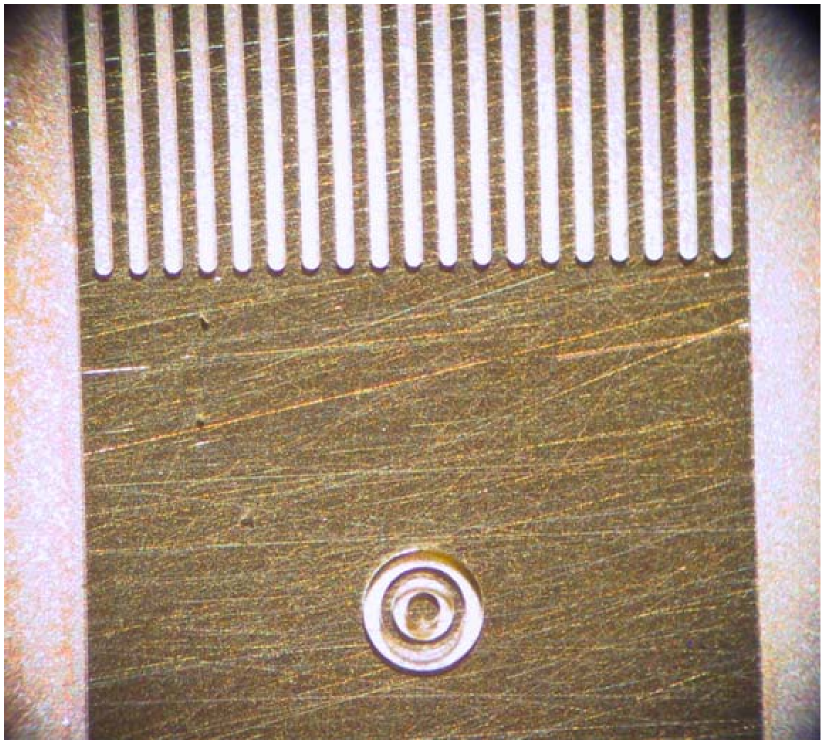

Figure A.4: Close-up of Wafer with PMMA Mold

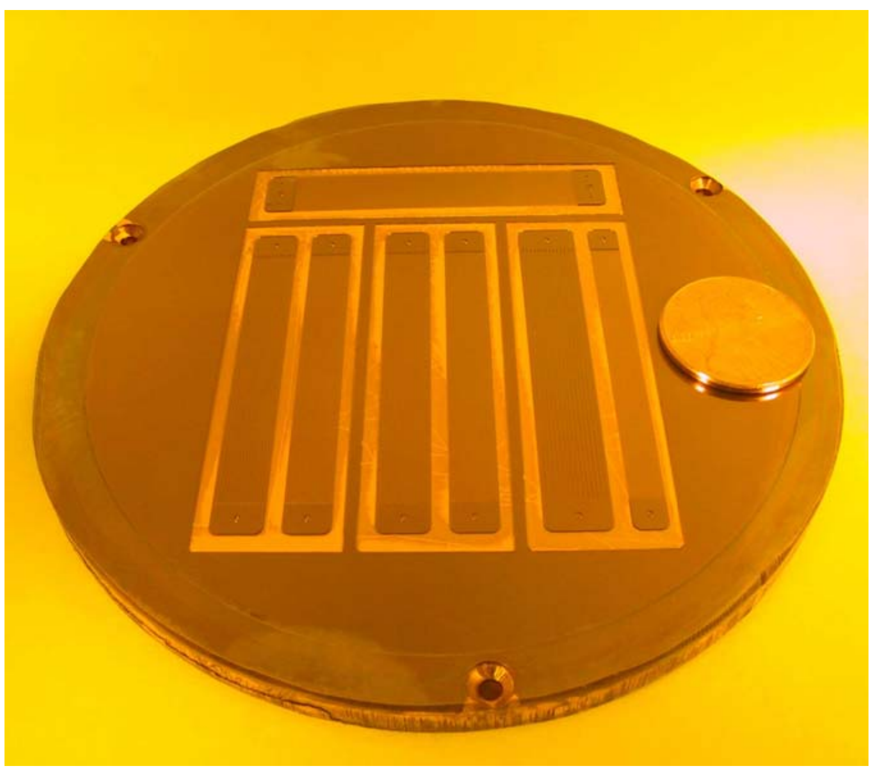

Figure A.5: Wafer after Deposition of Cu into PMMA Mold

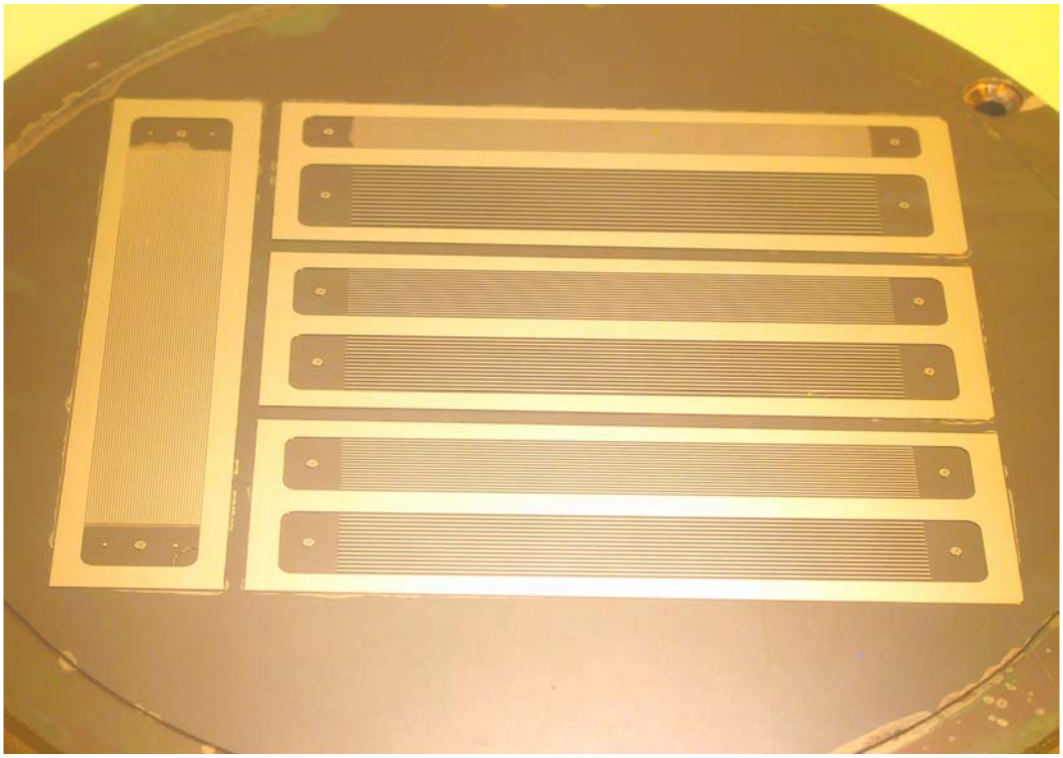

Figure A.6: Wafer after Plating and Lapping

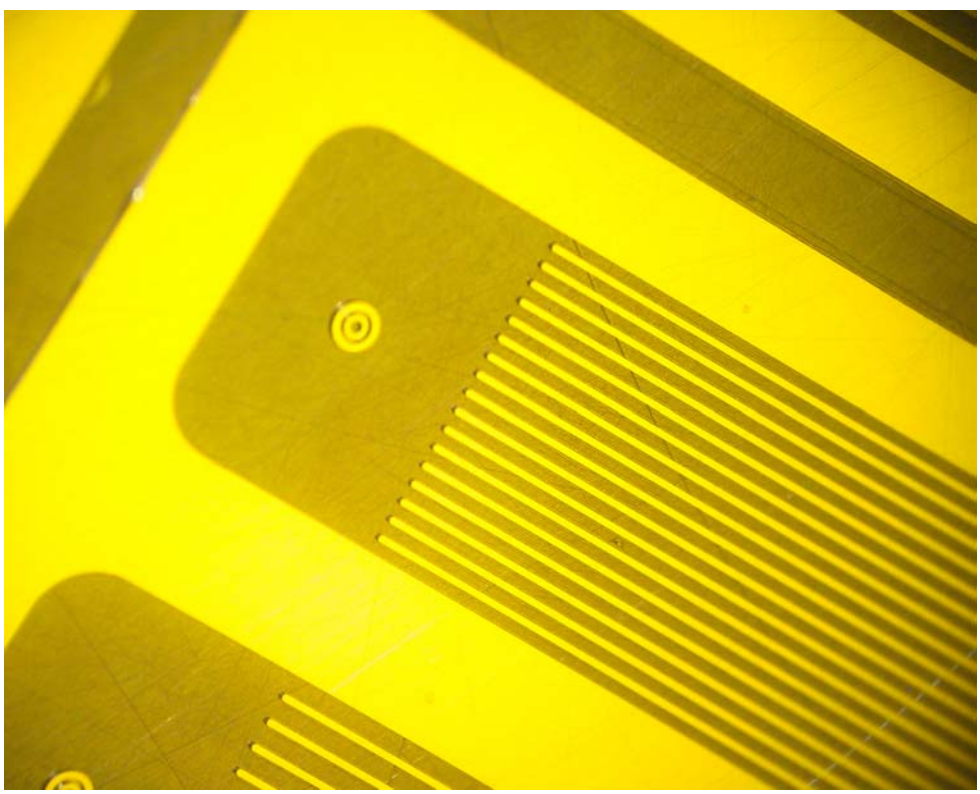

Figure A.7: Wafer Close-up of headers after Plating and Lapping

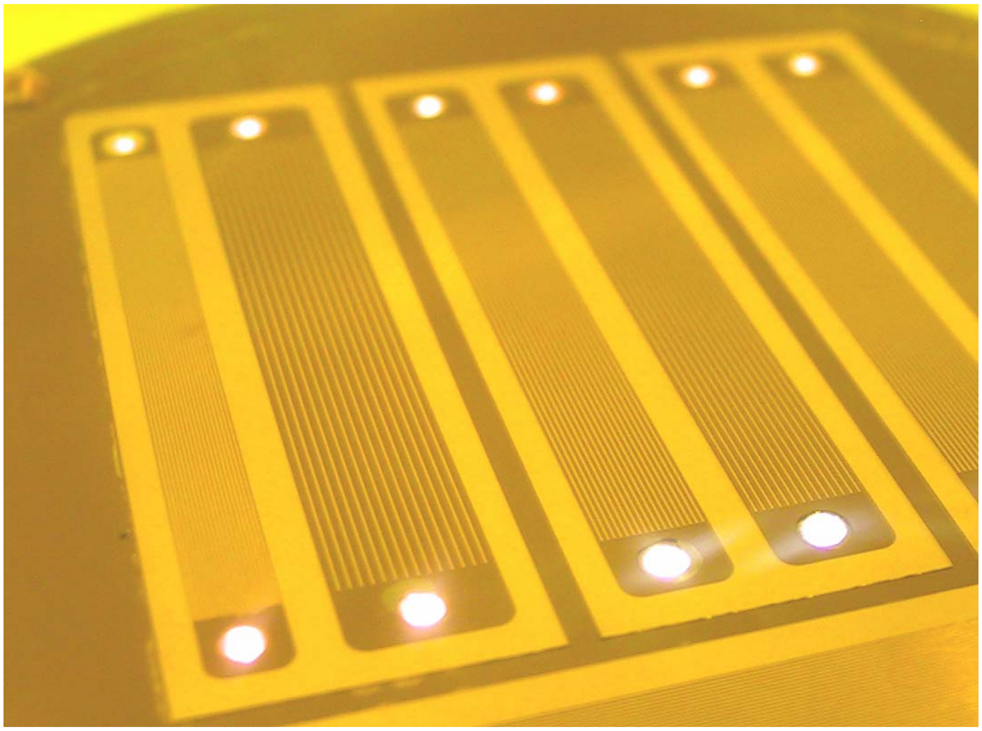

Figure A.8: Picture of Wafer after Drilling of Holes

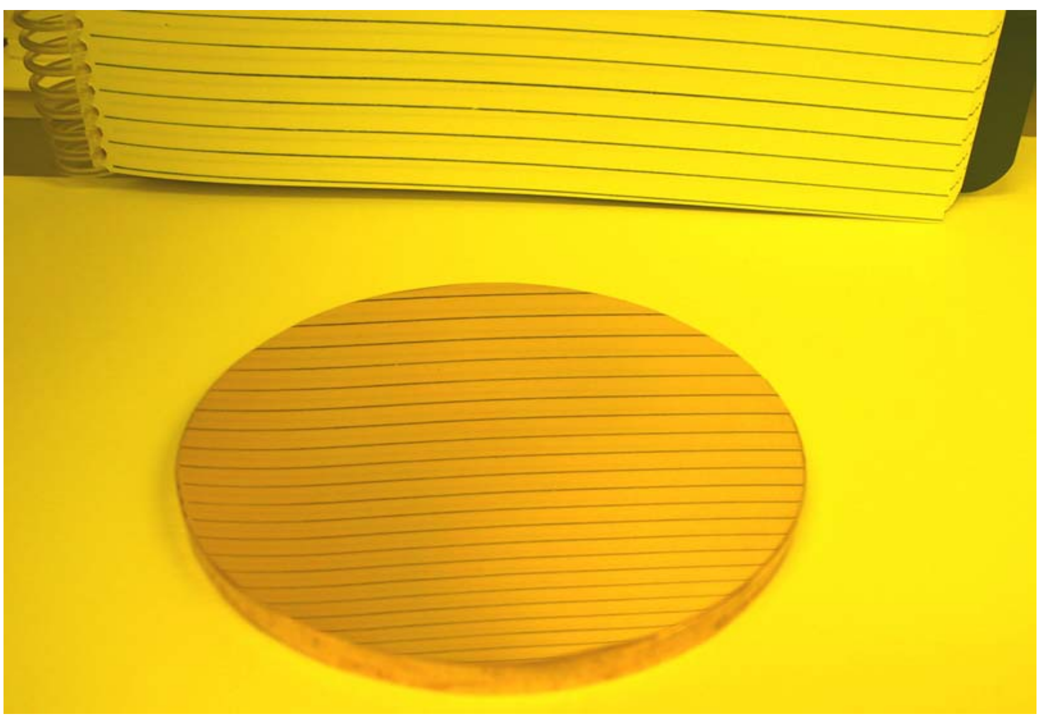

Figure A.9: Cu Substrate used to Cover Channels from Top by Diffusion Bonding

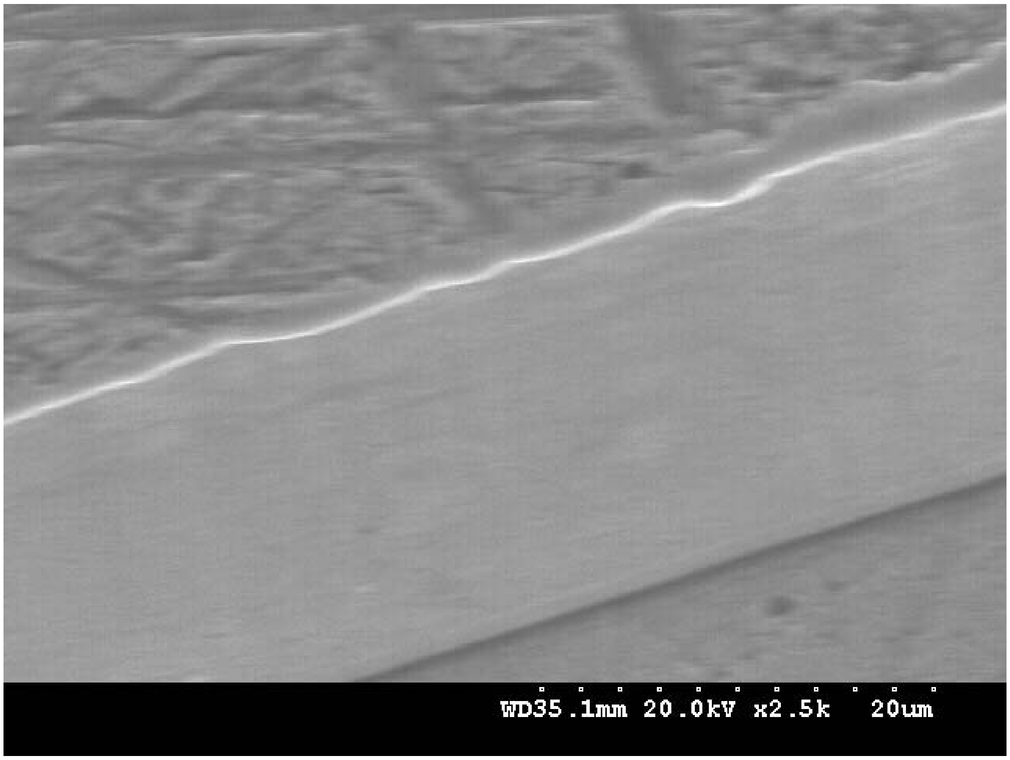

Figure A.10: SEM Image of Channel Wall Surface Profile

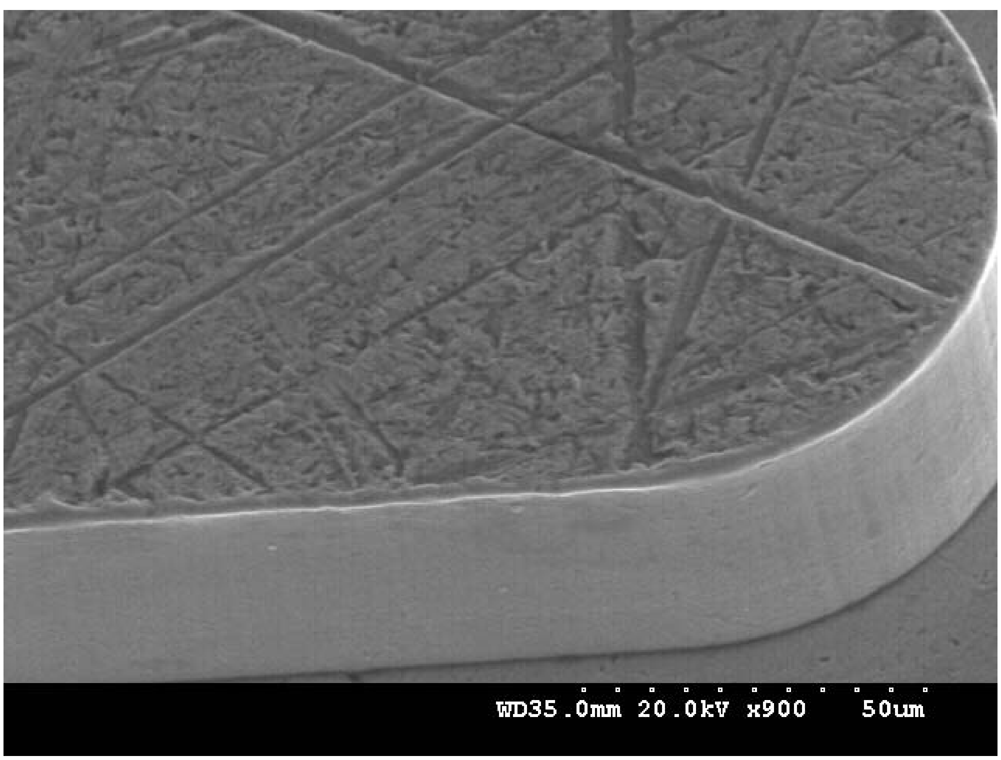

Figure A.11: SEM image of Channel Wall Surface Profile at Rounded Wall Ends

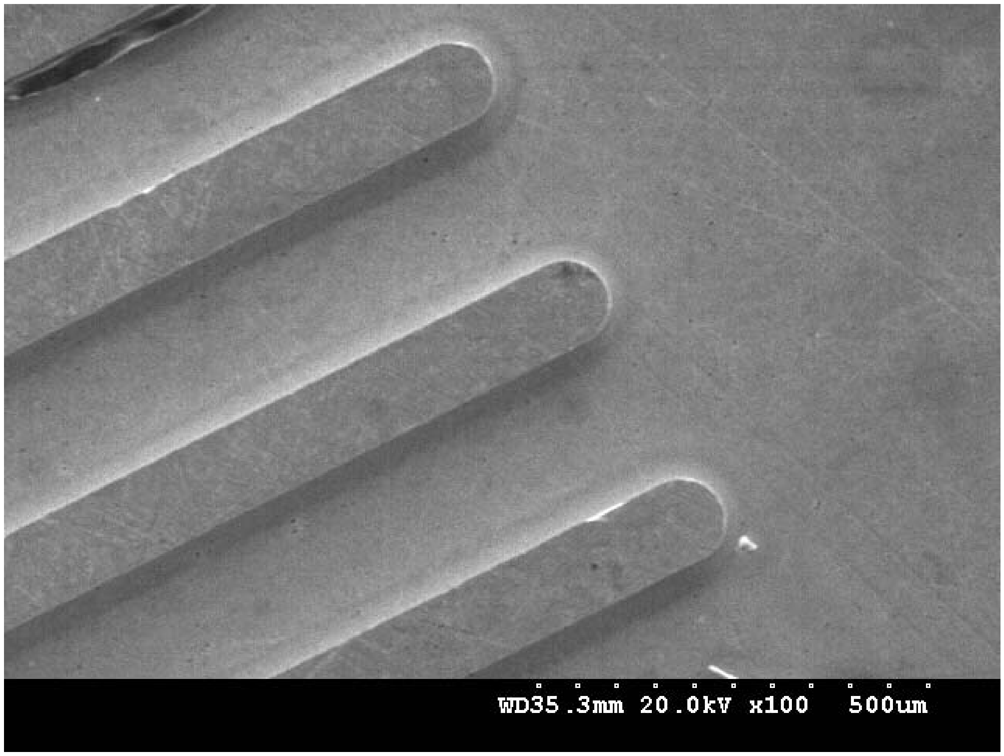

Figure A.12: Top SEM image Showing Negligible Taper in Channel Walls

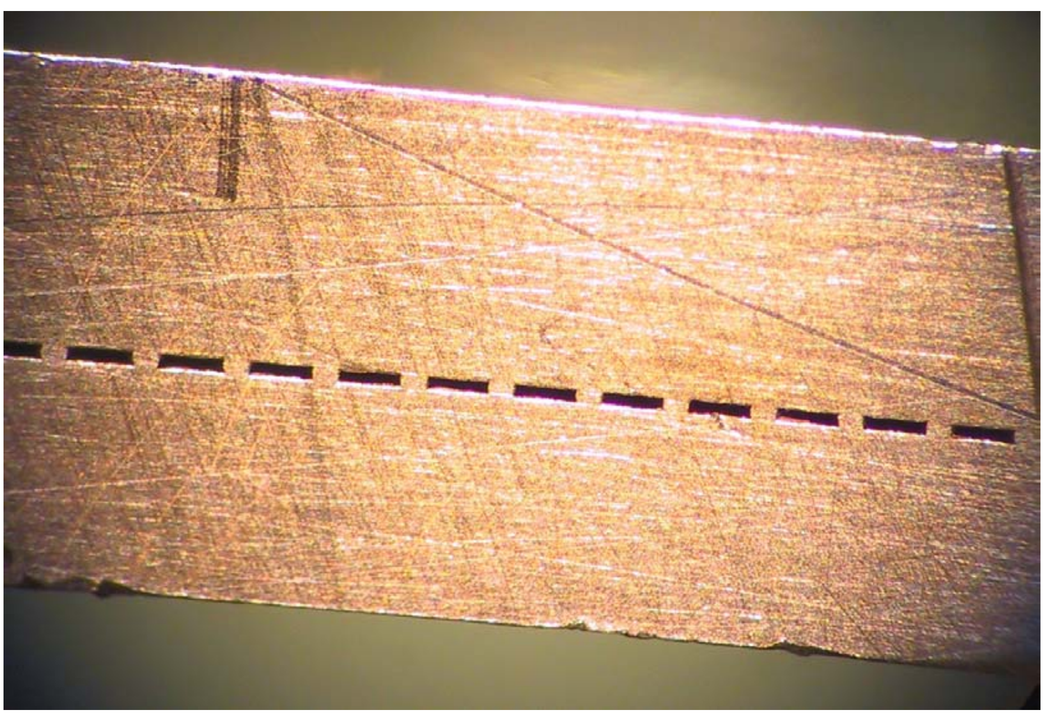

Figure A.13: Cut-section of Refrigerant Channels after Diffusion Bonding

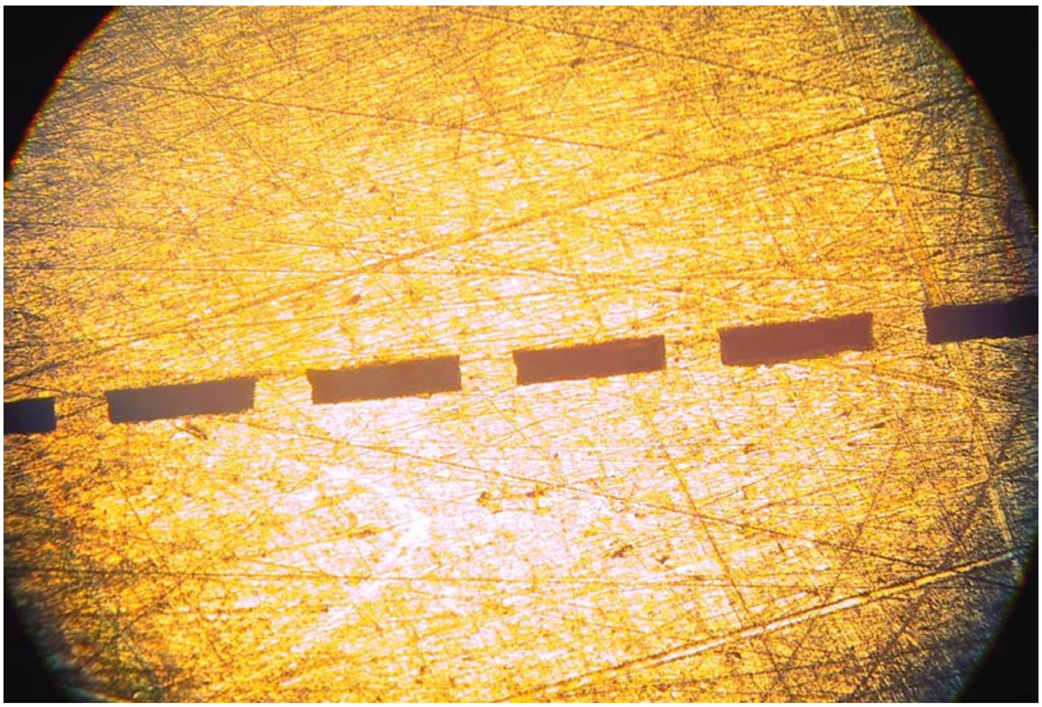

Figure A.14: Close-up of Cut Section Showing Joint Quality

A.2. Water Channel Block Engineering Drawings

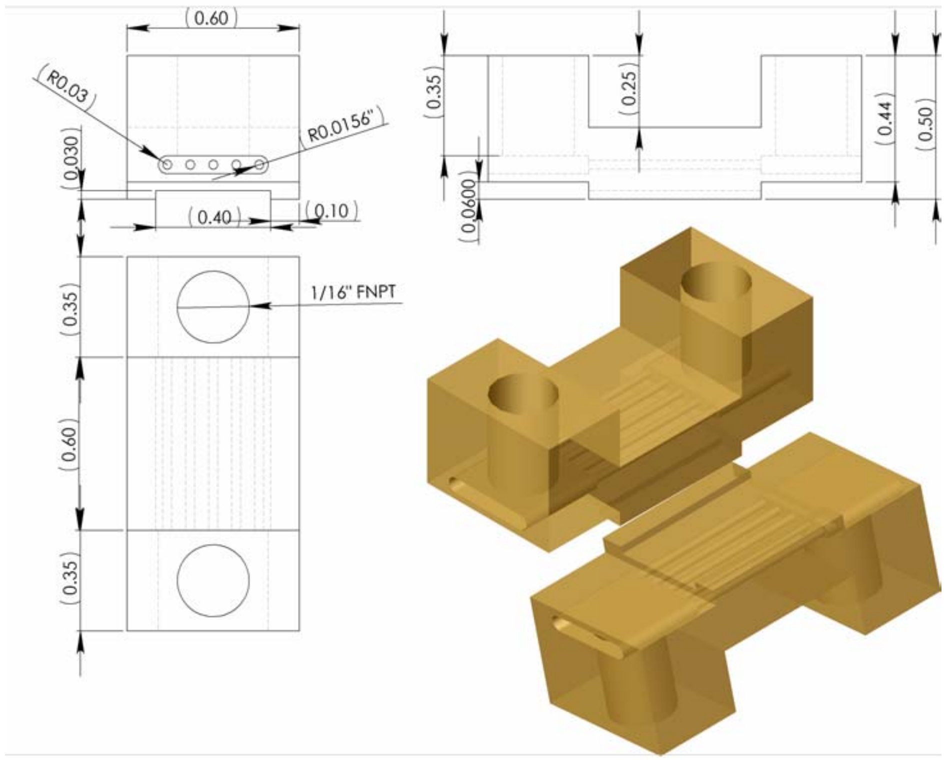

Figure A.15: Engineering Drawing for Water Channel Main Blocks

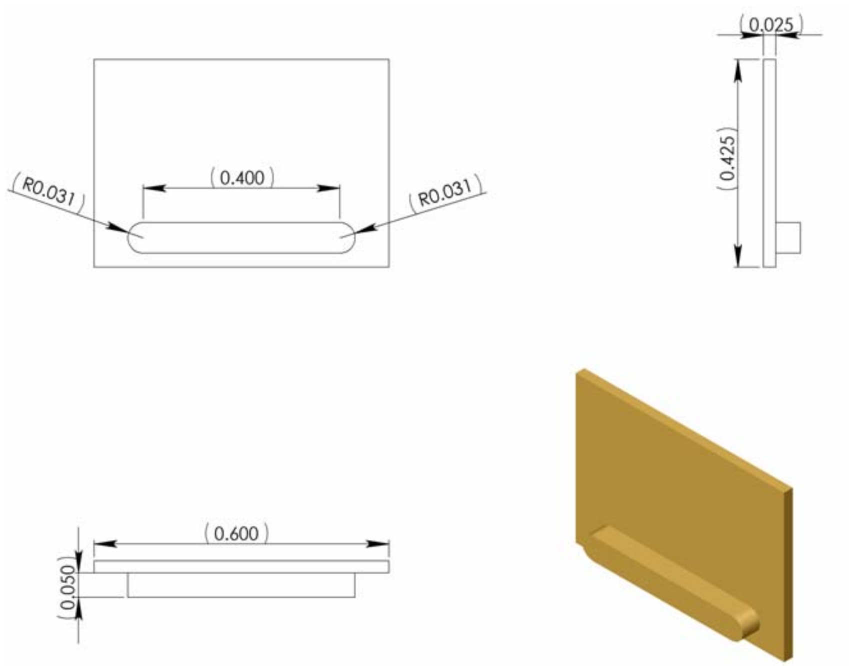

Figure A.16: Engineering Drawing for End Plates

A.3. Test Facility Equipment Details

Table A-1: Part Numbers for Swagelok Fittings used in Refrigerant Heaters

Fitting	Part No.	Specifications
Stainless Female Run Tee,	SS-600-3TFT	3/8 in. OD - 1/4 in. FNPT - 3/8 in. OD
Stainless Reducing Bushing	SS-4-RB-2	1/4 in. MNPT - 1/8 in. FNPT
Stainless Reducing Port Connector	SS-601-PC-2	3/8 in. OD - 1/8 in. OD

Table A-2: Refrigerant Cartridge Heater Specifications

Product Name	**Cartridge Heater (Firerod)**
Manufacturer	Watlow
Supplier	Star Electric
Part Number	E2A136-BG12
Sheath Length	2 in (50.8 mm)
Volts	120
Watts	80
Watt Density	68 W/in^2 (11 W/cm^2)
No Heat Length	¾ in (19 mm)
Threaded Fitting Specification	1/8 in MNPT Threading ½ in (13 mm) Long

Table A-3: Refrigerant Pre- and Post-heater Dimensional Details

Parameter	**Dimension**
Refrigerant heater Swagelok fitting ID	10.16 mm (0.4")
Refrigerant heater Swagelok fitting OD	15.24 mm (0.6")
Heater insulation thickness	12.70 mm (0.5")
Heater rod diameter	6.35 mm (0.25")
Refrigerant heater assembly length *Note: Actual length of the heater inside the fitting is 5.08 cm (2"). This is the end to end outside length of the fitting assembly with heater inside. (Please see* Figure B.1*)*	65 mm (Hor.) 30 mm (Ver.)
Total length of Cu tubing from heater to channels including bend	67 mm
Horizontal length of the Cu tubing from heater to test section	42 mm
Vertical length of the Cu tubing from heater to test section	10 mm

Table A-4: Refrigerant Condenser Details

Heat Exchanger Type	**Tube-in-tube Counter Flow**
Fluids	Annulus: Ethylene-Glycol/water Solution - Center: R134a
Inner copper tube OD	6.35 mm (1/4")
Inner copper tube thickness	0.81 mm (0.032")
Outer steel tube OD	12.70 mm (0.5")
Outer steel tube thickness	0.89 mm (0.035")
Heat transfer length	19 cm

Table A-5: Refrigerant Pump Specifications

Model	GA-X21-P9FSA Gear Pump
Manufacturer	Micropump Inc.
Supplier	GPM Inc., Macon, GA 31221 (Ph: 478 471 7867)
Part Number	L21179
Pump type	▪ Magnetic Drive External Gear Pump ▪ Material 316SS ▪ Suction Shoe Style ▪ Spur Gears ▪ Stationary Shafts ▪ PTFE Static Seal ▪ MP Drive Mount
Series	GA 180
Gear set	Carbon Fiber/PTFE X21 gears
Pumping rate	0.017 ml/revolution
Maximum differential pressure	38 psi
Maximum system pressure	300 psi
Temperature range	-48 to 177° C
Viscosity range	0.2 to 1500 cps
Maximum Speed	8000 rpm
Mounting	A
Bypass Loop Valve	Swagelok S series metering valve 1/8" with Vernier Handle (Part No.:SS-SS2-VH)

Table A-6: Refrigerant Pump Drive Specifications

Model	306 A
Manufacturer	Micropump, Inc.
Supplier	GPM Inc., Macon, GA 31221 (Ph: 478 471 7867)
Part Number	81101
Drive Type	DC - Brush Type Permanent Magnet
Mount code	A
Enclosure	• IP55/Totally enclosed non-ventilated • Suitable for humid, dusty atmospheres • Requires good ventilation
Speed range (RPM)	500-4000
Max. rated torque (NMn/In-oz)	212/30
Nominal (Watts/ HP)	112/0.16
Power Source	24 V
Connections	Wire Leads
Weight (max.)	1.14 kg

Table A-7: Refrigerant Pump Drive DC Regulated Power Supply Specifications

Model	1627 A
Manufacturer	B&K Precision Corporation
Input	115/230 VAC; 50/60 Hz; 220 W
Output	0 – 30 VDC; 0-3 A
Serial No.	D30301638
Metering	3 Digit LED
Operating Temperature	0 to 40^{o}C and ≤ 75% RH
Storage Temperature	-5 to 70^{o}C and ≤ 85% RH
Dimensions (H×W×D)	8.07 x 4.53 x 10.63" (205 x 115 x 270 mm)
Weight	7.4 kg

Table A-8: Refrigerant Sight Glass Specifications

Model	Bull's Eye See Thru
Manufacturer	Pressure Products Co., Inc.
Part Number	00136GXDTTTN
Rated	600 PSIG @ 400^{o}F
Serial No.	WAGG-12395 (Drawing No.: G0A6C04B)
Connection	1/8" Swagelok Tube
Glass	Tempered Pyrex – 1.026" OD
O-Rings	Teflon
Gasket	Teflon

Table A-9: Refrigerant Flow Meter Specifications

Model	**FMTD4 Nutating Flow Meter**
Manufacturer:	DEA Engineering Company
Wetted materials:	All materials in contact with the fluid media are 316 stainless steel and PTFE
Ranges:	< 0.015 - 4.00 GPH [1-250 ccpm]
Displacement	Approximately 50 pulses per cc
Calibration Constant*	49.47 pulses per cc
Accuracy	± 0.5%
Repeatability	± 0.1%
Temperature Range	-40 to +80^{o}C
Output Signal	0 - 5 Volt Square Wave
Power	8-30 VDC, 50 mA maximum
Maximum Operating Pressure:	3,000 psig [21 MPa]
Process Connection	¼" NPT
Max. ΔP:	5 psi [34kPa]
Conduit Connection	½" NPT
Dimensions:	2.50" D. × 4.63" L. [6.4 cm D. × 11.8 cm L.]
Viscosity:	100 SSU [25 cp] Maximum Recommended. Higher Viscosities Reduce Low Flow Rate Capabilities.

* Calibration constant is unique for each flow meter based on its calibration. It is needed to program the FME2 Display for a particular flow meter.

Table A-10: Refrigerant Flow Meter Display Specifications

Model	FME2 Flow Rate / Totalizer Display
Manufacturer	DEA Engineering Company
Numeric Display	• 6 digit (back illuminated) • 3/8"characters • Locatable decimal point to 0, 1, 2 or 3 places
Accuracy	± 1 least significant figure or 0.18% whichever is greater
Input	• 50 KHZ maximum frequency • Open collector • TTL/CMOS compatible • Maximum input 18V • 10 µS minimum pulse width • Negative edge triggered
Power	8 - 30 VDC, 8 mA max., [jumpered 12 VDC OR 24VDC with backlighting, 100 mA maximum]
Operating Temperatures	15 - 120 °F (-10 - 50 °C)
Housing	• Black die-cast aluminum • IP65/NEMA4 using supplied gasket

Table A-11: Rosemount Absolute Pressure Transducer Specifications

Location	Pre-Heater Inlet	Pre-heater Exit	Post-heater Inlet	Post-heater Exit
Model	2088 A3M22A1M7	2088 A3M22A1M7	2088 A3S2BA1M7	2088 A3M22A1M7
Serial No.	138875	138873	237200	138872
Supply	6-14 VDC	6 -14 VDC	10.5-36 VDC	6-14 VDC
Output	1-5 V	1-5 V	4-20 mA	1-5 V
Range	0-800 PSIA			
Max W.P.	800 PSI (50 Bar)			
Accuracies	±0.25% of the span (400 psi in current facility)			
Operating Conditions	-40 to 121^{o}C			

Table A-12: Rosemount Differential Pressure Transducer Specifications

Location	Between Pre-heater Exit and Post-heater Inlet
Model	3051 CD3A22A1AB4M5
Serial No.	0443046
Supply	10.5-55 VDC
Output	4-20 mA
Range	0-36 PSI
Max W.P.	3626 PSI (250 Bar)
Accuracies	±0.075% of the span
Operating Conditions	-40 to 121^{o}C

Table A-13: Temperature Measurement Probes

Model	PT-6 Thermocouple Sensors (17 ga x 4" SS tubes installed)
Manufacturer	Physitemp Instrument Inc. (www.physitemp.com)
Supplier	ThermoWorks Inc.
Temp. range at tip	-273 to 350^{o}C
Time Constant	0.01 seconds
Sensor	Type T Thermocouple (Copper-Constantan)
Sensor Diameter	0.029"
Length	5 ft
Wire Report Number	R2577
Thermocouple Extension Wire	T-TW-26 Thermocouple wire Wire Report # 2115

Table A-14: AC Watt Transducer Specifications

Model	GW5-103E
Manufacturer	Ohio Semitronics Inc.
Input	0-150 V AC 0-1 AC Amps
Output	4-20 mA
Calibration Range	0 – 100 Watts
Accuracy	0.2% of reading
Response Time	< 400 milliseconds
Temperature Range	-20 to 60^{o}C

Table A-15: Water Pump Specifications

Produce	**Micro-External Gear Pump**
Manufacturer	Micropump Inc.
Supplier	GPM Inc., Macon, GA 31221 (Ph: 478 471 7867)
Part Number	81282
Pump type	• Magnetic Drive Gear Pump • Suction Shoe Style • Two or Three Helical Gears • Stationary Shafts • O-ring Seal
Series	GB (Model 201)
Gear set	PPS P35 gears
Pumping rate	1.17 ml/revolution
Maximum differential pressure	125 psi
Maximum system pressure	300 psi
Temperature range	-46 to 177°C
Viscosity range	0.2 to 1500 cps
Maximum Speed	10000 rpm
Mounting	A

Table A-16: Water Loop Pump Drive and Controller Specifications

Drive Type	AC – Universal Brush Type Permanent Magnet
Manufacturer	Micropump Inc.
Supplier	GPM Inc., Macon, GA 31221 (Ph: 478 471 7867)
Part Number	83433A
Drive Model	415 A
Supplier	Micropump, Inc.
Mount code	A
Speed range (RPM)	500 - 9000
Max. rated torque (NMn/In-oz)	92/13
Nominal (Watts/ HP)	66/0.089
Power Source	115 V AC
Connections	Cord & plug
Weight (max.)	5.50 kg

Table A-17: Water Pump Static Head Provider Specification

Product Name	Full-View Flow and Overflow Sights
Supplier	McMaster-Carr
Part Number	5072K91
Material	Aluminum body, plated-steel stand pipe, acrylic window, and Buna-N seals
Maximum Temperature	160^{o}F
Pipe Size	½”

Table A-18: Water Flow Meter Specifications

Product Name	**Polycarbonate Panel-Mount Flowmeter (Rotameter)**
Supplier	McMaster-Carr
Part No.	5079k18
Max. Pressure	100 psi @ 150^{o}F
Maximum Temperature	150^{o}F
Flow Range	4 – 40 gph
Pipe Size	1/8”
Scale Height	1 5/8”
Overall Height	4 13/16”
Accuracy	±4%
Control Valve	None

Table A-19: Water Loop Chiller Specifications

Heat Exchanger Type	**Tube-in-tube Counter Flow**
Fluids	Annulus: Ethylene-Glycol/Water Center: Water
Inner copper tube OD	6.35 mm (1/4”)
Inner copper tube thickness	0.81 mm (0.032”)
Outer steel tube OD	12.70 mm (0.5”)
Outer steel tube thickness	0.89 mm (0.035”)
Heat transfer length	5” (12.7 cm)

Table A-20: Water Loop Heater Specifications

Fittings Used	SS-810-3TFT	Stainless Female Run Tee, 1/2 in. OD - 3/8 in. FNPT - 1/2 in. OD
	SS-6-RB-2	Stainless Reducing Bushing, 3/8 in. MNPT - 1/8 in. FNPT
Cartridge Heater	Same as Refrigerant Heater Table A-2	

Table A-21: Data Acquisition System Specifications

Manufacturer	Iotech, Inc.
High Speed Temperature Measurement System	
Model	TempScan/1100
Serial No.	147648
Maximum Scan Rate	960 channels/s
Maximum Single Channel Scan Rate	60 Hz
Minimum Channel Configuration	32 Channels
Maximum Channel Configuration	992 Channels
Expansion Chassis	
Model	Exp/10A
Serial No.	139835
No. of Slots	2
Voltage Scanning Card	
Model	Temp V/32B
Serial No.	141934
No. of Channels	32
Thermocouple Scanning Card	
Model	Temp TC/32B
Serial No.	250834
No. of Channels	32

APPENDIX-B. REPRESENTATIVE CASE DATA ANALYSIS

B.1. Refrigerant Pre- and Post-Heater Heat Loss Calculation

For each of the heaters, two separate heat losses are considered: from the heater assembly to the ambient, and from the Copper tubing between the heaters and the test-section refrigerant channels to the ambient. As explained in Chapter 3, the refrigerant heaters are made by fitting a 2” long, ¼” diameter cartridge heater inside a Swagelok Female Run Tee fitting (Part No.: SS-600-3TFT). Figure B.1 shows a schematic of the refrigerant heater assembly.

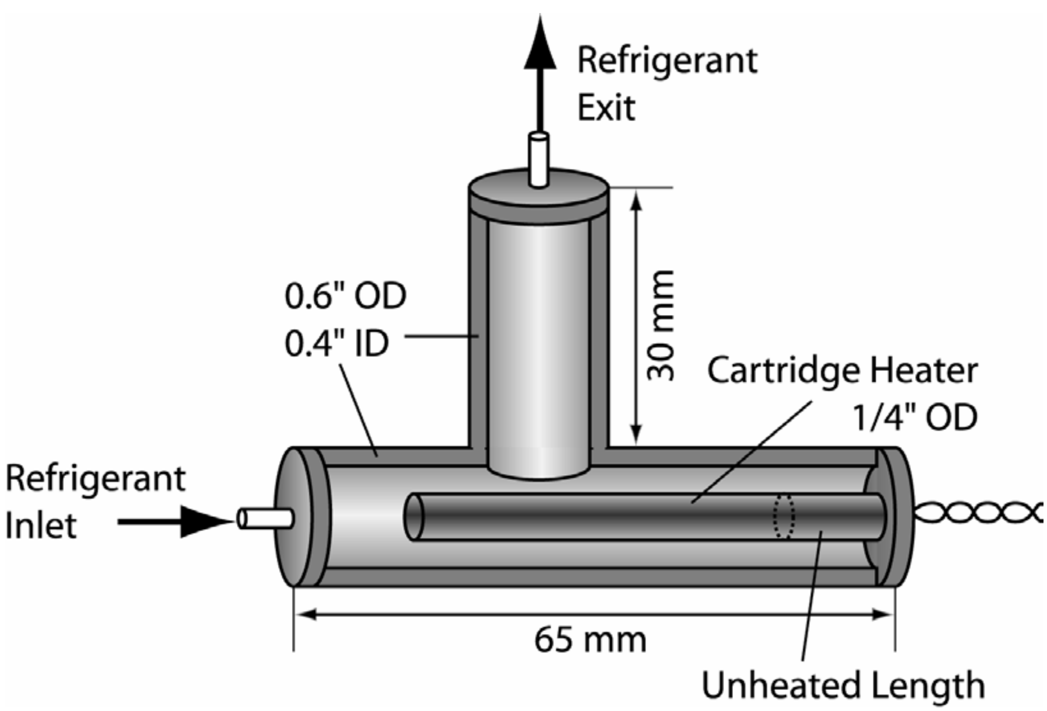

Figure B.1: Refrigerant Heater Schematic

The total length of the heater assembly is 65 mm along the length of the heater and approximately 30 mm perpendicular to the length of the heater. Thus, for the purpose of heat loss estimation, it is assumed to be a stainless steel tube of 10.16 mm (0.4") ID, 15.24 mm (0.6") OD and 95 mm (65 mm + 30 mm) length. The heater is installed in the center of the Swagelok Female Run Tee fitting with an unheated length in the beginning, thus the heater rod is surrounded by saturated refrigerant on all sides. Further, the refrigerant inventory in the heaters is large as compared to the refrigerant flow rate through the heater. Thus, even though the refrigerant enters the pre-heater in a subcooled state, the heater assembly is primarily filled with refrigerant at saturation temperature. Hence, the heat loss is calculated from the refrigerant at saturation temperature (corresponding to the measured pressure) to the ambient. Since the refrigerant flow velocities in the heater and the tubing between the heater and refrigerant channels are very small in all cases, the stratified flow heat transfer coefficient correlation (equation B.1) by Chato (1962) is used to determine the refrigerant heat transfer coefficient in the heaters.

$$h_{refg,H} = 0.728 \cdot K_c \cdot \left[\frac{g \cdot \rho_l \cdot (\rho_l - \rho_v) \cdot k_l^3 \cdot h_{lv}'}{\mu_l \cdot \left(T_{Refg} - T_{wall}\right) \cdot D_{TS,tube,ID}} \right]^{1/4} \qquad \text{(B.1)}$$

This condensation correlation is used even though there is boiling taking place in the heater due to the following reason. Boiling occurs at the surface of the cartridge heater where the heat is transferred from the heater to the refrigerant. At the inner surface of the fitting (from where the heat losses are being estimated), the heat is transferred from the refrigerant to the wall, which in turn leads to condensation at the wall. It should be noted that in all the heat loss calculations, the refrigerant convective thermal resistance and the tube conduction resistance are negligible compared to the thermal resistance of the insulation layer. The average insulation thickness for the heaters and the tube is 12.70 mm (0.5").

Table B-3 provides a detailed step-by-step calculation procedure for heat losses in each of the heaters. A brief summary is presented here for the pre-heater and post-heater energy balance. For the representative case being discussed, the refrigerant enters the pre-heater at 1727 kPa and a nominal subcooled temperature of 29.3°C (saturation temperature in pre-heater for this case is 61.1°C). A power input of 31.02 W is supplied to the pre-heater to heat the refrigerant to the desired saturation temperature and quality. Using the Chato (1962) heat transfer correlation, the refrigerant heat transfer coefficient in the pre-heater is determined to be 5200 W/m^2-K. With the heater tube ID, $D_{H,tube,ID}$, equal to 10.16 mm (0.4"), the refrigerant-side convective thermal resistance is 0.06 K/W (equation B.2).

$$R_{refg} = \frac{1}{h_{refg,H1} \cdot \pi \cdot D_{H,tube,ID} \cdot L_H} \tag{B.2}$$

With a tube ID of 10.16 mm (0.4"), OD of 15.24 mm (0.6") and an insulation thickness around the heater of 12.70 mm (0.5"), the tube and insulation resistances are determined using equation (B.3) and (B.4) to be 0.04 K/W and 38.21 K/W, respectively.

$$R_{tube} = \frac{\ln\left(\dfrac{D_{H,tube,OD}}{D_{H,tube,ID}}\right)}{k_{st} \cdot 2 \cdot \pi \cdot L_H} \tag{B.3}$$

$$R_{ins} = \frac{\ln\left(\dfrac{D_{H,ins,OD}}{D_{H,tube,OD}}\right)}{k_{ins} \cdot 2 \cdot \pi \cdot L_H} \tag{B.4}$$

It can be seen that the refrigerant convective thermal resistance and the tube conduction thermal resistance are negligible compared to the insulation resistance. For the complete range of test conditions, the refrigerant side convective heat transfer coefficient in the pre- and post-heater varies from 5000 to 6500 W/m^2-K, yielding a maximum convective thermal resistance of 0.07 K/W. This is still insignificant compared to the insulation thermal resistance of 38 K/W.

For an ambient temperature of 23^{o}C, the combined natural convection (3.4 W/m^2-K) and radiation (5.2 W/m^2-K) heat transfer coefficient is 8.6 W/m^2-K, which yields an insulation surface temperature of 30.6^{o}C. With the above resistances, the heat loss to the ambient from the pre-heater assembly is determined to be 0.80 W. The heat loss in the Copper tubing (ID 1.55 mm, OD 3.18 mm, Length 67 mm) from the pre-heater to the test section is calculated in a similar manner. Using the Chato (1962) correlation, the refrigerant heat transfer coefficient is determined to be 6500 W/m^2-K, and the three thermal resistances, i.e. refrigerant convection, tube conduction and insulation conduction resistance are determined to be 0.47, 0.004 and 121.4 K/W respectively. Again, it can be seen that the refrigerant and tube resistances are insignificant compared to the insulation resistance. With an ambient temperature of 23^{o}C and effective insulation surface area of 6×10^{-3} m^2, the combined natural convection and radiation heat transfer coefficient is again 8.6 W/m^2-K, which yields an insulation surface temperature of 28.2^{o}C. With the above resistances, the heat loss to the ambient from the tubing between the pre-heater assembly and the refrigerant channels is 0.27 W. This results in an overall heat loss of 1.07 W for the pre-heater and tubing assembly (equation B.5). For the purpose of uncertainty calculation, a conservative 50% uncertainty is assumed in the calculated heat losses.

$$Q_{H1,loss} = Q_{H1,heater,loss} + Q_{H1,2,TS,loss} \tag{B.5}$$

The post-heater heat losses are estimated in a similar manner. The pressure measured at the exit of the test section is 1678 kPa, representing a saturation temperature of 59.9°C. The losses include those from the tubing from the refrigerant channels to the post-heater assembly, and those from the post-heater assembly itself. For the post-heater assembly, the refrigerant heat transfer coefficient based on the Chato (1962) correlation is 5.2 kW/m^2-K, yielding a refrigerant convective thermal resistance of 0.06 K/W. The tube and the insulation conduction resistances are 0.04 K/W and 38.21 K/W, respectively, yielding an overall resistance of 38.32 K/W. With an ambient temperature of 23°C, the combined natural convection and radiation heat transfer coefficient is again 8.6 W/m^2-K, which yields an insulation surface temperature of 30.4°C and a heat loss from the post-heater of 0.77 W. Similarly, the heat loss from the tubing between the refrigerant channels and the post-heater is 0.26 W, resulting in an overall heat loss of 1.03 W from the post-heater and tubing assembly. Additional details of these calculations are provided in Table B-3.

B.2. Representative Case Analysis Tables

Table B-1: Fixed Experimental Parameters for Representative Case

Description	Symbol	Value
Test Section Details		
Refrigerant channel depth/height	d_{TS}	0.1 mm
Refrigerant channel width	w_{TS}	0.2 mm
Number of parallel refrigerant channels	N	18
Total length of channels	L_{Tube}	40 mm
Overall external width of refrigerant channels	$W_{channels}$	7.8 mm
Heat transfer length *(i.e. length of refrigerant channels in direct contact with the water channel block)*	$L_{TS,HT}$	15 mm
Refrigerant channel side fin length *(i.e. length of the refrigerant channels not in direct contact with the water channel blocks, on either side)*	$L_{TS,f,refg,side}$	12.5 mm
Diameter of the water channels in Cu blocks	D_w	0.79 mm (1/32")
Total number of water channels in both the blocks ($2 \times 5 = 10$)	N_w	10
Cu water block wall thickness from interface to water channels	$T_{wb,wall}$	1.9 mm
Outside diameter of the Cu tubing attached to the test section	$D_{TS,tube,OD}$	3.18 mm (1/8")
Thickness of the Cu tubing attached to the test section	$t_{TS,tube}$	0.81 mm (0.032")
Inside diameter of the Cu tubing attached to the test section	$D_{TS,tube,ID}$	1.55 mm
Thickness of the Cu wafer used in the fabrication of refrigerant channels	t_{wafer}	1.0 mm

Table B-1 continued…

Description	Symbol	Value
<u>Refrigerant Heater Details</u>		
Refrigerant heater Swagelok fitting ID	$D_{H,tube,ID}$	10.16 mm (0.4”)
Refrigerant heater Swagelok fitting OD	$D_{H,tube,OD}$	15.24 mm (0.6”)
Heater insulation thickness	$t_{H,ins}$	12.70 mm (0.5”)
Heater rod diameter	$D_{H,heater}$	6.35 mm (0.25”)
Refrigerant heater assembly length *Note: Actual length of the heater inside the fitting is 5.08 cm (2”). This is the end to end outside length of the fitting assembly with heater inside.*	L_H	65 mm (Hor.) + 30 mm (Ver.) = 95 mm
Total length of Cu tubing from heater to channels including bend	$L_{H,2,TS}$	67 mm
Horizontal length of the Cu tubing from heater to test section	$L_{H,2,TS,Hor}$	42 mm
Vertical length of the Cu tubing from heater to test section	$L_{H,2,TS,Ver}$	10 mm

Table B-2: Relevant Measured Parameters for Representative Case (D = 133 μm; AR = 2; T_{sat} = 60.5°C, G = 606 kg/m^2-s; x_{ave} = 0.39)

Description	Symbol	Value	Uncertainty
Refg. Pre-heater inlet pressure	$P_{H1,in}$	1727 kPa (250.4 psi)	± 6.9 kPa
Refg. Pre-heater exit pressure	$P_{H1,out}$	1727 kPa (250.4 psi)	± 6.9 kPa
Refg. Post-heater inlet pressure	$P_{H2,in}$	1678 kPa (243.4 psi)	± 6.9 kPa
Refg. Post-heater exit pressure	$P_{H2,out}$	1679 kPa (243.5 psi)	± 6.9 kPa
Refg. Pre-heater inlet temperature	$T_{H1,in}$	29.3°C	± 0.1°C
Refg. Post-heater exit temperature	$T_{H2,out}$	65.7°C	± 0.1°C
Pre-heater power input	Q_{H1}	31.02 W	± 0.2%
Post-heater power input	Q_{H2}	28.86 W	± 0.2%
Refrigerant flow rate	FR_{refg}	1.8×10^{-7} m^3/s (10.83 ml/min)	± 0.5%
Flow meter refrigerant temperature	$T_{R,FM}$	25.9°C	± 0.5°C
Flow rate for water loop	FR_{water}	3.878×10^{-5} m^3/s (36 gph)	± 2%
Upper block water inlet temperature	$T_{w,U,in}$	56.3°C	± 0.1°C
Upper block water exit temperature	$T_{w,U,out}$	56.4°C	± 0.1°C
Lower block water inlet temperature	$T_{w,L,in}$	56.3°C	± 0.1°C
Lower block water exit temperature	$T_{w,L,out}$	56.3°C	± 0.1°C
Measured pressure drop	$\Delta P_{measured}$	47.24 kPa (6.85 psi)	± 0.19 kPa

Table B-3: Pre-heater and Post-heater Energy Balance Calculations (D = 133 μm; AR = 2; T_{sat} = 60.5°C, G = 606 kg/m²-s; x_{ave} = 0.39)

Inputs	Equations	Results
Mass Flux Calculation		
$T_{R,FM}$ = 25.9°C	$\rho_{fm,refg} = f\left(T_{amb}, P_{H1,in}\right)$	$\rho_{fm,refg} = 1210 \text{ kg/m}^3$
$P_{H1,in}$ = 1727 kPa	$\dot{m} = FR_{refg} \times \rho_{fm,refg}$	$\dot{m} = 2.18\times10^{-4}$ kg/s
$FR_{refg} = 1.8\times10^{-7}$ m³/s	$A_{tot,TS} = d_{TS} \cdot w_{TS} \cdot N$	$A_{tot,TS} = 3.6\times10^{-7}$ m²
d_{TS} = 0.1 mm		
w_{TS} = 0.2 mm	$G = \dfrac{\dot{m}}{A_{tot,TS}}$	G = 606 kg/m²-s
Pre-Heater Heat Loss Estimation		
Heat losses in the pre-heater	$T_{H1,out} = T_{sat}\left(P = P_{H1,out}\right)$	
	Refrigerant properties:	$T_{H1,out}$ = 61.1°C
$P_{H1,out}$ = 1727 kPa	$k_l = k_l\left(T = T_{H1,out}, P = P_{H1,out}\right)$	$k_l = 64\times10^{-3}$ W/m-K
	$\rho_l = \rho_l\left(T = T_{H1,out}, P = P_{H1,out}\right)$	ρ_l = 1047 kg/m³
	$\mu_l = \mu_l\left(T = T_{H1,out}, P = P_{H1,out}\right)$	$\mu_l = 1.22\times10^{-4}$ kg/m-s
	$Cp_l = Cp_l\left(T = T_{H1,out}, P = P_{H1,out}\right)$	Cp_l = 1.7 kJ/kg-K

Table B-3 continued …

Inputs	Equations	Results
$D_{H,heater}$ = 6.35 mm $D_{H,tube,ID}$ = 10.16 mm	$\rho_v = \rho_v\left(T = T_{H1,out}, P = P_{H1,out}\right)$ $\mu_v = \mu_v\left(T = T_{H1,out}, P = P_{H1,out}\right)$ $h_l = f\left(x = 0, P = P_{H1,out}\right)$ $h_v = f\left(x = 1, P = P_{H1,out}\right)$ $h_{lv} = h_v - h_l$ $D_{H,ann} = D_{H,tube,ID} - D_{heater}$ Using Chato (1962) model: *Note: For applying Chato's correlation to determine the refrigerant heat transfer coefficient, the wall temperature needs to be known. Due to the thick insulation, the heat losses are quite low, leading to an almost insignificant temperature difference between the wall and refrigerant temperatures. Thus, the wall temperature is assumed to be 0.1°C less than the corresponding refrigerant temperature solely to enable calculations of heat losses.*	ρ_v = 90 kg/m^3 μ_v = 1.4×10^{-5} kg/m-s h_l = 141 kJ/kg h_v = 279 kJ/kg h_{lv} = 138 kJ/kg $D_{H,ann}$ = 3.81 mm

Table B-3 continued …

Inputs	Equations	Results
	$h_{lv}^{'} = h_{lv} \cdot \left[1 + 0.68 \cdot \dfrac{Cp_l \cdot \left(T_{H1,out} - T_{wall} \right)}{h_{lv}} \right]$	$h_{lv}^{'}$ = 138 kJ/kg
	$h_{refg,H1} = 0.728 \cdot K_c \cdot \left[\dfrac{g \cdot \rho_l \cdot \left(\rho_l - \rho_v \right) \cdot k_l^3 \cdot h_{lv}^{'}}{\mu_l \cdot \left(T_{H1,out} - T_{wall} \right) \cdot D_{H,ann}} \right]^{1/4}$	$h_{refg,H1}$ = 5.2 kW/m^2-K
g = 9.8 m/s^2 K_c = 0.76	$R_{refg} = \dfrac{1}{h_{refg,H1} \cdot \pi \cdot D_{H,tube,ID} \cdot L_H}$	R_{refg} = 6×10^{-2} K/W
	$k_{st} = f\left(T_{H1,out} \right)$	k_{st} = 15.9 W/m-K
L_H = 95 mm $D_{H,tube,OD}$ = 15.24 mm	$R_{tube} = \dfrac{\ln\left(\dfrac{D_{H,tube,OD}}{D_{H,tube,ID}} \right)}{k_{st} \cdot 2 \cdot \pi \cdot L_H}$	R_{tube} = 4×10^{-2} K/W
$t_{H,ins}$ = 12.70 mm	$D_{H,ins,OD} = D_{H,tube,OD} + 2 \cdot t_{H,ins}$	$D_{H,ins,OD}$ = 40.64 mm
k_{ins} = 0.043 W/m-K	$R_{ins} = \dfrac{\ln\left(\dfrac{D_{H,ins,OD}}{D_{H,tube,OD}} \right)}{k_{ins} \cdot 2 \cdot \pi \cdot L_H}$	R_{ins} = 38.21 K/W
	$R = R_{ins} + R_{tube} + R_{refg}$	R = 38.32 K/W

Table B-3 continued …

Inputs	Equations	Results
T_{amb} = 23°C $T_{H1,out}$ = 61.1°C	$A_{ins,H} = \pi \cdot D_{H,ins,OD} \cdot L_H$ The next four equations are solved iteratively to determine the value of T_{air}, $T_{S,ins}$, $Q_{H1,heater,loss}$ and h_{air} . $T_{air} = \frac{T_{amb} + T_{S,ins}}{2}$ $h_{air} = f\left(T_{air}, T_{S,ins}, D_{ins,OD}\right)$ A sample calculation for h_{air} (convection + radiation) is shown at the end of this table. $Q_{H1,heater,loss} = \frac{1}{R} \cdot \left(T_{H1,out} - T_{S,ins}\right)$ $Q_{H1,heater,loss} = h_{air} \cdot A_{ins,H} \cdot \left(T_{S,ins} - T_{amb}\right)$	$A_{ins,H}$ = 12.1×10^{-3} m^2 T_{air} = 26.8°C h_{air} = 8.6 W/m^2-K $T_{S,ins}$ = 30.6°C $Q_{H1,heater,loss}$ = 0.80 W

Table B-3 continued …

Inputs	Equations	Results
Heat loss in tubing from the pre-heater to the test section $T_{H1,out}$ = 61.1°C $k_l = 64 \times 10^{-3}$ W/m-K ρ_l = 1047 kg/m^3 $\mu_l = 1.22\times10^{-4}$ kg/m-s ρ_v = 90 kg/m^3 h_{lv}' = 138 kJ/kg K_c = 0.76 g = 9.81 m/s^2 $D_{TS,tube,ID}$ = 1.55 mm $L_{H,2,TS}$ = 67 mm $D_{TS,tube,OD}$ = 3.18 mm $t_{TS,tube,ins}$ = 12.7 mm k_{ins} = 0.043 W/m-K	Using Chato (1962) correlation: Again assuming the wall temperature to be 0.1°C less than the refrigerant temperature and using, h_{lv}' calculated earlier, we get: $h_{refg,H1,2,TS} = 0.728 \cdot K_c \cdot \left[\frac{g \cdot \rho_l \cdot (\rho_l - \rho_v) \cdot k_l^3 \cdot h_{lv}'}{\mu_l \cdot (T_{H1,out} - T_{wall}) \cdot D_{TS,tube,ID}} \right]^{1/4}$ $R_{refg} = \frac{1}{h_{refg,H1,2,TS} \cdot \pi \cdot D_{TS,tube,ID} \cdot L_{H,2,TS}}$ $k_{Cu} = f(T_{H1,out})$ $R_{tube} = \frac{\ln\left(\frac{D_{TS,tube,OD}}{D_{TS,tube,ID}}\right)}{k_{Cu} \cdot 2 \cdot \pi \cdot L_{H,2,TS}}$ $D_{tube,ins} = D_{TS,tube,OD} + 2 \cdot t_{TS,tube,ins}$ $R_{ins} = \frac{\ln\left(\frac{D_{tube,ins}}{D_{TS,tube,OD}}\right)}{k_{ins} \cdot 2 \cdot \pi \cdot L_{H,2,TS}}$	$h_{refg,H1,2,TS}$ = 6.5 kW/m^2-K R_{refg} = 0.47 K/W k_{Cu} = 398.3 W/m-K $R_{tube} = 4\times10^{-3}$ K/W $D_{tube,ins}$ = 28.58 mm R_{ins} = 121.4 K/W

Table B-3 continued …

Inputs	Equations	Results
T_{amb} = 23°C $T_{H1,out}$ = 61.1°C	$R = R_{ins} + R_{tube} + R_{refg}$ $A_{ins} = \pi \cdot D_{tube,ins} \cdot L_{H,2,TS}$ The next four equations are solved iteratively to determine the value of T_{air}, $T_{S,ins}$, $Q_{H1\_2\_TS,loss}$, h_{air} . $T_{air} = \frac{T_{amb} + T_{S,ins}}{2}$ $h_{air} = f\left(T_{air}, T_{S,ins}, D_{tube,ins}\right)$ $Q_{H1,2,TS,loss} = \frac{1}{R} \cdot \left(T_{H1,out} - T_{S,ins}\right)$ $Q_{H1,2,TS,loss} = h_{air} \cdot A_{ins} \cdot \left(T_{S,ins} - T_{amb}\right)$	R = 121.9 K/W A_{ins} = 6.0×10^{-3} m^2 T_{air} = 25.6°C h_{air} = 8.6 W/m^2-K $T_{S,ins}$ = 28.2°C $Q_{H1,2,TS,loss}$ = 0.27 W
Total Heat losses in the pre-heater $Q_{H1,2,TS,loss}$ = 0.27 W $Q_{H1,heater,loss}$ = 0.80 W	$Q_{H1,loss} = Q_{H1,heater,loss} + Q_{H1,2,TS,loss}$	$Q_{H1,loss}$ = 1.07 W
<u>Test Section Inlet Quality Estimation</u>		
Q_{H1} = 31.02 W $Q_{H1,loss}$ = 1.07 W	$Q_{H1,refg} = Q_{H1} - Q_{H1,loss}$	$Q_{H1,refg}$ =29.95 W

Table B-3 continued …

Inputs	Equations	Results
$P_{H1,in}$ = 1727 kPa $T_{H1,in}$ = 29.3°C $T_{H1,sat}$ = 61.1°C $\dot{m}$ = 2.18×10^{-4} kg/s P_{in} = 1724 kPa (at channels inlet)	$h_{H1,in} = f\left(T_{H1,in}, P_{H1,in}\right)$ $\Delta T_{sub} = T_{H1,sat} - T_{H1,in}$ $Q_{H1,refg} = \dot{m} \cdot \left(h_{H1,out} - h_{H1,in}\right)$ $h_{H1,out} = f\left(P_{in}, x_{in}\right)$	$h_{H1,in}$ = 93 kJ/kg ΔT_{sub} = 31.8°C $h_{H1,out}$ = 230 kJ/kg x_{in} = 0.64
Post Heater Heat Loss Estimation		
Heat loss in the post-heater $P_{H2,in}$ = 1678 kPa	$T_{H2,in} = T_{sat}(P = P_{H2,in})$ Refrigerant properties: $k_l = k_l\left(T = T_{H2,in}, P = P_{H2,in}\right)$ $\rho_l = \rho_l\left(T = T_{H2,in}, P = P_{H2,in}\right)$ $\mu_l = \mu_l\left(T = T_{H2,in}, P = P_{H2,in}\right)$ $Cp_l = Cp_l\left(T = T_{H2,in}, P = P_{H2,in}\right)$	$T_{H2,in}$ = 59.9°C k_l = 65×10^{-3} W/m-K ρ_l = 1054 kg/m^3 μ_l = 1.24×10^{-4} kg/m-s Cp_l = 1.7 kJ/kg-K ρ_v = 87 kg/m^3

Table B-3 continued …

Inputs	Equations	Results
$g = 9.81$ m/s^2 $D_{H,ann} = 3.81$ mm $K_c = 0.76$ $D_{H,tube,ID} = 10.16$ mm $L_H = 95$ mm	$\rho_v = \rho_v\left(T = T_{H2,in}, P = P_{H2,in}\right)$ $\mu_v = \mu_v\left(T = T_{H2,in}, P = P_{H2,in}\right)$ $h_l = f\left(x = 0, P = P_{H2,in}\right)$ $h_v = f\left(x = 1, P = P_{H2,in}\right)$ $h_{lv} = h_v - h_l$ Using Chato (1962) model: Assuming that T_{wall} is 0.1°C less than the refrigerant temperature. $h_{lv}^{'} = h_{lv} \cdot \left[1 + 0.68 \cdot \frac{Cp_l \cdot \left(T_{H2,in} - T_{wall}\right)}{h_{lv}}\right]$ $h_{refg,H2} = 0.728 \cdot K_c \cdot \left[\frac{g \cdot \rho_l \cdot \left(\rho_l - \rho_v\right) \cdot k_l^3 \cdot h_{lv}^{'}}{\mu_l \cdot \left(T_{H2,in} - T_{wall}\right) \cdot D_{H,ann}}\right]^{1/4}$ $R_{refg} = \frac{1}{h_{refg,H2} \cdot \pi \cdot D_{H,tube,ID} \cdot L_H}$ $k_{st} = f\left(T_{H1,out}\right)$	$\mu_v = 1.39 \times 10^{-5}$ kg/m-s $h_l = 139$ kJ/kg $h_v = 278$ kJ/kg $h_{lv} = 139$ kJ/kg $T_{wall} = 59.8$ °C $h_{lv}^{'} = 139$ kJ/kg $h_{refg,H2} = 5.2$ kW/m^2-K $R_{refg} = 6 \times 10^{-2}$ K/W $k_{st} = 15.9$ W/m-K

Table B-3 continued …

Inputs	Equations	Results
$D_{H,tube,OD}$ = 15.24 mm	$R_{tube} = \dfrac{\ln\left(\dfrac{D_{H,tube,OD}}{D_{H,tube,ID}}\right)}{k_{st}\cdot 2\cdot\pi\cdot L_H}$	R_{tube} = 4×10^{-2} K/W
$D_{H,ins,OD}$ = 40.64 mm k_{ins} = 0.043 W/m-K	$R_{ins} = \dfrac{\ln\left(\dfrac{D_{H,ins,OD}}{D_{H,tube,OD}}\right)}{k_{ins}\cdot 2\cdot\pi\cdot L_H}$	R_{ins} = 38.21 K/W
	$R = R_{ins} + R_{tube} + R_{refg}$	R = 38.32 K/W
T_{amb} = 23°C $T_{H2,in}$ = 59.9°C $A_{,ins,H}$ = 12.13×10^{-3} m^2	The next four equations are solved iteratively to determine the value of T_{air}, $T_{S,ins}$, $Q_{H2\_heater,loss}$, and h_{air} . $T_{air} = \dfrac{T_{amb}+T_{S,ins}}{2}$ $h_{air} = f\left(T_{air}, T_{s,ins}, D_{ins,OD}\right)$ $Q_{H2,heater,loss} = \dfrac{1}{R}\cdot\left(T_{H2,in} - T_{S,ins}\right)$ $Q_{H2,heater,loss} = h_{air}\cdot A_{ins,H}\cdot\left(T_{S,ins} - T_{amb}\right)$	T_{air} = 26.7°C h_{air} = 8.6 W/m^2-K $T_{S,ins}$ = 30.4°C $Q_{H2,heater,loss}$ = 0.77 W

Table B-3 continued …

Inputs	Equations	Results
Heat loss in tubing from the post-heater to the test section $T_{H2,in}$ = 59.9°C k_l = 65×10^{-3} W/m-K ρ_l = 1054 kg/m^3 μ_l = 1.24×10^{-4} kg/m-s ρ_v = 87 kg/m^3 T_{wall} = 59.8 °C $h_{lv}^{'}$ = 142.6 kJ/kg K_c = 0.76 $D_{TS,tube,ID}$ = 1.549 mm $L_{H,2,TS}$ = 67 mm $D_{TS,tube,OD}$ = 3.18 mm $D_{tube,ins}$ = 28.58 mm	Again assuming the wall temperature to be 0.1°C less than the refrigerant temperatures and using Chato (1962) correlation. $h_{lv}^{'}$ is known from the previous section. $h_{refg,TS,2,H2} = 0.728 \cdot K_c \cdot \left[\frac{g \cdot \rho_l \cdot (\rho_l - \rho_v) \cdot k_l^3 \cdot h_{lv}^{'}}{\mu_l \cdot (T_{H2,in} - T_{wall}) \cdot D_{TS,tube,ID}} \right]^{1/4}$ $R_{refg} = \frac{1}{h_{refg,TS\_2\_H2} \cdot \pi \cdot D_{TS,tube,ID} \cdot L_{H,2,TS}}$ $k_{Cu} = f(T_{H2,in})$	$h_{refg,TS,2,H2}$ = 6.6 kW/m^2-K R_{refg} = 0.47 K/W k_{cu} = 398 W/m-K R_{tube} = 4×10^{-3} K/W

Table B-3 continued …

Inputs	Equations	Results
K_{ins} = 0.043 W/m-K $L_{TS,2,H}$ = 67 mm	$R_{tube} = \dfrac{\ln\left(\dfrac{D_{TS,tube,OD}}{D_{TS,tube,ID}}\right)}{k_{Cu} \cdot 2 \cdot \pi \cdot L_{H1,2,TS}}$	R_{ins} = 121.4 K/W
	$R_{ins} = \dfrac{\ln\left(\dfrac{D_{tube,ins}}{D_{TS,tube,OD}}\right)}{k_{ins} \cdot 2 \cdot \pi \cdot L_{TS,2,H}}$	R = 121.9 K/W
	$R = R_{ins} + R_{tube} + R_{refg}$	$A_{ins} = 6.02\times10^{-3}$ m^2
	$A_{ins} = \pi \cdot D_{tube,ins} \cdot L_{TS,2,H}$	
T_{amb} = 23°C	The next four equations are solved iteratively to determine the value of T_{air}, $T_{S,ins}$, $Q_{TS,2,H2,loss}$, and h_{air} .	T_{air} = 25.5°C
	$T_{air} = \dfrac{T_{amb} + T_{S,ins}}{2}$	h_{air} = 8.6 W/m^2-K
	$h_{air} = f\left(T_{air}, T_{S,ins}, D_{tube,ins}\right)$	$T_{S,ins}$ = 28.1°C
$T_{H2,in}$ = 59.9°C	$Q_{TS,2,H2,loss} = \dfrac{1}{R} \cdot \left(T_{H2,in} - T_{S,ins}\right)$	$Q_{TS,2,H2,loss}$ = 0.26 W
	$Q_{TS\_2\_H2,loss} = h_{air} \cdot A_{eff,ins} \cdot \left(T_{S,ins} - T_{amb}\right)$	

Table B-3 continued …

Inputs	Equations	Results
Total heat losses in the post-heater $Q_{TS,2,H2,loss}$ = 0.26 W $Q_{H2,heater,loss}$ = 0.77 W	$Q_{H2,loss} = Q_{H2,heater,loss} + Q_{TS,2,H2,loss}$	$Q_{H2,loss}$ = 1.03 W
<u>Test Section Exit Quality Estimation</u>		
Q_{H2} = 28.86 W $Q_{H2,loss}$ = 1.03 W $T_{H2,out}$ = 65.7°C $T_{H2,sat}$ = 59.9°C $P_{H2,out}$ = 1679 kPa $\dot{m} = 2.18\times10^{-4}$ kg/s P_{out} = 1679 kPa	$Q_{H2,refg} = Q_{H2} - Q_{H2,loss}$ $h_{H2,out} = f\left(T_{H2,out}, P_{H2,out}\right)$ $\Delta T_{\sup} = T_{H2,out} - T_{H2,sat}$ $Q_{H2,refg} = \dot{m}\cdot\left(h_{H2,out} - h_{H2,in}\right)$ $h_{H2,in} = f\left(P_{H2,in}, x_{out}\right)$	$Q_{H2,refg}$ = 27.83 W $h_{H2,out}$ = 286 kJ/kg $\Delta T_{sup} = 5.8^{o}$C $h_{H2,in}$ = 159 kJ/kg x_{out} = 0.14
<u>Test Section Heat Duty</u>		
$\dot{m} = 2.18\times10^{-4}$ kg/s $h_{H2,in}$ = 159 kJ/kg $h_{H1,out}$ = 230 kJ/kg	$Q_{TS} = \dot{m}\left(h_{H1,out} - h_{H2,in}\right)$	Q_{TS} = 15.54 W

Table B-4: Sample Air Heat Transfer Coefficient Calculation

Inputs	Equations	Results
Sample Calculation for Air Heat Transfer Coefficient: ***(Used in pre-heater heat loss calculation)***		
$T_{s,ins}$ = 30.6°C T_{amb} = 23°C	$T_{air} = \frac{T_{S,ins} + T_{amb}}{2}$ $k_{air} = f\left(T_{air}\right)$	T_{air} = 26.8°C k_{air} = 25.6×10^{-3} W/m-K
$P_{air} = 101\ kPa$	$\mu_{air} = f\left(T_{air}\right)$ $\rho_{air} = f\left(T_{air}, P_{air}\right)$ $Cp_{air} = f\left(T_{air}\right)$ $\beta_{air} = \beta\left(T_{air}\right)$	μ_{air} = 1.86×10^{-5} kg/m-s ρ_{air} = 1.173 kg/m^3 Cp_{air} = 1.01 kJ/kg-K
g = 9.81 m/s^2 D_{OD} = 40.64 mm	$\Pr_{air} = Cp_{air}\frac{\mu_{air}}{k_{air}}$ $\nu_{air} = \frac{\mu_{air}}{\rho_{air}}$ $Ra_{air} = g \cdot \beta_{air} \cdot \left(T_{s,ins} - T_{air}\right) \cdot D_{OD}{}^3 \cdot \frac{\Pr_{air}}{\nu_{air}{}^2}$ Using free convection Nu correlation for flow around horizontal cylinder (Churchill and Chu, 1975) recommended by Incropera and Dewitt (1996) pp. 502.	β_{air} = 3.3×10^{-3} 1/K $\Pr_{air}$ = 0.73 ν_{air} = 1.6×10^{-5} m^2/s Ra_{air} = 24×10^3

Table B-4 continued …

Inputs	Equations	Results
Assuming $\varepsilon = 0.85$ for insulation surface	$$Nu_{air} = \left[0.6 + 0.387 \cdot \frac{Ra_{air}^{1/6}}{\left[1+\left(\frac{0.559}{\Pr_{air}}\right)^{\left(\frac{9}{16}\right)}\right]^{\left(\frac{8}{27}\right)}} \right]^2$$	$Nu_{air} = 5.4$
	$$h_{conv} = Nu_{air} \cdot \frac{k_{air}}{D_{OD}}$$	$h_{conv} = 3.4$ W/m^2-K
	$$h_{rad} = \varepsilon \times 5.67 \times 10^{-8} \times \left[\left(T_S + 273.15\right)^2 + \left(T_{amb} + 273.15\right)^2 \right] \times \left(T_S + 273.15 + T_{amb} + 273.15\right)$$	$h_{rad} = 5.2$ W/m^2-K
	$$h_{air} = h_{rad} + h_{conv}$$	$h_{air} = 8.6$ W/m^2-K

Table B-5: Pressure Drop Analysis Calculations (D = 133 μm; AR = 2; T_{sat} = 60.5°C, G = 606 kg/m²-s; x_{ave} = 0.39)

Inputs	Equations	Results
	<u>Area Calculations</u>	
$D_{TS,tube,ID}$ = 1.55 mm *Fitting ID* = 2.29 mm	$A_{tube,TS} = \pi\left(\frac{D_{TS,tube,ID}}{2}\right)^2$ $A_{fitting,TS} = \pi\left(\frac{0.00229}{2}\right)^2$	$A_{tube,TS} = 1.89\times10^{-6}$ m² $A_{fitting} = 4.10\times10^{-6}$ m²
	<u>Contraction ΔP from Fitting to Inlet Tubing (Section-AA)</u>	
$\dot{m} = 2.18\times10^{-4}$ kg/s $A_{tube,TS} = 1.89\times10^{-6}$ m² $A_{fitting} = 4.10\times10^{-6}$ m² $T_{H1,out}$ = 61.1°C $P_{H1,out}$ = 1727 kPa x_{in} = 0.64	$G_{tube} = \frac{\dot{m}}{A_{tube,TS}}$ Homogenous flow model (Recommended by Hewitt *et al.* (1993), pp. 402) $\gamma_{con} = \frac{A_{fitting}}{A_{tube,TS}}$ $C_C = \frac{1}{0.639\left(1-\frac{1}{\gamma_{con}}\right)^{0.5}+1}$	G_{tube} = 116 kg/m²-s γ_{con} = 2.18 C_c = 0.68

Table B-5 continued …

Inputs	Equations	Results
$\rho_l = 1047$ kg/m^3 $\rho_g = 90$ kg/m^3	$\Psi_{H,x_{in}} = \left\lvert 1 + x_{in}\left(\frac{\rho_l}{\rho_g} - 1\right)\right\rvert$ $\Delta P_{con,H1} = \frac{G_{tube}{}^2}{2\rho_l}\left[\left(\frac{1}{C_C} - 1\right)^2 + 1 - \frac{1}{\gamma_{con}{}^2}\right]\Psi_{H,xin}$	$\Psi_{H,xin} = 7.85$ $\Delta P_{con,H1} = 51$ Pa
Frictional ΔP in Tubing from Pre-Heater to Refrigerant Channels		
$x = x_{in} = 0.64$ $\rho_l = 1047$ kg/m^3 $\rho_v = 90$ kg/m^3 $\mu_l = 1.2 \times 10^{-4}$ kg/m-s $\mu_v = 1.4 \times 10^{-5}$ kg/m-s $D = D_{TS,tube,ID} = 1.55$ mm $G = G_{tube} = 116$ kg/m^2-s	Void fraction, $\alpha = \left[1 + \left(\frac{1-x}{x}\right)^{0.74}\left(\frac{\rho_v}{\rho_l}\right)^{0.65}\left(\frac{\mu_l}{\mu_v}\right)^{0.13}\right]^{-1}$ (Baroczy, 1965) Liquid Reynolds number, $\mathrm{Re}_l = \frac{GD(1-x)}{\left(1+\sqrt{\alpha}\right)\mu_l}$ Vapor Reynolds number, $\mathrm{Re}_v = \frac{GDx}{\mu_v\sqrt{\alpha}}$ Friction factor for laminar film, $f_l = \frac{64}{\mathrm{Re}_l}$ In the current case liquid film is laminar, but if for other data points the	$\alpha = 0.852$ $Re_l = 273$ $Re_v = 8.9\times10^3$ $f_l = 0.235$

Table B-5 continued …

Inputs	Equations	Results
$\sigma = 3.6\times10^{-3}$ N/m	liquid film is turbulent, then the Blassius friction factor should be used. Vapor friction factor, $f_v = 0.316 \cdot \mathrm{Re}_v^{-0.25}$ $\left(dP/dz\right)_l = \dfrac{f_l \cdot G^2 \cdot (1-x)^2}{2 \cdot D.\rho_l}$ $\left(dP/dz\right)_v = \dfrac{f_v \cdot G^2 \cdot x^2}{2 \cdot D.\rho_v}$ Annular flow model proposed by Garimella *et al.* (2005) Martinelli Parameter, $X = \left[\dfrac{\left(dP/dz\right)_l}{\left(dP/dz\right)_v}\right]^{1/2}$ $j_l = \dfrac{G(1-x)}{\rho_l(1-\alpha)}$ $\psi = \dfrac{j_l \mu_l}{\sigma}$ $\dfrac{f_i}{f_l} = A \cdot X^a \mathrm{Re}_l^{\,b} \psi^c$ where, Laminar region ($\mathrm{Re}_l < 2100$): $A = 1.308\times10^{-3}$; $a = 0.4273$; $b = 0.9295$; $c = -0.1211$	$f_v = 0.033$ $\left(dP/dz\right)_l = 123$ Pa/m $\left(dP/dz\right)_v = 648$ Pa/m $X = 0.435$ $j_l = 0.266$ m/s $\psi = 9.03\times10^{-3}$ $f_i = 69.8\times10^{-3}$

Table B-5 continued …

Inputs	Equations	Results
$L_{H,2,TS,Hor}$ = 42 mm $L_{H,2,TS,Ver}$ = 10 mm	$\frac{\Delta P}{L} = \frac{1}{2} \cdot f_i \rho_v V_v^2 \cdot \frac{1}{D_i} = \frac{1}{2} \cdot f_i \frac{G^2 \cdot x^2}{\rho_v \cdot \alpha^{2.5}} \cdot \frac{1}{D}$ $\Delta P_{H1,2,TS,Hor} = \frac{\Delta P}{L} \times L_{H,2,TS,Hor}$ $\Delta P_{H1,2,TS,Ver} = \frac{\Delta P}{L} \times L_{H,2,TS,Ver}$	$\frac{\Delta P}{L} = 2.1$ kPa/m $\Delta P_{H1,2,TS,Hor}$ = 87 Pa $\Delta P_{H1,2,TS,ver}$ = 21 Pa
Bend ΔP in Inlet Tubing		
G_{tube} = 116 kg/m^2-s ρ_l = 1047 kg/m^3 $\Psi_{H,xin}$ = 7.85 k_B = 0.15	Homogenous flow model (Recommended by Hewitt *et al. (1993)*, pp. 402, Eq. 10.36). $\Delta P_{Bend,in} = k_B \cdot \frac{G_{tube}^{\;2}}{2 \cdot \rho_l} \cdot \Psi_{H,x_{in}}$	$\Delta P_{Bend,in}$ = 8 Pa
Expansion and Bend Pressure Drop from Inlet Tube to Header (Section-BB: Figure 4.1)		
Expansion ΔP from inlet tube to header N = 18 w_{TS} = 0.2 mm	$A_{header,up} = 0.004 \times \left[(N-1) \times 0.0001 + N \cdot w_{TS} \right]$	$A_{header,up}$ = 2.12×10^{-5} m^2 γ_{exp} = 0.089

Table B-5 continued …

Inputs	Equations	Results
$A_{tube,TS} = 1.89\times10^{-6}$ m^2 $x_{in} = 0.64$ $T_{H1,out} = 61.1$°C $\rho_l = 1047$ kg/m^3 $\rho_v = 90$ kg/m^3 $B_B = 0.25$ $G_{tube} = 116$ kg/m^2-s	$\gamma_{\exp} = \frac{A_{tube,TS}}{A_{header,up}}$ $\Psi_{S,x_{in}} = \left[1+\left(\frac{\rho_l}{\rho_g}-1\right)\left(B_B.x_{in}(1-x_{in})+x_{in}^2\right)\right]$ Separated Flow Model (Recommended by Hewitt et al. (1993), pp. 402 & 410, Eq. 10.34) $\Delta P_{\exp,TS,header,in} = -\frac{G_{tube}^2\gamma_{\exp}(1-\gamma_{\exp})\Psi_S}{\rho_L}$	$\Psi_{S,xin} = 6.03$ $\Delta P_{exp,TS,header,in} = -6$ Pa
Bend ΔP for change in flow direction in header $\dot{m} = 2.18\times10^{-4}$ kg/s $d_{TS} = 100$ µm $\rho_l = 1047$ kg/m^3 $\Psi_{H,xin} = 7.85$ $k_B = 0.6$	Homogenous flow model (Recommended by Hewitt (1993), pp. 402, Eq. 10.36). $G_{header} = \frac{\dot{m}}{\pi\cdot D_{TS,tube,ID}\cdot d_{TS}}$ $\Delta P_{Bend,Header,in} = k_B\cdot\frac{G_{header}^2}{2\cdot\rho_l}\cdot\Psi_{H,x_{in}}$	$G_{header} = 448$ kg/m^2-s $\Delta P_{Bend,header,in} = 452$ Pa

Table B-5 continued …

Inputs	Equations	Results
Contraction Pressure Drop from Inlet Header to Channel (Section-CC: Figure 4.1)		
$A_{header,TS} = 5.3\times10^{-7}$ m^2 $A_{tot,TS} = 3.6\times10^{-7}$ m^2	$\gamma_{con} = \dfrac{A_{header,TS}}{A_{tot,TS}}$ $C_C = \dfrac{1}{0.639\left(1-\dfrac{1}{\gamma_{con}}\right)^{0.5}+1}$	$\gamma_{con} = 1.472$ $C_c = 0.734$
$G = 606$ kg/m^2-s $\rho_l = 1047$ kg/m^3 $\Psi_{H,xin} = 7.85$	Homogenous flow model (Recommended by Hewitt, pp. 402, Eq. 10.35). $\Delta P_{con,TS,in} = \dfrac{G^2}{2\rho_l}\left[\left(\dfrac{1}{C_C}-1\right)^2+1-\dfrac{1}{\gamma_{con}^{\;2}}\right]\Psi_{H,xin}$	$\Delta P_{con,TS,in} = 923$ Pa
Deceleration Pressure Gain in Channels		
$T_{in} = 61.1$°C $P_{in} = 1727$ kPa $x_{in} = 0.64$ $\rho_{l,in} = 1047$ kg/m^3 $\mu_{l,in} = 1.22\times10^{-4}$ kg/m-s $\rho_{v,in} = 90$ kg/m^3	Eq. 10.91 of "Liquid Vapor Phase Change Phenomena" by Carey (1992). $\alpha\big\|_{x=x_{in}} = \left[1+\left(\dfrac{1-x_{in}}{x_{in}}\right)^{0.74}\left(\dfrac{\rho_{v,in}}{\rho_{l,in}}\right)^{0.65}\left(\dfrac{\mu_{l,in}}{\mu_{v,in}}\right)^{0.13}\right]^{-1}$	$\alpha\big\|_{x=x_{in}} = 0.852$

Table B-5 continued …

Inputs	Equations	Results
$\mu_{v,in} = 1.4\times10^{-5}$ kg/m-s $T_{out} = 59.9°C$ $P_{out} = 1679$ kPa $\rho_{l,out} = 1054$ kg/m^3 $\mu_{l,out} = 1.24\times10^{-4}$ kg/m-s $\rho_{v,out} = 87$ kg/m^3 $\mu_{v,out} = 1.4\times10^{-5}$ kg/m-s $x_{out} = 0.14$ $G = 606$ kg/m^2-s	$\alpha\big\|_{x=x_{out}} = \left[1+\left(\frac{1-x_{out}}{x_{out}}\right)^{0.74}\left(\frac{\rho_{v,out}}{\rho_{l,out}}\right)^{0.65}\left(\frac{\mu_{l,out}}{\mu_{v,out}}\right)^{0.13}\right]^{-1}$ Eq. 10.111 of "Liquid Vapor Phase Change Phenomena" by Carey (1992). (Assuming Entrainment E = 0) $\Delta P_{deceleration} = \left[\frac{G^2x^2}{\rho_v\alpha}+\frac{G^2(1-x)^2}{\rho_l(1-\alpha)}\right]_{x=x_{in}} - \left[\frac{G^2x^2}{\rho_v\alpha}+\frac{G^2(1-x)^2}{\rho_l(1-\alpha)}\right]_{x=x_{out}}$	$\alpha\big\|_{x=x_{out}} = 0.497$ $\Delta P_{decleration} = 1610$ Pa (Pressure Gain)
Expansion Pressure Drop From Channels to Exit Header (Section-DD: Figure 4.1)		
$A_{header,TS} = 5.3\times10^{-7}$ m^2 $A_{tot,TS} = 3.6\times10^{-7}$ m^2 $T_{H2,in} = 59.9°C$ $P_{H2,in} = 1678$ kPa $x_{out} = 0.14$ $\rho_l = 1054$ kg/m^3	$\gamma_{\exp} = \frac{A_{tot,TS}}{A_{header,TS}}$ $\Psi_{S,x_{out}} = \left[1+\left(\frac{\rho_l}{\rho_v}-1\right)\left(B_B.x_{out}(1-x_{out})+x_{out}{}^2\right)\right]$ Separated Flow Model (Recommended by Hewitt, pp. 402 & 410, Eq.	$\gamma_{exp} = 0.679$ $\Psi_{S,xout} = 1.55$

Table B-5 continued …

Inputs	Equations	Results
$\rho_v = 87$ kg/m^3 $B_B = 0.25$ $G = 606$ kg/m^2-s	10.34) $\Delta P_{\exp} = -\frac{G^2 \gamma_{\exp}(1-\gamma_{\exp})\Psi_S}{\rho_L}$	$\Delta P_{exp,\ TS,out} = -118$ Pa
<u>Contraction and Bend Pressure Drop in Exit Header (Section-EE: Figure 4.1)</u>		
Bend ΔP from header to tube $G_{header} = 448$ kg/m^2-s $\rho_l = 1054$ kg/m^3 $\Psi_{H,xin} = 2.55$ $k_B = 0.6$	Homogenous flow model (Recommended by Hewitt, pp. 402, Eq. 10.36). $\Delta P_{Bend,header,out} = k_B \cdot \frac{G_{header}{}^2}{2 \cdot \rho_l} \cdot \Psi_{H,xout}$	$\Delta P_{Bend,header,in} = 146$ Pa
Contraction pressure drop from header to exit tube $A_{tube,TS} = 1.89\times10^{-6}$ m^2 $A_{header} = 2.12\times10^{-5}$ m^2 $T_{H2,in} = 59.9$°C $x_{out} = 0.14$	$\gamma_{con} = \frac{A_{header,TS}}{A_{tube,TS}}$ $C_C = \frac{1}{0.639\left(1-\frac{1}{\gamma_{con}}\right)^{0.5}+1}$	$\gamma_{con} = 11.24$ $C_c = 0.62$

Table B-5 continued …

Inputs	Equations	Results
ρ_l = 1054 kg/m^3 ρ_v = 87 kg/m^3 G_{tube} = 116 kg/m^2-s	$\Psi_{H,x_{out}} = \left\lvert 1 + x_{out}\left(\frac{\rho_l}{\rho_v} - 1\right)\right\rvert$ Homogenous flow model (Recommended by Hewitt, pp. 402, Eq. 10.35). $\Delta P_{con,TS,header,out} = \frac{G_{tube}^{2}}{2\rho_l}\left[\left(\frac{1}{C_C} - 1\right)^2 + 1 - \frac{1}{\gamma_{con}^{2}}\right]\Psi_H$	$\Psi_{H,xout}$ = 2.55 $\Delta P_{con,TS,header,out}$ = 22 Pa
<u>Frictional ΔP in Outlet Tubing</u>		
$x = x_{out}$ = 0.14 ρ_l = 1054 kg/m^3 ρ_v = 87 kg/m^3 μ_l = 1.24 × 10^{-4} μ_v = 1.4 × 10^{-5} D = 1.55 mm $G = G_{tube}$ = 116 kg/m^2-s	Annular flow model proposed by Garimella *et al.* (2005): Void fraction, $\alpha = \left[1 + \left(\frac{1-x}{x}\right)^{0.74}\left(\frac{\rho_v}{\rho_l}\right)^{0.65}\left(\frac{\mu_l}{\mu_v}\right)^{0.13}\right]^{-1}$ (Baroczy, 1965) Liquid Reynolds number, $\mathrm{Re}_l = \frac{GD(1-x)}{\left(1+\sqrt{\alpha}\right)\mu_l}$ Vapor Reynolds number, $\mathrm{Re}_v = \frac{GDx}{\mu_v\sqrt{\alpha}}$ Friction factor for laminar film, $f_l = \frac{64}{\mathrm{Re}_l}$	α = 0.4975 Re_l = 731 Re_v = 2553 f_l = 0.088

Table B-5 continued …

Inputs	Equations	Results
ReCL = 2100 ReCU = 3400	Vapor friction factor, $f\left(\mathrm{Re}_{CL}\right)=\dfrac{64}{\mathrm{Re}_{CL}}$ & $f\left(\mathrm{Re}_{CU}\right)=0.316\cdot\mathrm{Re}_{CU}{}^{-0.25}$ $f_v=\exp\left[\left(\dfrac{\ln\left(\mathrm{Re}_v\right)-\ln\left(\mathrm{Re}_{CL}\right)}{\ln\left(\mathrm{Re}_{CU}\right)-\ln\left(\mathrm{Re}_{CL}\right)}\right)\times\left(\ln\left(f\left(\mathrm{Re}_{CU}\right)\right)-\ln\left(f\left(\mathrm{Re}_{CL}\right)\right)\right)+\ln\left(f\left(\mathrm{Re}_{CL}\right)\right)\right]$	$f(Re_{CL}) = 0.030$ $f(Re_{CU}) = 0.041$ $f_v = 0.034$
	$\left(dP/dz\right)_l=\dfrac{f_l\cdot G^2\cdot\left(1-x\right)^2}{2\cdot D.\rho_l}$	$\left(dP/dz\right)_l = 266$ Pa/m
	$\left(dP/dz\right)_v=\dfrac{f_v\cdot G^2\cdot x^2}{2\cdot D.\rho_v}$	$\left(dP/dz\right)_v = 33$ Pa/m
	Martinelli Parameter, $X=\left[\dfrac{\left(dP/dz\right)_l}{\left(dP/dz\right)_v}\right]^{1/2}$	$X = 2.84$
	$j_l=\dfrac{G\left(1-x\right)}{\rho_l\left(1-\alpha\right)}$	$j_l = 0.188$ m/s
$\sigma = 3.73\times10^{-3}$ N/m	$\psi=\dfrac{j_l\mu_l}{\sigma}$	$\psi = 6.25\times10^{-3}$
	$\dfrac{f_i}{f_l}=A\cdot X^a\,\mathrm{Re}_l{}^b\,\psi^c$	

Table B-5 continued …

Inputs	Equations	Results
$L_{H,2,TS,Hor}$ = 42 mm $L_{H,2,TS,Ver}$ = 10 mm	where, Laminar region (Re_l < 2100): A = 1.308×10^{-3}; a = 0.4273; b = 0.9295; c = -0.1211 $\frac{\Delta P}{L} = \frac{1}{2} \cdot f_i \rho_v V_v^2 \cdot \frac{1}{D_i} = \frac{1}{2} \cdot f_i \frac{G^2 \cdot x^2}{\rho_v \cdot \alpha^{2.5}} \cdot \frac{1}{D}$ $\Delta P_{TS,2,H2,Hor} = \frac{\Delta P}{L} \times L_{H,2,TS,Hor}$ $\Delta P_{TS,2,H2,Ver} = \frac{\Delta P}{L} \times L_{H,2,TS,Ver}$	f_i = 0.154 $\frac{\Delta P}{L} = 853$ Pa/m $\Delta P_{TS,2,H2,Hor}$ = 36 Pa $\Delta P_{TS,2,H2,Ver}$ = 9 Pa
<u>Bend Pressure Drop in the tubing</u>		
G_{tube} = 116 kg/m^2-s ρ_l = 1054 kg/m^3 $\Psi_{H,xout}$ = 2.55 k_B = 0.15	Homogenous Flow Model (Recommended by Hewitt, pp. 402, Eq. 10.36) $\Delta P_{Bend,out} = k_B \cdot \frac{G_{tube}{}^2}{2 \cdot \rho_l} \cdot \Psi_{H,x_{out}}$	$\Delta P_{Bend,out}$ = 2 Pa
<u>Expansion Pressure Drop from tubing to fitting at exit</u>		
$A_{fitting}$ = 4.10×10^{-6} m^2 $A_{tube,TS}$ = 1.89×10^{-6} m^2	$\gamma_{exp} = \frac{A_{tube,TS}}{A_{fitting}}$	γ_{exp} = 0.459

Table B-5 continued …

Inputs	Equations	Results
G_{tube} = 116 kg/m^2-s $\Psi_{S,xout}$ = 1.55 ρ_l = 1054 kg/m^3	Separated Flow Model (Recommended by Hewitt, pp. 402 & 410, Eq. 10.34) $\Delta P_{\exp,H2} = -\frac{G_{tube}{}^2 \gamma_{\exp}(1-\gamma_{\exp})\Psi_S}{\rho_L}$	$\Delta P_{exp,H2}$ = - 5 Pa
<u>Net Frictional Pressure Drop in the Test Section channels</u>		
$\Delta P_{con,H1}$ = 51 Pa $\Delta P_{H1,2,TS,Hor}$ = 87 Pa $\Delta P_{H1,2,TS,ver}$ = 21 Pa $\Delta P_{Bend,in}$ = 8 Pa $\Delta P_{exp,TS,header,in}$ = - 6 Pa $\Delta P_{Bend,header,in}$ = 452 Pa $\Delta P_{con,TS,in}$ = 923 Pa $\Delta P_{exp,\ TS,out}$ = - 118 Pa $\Delta P_{con,TS,header,out}$ = 22 Pa $\Delta P_{Bend,header,out}$ = 146 Pa	$\Delta P_{others,in} = \Delta P_{con,H1} + \Delta P_{H1,2,TS,Hor} + \Delta P_{H1,2,TS,Ver} + \Delta P_{Tube,Bend,in}$ $+\Delta P_{\exp,TS,header,in} + \Delta P_{Bend,header,in} + \Delta P_{con,TS,in}$ $\Rightarrow \Delta P_{others,in} = 51+87+28+8+(-6)+452+923 \quad \text{Pa}$	$\Delta P_{others,in}$ = 1.54 kPa $\Delta P_{others,out}$ = 89 Pa

Table B-5 continued …

Inputs	Equations	Results
$\Delta P_{TS,2,H2,Hor} = 36$ Pa $\Delta P_{TS,2,H2,Ver} = 9$ Pa $\Delta P_{Bend,out} = 2$ Pa $\Delta P_{exp,H2} = -5$ Pa	$\Delta P_{others,out} = \Delta P_{\exp,TS,out} + \Delta P_{Bend,header,out} + \Delta P_{con,TS,header,out} + \Delta P_{TS,2,H2,Ver}$ $+\Delta P_{TS,2,H2,Hor} + \Delta P_{Tube,Bend,out} + \Delta P_{\exp,H2}$ $\Rightarrow \Delta P_{others,out} = (-118) + 146 + 22 + 9 + 36 + 2 + (-5) \quad \text{Pa}$	
$\Delta P_{deccleration} = 1610$ Pa $\Delta P_{measured} = 47.2$ kPa	$\Delta P_{fric,TS} = \Delta P_{measured} - \Delta P_{others,in} - \Delta P_{others,out} + \Delta P_{decleration}$ $\Rightarrow \Delta P_{fric,TS} = 47.2 - 1.5 - 0.1 + 1.6 \quad \text{kPa}$	$\Delta P_{fric,TS} = 47.2$ kPa
$P_{H1,out} = 1727$ kPa $P_{H2,in} = 1678$ kPa	To minimize the uncertainty in the channel inlet/exit pressures, they are determined as follows. The measured differential pressure is added or subtracted from the average to determine the absolute pressure at the point of entrance/exit of the copper tube. From this, the minor losses till the beginning/end of the channels are subtracted or added to get the pressure at channel inlet/exit. $P_{in} = \left(\frac{P_{H1,out} + P_{H2,in}}{2}\right) + \frac{\Delta P_{measured}}{2} - \Delta P_{others,in}$ $P_{out} = \left(\frac{P_{H1,out} + P_{H2,in}}{2}\right) - \frac{\Delta P_{measured}}{2} + \Delta P_{others,out}$	$P_{in} = 1724$ kPa $P_{out} = 1679$ kPa

Table B-6: Segmental Heat Transfer Analysis Calculation Procedure (D = 133 μm; AR = 2; T_{sat} = 60.5°C, G = 606 kg/m²-s; x_{ave} = 0.39)

Main Parameters	Equations
NOTE: Tables B-7 and B-8 provide the values for all array variables used in this table.	
Segmental Division	
$N_{seg,fin} = 10$ $N_{seg,HE} = 10$ $L_{fin,section} = 12.5$ mm $L_{HE,section} = 15$ mm	$N_{seg} = 2 \times N_{seg,fin} + N_{seg,HE} = 30$ $L_{seg,i} = \dfrac{L_{fin,section}}{N_{seg,fin}} \quad \begin{cases} 1 \le i \le N_{seg,fin} \\ \left(N_{seg,fin} + N_{seg,HE} + 1\right) \le i \le N_{seg} \end{cases} = 1.25 \text{ mm}$ $L_{seg,i} = \dfrac{L_{HE.section}}{N_{seg,HE}} \quad \left\{\left(N_{seg,fin} + 1\right) \le i \le \left(N_{seg,fin} + N_{seg,HE}\right)\right. = 1.5 \text{ mm}$
Refrigerant and Water-side Temperature Calculation	
Water-Side Temperature $T_{w,U,,in} = 56.3°C$ $T_{w,L,,in} = 56.3°C$ $T_{w,U,out} = 56.4°C$ $T_{w,L,out} = 56.3°C$ $L_{HE,section} = 15$ mm	$T_{water,in} = \dfrac{T_{w,U,in} + T_{w,L,in}}{2} = 56.3°C$ $T_{water,out} = \dfrac{T_{w,U,out} + T_{w,L,out}}{2} = 56.4°C$ $T_{water,N_{seg,fin}+1} = T_{water,out} - \left(\dfrac{T_{water,out} - T_{water,in}}{L_{HE.section}}\right) \cdot \dfrac{L_{seg,N_{seg,fin}+1}}{2}$

Table B-6 continued …

Main Parameters	Equations
$N_{seg,fin} = 10$ $N_{seg,HE} = 10$	$T_{water,i} = T_{water,i-1} - \left(\frac{T_{water,out} - T_{water,in}}{L_{HE.section}}\right) \cdot L_{seg,i} \quad \{N_{seg,fin} + 2 \leq \mathrm{i} \leq N_{seg,fin} + N_{seg,HE}$
Refrigerant-Side Temperature For Representative Case Data Set: $a_{dPdL} = 18063$ $b_{dPdL} = 75582$ $c_{dPdL} = 0$ $P_{in} = 1724$ kPa $N_{seg,fin} = 10$ $N_{seg,HE} = 10$ $N_{seg} = 30$	$\Delta P_{TS,fric} = f(x) = a_{dPdL} + b_{dPdL} \cdot x + c_{dPdL} \cdot x^2$ NOTE: Values of constants a_{dPdL}, b_{dPdL} and c_{dPdL} are determined empirically and are provided in Tables B-9 to B-10 for data sets belonging to all tubes. $\left(\frac{dP}{dL}\right)_0 = \frac{a_{dPdL} + b_{dPdL}\left(\frac{x_{in} + x_1}{2}\right) + c_{dPdL}\left(\frac{x_{in} + x_1}{2}\right)^2}{0.04}$ $P_{emp,1} = P_{in} - \left(\frac{dP}{dL}\right)_0 \left(\frac{L_{seg,1}}{2}\right) + \Delta P_{decceleration,0}$ NOTE: Subscript 0 is used to either denote the inlet of the channels or the quantities between the inlet and the first node. $\left(\frac{dP}{dL}\right)_i = \frac{a_{dPdL} + b_{dPdL}\left(\frac{x_i + x_{i+1}}{2}\right) + c_{dPdL}\left(\frac{x_i + x_{i+1}}{2}\right)^2}{0.04} \quad \{1 \leq i \leq (N_{seg} - 1)$

Table B-6 continued …

Main Parameters	Equations
$P_{emp,N_{seg}+1}$ = 1679 kPa P_{out} = 1679 kPa	$P_{emp,i} = P_{emp,i-1} - \left(\frac{dP}{dL}\right)_{i-1}\left(\frac{L_{seg,i} + L_{seg,i-1}}{2}\right) + \Delta P_{decceleration,i-1} \quad \{2 \le i \le N_{seg}$ $\left(\frac{dP}{dL}\right)_{N_{seg}} = \frac{a_{dPdL} + b_{dPdL}\left(\frac{x_i + x_{out}}{2}\right) + c_{dPdL}\left(\frac{x_i + x_{out}}{2}\right)^2}{0.04}$ $P_{emp,N_{seg}+1} = P_{emp,N_{seg}} - \left(\frac{dP}{dL}\right)_{N_{seg}}\left(\frac{L_{seg,N_{seg}}}{2}\right) + \Delta P_{decceleration,N_{seg}} =$ (Refer to Figure 4.5 for definition of the variables in the next three equations) $EP_{out} = P_{emp,N_{seg}+1} - P_{out} = 88 \text{ Pa}$ $P_i = P_{emp,i} - \frac{EP_{out}}{2} \quad \{0 \le i \le \left(N_{seg} + 1\right)$ $Error_{P_{out}} = \frac{\left(P_{N_{seg}+1} - P_{out}\right)}{\left(P_{in} - P_{out}\right)} \times 100 = 0.9\%$
Refrigerant Quality Determination	
h_{in} = 230 kJ/kg $\dot{m} = 2.18\times10^{-4}$ kg/s	$\frac{Q_{refg,1}}{2} = \dot{m} \cdot \left(h_{in} - h_1\right)$

Table B-6 continued …

Main Parameters	Equations
$N_{seg} = 30$	$\frac{\left(Q_{refg,i-1} + Q_{refg,i}\right)}{2} = \dot{m} \cdot \left(h_{i-1} - h_i\right) \quad \{2 \le i \le N_{seg}$ $x_i = f\left('R134a', P = P_i, h = h_i\right) \quad \{1 \le i \le N_{seg}$
<u>Thermal Resistance Calculation</u>	
Refrigerant side convective thermal resistance $d_{TS} = 100\ \mu m$ $w_{TS} = 200\ \mu m$ $N_{seg} = 30$	$L_{f,refg} = \frac{d_{TS}}{2}$ $k_{Cu,wf,i} = f\left(T_{Cu,wf,i}\right) \quad \{1 \le i \le N_{seg}$ $m_{refg,i} = \sqrt{\frac{h_{refg} \cdot 2}{k_{Cu,wf,i} \cdot t_{f,refg}}} \quad \{1 \le i \le N_{seg}$ $\eta_{f,refg,i} = \frac{\tanh\left(m_{refg,i} \times L_{f,refg}\right)}{m_{refg,i} \times L_{f,refg}} \quad \{1 \le i \le N_{seg}$ $A_{eff,refg,i} = L_{seg,i} \times N \times \left(\eta_{f,refg,i} \times L_{f,refg} \times 2 + w_{TS}\right) \times 2 \quad \{1 \le i \le N_{seg}$ $Q_{refg,i} = h_{refg} \cdot A_{eff,refg,i} \cdot \left(T_{refg,i} - T_{w,refg,i}\right) \quad \{1 \le i \le N_{seg}$

Table B-6 continued …

Main Parameters	Equations
Heat flow from Cu wafer wall to center $t_{wafer} = 1$ mm $W_{channels} = 7.8$ mm $N_{seg} = 30$	$A_{seg,H,i} = W_{channels} \cdot L_{seg,i} \cdot 2 \quad \{1 \le i \le N_{seg}$ $Q_{refg,i} = k_{Cu,wf,i} \cdot \dfrac{A_{seg,H,i}}{t_{wafer}/2} \cdot \left(T_{w,refg,i} - T_{Cu,wf,i}\right) \quad \{1 \le i \le N_{seg}$
Heat flow between the Cu wafer nodes $w_{TS} = 200$ µm $d_{TS} = 100$ µm $W_{channels} = 7.8$ mm $t_{wafer} = 1$ mm $N = 18$ $N_{seg} = 30$	$A_{wf,V} = \left[W_{channels} \cdot \left(t_{wafer} + \dfrac{d_{TS}}{2}\right) - N \cdot \dfrac{d_{TS}}{2} w_{TS}\right] \cdot 2 \quad \{1 \le i \le N_{seg}$ $Q_{wf,i} = k_{Cu,wf,i} \cdot \left(\dfrac{A_{wf,V}}{\left\{\left(L_{seg,i} + L_{seg,i+1}\right)/2\right\}}\right) \cdot \left(T_{Cu,wf,i} - T_{Cu.wf,i+1}\right) \quad \{1 \le i \le \left(N_{seg} - 1\right)$

Table B-6 continued …

Main Parameters	Equations
Heat flow from Cu wafer nodes to respective water block nodes $N_{seg,fin} = 10$ $N_{seg,HE} = 10$ $W_{slot} = 10.16$ mm $t_{wafer} = 1$ mm $t_{wb,wall} = 1.9$ mm	$A_{w,seg,i} = W_{slot} \times L_{seg,i} \times 2 \quad \{(N_{seg,fin}+1) \le i \le (N_{seg,fin}+N_{seg,HE})$ $k_{Cu,wb,i} = f(T_{wb,i}) \quad \{(N_{seg,fin}+1) \le i \le (N_{seg,fin}+N_{seg,HE})$ $Q_{wall,V,i} = \dfrac{T_{Cu,wf,i} - T_{wb,i}}{\dfrac{t_{wafer}/2}{k_{Cu,wf,i} \cdot A_{seg,H,i}} + \dfrac{t_{wb,wall}/2}{k_{Cu,wb,i} \cdot A_{w,seg,i}}} \quad \{(N_{seg,fin}+1) \le i \le (N_{seg,fin}+N_{seg,HE})$
Heat flow between neighboring water block segments $N_{seg,fin} = 10$ $N_{seg,HE} = 10$ $W_{slot} = 10.16$ mm	$Q_{wb,H,i} = k_{Cu,wb,i} \cdot \dfrac{t_{wb,wall} \times W_{slot} \times 2}{L_{seg,i}} \cdot (T_{wb,i} - T_{wb,i+1}) \quad \{(N_{seg,fin}+1) \le i \le (N_{seg,fin}+N_{seg,HE}-1)$

Table B-6 continued …

Main Parameters	Equations
Heat flow from water block to water flowing in counter flow P_{water} = 234 kPa D_w = 0.79 mm $FR_w = 3.79\times10^{-5}$ m^3/s ρ_w = 985 kg/m^3 N_w = 10 $\mu_w = 4.94 \times 10^{-4}$ kg/m-s Pr_w = 3.24 k_w = 0.637 W/m-K $N_{seg,fin}$ = 10 $N_{seg,HE}$ = 10	$A_w = \pi \cdot \frac{D_w^{\ 2}}{4} \cdot N_w = 4.95\times10^{-6}$ m^2 For all cases, the gauge pressure at pump exit was 40 psi and the inlet pressure was atmospheric. Hence, for property calculation, water pressure is assumed to be 34 psi (absolute). $T_{water} = \frac{T_{water,in} + T_{water,out}}{2} = 56.3°C$ $\dot{m}_w = FR_w \cdot \rho_w = 3.73\times10^{-2}$ kg/s $V_w = \frac{\dot{m}_w}{\rho_w A_w} = 7.65$ m/s $\mathrm{Re}_w = \frac{\rho_w V_w D_w}{\mu_w} = 12.1\times10^3$ Using the Dittus-Bolter equation: $Nu_w = 0.023 \cdot \mathrm{Re}_w^{\ 0.8}\,\mathrm{Pr}_w^{\ 0.4} = 68$ $h_w = Nu_w \frac{k_w}{D_w} = 54.6\times10^3$ W/m^2-K

Table B-6 continued …

Main Parameters	Equations
$t_{wb,wall}$ = 1.9 mm	$A_{eff,water,i} = 2 \cdot \pi \cdot \frac{D_{h,water}}{2} \times L_{seg,i} \times N_{water} \quad \{(N_{seg,fin}+1) \le i \le (N_{seg,fin}+N_{seg,HE}) \; \dot{m}_w = FR_w \cdot \rho_w$ $Q_{water,i} = \frac{T_{wb,i} - T_{water,i}}{\frac{t_{wb,wall}/2}{k_{Cu,wb,i} \cdot A_{w,seg,i}} + \frac{1}{h_{water} \cdot A_{eff,water,i}}} \quad \{(N_{seg,fin}+1) \le i \le (N_{seg,fin}+N_{seg,HE})$
Energy Balance	
Overall condensation heat duty Q_{TS} = 15.54 W	$\dot{Q}_{TS} = \sum_{i=1}^{N_{seg}} Q_{refg,i}$
Cu wafer Fin nodes $N_{seg,fin}$ = 10 $N_{seg,HE}$ = 10	$Q_{wf,1} = Q_{refg,i}$ $Q_{refg,N_{seg}} + Q_{wf,N_{seg}-1} = 0$ $Q_{wf,i-1} + Q_{refg,i} = Q_{wf,i} \quad \begin{cases} 2 \le i \le N_{seg,fin} \\ (N_{seg,fin}+N_{seg,HE}+1) \le i \le (N_{seg}-1) \end{cases}$
Cu wafer central HE section nodes $N_{seg,fin}$ = 10 $N_{seg,HE}$ = 10	$Q_{wf,i-1} + Q_{refg,i} = Q_{wf,i} + Q_{wall,V,i} \quad \{N_{seg,fin}+1 \le i \le (N_{seg,fin}+N_{seg,HE})$

Table B-6 continued …

Main Parameters	Equations
Water block nodes $N_{seg,fin} = 10$ $N_{seg,HE} = 10$	$Q_{wall,V,N_{seg,fin}+1} = Q_{wb,H,N_{seg,fin}+1} + Q_{water,N_{seg,fin}+1}$ $Q_{wall,V,(N_{seg,fin}+N_{seg,HE})} + Q_{wb,H,(N_{seg,fin}+N_{seg,HE}-1)} = Q_{water,(N_{seg,fin}+N_{seg,HE})}$ $Q_{wall,V,i} + Q_{wb,H,i-1} = Q_{wb,H,i} + Q_{water,i} \quad \{(N_{seg,fin}+2) \le i \le (N_{seg,fin}+N_{seg,HE}-1)$
	$\boldsymbol{h_{refg}}$ **= 21.7 kW/m^2-K**
Average Refrigerant and Wall Temperature	
$N_{seg} = 30$ $Q_{TS} = 15.54$ W	$TQ_{refg,wall,i} = Q_{refg,i} \cdot T_{w,refg,i} \quad \{1 \le i \le N_{seg}$ $TQ_{refg,i} = Q_{refg,i} \cdot T_{refg,i} \quad \{1 \le i \le N_{seg}$ $T_{refg,wall,Qave} = \dfrac{\sum_{i=1}^{N_{seg}} TQ_{refg,wall,i}}{\dot{Q}_{TS}} = 58.1°\text{C}$ $T_{refg,Qave} = \dfrac{\sum_{i=1}^{N_{seg}} TQ_{refg,i}}{\dot{Q}_{TS}} = 60.37°\text{C}$

Table B-6 continued …

Main Parameters	Equations
Resistance Ratio	
$N_{seg} = 30$ $N_{seg,fin} = 10$ $N_{seg,HE} = 10$	$\dot{Q}_{TS,Fin,in} = \sum_{i=1}^{N_{seg,fin}} Q_{refg,i} = 3.03\ \text{W}$ $\dot{Q}_{TS,Fin,out} = \sum_{i=(N_{seg,fin}+N_{seg,HE}+1)}^{N_{seg}} Q_{refg,i} = 2.52\ \text{W}$ $T_{refg,Qave,fin,in} = \frac{\sum_{i=1}^{N_{seg,fin}} TQ_{refg,i}}{\dot{Q}_{TS,Fin,in}} = 60.7°\text{C}$ $T_{refg,Qave,fin,out} = \frac{\sum_{i=(N_{seg,fin}+N_{seg,HE}+1)}^{N_{seg}} TQ_{refg,i}}{\dot{Q}_{TS,Fin,out}} = 60.1°\text{C}$
$T_{Cu,wf,N_{seg,fin}+1} = 57.8°\text{C}$	$A_{eff,refg,fin,in} = \frac{\dot{Q}_{TS,Fin,in}}{h_{refg} \cdot \left(T_{refg,Qave,fin,in} - T_{Cu,wf,N_{seg,fin}+1}\right)} = 4.77\times10^{-5}\ \text{m}^2$
$T_{Cu,wf,N_{seg,fin}+N_{seg,HE}} = 57.6°\text{C}$	$A_{eff,refg,fin,out} = \frac{\dot{Q}_{TS,Fin,out}}{h_{refg} \cdot \left(T_{refg,Qave,fin,out} - T_{Cu,wf,N_{seg,fin}+N_{seg,HE}}\right)} = 4.78\times10^{-5}\ \text{m}^2$

Table B-6 continued …

Main Parameters	Equations
	$A_{eff,refg,HE} = \sum_{i=N_{seg,fin}+1}^{N_{seg,fin}+N_{seg,HE}} A_{eff,refg,i}$ = 1.62×10^{-4} m^2 $A_{eff,refg,Total} = A_{eff,refg,fin,in} + A_{eff,refg,HE} + A_{eff,refg,fin.out}$ = 2.574×10^{-4} m^2 $R_{Total} = \frac{T_{refg,Qave} - T_{water}}{\dot{Q}_{TS}}$ = 0.2591 K/W $R_{refg} = \frac{1}{h_{refg} \cdot A_{eff,refg,Total}}$ = 0.1791 K/W $R_{ratio} = \frac{R_{refg}}{R_{Total} - R_{refg}}$ = 2.25

Table B-7: Segmental Heat Transfer Variable Array Table-1 for Representative case (D = 133 μm; AR = 2; T_{sat} = 60.5°C, G = 606 kg/m²-s; x_{ave} = 0.39)

i	x_i	$\left(\frac{dP}{dL}\right)_i$ (MPa/m)	$\Delta P_{decceleration.,i}$ (Pa)	$P_{emp,i}$ (MPa)	P_i (MPa)	$T_{refg,i}$ (°K)	$T_{w,refg,i}$ (°K)	$T_{Cu,wf,i}$ (°K)	$T_{wb,i}$ (°K)	$T_{water,i}$ (°K)	h_i (× 10^5 J/kg)
0	0.6444	1.67	11.1	1.7244	1.7244	61.03					
1	0.6416	1.66	21.88	1.7234	1.7234	61.01	60.39	60.38			2.29
2	0.636	1.65	21.89	1.7213	1.7213	60.96	60.36	60.35			2.29
3	0.6303	1.64	23.34	1.7193	1.7193	60.91	60.29	60.28			2.28
4	0.6243	1.63	26.3	1.7172	1.7172	60.86	60.18	60.17			2.27
5	0.6176	1.61	30.89	1.7152	1.7152	60.81	60.04	60.03			2.26
6	0.6097	1.60	37.31	1.7133	1.7133	60.76	59.86	59.84			2.25
7	0.6004	1.58	45.85	1.7113	1.7113	60.71	59.62	59.6			2.23
8	0.5888	1.55	56.81	1.7094	1.7094	60.66	59.32	59.3			2.22
9	0.5745	1.52	70.57	1.7075	1.7075	60.62	58.95	58.92			2.20
10	0.5566	1.48	98.37	1.7057	1.7057	60.57	58.48	58.45			2.17
11	0.5312	1.43	120.5	1.7037	1.7037	60.52	57.84	57.79	57.42	56.36	2.14
12	0.4992	1.36	121.9	1.7017	1.7017	60.47	57.58	57.53	57.32	56.36	2.09
13	0.4655	1.30	118.9	1.6998	1.6998	60.43	57.46	57.4	57.23	56.35	2.05
14	0.4312	1.23	114.1	1.6980	1.6980	60.38	57.38	57.33	57.17	56.35	2.00
15	0.3967	1.17	108.3	1.6962	1.6962	60.34	57.34	57.29	57.14	56.34	1.95

Table B-7 continued …

i	x_i	$\left(\frac{dP}{dL}\right)_i$ (MPa/m)	$\Delta P_{decceleration.,i}$ (Pa)	$P_{emp,i}$ (MPa)	P_i (MPa)	$T_{refg,i}$ (°K)	$T_{w,refg,i}$ (°K)	$T_{Cu,wf,i}$ (°K)	$T_{wb,i}$ (°K)	$T_{water,i}$ (°K)	h_i (× 10^5 J/kg)
16	0.3625	1.11	101.9	1.6946	1.6946	60.3	57.33	57.27	57.12	56.34	1.90
17	0.3287	1.04	94.88	1.6930	1.6930	60.26	57.34	57.28	57.13	56.33	1.85
18	0.2956	0.98	87.14	1.6916	1.6916	60.22	57.38	57.33	57.17	56.33	1.81
19	0.2637	0.92	77.61	1.6902	1.6902	60.18	57.47	57.42	57.23	56.32	1.76
20	0.2339	0.87	58.33	1.6889	1.6889	60.15	57.68	57.63	57.3	56.32	1.72
21	0.2106	0.83	39.58	1.6877	1.6877	60.12	58.21	58.17			1.69
22	0.1943	0.81	30.53	1.6867	1.6867	60.1	58.58	58.55			1.67
23	0.1814	0.78	23.7	1.6858	1.6858	60.07	58.87	58.85			1.65
24	0.1712	0.77	18.53	1.6848	1.6848	60.05	59.09	59.07			1.63
25	0.1631	0.75	14.61	1.6839	1.6839	60.03	59.26	59.25			1.62
26	0.1567	0.74	11.64	1.6829	1.6829	60	59.39	59.37			1.61
27	0.1515	0.734	9.431	1.6820	1.6820	59.98	59.48	59.47			1.60
28	0.1473	0.727	7.821	1.6811	1.6811	59.96	59.54	59.53			1.60
29	0.1437	0.72	6.71	1.6802	1.6802	59.93	59.57	59.57			1.59
30	0.1407	0.716	3.107	1.6793	1.6793	59.91	59.59	59.59			1.59
31	0.1393			1.6789	1.6789	59.9					

Table B-8: Segmental Heat Transfer Variable Array Table-2 for Representative case (D = 133 μm; AR = 2; T_{sat} = 60.5°C, G = 606 kg/m^2-s; x_{ave} = 0.39)

i	$A_{eff,refg,i}$ (×10^{-5} m^2)	$A_{seg,H,i}$ (×10^{-5} m^2)	$A_{,w,seg,i}$ (×10^{-5} m^2)	$A_{eff.water,i}$ (×10^{-5} m^2)	$Q_{refg,i}$ (W)	$Q_{wf,i}$ (W)	$Q_{wall,V,i}$ (W)	$Q_{wb,H,i}$ (W)	$Q_{water,i}$ (W)	$k_{Cu,wf,i}$ (W/m^2-K)	$k_{Cu,wb,i}$ (W/m^2-K)
0											
1	1.35	1.95			0.1802	0.1802				398.3	
2	1.35	1.95			0.1758	0.3559				398.3	
3	1.35	1.95			0.1813	0.5373				398.3	
4	1.35	1.95			0.1972	0.7345				398.3	
5	1.35	1.95			0.2243	0.9588				398.3	
6	1.35	1.95			0.2642	1.223				398.4	
7	1.35	1.95			0.3191	1.542				398.4	
8	1.35	1.95			0.3922	1.934				398.4	
9	1.35	1.95			0.4877	2.422				398.4	
10	1.35	1.95			0.611	3.033				398.5	
11	1.62	2.34	3.05	3.74	0.9419	1.122	2.85	0.997	1.856	398.5	398.6
12	1.62	2.34	3.05	3.74	1.015	0.5459	1.59	0.8946	1.694	398.5	398.6
13	1.62	2.34	3.05	3.74	1.043	0.3091	1.28	0.6256	1.549	398.6	398.6
14	1.62	2.34	3.05	3.74	1.053	0.1698	1.19	0.367	1.45	398.6	398.6
15	1.62	2.34	3.05	3.74	1.051	0.06074	1.16	0.1313	1.396	398.6	398.6
16	1.62	2.34	3.05	3.74	1.042	-0.04645	1.15	-0.1019	1.382	398.6	398.6

Table B-8 continued …

i	$A_{eff,refg,i}$ ($\times10^{-5}$ m^2)	$A_{seg,H,i}$ ($\times10^{-5}$ m^2)	$A_{,w,seg,i}$ ($\times10^{-5}$ m^2)	$A_{eff.water,i}$ ($\times10^{-5}$ m^2)	$Q_{refg,i}$ (W)	$Q_{wf,i}$ (W)	$Q_{wall,V,i}$ (W)	$Q_{wb,H,i}$ (W)	$Q_{water,i}$ (W)	$k_{Cu,wf,i}$ (W/m^2-K)	$k_{Cu,wb,i}$ (W/m^2-K)
17	1.62	2.34	3.05	3.74	1.025	-0.1783	1.16	-0.3539	1.409	398.6	398.6
18	1.62	2.34	3.05	3.74	0.9978	-0.3932	1.21	-0.6194	1.478	398.6	398.6
19	1.62	2.34	3.05	3.74	0.954	-0.8946	1.46	-0.7574	1.593	398.6	398.6
20	1.62	2.34	3.05	3.74	0.8703	-2.514	2.49		1.732	398.5	398.6
21	1.35	1.95			0.5614	-1.953				398.5	
22	1.35	1.95			0.4443	-1.508				398.5	
23	1.35	1.95			0.3524	-1.156				398.4	
24	1.35	1.95			0.2804	-0.8755				398.4	
25	1.35	1.95			0.2243	-0.6512				398.4	
26	1.35	1.95			0.181	-0.4703				398.4	
27	1.35	1.95			0.1479	-0.3224				398.4	
28	1.35	1.95			0.1232	-0.1992				398.4	
29	1.35	1.95			0.1055	-0.09373				398.4	
30	1.35	1.95			0.0937					398.4	
31											

Table B-9: Uncertainty Analysis Table for the Representative Case

Inputs	Equations	Results
Mass Flow-rate Uncertainty		
$T_{R,FM}$ = 25.9±0.5°C $P_{H1,in}$ = 1727±6.89 kPa FR_{refg} = 1.8×10^{-7} m^3/s (±0.5%) d_{TS} = 100±0.5 μm w_{TS} = 200±0.5 μm	$\rho_{fm,refg} = f\left(T_{amb}, P_{H1,in}\right)$ $\dot{m} = FR_{refg} \times \rho_{fm,refg}$ $A_{tot,TS} = d_{TS} \cdot w_{TS} \cdot N$ $G = \dfrac{\dot{m}}{A_{tot,TS}}$	$\rho_{fm,refg} = 1210 \pm 2$ kg/m^3 (±0.17%) $\dot{m}$ = 2.18×10^{-4}±1.1×10^{-6} (±0.52%) $A_{tot,TS}$ = 3.6×10^{-7}±2×10^{-7} m^2 (±0.56%). G = 606±4.6 kg/m^2-s (±0.8%)
Inlet Quality Uncertainty		
Q_{H1} = 31.02 W (±0.2%) $Q_{H1,loss}$ = 1.07 W (±50%) $P_{H1,in}$ = 1727±6.9 kPa $T_{H1,in}$ = 29.3±0.1°C $\dot{m}$ = 2.18×10^{-4}±1.1×10^{-6} (±0.52%) P_{in} = 1724±4.9 kPa	$Q_{H1,refg} = Q_{H1} - Q_{H1,loss}$ $h_{H1,in} = f\left(T_{H1,in}, P_{H1,in}\right)$ $Q_{H1,refg} = \dot{m} \cdot \left(h_{H1,out} - h_{H1,in}\right)$ $h_{H1,out} = f\left(P_{in}, x_{in}\right)$	$Q_{H1,refg}$ =29.95±0.54 W (±1.8%) $h_{H1,in}$ = 93±0.14 kJ/kg (±0.15%) $h_{H1,out}$ = 230±2.6 kJ/kg (±1.13%) x_{in} = 0.64 ±0.02

Table B-9 continued …

Inputs	Equations	Results
Exit Quality Uncertainty		
Q_{H2} = 28.86 W (±0.2%) $Q_{H2,loss}$ = 1.03 W (±50%) $T_{H2,out}$ = 65.7±0.1°C $P_{H2,out}$ = 1679±6.9 kPa $\dot{m}$ = 2.18×10^{-4}±1.1×10^{-6} (±0.52%) P_{out} = 1679±4.9 kPa	$Q_{H2,refg} = Q_{H2} - Q_{H2,loss}$ $h_{H2,out} = f\left(T_{H2,out}, P_{H2,out}\right)$ $Q_{H2,refg} = \dot{m}\cdot\left(h_{H2,out} - h_{H2,in}\right)$ $h_{H2,in} = f\left(P_{H2,in}, x_{out}\right)$	$Q_{H2,refg}$ = 27.83±0.52 W (±1.9%) $h_{H2,out}$ = 286±0.2 kJ/kg (±0.07%) $h_{H2,in}$ = 159±2.5 kJ/kg (±1.6%) x_{out} = 0.14±0.02
Test Section Heat Duty Uncertainty		
$h_{H2,in}$ = 159±2.5 kJ/kg $h_{H1,out}$ = 230±2.6 kJ/kg $\dot{m}$ = 2.18×10^{-4}±1.1×10^{-6} (±0.52%)	$Q_{TS} = \dot{m}\left(h_{H1,out} - h_{H2,in}\right)$	Q_{TS} = 15.54±0.78 W (±5%)
Pressure Drop Uncertainty		
$\Delta P_{others,in}$ = 1.54 kPa (±50%) $\Delta P_{others,in}$ = 89 Pa (±50%) $\Delta P_{decleration}$ = 1610 Pa (±50%) $\Delta P_{measured}$ = 47.2±0.19 kPa	$\Delta P_{fric,TS} = \Delta P_{measured} - \Delta P_{others,in} - \Delta P_{others,out} + \Delta P_{decleration}$	$\Delta P_{fric,TS}$ = 47.2±1.1 kPa (±2.3%)

Table B-9 continued …

Inputs	Equations	Results
$P_{H1,out}$ = 1727±6.9 kPa	$P_{in} = \left(\dfrac{P_{H1,out} + P_{H2,in}}{2}\right) + \dfrac{\Delta P_{measured}}{2} - \Delta P_{others,in}$	P_{in} = 1724±4.9 kPa (±0.28%)
$P_{H2,in}$ = 1678±6.9 kPa	$P_{out} = \left(\dfrac{P_{H1,out} + P_{H2,in}}{2}\right) - \dfrac{\Delta P_{measured}}{2} + \Delta P_{others,out}$	P_{out} = 1679±4.9 kPa (±0.29%)
Refrigerant Heat Transfer Coefficient Uncertainty		
Q_{TS} = 15.54±0.78 W (±5%) h_w = 54.6×10^3 W/m^2-K (±25%) $T_{water,in} = 56.3 \pm 0.1$°C $T_{water,out} = 56.4 \pm 0.1$°C $T_{refg,in} = 61.1 \pm 0.12$°C $T_{refg,out}$ = 59.9±0.13°C $W_{channels}$ = 7.8±0.1 mm	**Segmental Heat Transfer Analysis**	h_{refg} = 21.7±2.98 kW/m^2-K(±14%)

B.3. ΔP Empirical Equation Constants

As discussed in section 4.3.2, in order to determine the refrigerant saturation temperature at each of the nodes, the pressure at the nodes is determined empirically. Thus the pressure drop for each data set is modeled empirically in the form of equation (4.37). The values of constants a_{dpdL}, b_{dPdL} and c_{dPdL} in equation (4.37) for each data set are given in the tables in this section.

Table B-10: ΔP Empirical Equation Constants for 100x100 μm Channels

Data Set		$\Delta P_{TS,fric} = f(x) = a_{dPdL} + b_{dPdL} \cdot x + c_{dPdL} \cdot x^2$		
T **(°C)**	***G*** **(kg/m²-s)**	a_{dPdL}	b_{dPdL}	c_{dPdL}
30	**600**	41464	163157	0
30	**800**	Not tested.		
40	**600**	42578	122007	0
40	**800**	43478	256368	0
50	**600**	17473	143461	0
50	**800**	34624	198020	0
60	**600**	10434	114509	0
60	**800**	26053	158057	0

Table B-11: ΔP Empirical Equation Constants for 200x100 μm Channels

Data Set		$\Delta P_{TS,fric} = f(x) = a_{dPdL} + b_{dPdL} \cdot x + c_{dPdL} \cdot x^2$		
T (°C)	**G (kg/m²-s)**	a_{dPdL}	b_{dPdL}	c_{dPdL}
30	**300**	12678	33783	0
30	**400**	8926	85768	0
30	**600**	14045	175138	0
30	**800**	25617	294339	0
40	**300**	17616	16087	0
40	**400**	13128	57725	0
40	**600**	19031	137004	0
40	**800**	17077	231200	0
50	**300**	7628	25082	0
50	**400**	7804	49024	0
50	**600**	16535	98985	0
50	**800**	24209	181368	0
60	**300**	15293	3477	0
60	**400**	13469	25709	0
60	**600**	18063	75582	0
60	**800**	26430	132670	0

Table B-12: ΔP Empirical Equation Constants for 300x100 μm Channels

Data Set		$\Delta P_{TS,fric} = f(x) = a_{dPdL} + b_{dPdL} \cdot x + c_{dPdL} \cdot x^2$		
T (°C)	**G (kg/m^2-s)**	a_{dPdL}	b_{dPdL}	c_{dPdL}
30	**300**	18019	28827	0
30	**400**	17855	53656	0
30	**600**	17219	149830	0
30	**800**	6608	305374	0
40	**300**	15499	23256	0
40	**400**	13819	49619	0
40	**600**	20075	92243	0
40	**800**	36223	157315	0
50	**300**	9063	18909	0
50	**400**	14176	27830	0
50	**600**	20452	68410	0
50	**800**	30044	123447	0
60	**300**	Not tested.		
60	**400**	17672	10862	0
60	**600**	17680	52511	0
60	**800**	30740	80283	0

Table B-13: ΔP Empirical Equation Constants for 400x100 μm Channels

Data Set		$\Delta P_{TS,fric} = f(x) = a_{dPdL} + b_{dPdL} \cdot x + c_{dPdL} \cdot x^2$		
***T* (°C)**	***G* (kg/m²-s)**	a_{dPdL}	b_{dPdL}	c_{dPdL}
30	**300**	19998	47601	0
30	**400**	21799	97481	0
30	**600**	16053	257489	0
30	**800**	53611	390712	0
40	**300**	22065	28333	0
40	**400**	15106	87801	0
40	**600**	21514	185047	0
40	**800**	51237	225214	149387
50	**300**	11123	35438	0
50	**400**	19493	52004	0
50	**600**	24685	132772	0
50	**800**	40857	219903	0
60	**300**	11705	23122	0
60	**400**	12893	47328	0
60	**600**	24661	86938	0
60	**800**	31926	166030	0

B.4. Single Phase Pressure Drop Tests

Single-phase pressure drop in internal flows has been much more widely studied compared to two-phase pressure drop. Experimental results for pressure head loss coefficients (K_L) for a wide range of bends, fittings, and valves are available in literature (Idelchik, 1986). Single-phase tests were conducted with the objective of ensuring that all the relevant minor losses in the fluid flow path are properly accounted for.

The single-phase friction factor for flow in rectangular channels in the test section was calculated in a manner similar to that used to calculate the slug friction factor in chapter 6. Frictional pressure drop in the channels is thus determined using equation (B.6) where the friction factor is determined as described above based on *Re*.

$$\Delta P = \frac{1}{2} \cdot f \cdot \frac{G^2}{\rho_L} \cdot \frac{L}{D} \tag{B.6}$$

The friction factors to determine the pressure drop in the inlet/exit copper tubes were calculated using the Churchill (1977b) correlation assuming smooth tubes ($\varepsilon = 0$):

$$f = 8 \cdot \left[\left(\frac{8}{\mathrm{Re}} \right)^{12} + \left(\left[2.457 \cdot \ln \left(\frac{1}{\left[\frac{7}{\mathrm{Re}} \right]^{0.9} + 0.27 \cdot \left[\frac{\varepsilon}{D} \right]} \right) \right]^{16} + \left[\frac{37530}{\mathrm{Re}} \right]^{16} \right)^{-1.5} \right]^{\left(\frac{1}{12}\right)} \tag{B.7}$$

Thus, the pressure drop in the horizontal and vertical sections of the copper tubing was calculated using equation (B.7).

Minor losses due to a change in flow area, bend or header geometry are calculated using the following equation:

$$\Delta P = \frac{1}{2} \cdot K \cdot \frac{G^2}{\rho} \tag{B.8}$$

where G is the mass flux in the smaller flow cross-section and K is the pressure head loss coefficient characteristic to the bend, expansion/contraction or other geometric features. The 1.55 mm ID inlet and exit copper tubing have bends with a radius of approximately 10 mm. For such bends, the pressure head loss coefficient is approximately $K_L = 0.1$ (Munson *et al.*, 2002). For a sudden enlargement of the flow area, $K_L = \left(1 - \frac{A_{Small}}{A_{Large}}\right)^2$ (Munson *et al.*, 2002), and for a sudden decrease in flow area, $K_L = \left(\frac{1}{C_c} - 1\right)^2$ (Streeter and Wylie, 1981), where, C_c is the contraction coefficient dependent on the contraction area ratio $\left({A_{Small}}/{A_{Large}} \right)$. The flow in the inlet header can be visualized as flow at the entrance of a rectangular duct, closed at the end, with the flow entering the duct from the opening on the side wall. For a similar geometry but with different dimensional ratios, Idelchik (1986) suggested a head loss coefficient of $K_L = 12.6$. Similarly, the flow in the exit side header can be visualized as flow in a rectangular duct that is closed at the end, with flow exiting from an opening on the side. For such a geometry, the head loss coefficient is $K_L = 15.5$ (Idelchik, 1986).

Based on the above discussion, the theoretically expected single-phase pressure drop across the measurement ports was calculated and compared with the experimentally measured single-phase pressure drops across the range of flow rates achievable by the pump. Figure B.2 shows each of the components of this total pressure drop for a sample single-phase case of the 300×100 μm test section. The marked sections are the same as those shown in Figure 4.1.

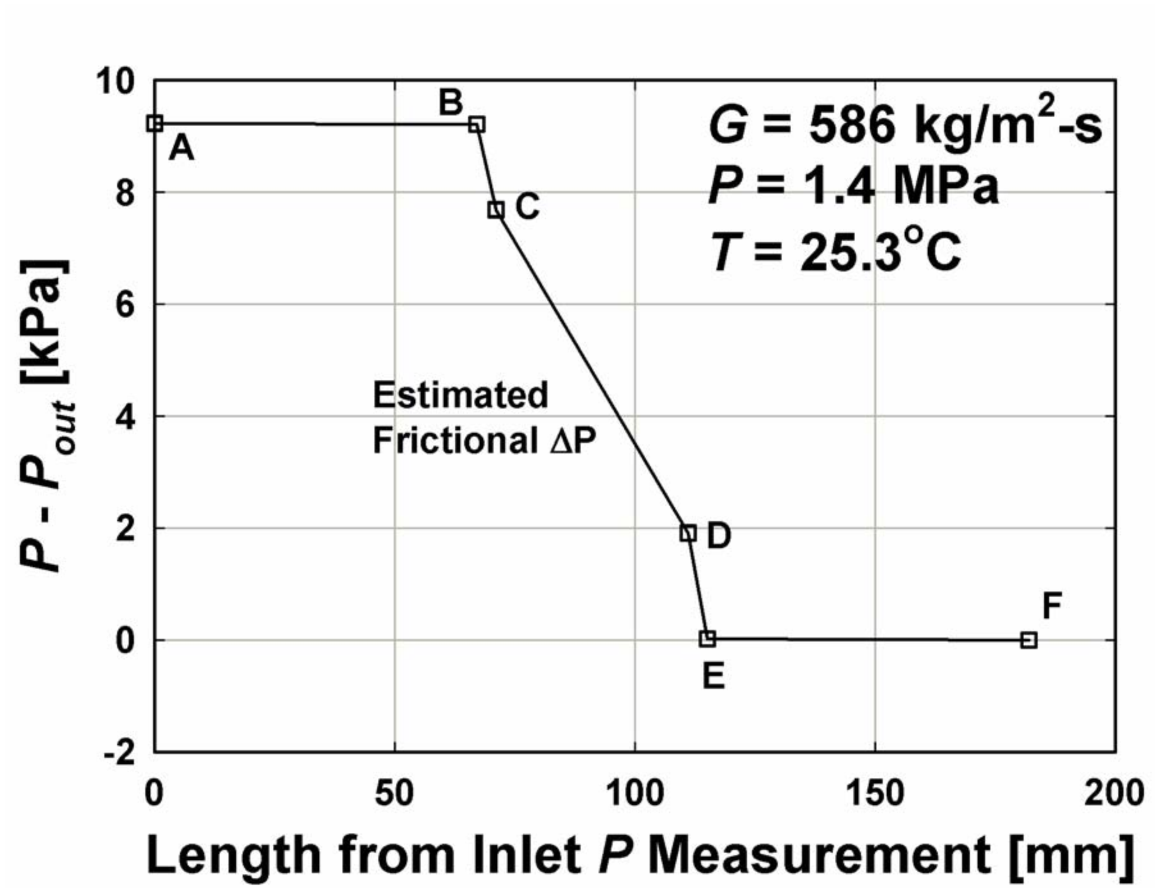

Figure B.2: ΔP along the Length of Test Section in Single Phase for Sample Case

For this particular case, the theoretical and measured pressure drops agreed within 1%. The frictional pressure drop in the test section contributes 62% of the total measured pressure drop. As the flow velocities increase, the relative contribution of the minor losses also increases. For the 400×100 μm and 300×100 μm test sections, 100% and 82%

of the data, respectively, were predicted within 20% of the measured pressure drop. For the 200×100 μm and 100×100 μm test sections, the measured single-phase pressure drop was under predicted by 37% and 51% on average. The head loss coefficients for various bends and expansion/contraction losses available in literature were mostly determined for highly turbulent flows. Idelchik (1986) has for some cases presented head loss coefficients for laminar flows as well in graphical form. In those plots, it can be seen that at lower Reynolds numbers, the head loss coefficients are much higher than those for turbulent flows. Thus, for the low Re values in the current study, the head loss coefficients from the literature are probably lower than the actual values. In the 200×100 μm and 100×100 μm channels, the estimated single-phase pressure drop is lower than the measured single-phase pressure drops because the fluid flow velocities in those cases are much lower than those for the 400×100 μm and 300×100 μm test sections. Small changes in the dimensions of the geometry may have a significant impact on the head loss coefficients. Head loss coefficients for exactly the same geometry as the inlet/exit headers in the present study were not available in literature. Therefore, the head loss coefficients, available for the conditions closest to those of interest in the current study, were used from the literature (Streeter and Wylie, 1981; Idelchik, 1986; Munson *et al.*, 2002).

B.5. Copper Tube ΔP Calculation

The multiple flow regime pressure drop model of Garimella *et al.* (2005) for condensing flows of refrigerant R134a in tubes with $0.5 < D < 4.9\ mm$ was used for the purpose of determining the pressure drop in the inlet and exit copper tubing attached to the test section. Although this model consists of separate sub-models for the intermittent flow regime and the annular/mist/disperse flow regimes, in the current study, the annular flow portion is used. This assumption of using only the annular pressure drop model instead of complete model greatly simplifies the calculations.

For the complete range of test conditions the refrigerant mass flux in the inlet/exit copper tubes varies from 65 to 260 kg/m^2-s. The transition criteria provided by Garimella *et al.* (2005) are only valid for mass fluxes > 150 kg/m^2-s as shown in Figure B.3. The inlet/exit Copper tube inner diameter is 1.55 mm.

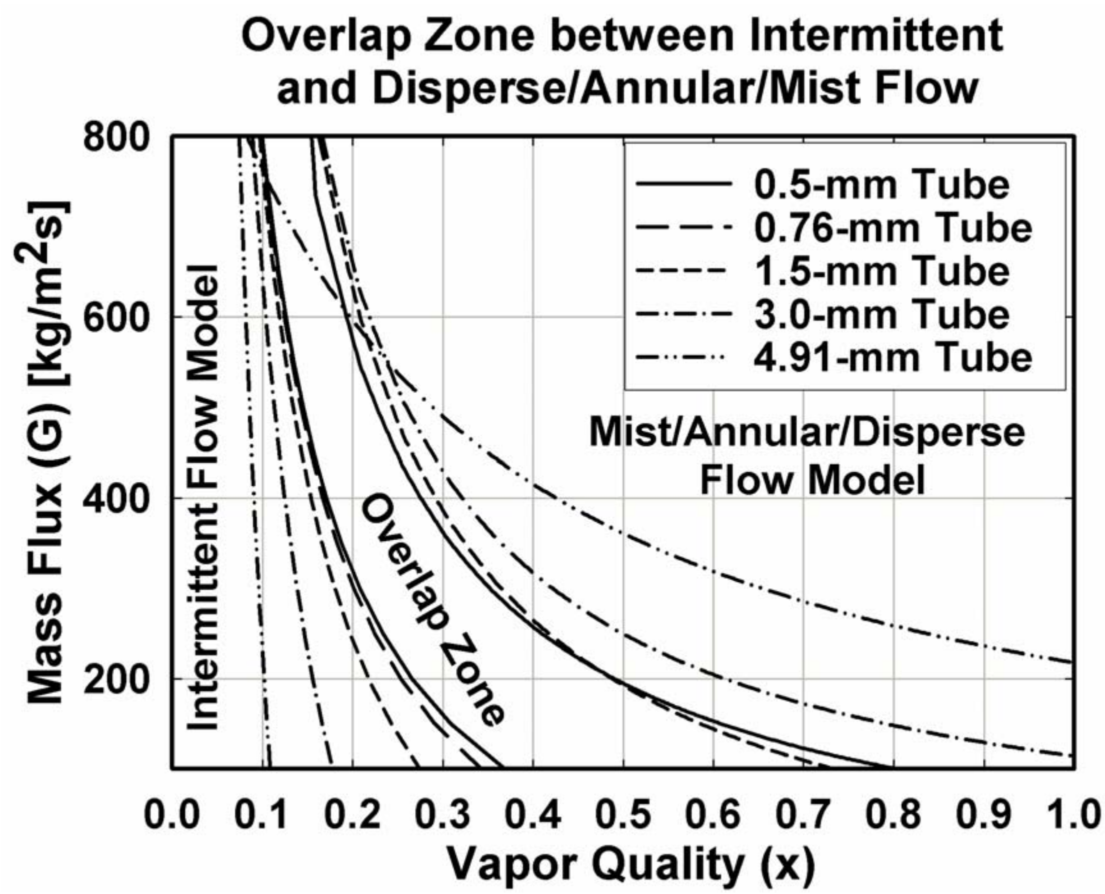

Figure B.3: Flow Regime Assignment using Garimella *et al* (2005) ΔP Model

For the complete range of data, the inlet qualities in the test section vary from 0.35 to 0.99 with more that 60% of them greater than 0.7. Lower inlet qualities could only be achieved at higher mass fluxes. Hence, for most of the data, flow in the inlet copper tube is either annular or in the overlap zone close to annular flow. In the exit-side copper tube, the quality varies from 0.01 to 0.51 for the complete range of data, indicating that flow may be completely intermittent for certain cases, but its contribution to the overall pressure losses is insignificant. Tables C-5 to C-8 show the range and average contributions of the inlet/exit losses to the overall measured pressure drop. The contribution of exit pressure losses is insignificant compared to the other contributions. The other major contributors to the inlet/exit pressure losses are the expansion/contraction losses, and the relative contribution of frictional pressure drop in the inlet and outlet tubing is minimal.

For the representative case discussed in Chapter 4, the mass flux in the copper tube is 116 kg/m^2-s, and the refrigerant qualities in the inlet and exit tube are 0.64 and 0.14, respectively. The frictional pressure drop for this case is approximately 100% of the measured pressure drop, as the deceleration pressure gain cancels the effect of inlet/exit minor losses. For the representative case, the deceleration, inlet and outlet pressure drops/gains are 3.4, 3.2, and 0.2 % of the measured pressure drop, respectively. The frictional pressure drop for flow in the inlet tube, which is very clearly close to annular flow, is only 108 Pa compared to the overall inlet pressure losses of 1.5 kPa, which in turn are only about 3.2% of the measured pressure drop. The frictional pressure drop in the exit copper tube (where x = 0.14, a good example of a fully intermittent point) is determined to be 45 Pa (36 Pa in horizontal and 9 Pa in vertical section) using the annular flow model, while the intermittent flow model would have yielded a pressure drop of 25 Pa. This difference of 20 Pa is very small compared to the other contributing factors in the exit losses (such as $\Delta P_{exp,\ TS,out}$ = -118 Pa and $\Delta P_{Bend,header,out}$ = 146 Pa) and is insignificant compared to the total frictional pressure drop of 47.2 kPa, inlet pressure losses of 1.5 kPa, and a deceleration pressure gain of 1.6 kPa. It should be noted that a 50% uncertainty is assumed in the inlet/exit pressure losses and deceleration pressure gain.

Thus, the annular flow model, which leads to simplification in the calculations, was assumed to be valid for computing frictional pressure drops in the inlet and outlet tubing over the entire range of conditions investigated here.

APPENDIX-C. DATA STATISITICS

C.1. Uncertainty Tables for Each Test Section

Table C-1: Data Statistics for 100×100 μm Test Section

Test Conditions		No. of Data Points	Δx Range	Resistance Ratio Range	Average x_{ave} Uncertainty	Average G Uncertainty (kg/m^2-s)	Average ΔP Uncertainty (%)	Average h Uncertainty (%)	Average $P_{in,emp\_}$ Error (%)
T_{sat} (^oC)	G (kg/m^2-s)								
30	**600**	7	0.64 – 0.80	1.8 – 1.2	0.005	5.3	3.1	17.7	2.8
40	**600**	5	0.71 – 0.82	1.8 – 1.5	0.008	5.3	3.1	15.8	1.9
40	**800**	4	0.58 – 0.76	1.5 – 1.0	0.007	7.1	2.8	19.0	2.91
50	**600**	3	0.75 – 0.82	2.0 – 1.7	0.015	5.3	2.8	15.3	1.8
50	**800**	4	0.63 – 0.73	1.7 – 1.3	0.012	7.1	2.3	16.7	1.2
60	**600**	1	0.87	1.9	0.022	5.4	3.1	15.8	1.4
60	**800**	4	0.70 – 0.76	1.8 – 1.5	0.017	7.1	3.0	16.5	1.5
Total/Overall Average		**28**	**0.73**	**1.5**	**0.010**	**0.88%**	**3.0**	**17.0**	**1.6**

Table C-2: Data Statistics for 200×100 μm Test Section

Test Conditions		No. of Data Points	Δx Range	Resistance Ratio Range	Average x_{ave} Uncertainty	Average G Uncertainty (kg/m^2-s)	Average ΔP Uncertainty (%)	Average h Uncertainty (%)	Average $P_{in,emp\_}$ Error (%)
T_{sat} (^oC)	G (kg/m^2-s)								
30	**300**	3	0.74 – 0.76	2.2 – 1.9	0.005	2.3	3.6	14.6	0.7
30	**400**	6	0.56 – 0.62	2.0 – 1.6	0.004	3.1	3.1	16.4	1.4
30	**600**	6	0.33 – 0.56	2.1 – 1.0	0.003	4.6	2.6	18.6	1.9
30	**800**	7	0.29 – 0.57	1.5 – 0.8	0.003	6.2	2.5	24.2	2.8
40	**300**	3	0.79 – 0.81	2.3 – 2.2	0.010	2.4	3.5	12.6	0.3
40	**400**	5	0.55 – 0.66	2.4 – 1.9	0.008	3.1	3.0	13.7	0.8
40	**600**	5	0.40 – 0.56	2.1 – 1.3	0.005	4.6	2.5	16.5	1.7
40	**800**	8	0.30 – 0.52	1.9 – 1.0	0.004	6.2	2.6	18.6	1.8
50	**300**	2	0.83 – 0.80	2.4 – 2.4	0.016	2.4	3.7	12.8	0.4
50	**400**	5	0.63 – 0.69	2.4 – 2.1	0.012	3.1	3.2	13.3	0.6
50	**600**	7	0.41 – 0.55	2.4 – 1.6	0.009	4.7	2.7	14.5	1.0
50	**800**	6	0.34 – 0.53	1.9 – 1.0	0.007	6.2	2.5	17.8	1.3
60	**300**	1	0.90	2.6	0.023	2.5	3.8	12.8	0.1
60	**400**	3	0.71 – 0.76	2.5 – 2.3	0.018	3.2	3.3	13.3	0.3
60	**600**	7	0.46 – 0.60	2.4 – 1.7	0.012	4.7	2.6	14.3	0.6
60	**800**	10	0.38 – 0.55	2.2 – 1.2	0.009	6.2	2.5	16.3	0.8
Total/Overall Average		**84**	**0.53**	**1.8**	**0.008**	**0.77%**	**2.8**	**16.3**	**1.2**

Table C-3: Data Statistics for 300×100 μm Test Section

Test Conditions		No. of Data Points	Δx Range	Resistance Ratio Range	Average x_{ave} Uncertainty	Average G Uncertainty (kg/m^2-s)	Average ΔP Uncertainty (%)	Average h Uncertainty (%)	Average $P_{in,emp\_}$ Error (%)
T_{sat} (°C)	G (kg/m^2-s)								
30	**300**	1	0.71	1.5	0.004	2.5	3.8	17.8	0.6
30	**400**	6	0.48 – 0.59	1.6 – 1.3	0.003	3.0	3.3	19.0	1.5
30	**600**	8	0.36 – 0.47	1.6 – 1.0	0.003	4.5	2.9	21.0	1.9
30	**800**	6	0.27 – 0.36	1.0 – 0.8	0.003	6.1	3.0	28.0	2.2
40	**300**	4	0.73 – 0.78	1.6 – 1.5	0.007	2.5	3.8	16.9	1.2
40	**400**	6	0.50 – 0.63	1.6 – 1.4	0.006	3.2	3.5	17.3	1.4
40	**600**	7	0.39 – 0.51	1.5 – 1.0	0.004	4.5	3.1	19.5	0.9
40	**800**	9	0.35 – 0.42	1.2 – 0.9	0.004	6.0	2.9	22.0	1.3
50	**300**	4	0.85 – 0.87	1.7 – 1.6	0.012	2.3	4.3	15.3	0.3
50	**400**	6	0.64 – 0.69	1.7 – 1.6	0.010	3.0	3.7	15.5	0.8
50	**600**	12	0.45 – 0.55	1.6 – 1.2	0.007	4.5	3.3	17.4	0.7
50	**800**	9	0.39 – 0.44	1.3 – 1.0	0.005	6.0	3.0	20.0	0.8
60	**300**	–	–	–	–	–	–	–	–
60	**400**	6	0.66 – 0.72	1.9 – 1.8	0.014	3.1	3.8	14.6	1.4
60	**600**	9	0.48 – 0.58	1.8 – 1.4	0.010	4.6	3.4	16.0	1.0
60	**800**	9	0.41 – 0.49	1.4 – 1.1	0.008	6.0	3.2	19.1	0.8
Total/Overall Average		**102**	**0.51**	**1.4**	**0.007**	**0.74%**	**3.3**	**18.8**	**1.1**

Table C-4: Data Statistics for 400×100 μm Test Section

Test Conditions		No. of Data Points	Δx Range	Resistance Ratio Range	Average x_{ave} Uncertainty	Average G Uncertainty (kg/m^2-s)	Average ΔP Uncertainty (%)	Average h Uncertainty (%)	Average $P_{in,emp\_}$ Error (%)
T_{sat} (^oC)	G (kg/m^2-s)								
30	**300**	5	0.60 – 0.69	1.3 – 1.0	0.003	2.3	2.6	22.7	1.0
30	**400**	8	0.41 – 0.58	1.2 – 0.8	0.003	3.0	2.4	24.7	1.5
30	**600**	8	0.30 – 0.48	1.1 – 0.7	0.002	4.5	2.2	27.3	2.7
30	**800**	2	0.35 – 0.39	0.4 – 0.4	0.002	6.0	2.2	57.3	4.0
40	**300**	5	0.60 – 0.68	1.4 – 1.2	0.006	2.3	2.6	18.7	0.7
40	**400**	8	0.42 – 0.59	1.4 – 0.8	0.005	3.1	2.3	22.6	1.2
40	**600**	12	0.31 – 0.50	1.3 – 0.7	0.004	4.5	2.2	24.7	1.7
40	**800**	8	0.31 - 0.42	0.7 – 0.5	0.003	6.0	2.2	36.6	1.5
50	**300**	5	0.67 – 0.73	1.5 – 1.3	0.010	2.3	2.6	17.4	0.6
50	**400**	9	0.46 – 0.67	1.5 – 1.1	0.008	3.0	2.4	19.2	1.2
50	**600**	11	0.35 – 0.52	1.3 – 0.7	0.005	4.5	2.3	24.1	1.2
50	**800**	10	0.35 – 0.46	0.8 – 0.6	0.004	6.0	2.2	31.0	1.6
60	**300**	2	0.76 – 0.76	1.6 – 1.5	0.014	2.3	2.7	16.0	0.4
60	**400**	10	0.54 – 0.69	1.6 – 1.2	0.011	3.6	2.5	17.7	0.7
60	**600**	11	0.40 – 0.57	1.4 – 0.9	0.008	4.5	2.4	21.2	0.8
60	**800**	7	0.35 – 0.43	1.1 – 0.7	0.006	6.0	2.3	25.9	1.1
Total/Overall Average		**121**	**0.48**	**1.0**	**0.006**	**0.74%**	**2.3**	**24.5**	**1.3**

C.2. Pressure Drop Contributions Tables for Each Test Section

Table C-5: Pressure Drop Contributions Statistics for 100×100 μm Test Section

Test Conditions		Δx Range	Range (% of Measured ΔP)				Average (% of Measured ΔP)			
T_{sat} (^oC)	G (kg/m^2-s)		$\Delta P_{frictional}$	$\Delta P_{decel.}$	$\Delta P_{others,in}$	$\Delta P_{others,out}$	$\Delta P_{frictional}$	$\Delta P_{decel.}$	$\Delta P_{others,in}$	$\Delta P_{others,out}$
30	**600**	0.64 – 0.80	101.1 - 102.1	4.3 - 5.4	3.2 - 3.4	0.1 - 0.1	101.7	4.9	3.3	0.1
30	**800**	–	–	–	–	–	–	–	–	–
40	**600**	0.71 – 0.82	101.5 – 102.1	4.7 – 5.3	3.2 – 3.3	0.1 – 0.1	101.8	5.0	3.3	0.1
40	**800**	0.58 – 0.76	100.8 – 101.7	4.0 – 4.8	3.1 – 3.2	0.1 – 0.1	101.2	4.3	3.2	0.1
50	**600**	0.75 – 0.82	101.4 – 101.6	4.3 – 4.4	3.1 – 3.2	0.1 – 0.1	101.5	4.3	2.9	0.1
50	**800**	0.63 – 0.73	101.1 – 101.5	4.2 – 4.6	3.2 – 3.4	0.1 – 0.1	101.2	4.4	3.2	0.1
60	**600**	0.87	101.8	4.8	3.1	0.1	101.8	4.8	3.1	0.1
60	**800**	0.70 – 0.76	101.3 – 101.5	4.5 – 4.6	3.2 – 3.4	0.1 – 0.1	101.4	4.6	3.2	0.1
Total/Overall Average							**101.5**	**4.7**	**3.2**	**0.1**

Table C-6: Pressure Drop Contributions Statistics for 200×100 μm Test Section

Test Conditions		Δx Range	Range (% of Measured ΔP)				Average (% of Measured ΔP)			
T_{sat} (°C)	G (kg/m²-s)		$\Delta P_{frictional}$	$\Delta P_{decel.}$	$\Delta P_{others,in}$	$\Delta P_{others,out}$	$\Delta P_{frictional}$	$\Delta P_{decel.}$	$\Delta P_{others,in}$	$\Delta P_{others,out}$
30	**300**	0.74 – 0.76	101.6 – 101.9	5.6 – 6.0	3.8 – 4.0	0.0 – 0.2	101.7	5.7	3.9	0.1
30	**400**	0.56 – 0.62	100.6 – 100.9	4.4 – 4.7	3.5 – 4.0	0.1 – 0.3	100.7	4.6	3.7	0.2
30	**600**	0.33 – 0.56	99.1 – 100.4	3.1 – 4.1	3.4 – 4.0	0.2 – 0.3	99.6	3.5	3.6	0.3
30	**800**	0.29 – 0.57	99.0 – 100.3	3.0 - 3.9	3.3 – 3.8	0.2 – 0.3	99.5	3.3	3.5	0.3
40	**300**	0.79 – 0.81	101.6 – 101.8	5.3 – 5.6	3.6 – 3.6	0.0 – 0.2	101.7	5.5	3.6	0.1
40	**400**	0.55 – 0.66	100.5 – 101.0	4.2 – 4.6	3.3 – 3.7	0.1 – 0.2	100.7	4.3	3.5	0.2
40	**600**	0.40 – 0.56	99.6 – 100.4	3.1 – 3.8	3.1 – 3.4	0.2 – 0.3	99.9	3.4	3.2	0.2
40	**800**	0.30 – 0.52	99.0 – 100.1	3.0 – 3.7	3.4 – 4.0	0.2 – 0.3	99.4	3.3	3.6	0.3
50	**300**	0.83 – 0.80	101.8 – 101.7	5.6 – 5.7	3.7 – 3.9	0.1 – 0.2	101.8	5.5	3.8	0.1
50	**400**	0.63 – 0.69	100.8 – 101.1	4.5 – 4.9	3.5 – 3.7	0.1 – 0.2	100.9	4.7	3.6	0.2
50	**600**	0.41 – 0.55	99.6 – 100.3	3.4 – 3.9	3.3 – 3.6	0.1 – 0.3	99.9	3.5	3.4	0.2
50	**800**	0.34 – 0.53	99.3 – 100.1	2.9 – 3.6	3.2 – 3.4	0.2 – 0.3	99.6	3.2	3.3	0.2
60	**300**	0.90	101.9	5.7	3.7	0.1	101.9	5.7	3.7	0.1
60	**400**	0.71 – 0.76	101.1 – 101.2	4.8 – 5.0	3.5 – 3.6	0.1 – 0.2	101.1	4.8	3.6	0.1
60	**600**	0.46 – 0.60	99.8 – 100.4	3.3 – 3.7	3.1 – 3.3	0.1 – 0.2	100.1	3.5	3.2	0.2
60	**800**	0.38 – 0.55	99.6 – 100.1	2.9 – 3.5	3.1 – 3.4	0.1 – 0.3	99.7	3.2	3.2	0.2
Total/Overall Average							**100.2**	**3.9**	**3.5**	**0.2**

Table C-7: Pressure Drop Contributions Statistics for 300×100 μm Test Section

Test Conditions		**Δx Range**	**Range (% of Measured ΔP)**				**Average (% of Measured ΔP)**			
T_{sat} (°C)	**G (kg/m²-s)**		**$\Delta P_{frictional}$**	**$\Delta P_{decel.}$**	**$\Delta P_{others,in}$**	**$\Delta P_{others,out}$**	**$\Delta P_{frictional}$**	**$\Delta P_{decel.}$**	**$\Delta P_{others,in}$**	**$\Delta P_{others,out}$**
30	**300**	0.71	101.0	5.8	4.3	0.5	101.1	5.8	4.3	0.5
30	**400**	0.48 – 0.59	99.4 – 100.2	4.3 – 5.0	4.1 – 4.4	0.4 – 0.7	99.8	4.6	4.2	0.6
30	**600**	0.36 – 0.47	98.6 – 99.0	3.4 – 3.8	3.9 – 4.4	0.5 – 0.9	98.7	3.5	4.1	0.8
30	**800**	0.27 – 0.36	97.8 – 98.5	3.1 – 3.5	4.3 – 4.6	0.6 – 0.8	98.1	3.3	4.5	0.7
40	**300**	0.73 – 0.78	101.0 – 101.3	5.7 – 5.9	4.3 – 4.3	0.3 – 0.5	101.1	5.8	4.3	0.4
40	**400**	0.50 – 0.63	99.7 – 100.3	4.6 – 5.3	4.3 – 4.4	0.5 – 0.8	99.9	4.9	4.4	0.6
40	**600**	0.39 – 0.51	99.8 – 99.4	3.7 – 4.3	4.0 – 4.5	0.3 – 0.8	99.1	3.9	4.2	0.6
40	**800**	0.35 – 0.42	98.2 – 98.6	3.2 – 3.2	4.1 – 4.3	0.7 – 1.0	98.3	3.3	4.1	0.9
50	**300**	0.85 – 0.87	101.6 – 101.9	6.5 – 6.8	4.5 – 4.6	0.2 – 0.4	101.7	6.6	4.6	0.3
50	**400**	0.64 – 0.69	100.4 – 100.6	5.1 – 5.6	4.3 – 4.4	0.3 – 0.6	100.5	5.3	4.3	0.5
50	**600**	0.45 – 0.55	98.9 – 99.6	4.0 – 4.9	4.2 – 4.4	0.4 – 0.9	99.2	4.2	4.3	0.7
50	**800**	0.39 – 0.44	98.6 – 99.0	3.5 – 3.9	4.2 – 4.3	0.4 – 1.0	98.7	3.7	4.3	0.8
60	**300**	–	–	–	–	–	–	–	–	–
60	**400**	0.66 – 0.72	100.2 – 100.6	4.9 – 5.5	4.3 – 4.4	0.3 – 0.6	100.4	5.2	4.4	0.5
60	**600**	0.48 – 0.58	99.1 – 99.6	4.0 – 4.7	4.3 – 4.4	0.5 – 0.8	99.4	4.3	4.3	0.7
60	**800**	0.41 – 0.49	98.7 – 98.9	3.7 – 4.1	4.3 – 4.4	0.5 – 0.9	98.8	3.9	4.3	0.8
Total/Overall Average							**99.3**	**4.3**	**4.3**	**0.7**

Table C-8: Pressure Drop Contributions Statistics for 400×100 μm Test Section

Test Conditions		Δx Range	Range (% of Measured ΔP)				Average (% of Measured ΔP)			
T_{sat} (°C)	G (kg/m²-s)		$\Delta P_{frictional}$	$\Delta P_{decel.}$	$\Delta P_{others,in}$	$\Delta P_{others,out}$	$\Delta P_{frictional}$	$\Delta P_{decel.}$	$\Delta P_{others,in}$	$\Delta P_{others,out}$
30	**300**	0.60 – 0.69	98.9 – 99.2	3.1 – 3.7	3.6 – 3.6	0.5 – 0.9	99.0	3.3	3.6	0.7
30	**400**	0.41 – 0.58	98.1 – 98.6	2.3 – 3.0	3.4 – 3.7	0.6 – 1.1	98.3	2.7	3.5	0.9
30	**600**	0.30 – 0.48	97.4 – 97.9	1.9 – 2.3	3.2 – 3.7	0.8 – 1.2	97.5	2.0	3.4	1.1
30	**800**	0.35 – 0.39	97.7 – 98.0	2.0 – 2.2	3.4 – 3.4	0.8 – 0.8	97.8	2.1	3.4	0.8
40	**300**	0.60 – 0.68	98.9 – 99.1	3.0 – 3.4	3.5 – 3.6	0.5 – 0.8	99.0	3.2	3.5	0.7
40	**400**	0.42 – 0.59	98.2 – 98.7	2.3 – 2.9	3.3 – 3.5	0.6 – 1.0	98.4	2.6	3.4	0.8
40	**600**	0.31 – 0.50	97.6 – 98.0	2.0 – 2.4	3.2 – 3.7	0.7 – 1.2	97.7	2.1	3.4	1.0
40	**800**	0.31 - 0.42	97.5 – 97.8	2.0 – 2.1	3.3 – 3.6	0.6 – 1.1	97.7	2.0	3.5	0.9
50	**300**	0.67 – 0.73	99.1 – 99.2	3.1 – 3.3	3.4 – 3.6	0.5 – 0.7	99.2	3.2	3.5	0.6
50	**400**	0.46 – 0.67	98.4 – 99.0	2.4 – 3.3	3.3 – 3.5	0.5 – 0.9	98.6	2.7	3.4	0.7
50	**600**	0.35 – 0.52	97.7 – 98.1	2.1 – 2.6	3.3 – 3.6	0.6 – 1.2	97.9	2.3	3.4	0.9
50	**800**	0.35 – 0.46	97.5 – 97.8	2.0 – 2.2	3.2 – 3.7	0.7 – 1.2	97.6	2.1	3.4	1.1
60	**300**	0.76 – 0.76	99.3 – 99.4	3.3 – 3.3	3.4 – 3.5	0.4 – 0.6	99.3	3.3	3.5	0.5
60	**400**	0.54 – 0.69	98.5 – 98.9	2.6 – 3.1	3.4 – 3.5	0.6 – 0.8	98.7	2.8	3.4	0.7
60	**600**	0.40 – 0.57	97.7 – 98.1	2.1 – 2.8	3.5 – 3.7	0.6 – 1.1	98.0	2.5	3.5	0.9
60	**800**	0.35 – 0.43	97.4 – 97.8	2.1 – 2.2	3.4 – 3.7	0.7 – 1.3	97.5	2.2	3.6	1.1
Total/Overall Average							**98.2**	**2.5**	**3.5**	**0.9**

APPENDIX-D. DETAILED DERIVATIONS OF MODELS

D.1. Derivation of Interface Velocity

The interface velocity is determined by conducting a shear balance at the interface. Since the flow in the bubble is driven by the pressure gradient (Garimella *et al.*, 2002):

$$\tau_{interface} = -\frac{\left(D_{bubble}/2 \right)}{2}\left(\frac{dP}{dx}\right)_{f/b}$$

To determine the interfacial shear stress due to the film, the film velocity profile must first be determined. The liquid flow in the film is treated as a combination of Couette flow and Poiseuille flow and the film velocity is determined by superposition (Garimella *et al.*, 2002). The fluid motion in X direction is governed by:

$$\frac{d^2u}{dy^2} = \frac{1}{\mu}\frac{dP}{dx}$$

which yields

$$\Rightarrow \frac{du}{dy} = \frac{1}{\mu}\frac{dP}{dx}y + C_1$$

$$\Rightarrow u = \frac{1}{2\mu}\frac{dP}{dx}y^2 + C_1 y + C_2$$

Treating the interface as $y = 0$ and the tube wall as $y = \delta_{ave}$, the boundary conditions for fluid flow in the film are as follows:

At $y = 0$ $\quad u = U_{interface} \quad \Rightarrow U_{interface} = C_2$

At $y = \delta_{ave}$ $\quad u = 0 \quad \Rightarrow 0 = \dfrac{1}{2\mu}\dfrac{dP}{dx}\delta_{ave}{}^2 + C_1 \cdot \delta_{ave} + C_2$

$$\Rightarrow C_1 = -\frac{1}{2\mu}\frac{dP}{dx}\delta_{ave} - \frac{U_{interface}}{\delta_{ave}}$$

$$\Rightarrow u = \frac{1}{2\mu_L}\frac{dP}{dx}y^2 + \left(-\frac{1}{2\mu}\frac{dP}{dx}\delta_{ave} - \frac{U_{interface}}{\delta_{ave}}\right)y + U_{interface}$$

$$\Rightarrow u_{film} = \frac{1}{2\mu_L}\left(\frac{dP}{dx}\right)_{f/b} y\left(y - \delta_{ave}\right) + U_{interface}\left(1 - \frac{y}{\delta_{ave}}\right)$$

Now, $\tau_{interface} = \mu_L \left(\dfrac{du_{film}}{dy}\right)_{y=0}$

$$\frac{du_{film}}{dy} = \frac{1}{2\mu}\left(\frac{dP}{dx}\right)_{f/b}\left(2y - \delta_{ave}\right) + U_{interface}\left(0 - \frac{1}{\delta_{ave}}\right)$$

$$\Rightarrow \left(\frac{du_{film}}{dy}\right)_{y=0} = -\frac{1}{2\mu}\left(\frac{dP}{dx}\right)_{f/b}\delta_{ave} - \frac{U_{interface}}{\delta_{ave}}$$

$$\Rightarrow \tau_{interface} = \mu_L\left(-\frac{1}{2\mu}\left(\frac{dP}{dx}\right)_{f/b}\delta_{ave} - \frac{U_{interface}}{\delta_{ave}}\right)$$

$$\tau_{interface} = -\frac{\left(D_{bubble}/2\right)}{2}\left(\frac{dP}{dx}\right)_{f/b} = \mu_L\left(-\frac{1}{2\mu}\left(\frac{dP}{dx}\right)_{f/b}\delta_{ave} - \frac{U_{interface}}{\delta_{ave}}\right)$$

$$\Rightarrow U_{interface} = \left(\frac{dP}{dx}\right)_{f/b}\left(\frac{D_{bubble}}{2} - \delta_{ave}\right)\frac{\delta_{ave}}{2 \cdot \mu_L}$$

D.2. Calculation of Average Film Velocity:

$$u_{film} = \frac{1}{2\mu_L}\left(\frac{dP}{dx}\right)_{f/b} y\left(y-\delta_{ave}\right) + \left(\frac{dP}{dx}\right)_{f/b}\left(\frac{D_{bubble}}{2}-\delta_{ave}\right)\frac{\delta_{ave}}{2\cdot\mu_L}\left(1-\frac{y}{\delta_{ave}}\right)$$

$$\Rightarrow u_{film} = \frac{1}{2\mu_L}\left(\frac{dP}{dx}\right)_{f/b}\left[\left(y^2 - y\delta_{ave}\right) + \left(\frac{\delta_{ave}D_{bubble}}{2} - \delta_{ave}{}^2 - \frac{yD_{bubble}}{2} + y\delta_{ave}\right)\right]$$

$$U_{film} = \frac{1}{\delta_{ave}}\int_0^{\delta_{ave}} u_{film}dy$$

$$\Rightarrow U_{film} = \frac{1}{2\mu}\left(\frac{dP}{dx}\right)_{f/b}\frac{1}{\delta_{ave}}\left[\left(\frac{y^3}{3}-\frac{y^2}{2}\delta_{ave}\right) + \left(\frac{\delta_{ave}D_{bubble}}{2}y - \delta_{ave}{}^2 y - \frac{y^2 D_{bubble}}{4} + \frac{y^2\delta_{ave}}{2}\right)\right]_0^{\delta_{ave}}$$

$$\Rightarrow U_{film} = \frac{1}{2\mu_L}\left(\frac{dP}{dx}\right)_{f/b}\left[\left(\frac{1}{3}-\frac{1}{2}-1+\frac{1}{2}\right)\delta_{ave}{}^2 + \left(\frac{1}{2}-\frac{1}{4}\right)\delta_{ave}D_{bubble}\right]$$

$$\Rightarrow U_{film} = \frac{1}{4\mu_L}\left(\frac{dP}{dx}\right)_{f/b}\left[\left(\frac{1}{2}\right)D_{bubble} - \left(\frac{4}{3}\right)\delta_{ave}\right]\delta_{ave}$$

D.3. Derivation of Slip Velocity Ratio

The following equation (Equation 6.19 in main text) was derived from the liquid mass balance in Section 6.1.

$$\frac{G\cdot(1-x)}{\rho_L} = U_{slug}\cdot\left(\frac{l_{slug}}{l_{slug}+l_{bubble}}\right) + U_{film}\cdot\left(1-\frac{w_B\cdot d_B}{w_{TS}\cdot d_{TS}}\right)\cdot\left(1-\frac{l_{slug}}{l_{slug}+l_{bubble}}\right)$$

Following equation (Equation 6.15 in main text) was determined for relationship of bubble velocity with other velocities:

$$U_{slug} = U_{bubble}\left(\frac{w_B\cdot d_B}{w_{TS}\cdot d_{TS}}\right) + U_{film}\cdot\left(1-\frac{w_B\cdot d_B}{w_{TS}\cdot d_{TS}}\right)$$

Substituting the film velocity from the above expression into the liquid mass balance equation, we get:

$$\Rightarrow \frac{G\cdot(1-x)}{\rho_L} = U_{slug}\cdot\left(\frac{l_{slug}}{l_{slug}+l_{bubble}}\right) + \left[U_{slug} - U_{bubble}\left(\frac{w_B\cdot d_B}{w_{TS}\cdot d_{TS}}\right)\right]\cdot\left(1-\frac{l_{slug}}{l_{slug}+l_{bubble}}\right)$$

$$\Rightarrow \frac{G\cdot(1-x)}{U_{slug}\cdot\rho_L} = \left(\frac{l_{slug}}{l_{slug}+l_{bubble}}\right) + \left[1 - \frac{U_{bubble}}{U_{slug}}\left(\frac{w_B\cdot d_B}{w_{TS}\cdot d_{TS}}\right)\right]\cdot\left(1-\frac{l_{slug}}{l_{slug}+l_{bubble}}\right)$$

Substitute the void fraction definition below into the equation above.

$$\alpha = \left(1-\frac{l_{slug}}{l_{slug}+l_{bubble}}\right)\cdot\frac{w_B\cdot d_B}{w_{TS}\cdot d_{TS}}$$

$$\Rightarrow \frac{G\cdot(1-x)}{U_{slug}\cdot\rho_L} = \left(1-\alpha\cdot\frac{w_{TS}\cdot d_{TS}}{w_B\cdot d_B}\right) + \left[1 - \frac{U_{bubble}}{U_{slug}}\left(\frac{w_B\cdot d_B}{w_{TS}\cdot d_{TS}}\right)\right]\cdot\alpha\cdot\frac{w_{TS}\cdot d_{TS}}{w_B\cdot d_B}$$

$$\Rightarrow \frac{G\cdot(1-x)}{U_{slug}\cdot\rho_L} = \left(1-\cancel{\alpha\cdot\frac{w_{TS}\cdot d_{TS}}{w_B\cdot d_B}}\right) + \cancel{\alpha\cdot\frac{w_{TS}\cdot d_{TS}}{w_B\cdot d_B}} - \frac{U_{bubble}}{U_{slug}}\left(\cancel{\frac{w_B\cdot d_B}{w_{TS}\cdot d_{TS}}}\right)\cdot\alpha\cdot\cancel{\frac{w_{TS}\cdot d_{TS}}{w_B\cdot d_B}}$$

$$\Rightarrow \frac{G\cdot(1-x)}{U_{slug}\cdot\rho_L} = 1 - \frac{U_{bubble}}{U_{slug}}\cdot\alpha$$

Now, $U_{slug} = j_L + j_V = \frac{(1-x)G}{\rho_L} + \frac{x\cdot G}{\rho_V}$. Substituting this definition in the L.H.S. of the above equation we get:

$$\Rightarrow L.H.S. = \frac{G\cdot(1-x)}{\left[\frac{(1-x)G}{\rho_L}+\frac{x\cdot G}{\rho_V}\right]\cdot\rho_L} = \frac{\rho_V\cdot(1-x)}{(1-x)\rho_V + x\cdot\rho_L}$$

The homogenous void fraction, $\beta = \frac{x\cdot\rho_L}{x\cdot\rho_L + (1-x)\cdot\rho_V}$

$$\Rightarrow L.H.S. = 1-\beta$$

Thus equating the LHS and RHS, we get:

$$\Rightarrow 1-\beta = 1-\frac{U_{bubble}}{U_{slug}}\cdot\alpha$$

$$\Rightarrow \frac{U_{bubble}}{U_{slug}} = \frac{\beta}{\alpha}$$

According to the Armand (1946) correlation $\alpha = 0.833\times\beta$.

$$\Rightarrow \frac{U_{bubble}}{U_{slug}} = \frac{\beta}{0.833\times\beta} = \frac{1}{0.833} = 1.2$$

D.4. Average Film Thickness Integral

$$\delta_{ave} = \frac{1}{l_B}\int_0^{l_B}\delta\cdot dz$$

$$\Rightarrow \delta_{ave} = \frac{1}{l_B}\int_0^{l_B}\left(\delta_0 + \frac{h_f\left(T-T_{wall}\right)}{\rho_L\cdot h_{fg}}\cdot\frac{z}{U_{bubble}}\right)\cdot dz$$

$$\Rightarrow \delta_{ave} = \frac{1}{l_B}\left[\delta_0\cdot z + \frac{h_f\left(T-T_{wall}\right)}{\rho_L\cdot h_{fg}}\cdot\frac{z^2}{2\cdot U_{bubble}}\right]_0^{l_B}$$

$$\Rightarrow \delta_{ave} = \frac{1}{l_B}\left[\delta_0\cdot l_B + \frac{h_f\left(T-T_{wall}\right)}{\rho_L\cdot h_{fg}}\cdot\frac{l_B{}^2}{2\cdot U_{bubble}}\right]$$

$$\Rightarrow \delta_{ave} = \delta_0 + \frac{h_f\left(T-T_{wall}\right)}{\rho_L\cdot h_{fg}}\cdot\frac{l_B}{2\cdot U_{bubble}}$$

D.5. Derivation of Transient Wall Temperature Profile

If it is assumed that the wall is large in all directions perpendicular to the direction of heat flow the heat transfer may be approximated as being one dimensional. For a constant thermal conductivity *k*, the conduction heat transfer is governed by the following equation:

$$\frac{\partial^2 T(x,t)}{\partial x^2} = \frac{1}{\alpha}\frac{\delta T(x,t)}{\delta t} \tag{D.1}$$

Rather than solving for a periodic boundary condition (of liquid slugs and the film-bubble regions intermittently passing by), we will first solve the transient conduction problem for a constant convection boundary condition on one side (near the refrigerant) and a constant heat flux condition on the other side (near the coolant). Figure 6.29 shows a schematic of this transient problem.

The approach for solving a transient problem with a contant flux on one side and convection on the other side is derived based on the one-dimensional plain wall transient analysis of Myers (1998) and Powers (1999). Thus, the boundary conditions are given by the following two equations:

$$-k\frac{\delta T(L,t)}{\delta x} = h_R\left[T(L,t) - T_R\right] \tag{D.2}$$

$$-k\frac{\delta T(0,t)}{\delta x} = q'' \tag{D.3}$$

Let us assume that the wall initially has a known temperature distribution $T_0(x)$. The following notation for partial derivatives is adopted:

$$T_x = \frac{\partial T}{\partial x}, \quad T_{xx} = \frac{\partial^2 T}{\partial x^2} \quad \text{and} \quad T_t = \frac{\partial T}{\partial t}$$

To obtain the above non-homogenous problem, we will assume that the solution for $T(x, t)$ can be written as:

$$T(x,t) = A(x) + B(t) + u(x,t) \tag{D.4}$$

Substituting this assumed form of the solution into the partial differential equation yields:

$$A''(x) + u_{xx}(x,t) = \frac{1}{\alpha}\left[B'(t) + u_t(x,t)\right] \tag{D.5}$$

This equation can be satisfied by taking the *u(x,t)* to satisfy the homogenous partial differential equation:

$$u_{xx}(x,t) = \frac{1}{\alpha}u_t(x,t) \tag{D.6}$$

This means that *A(x)* and *B(t)* must satisfy:

$$A''(x) = \frac{1}{\alpha}B'(t) \tag{D.7}$$

The only way that a function of *x* can equal a function of *t* is if each function is equal to the same constant. Thus, we will require *A(x)* to satisfy the following second order differential equation:

$$A''(x) = c_1 \tag{D.8}$$

and *B(t)* satisfy the first-order ordinary differential equation:

$$\frac{1}{\alpha}B'(t) = c_1 \tag{D.9}$$

Substituting (D.4) into the boundary condition at $x = L$ given by (D.2) we get:

$$-k\left[A'(L) + u_x(L,t)\right] = h_R\left[A(L) + B(t) + u(L,t) - T_R\right]$$

This can be satisfied by requiring *u(x,t)* to obey the homogenous condition:

$$-k \cdot u_x(L,t) = h_R \cdot u(L,t) \tag{D.10}$$

In addition:

$$-k \cdot A'(L) = h_R \left[A(L) - T_R \right] \tag{D.11}$$

Therefore we must also require:

$$B(t) = 0 \tag{D.12}$$

Similarly, substituting (D.4) into the boundary condition at $x = 0$ given by (D.3), we get:

$$-k\left[A'(0) + u_x(0,t) \right] = q''$$

This can be satisfied by requiring *u(x,t)* to obey the homogenous condition:

$$-ku_x(0,t) = 0 \tag{D.13}$$

Therefore we must also require:

$$-k \cdot A'(0) = q'' \tag{D.14}$$

The initial condition for *u(x,t)* is found by substituting (D.4) into the initial condition for *T(x,t)* to obtain:

$$T(x,0) = T_0(x) = A(x) + B(0) + u(x,0)$$

Noting from (D.12) that *B(0)* = 0, we get:

$$u(x,0) = T_0(x) - A(x) \tag{D.15}$$

We now have enough relations to specify sub-problems for *A(x)*, *B(t)* and *u(x,t)*. The problem for *A(x)* is non-homogenous, but this does not matter since *A(x)* obeys an ordinary differential equation. The problem for *u(x,t)*, where homogeneity is important, has been constructed to be homogenous.

Equation (D.12) is the solution for *B(t)*. Since *B(t)* is a constant, $B^{'}(t)=0$ and from (D.9) we see that c_1 must be 0.

The solution for (D.8) for $c_1 = 0$ is as follows:

$$A''(x)=c_1=0$$
$$\Rightarrow A'(x)=a_1$$

$$\Rightarrow A(x)=a_1x+a_2 \tag{D.16}$$

Substituting the above solution into the boundary condition (D.11) at $x = L$, we get:

$$-k\cdot a_1=h\cdot\left[a_1L+a_2-T_R\right] \tag{D.17}$$

Substituting (D.16) into boundary condition (D.5.14) at $x = 0$, we get:

$$-k\cdot a_1=q''$$

$$\Rightarrow a_1=-\frac{q''}{k} \tag{D.18}$$

Substituting a_1 into (D.17) we get:

$$\cancel{-}\cancel{k}\cdot\left(\cancel{-}\frac{q''}{\cancel{k}}\right)=h\cdot\left[\left(-\frac{q''}{k}\right)L+a_2-T_R\right]$$
$$\Rightarrow q''=h\cdot\left[\left(-\frac{q''}{k}\right)L+a_2-T_R\right]$$

$$\Rightarrow a_2=T_R+q''\cdot\left(\frac{1}{h}+\frac{L}{k}\right) \tag{D.19}$$

Thus, *A(x)* is given by:

$$A(x) = -\frac{q''}{k}x + T_R + q'' \cdot \left(\frac{1}{h} + \frac{L}{k}\right)$$

$$\Rightarrow A(x) = \frac{q''}{k}(L - x) + \frac{q''}{h} + T_R \tag{D.20}$$

Substituting *A(x)* and *B(x)* in (D.4) we get:

$$T(x,t) = T_R + q''\left[\frac{1}{k}(L - x) + \frac{1}{h}\right] + u(x,t) \tag{D.21}$$

The homogenous problem for *u(x,t)* is defined by (D.6) and boundary conditions are given by (D.10) and (D.13). The initial state for the problem is given by (D.15). Since the problem is homogenous now, the Separation of Variables method can be used. Thus, the solution for *u(x,t)* can be written as a product of a function of *x*, *R(x)* and a function of *t*, *S(t)*:

$$u(x,t) = R(x) \cdot S(t) \tag{D.22}$$

Substituting this assumed solution into the PDE (D.6) yields:

$$R''(x) \cdot S(t) = \frac{1}{\alpha} R(x) \cdot S'(t)$$

$$\Rightarrow \frac{R''(x)}{R(x)} = \frac{1}{\alpha} \cdot \frac{S'(t)}{S(t)} \tag{D.23}$$

Upon setting each side of the above equation equal to $-\lambda^2$, we get the following equations for each of the functions:

$$R''(x) + \lambda^2 \cdot R(x) = 0 \tag{D.24}$$

$$S'(t) + \lambda^2 \cdot \alpha \cdot S(t) = 0 \tag{D.25}$$

Substituting (D.22) into the boundary condition at x = 0 (D.13) yields:

$$R'(0) \cdot S(t) = 0$$

$$\Rightarrow R'(0) = 0 \tag{D.26}$$

Substituting (D.22) into the boundary condition at x = L (D.10) yields:

$$-k \cdot R'(L) \cdot \cancel{S(t)} = h \cdot R(L) \cdot \cancel{S(t)}$$

$$\Rightarrow -k \cdot R'(L) = h \cdot R(L) \tag{D.27}$$

The general solution to (D.24) is of the form:

$$R(x) = A \cdot \sin(\lambda x) + B \cdot \cos(\lambda x) \tag{D.28}$$

$$\Rightarrow R'(x) = A\lambda \cdot \cos(\lambda x) - B\lambda \cdot \sin(\lambda x) \tag{D.29}$$

Substituting the above solution into the boundary condition at x = 0 (D.26) yields:

$$\begin{aligned} &A\lambda \cdot \cos(\lambda 0) - B\lambda \cdot \sin(\lambda 0) = 0 \\ &\Rightarrow A\lambda = 0 \end{aligned}$$

$$\Rightarrow A = 0 \tag{D.30}$$

Substituting (D.28) into the boundary condition at x = L (D.27) yields:

$$\begin{aligned} &-k \cdot R'(L) = h \cdot R(L) \\ &\Rightarrow -k \cdot \left[A\lambda \cdot \cos(\lambda L) - B\lambda \cdot \sin(\lambda L) \right] = h \cdot \left[A \cdot \sin(\lambda L) + B \cdot \cos(\lambda L) \right] \\ &\Rightarrow -k \cdot \left[-\cancel{B}\lambda \cdot \sin(\lambda L) \right] = h \cdot \left[\cancel{B} \cdot \cos(\lambda L) \right] \\ &\Rightarrow h \cdot \cos(\lambda L) - k\lambda \cdot \sin(\lambda L) = 0 \end{aligned}$$

Multiplying both sides by L/k yields the following equation where $\frac{hL}{k}$ is the Biot number.

$$\Rightarrow \frac{hL}{k} \cdot \cos(\lambda L) - \lambda L \cdot \sin(\lambda L) = 0 \tag{D.31}$$

Solution of the above equation yields the eigen-values of λ.

Equation (D.24) has a solution given by:

$$R_n(x) = B_n \cdot \cos(\lambda_n x) \tag{D.32}$$

Similarly, equation (D.25) has a solution given by:

$$S_n(t) = \exp\left(-\lambda_n^{\ 2} \cdot \alpha \cdot t\right) \tag{D.33}$$

The eigen-values λ_n in each of these equations are obtained from the eigen-condition (D.31). Substituting these functions into (D.22), we get:

$$u_n(x,t) = B_n \cdot \cos(\lambda_n x) \cdot \exp\left(-\lambda_n^{\ 2} \cdot \alpha \cdot t\right) \tag{D.34}$$

The solution satisfies the PDE (D.6) for *u(x,t)* and its boundary conditions (D.10) and (D.13), for n = 1, 2, … To satisfy the initial condition (D.15), these solutions are summed to obtain the general solution:

$$u(x,t) = \sum_{n=1}^{\infty} B_n \cdot \cos(\lambda_n x) \cdot \exp\left(-\lambda_n^{\ 2} \cdot \alpha \cdot t\right) \tag{D.35}$$

where, λ_n must satisfy the eigen-condition (D.31). Above equation also satisfies the PDE and its boundary conditions. Now the solution for *T(x,t)* is given by:

$$T(x,t) = T_R + q''\left[\frac{1}{k}(L-x) + \frac{1}{h}\right] + \sum_{n=1}^{\infty} B_n \cdot \cos(\lambda_n x) \cdot \exp(-\lambda_n{}^2 \cdot \alpha \cdot t) \qquad \text{(D.36)}$$

At the initial state, i.e. at time $t = 0$

$$T(x,0) = T_R + q''\left[\frac{1}{k}(L-x) + \frac{1}{h}\right] + \sum_{n=1}^{\infty} B_n \cdot \cos(\lambda_n x) \qquad \text{(D.37)}$$

Rearranging the above equation we get:

$$\sum_{n=1}^{\infty} B_n \cdot \cos(\lambda_n x) = T(x,0) - T_R - q''\left[\frac{1}{k}(L-x) + \frac{1}{h}\right] \qquad \text{(D.38)}$$

Let the right hand side of the above equation be the function *G(x)*

$$G(x) = T(x,0) - T_R - q''\left[\frac{1}{k}(L-x) + \frac{1}{h}\right] \qquad \text{(D.39)}$$

Thus, we have:

$$\sum_{n=1}^{\infty} B_n \cdot \cos(\lambda_n x) = G(x) \qquad \text{(D.40)}$$

We will now use the idea of orthogonality to determine the constant B_n. It may be shown by direct computation that:

$$\int_0^a \cos(\lambda_n x) \cdot \cos(\lambda_m x) \cdot dx = 0 \qquad \text{if } n \neq m \qquad \text{(D.41)}$$

Thus we multiply both the sides of (D.40) by $\cos(\lambda_m x)$ and integrate from 0 to L:

$$\int_0^L G(x)\cos(\lambda_m x) \cdot dx = \sum_{n=1}^{\infty} B_n \cdot \int_0^L \cos(\lambda_n x) \cdot \cos(\lambda_m x) \cdot dx \qquad \text{(D.42)}$$

where the integration is conducted term by term. According to (D.41), all the terms of the series disappear, except the one in which $n = m$, yielding the following equation for B_m:

$$B_m = \frac{\int_0^L G(x)\cos(\lambda_m x)\cdot dx}{\int_0^L \cos^2(\lambda_m x)\cdot dx} \tag{D.43}$$

The exact function for the initial state has still not been specified. In the foregoing, we have solved the problem where the wall at some known initial state is suddenly subjected to convection on one side and constant heat flux on the other side. In the current problem, the refrigerant side heat transfer coefficient varies periodically according to the following step function.

$$h = \begin{cases} h_f & 0 < t < t_f \quad \text{(film-bubble)} \\ h_s & t_f < t < (t_f + t_s) \quad \text{(slug)} \end{cases} \tag{D.44}$$

and then the cycle repeats itself. During $0 < t < t_f$, the temperature profile in the wall is given by $T_f(x,t)$ and during time $t_f < t < (t_f + t_s)$, the temperature profile is given by $T_s(x,t\text{-}t_f)$.

$$T_f(x,t) = T_R + q''\left[\frac{1}{k}(L-x) + \frac{1}{h_f}\right] + \sum_{n=1}^{\infty} B_{f,n}\cdot\cos(\lambda_{f,n}x)\cdot\exp(-\lambda_{f,n}{}^2\cdot\alpha\cdot t) \tag{D.45}$$

$$T_s(x,t) = T_R + q''\left[\frac{1}{k}(L-x) + \frac{1}{h_s}\right] + \sum_{n=1}^{\infty} B_{f,n}\cdot\cos(\lambda_{s,n}x)\cdot\exp(-\lambda_{s,n}{}^2\cdot\alpha\cdot t) \tag{D.46}$$

$$T(x,t)=\begin{cases} T_f(x,t) & 0<t<t_f \\ T_s(x,t-t_f) & t_f<t<(t_f+t_s) \end{cases} \tag{D.47}$$

Due to the periodic nature of the problem, we can relate the initial and final temperature profiles in the slug and film as follows:

$$T_f(x,0)=T_s(x,t_s) \tag{D.48}$$

$$T_s(x,0)=T_f(x,t_f) \tag{D.49}$$

where $t_f=\frac{l_{bubble}}{U_{Bubble}}$ and $t_s=\frac{l_{slug}}{U_{Bubble}}$. The above two equations provide the required initial states for the determination of the constants in $T_f(x,t)$ and $T_s(x,t)$. In (D.45) and (D.46), the heat flux, $q^{"}$ is given by:

$$q^{"}=-h_{refg,\exp}(T_R-T_{wall}) \tag{D.50}$$

In the above equation, the negative sign appears due to the sign convention for the heat flow direction used in defining the original boundary conditions. Here, $h_{refg,\exp}$ and T_{wall} are the experimentally determined quantities from the data analysis. We now have as many equations as unknowns to determine the complete wall temperature profile if both h_s and h_f are known. But, as in current case, if the objective is to determine the effective film heat transfer coefficient, h_f, using the experimentally determined $h_{refg,\exp}$ and theoretically determined h_s, we need one more equation. The refrigerant-side wall temperature determined during the analysis of the data provides that additional equation as follows:

$$T_{wall} = \frac{1}{\left(t_s + t_f\right)} \cdot \left(\int_0^{t_f} T_f\left(L,t\right) \cdot dt + \int_{t_f}^{t_f+t_s} T_s\left(L,t-t_f\right) \cdot dt \right) \tag{D.51}$$

This equation is further simplified before implementation into the analysis program, as described in the next section. The final solution to the above problem (walll temperature profile varying with time) is ploted in Figure 6.30. Figure D.1 (also shown as Figure 6.31 in the main text) shows the variation in wall temperature with time at various depths and futher compares it with the overall driving temperature difference between the refrigerant and the coolant. The results clearly indicate that the above analysis captures the variation in wall temperatrure with time and at the same time shows that these variations are insignificant compared to the overall temperature difference. Thus, this justifies the assumption of neglecting the transient effects in determining the refrigerant heat transfer coefficients from the data.

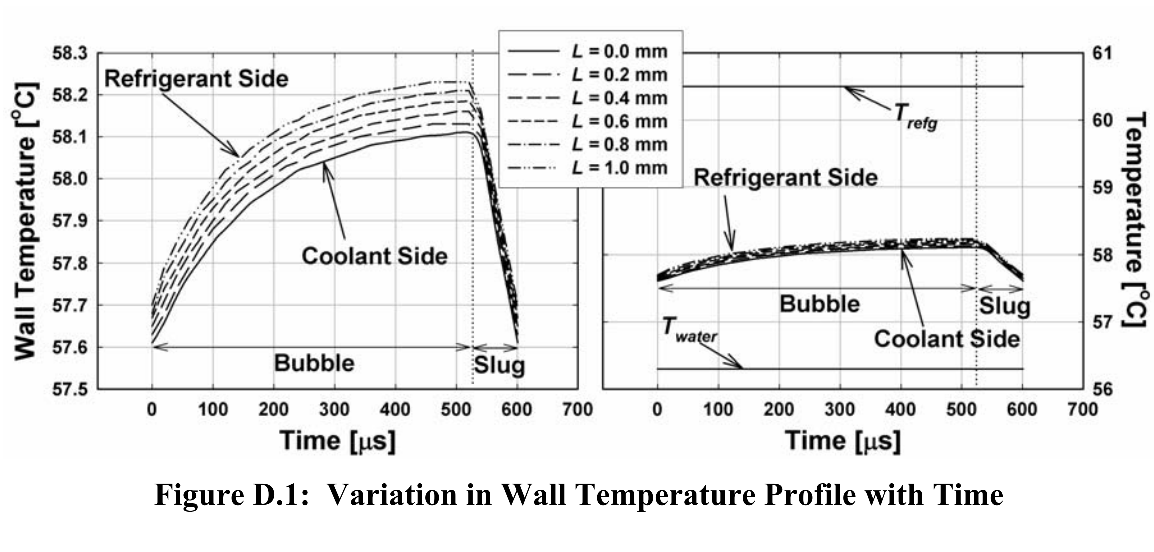

Figure D.1: Variation in Wall Temperature Profile with Time

D.6. Simplification of Transient Analysis Integrals

D.6.1. Integral to Calculate B_n

In this section, simplified equations for B_n in equation (D.43) are developed. The method is demonstrated using the calculation of $B_{f,n}$ (refered to as $B_{f,m}$ here) in equation (D.45).

$$B_{f,m} = \frac{\int_0^L G_f(x)\cos\left(\lambda_{f,m}x\right)\cdot dx}{\int_0^L \cos^2\left(\lambda_{f,m}x\right)\cdot dx}$$

Let $I_{f,N}$ and $I_{f,D}$ be the integrals in the numerator and denominator of the above equation, respectively. Thus,

$$I_{f,D} = \int_0^L \cos^2\left(\lambda_{f,m}x\right)\cdot dx$$

With $y = \lambda_{f,m}\cdot x$,

$$\begin{aligned}
I_{f,D} &= \frac{1}{\lambda_{f,m}}\int_0^{\lambda_{f,m}L}\cos^2(y)\cdot dy \\
&= \frac{1}{\lambda_{f,m}}\left[\frac{y}{2}+\frac{1}{4}\cdot\sin(2y)\right]_0^{\lambda_{f,m}L} \\
&= \frac{1}{\lambda_{f,m}}\left[\frac{\lambda_{f,m}L}{2}+\frac{1}{4}\cdot\sin\left(2\lambda_{f,m}L\right)\right] \\
&= \frac{L}{2}+\frac{1}{2\lambda_{f,m}}\cdot\sin\left(\lambda_{f,m}L\right)\cos\left(\lambda_{f,m}L\right) \quad \because \sin\left(2\lambda_{f,m}L\right) = 2\sin\left(\lambda_{f,m}L\right)\cos\left(\lambda_{f,m}L\right)
\end{aligned}$$

From the eigen-value equation (D.31), we have

$$\sin\left(\lambda_{f,m}L\right) = \frac{h_f}{k\lambda_m}\cos\left(\lambda_{f,m}L\right)$$

$$I_{f,D} = \frac{L}{2} + \frac{1}{2\lambda_{f,m}} \cdot \sin\left(\lambda_{f,m}L\right)\frac{k\lambda_{f,m}}{h_f}\sin\left(\lambda_{f,m}L\right)$$
$$= \frac{L}{2} + \frac{k}{2h_f} \cdot \sin^2\left(\lambda_{f,m}L\right)$$

The integral in the numerator $I_{f,N}$ is given by

$$I_{f,N} = \int_0^L G_f\left(x\right) \cdot \cos\left(\lambda_{f,m}x\right) \cdot dx$$

From (D.48), $T_f\left(x,0\right) = T_s\left(x,t_s\right)$. Substituting this in (D.39) for G_f(x) we get:

$$G_f\left(x\right) = T_s\left(x,t_s\right) - T_R - q^{"}\left[\frac{1}{k}\left(L-x\right) + \frac{1}{h_f}\right]$$

Substituting $T_s\left(x,t_s\right)$ from (D.46) we get:

$$G\left(x\right) = \cancel{T_R} + q^{"}\left[\cancel{\frac{1}{k}\left(L-x\right)} + \frac{1}{h_s}\right] + \sum_{n=1}^{\infty} B_{s,n} \cdot \cos\left(\lambda_{s,n}x\right) \cdot \exp\left(-\lambda_{s,n}{}^2 \cdot \alpha_s \cdot t_s\right)$$
$$-\cancel{T_R} - q^{"}\left[\cancel{\frac{1}{k}\left(L-x\right)} + \frac{1}{h_f}\right]$$

$$G\left(x\right) = q^{"}\left[\frac{1}{h_s} - \frac{1}{h_f}\right] + \sum_{n=1}^{\infty} B_{s,n} \cdot \cos\left(\lambda_{s,n}x\right) \cdot \exp\left(-\lambda_{s,n}{}^2 \cdot \alpha_s \cdot t_s\right)$$

$$\Rightarrow G\left(x\right) \cdot \cos\left(\lambda_{f,m}x\right) = q^{"}\left[\frac{1}{h_s} - \frac{1}{h_f}\right] \cdot \cos\left(\lambda_{f,m}x\right)$$
$$+ \sum_{n=1}^{\infty} B_{s,n} \cdot \cos\left(\lambda_{s,n}x\right) \cdot \exp\left(-\lambda_{s,n}{}^2 \cdot \alpha_s \cdot t_s\right) \cdot \cos\left(\lambda_{f,m}x\right)$$

$$I_{f,N} = \int_0^L G_f\left(x\right) \cdot \cos\left(\lambda_{f,m}x\right) \cdot dx = I_{f,N1} + I_{f,N2}$$

where $I_{f,N1} = \int_0^L q^{"}\left[\frac{1}{h_s} - \frac{1}{h_f}\right] \cdot \cos\left(\lambda_{f,m}x\right) \cdot dx$

$$I_{f,N2} = \int_0^L \sum_{n=1}^{\infty} B_{s,n} \cdot \cos\left(\lambda_{s,n} x\right) \cdot \exp\left(-\lambda_{s,n}{}^2 \cdot \alpha_s \cdot t_s\right) \cdot \cos\left(\lambda_{f,m} x\right) \cdot dx$$

First solving for I_{N1}:

$$\begin{aligned}
I_{f,N1} &= q^{"}\left[\frac{1}{h_s} - \frac{1}{h_f}\right] \cdot \int_0^L \cos\left(\lambda_{f,m} x\right) \cdot dx \\
&= q^{"}\left[\frac{1}{h_s} - \frac{1}{h_f}\right] \cdot \frac{1}{\lambda_{f,m}}\left[\sin\left(\lambda_{f,m} x\right)\right]_0^L \\
&= q^{"}\left[\frac{1}{h_s} - \frac{1}{h_f}\right] \cdot \frac{\sin\left(\lambda_{f,m} L\right)}{\lambda_{f,m}}
\end{aligned}$$

Now, solving for I_{N2}, we get:

$$\begin{aligned}
I_{f,N2} &= \int_0^L \sum_{n=1}^{\infty} B_{s,n} \cdot \cos\left(\lambda_{s,n} x\right) \cdot \exp\left(-\lambda_{s,n}{}^2 \cdot \alpha_s \cdot t\right) \cdot \cos\left(\lambda_{f,m} x\right) \cdot dx \\
&= \sum_{n=1}^{\infty} B_{s,n} \cdot \exp\left(-\lambda_{s,n}{}^2 \cdot \alpha_s \cdot t_s\right) \cdot \int_0^L \cos\left(\lambda_{s,n} x\right) \cdot \cos\left(\lambda_{f,m} x\right) \cdot dx \\
&= \sum_{n=1}^{\infty} B_{s,n} \cdot \exp\left(-\lambda_{s,n}{}^2 \cdot \alpha_s \cdot t_s\right) \cdot I_{f,CC}
\end{aligned}$$

where, $I_{f,CC} = \int_0^L \cos\left(\lambda_{s,n} x\right) \cdot \cos\left(\lambda_{f,m} x\right) \cdot dx$

The following trigonometric identity can be applied to further simplify I_{CC}:

$$\cos x \cdot \cos y = \frac{1}{2}\left[\cos\left(x + y\right) + \cos\left(x - y\right)\right]$$

Thus,

$$\begin{aligned}
I_{f,CC} &= \frac{1}{2}\left[\int_0^L \cos\left[\left(\lambda_{s,n} + \lambda_{f,m}\right)x\right] \cdot dx + \int_0^L \cos\left[\left(\lambda_{s,n} - \lambda_{f,m}\right)x\right] \cdot dx\right] \\
&= \frac{1}{2}\left[\frac{\sin\left[\left(\lambda_{s,n} + \lambda_{f,m}\right)x\right]}{\left(\lambda_{s,n} + \lambda_{f,m}\right)x} + \frac{\sin\left[\left(\lambda_{s,n} - \lambda_{f,m}\right)x\right]}{\left(\lambda_{s,n} - \lambda_{f,m}\right)x}\right]
\end{aligned}$$

$$I_{f,N2} = \sum_{n=1}^{\infty} \frac{B_{s,n}}{2} \cdot \exp\left(-\lambda_{s,n}{}^{2} \cdot \alpha_s \cdot t_s\right) \cdot \left[\frac{\sin\left[\left(\lambda_{s,n} + \lambda_{f,m}\right)x\right]}{\left(\lambda_{s,n} + \lambda_{f,m}\right)x} + \frac{\sin\left[\left(\lambda_{s,n} - \lambda_{f,m}\right)x\right]}{\left(\lambda_{s,n} - \lambda_{f,m}\right)x} \right]$$

$$B_{f,m} = \frac{I_{f,N1} + I_{f,N2}}{I_{f,D}}$$

Similarly, $B_{s,m} = \frac{I_{s,N1} + I_{s,N2}}{I_{s,D}}$

$$I_{s,D} = \frac{L}{2} + \frac{k}{2h_s} \cdot \sin^2\left(\lambda_{s,m} L\right)$$

$$I_{s,N1} = q^{"} \left[\frac{1}{h_f} - \frac{1}{h_s} \right] \cdot \frac{\sin\left(\lambda_{s,m} L\right)}{\lambda_{s,m}}$$

$$I_{s,N2} = \sum_{n=1}^{\infty} \frac{B_{f,n}}{2} \cdot \exp\left(-\lambda_{f,n}{}^{2} \cdot \alpha_f \cdot t_f\right) \cdot \left[\frac{\sin\left[\left(\lambda_{f,n} + \lambda_{s,m}\right)x\right]}{\left(\lambda_{f,n} + \lambda_{s,m}\right)x} + \frac{\sin\left[\left(\lambda_{f,n} - \lambda_{s,m}\right)x\right]}{\left(\lambda_{f,n} - \lambda_{s,m}\right)x} \right]$$

D.6.2. Integral to calculate T_{wall}

Based on the above considerations, the wall temperature can be computed as shown in this section. Thus,

$$\begin{aligned} T_{wall} &= \frac{1}{\left(t_s + t_f\right)} \cdot \left(\int_0^{t_f} T_f\left(L,t\right) \cdot dt + \int_0^{t_s} T_s\left(L,t\right) \cdot dt \right) \\ &= \frac{1}{\left(t_s + t_f\right)} \cdot \left(I_f + I_s\right) \end{aligned}$$

where, $I_f = \int_0^{t_f} T_f\left(L,t\right) \cdot dt$ and $I_s = \int_0^{t_s} T_s\left(L,t\right) \cdot dt$. Solving for I_f first, substitute $T_f\left(L,t\right)$ for equation (D.45)

$$
\begin{aligned}
I_f &= \int_0^{t_f} \left[T_R + q^{"} \left[\cancel{\frac{1}{k}(L-L)} + \frac{1}{h_f} \right] + \sum_{n=1}^{\infty} B_{f,n} \cdot \cos\left(\lambda_{f,n} L\right) \cdot \exp\left(-\lambda_{f,n}{}^2 \cdot \alpha \cdot t\right) \right] \cdot dt \\
&= \int_0^{t_f} \left(T_R + \frac{q^{"}}{h_f} \right) \cdot dt + \sum_{n=1}^{\infty} B_{f,n} \cdot \cos\left(\lambda_{f,n} L\right) \cdot \int_0^{t_f} \exp\left(-\lambda_{f,n}{}^2 \cdot \alpha \cdot t\right) \cdot dt \\
&= \left(T_R + \frac{q^{"}}{h_f} \right) \cdot t_f + \sum_{n=1}^{\infty} \frac{B_{f,n} \cdot \cos\left(\lambda_{f,n} L\right)}{\left(-\lambda_{f,n}{}^2 \cdot \alpha\right)} \cdot \left[\exp\left(-\lambda_{f,n}{}^2 \cdot \alpha \cdot t_f\right) - 1 \right]
\end{aligned}
$$

Similarly,

$$
I_s = \left(T_R + \frac{q^{"}}{h_s} \right) \cdot t_f + \sum_{n=1}^{\infty} \frac{B_{s,n} \cdot \cos\left(\lambda_{s,n} L\right)}{\left(-\lambda_{s,n}{}^2 \cdot \alpha\right)} \cdot \left[\exp\left(-\lambda_{s,n}{}^2 \cdot \alpha \cdot t_s\right) - 1 \right]
$$

D.7. Pressure Drop and Heat Transfer Model Implementation

Table D-1: Illustration of the Application of the Pressure Drop and Heat Transfer Models Developed in this Study (Representative Case: 200×100 μm channels; AR = 2; T_{sat} = 60.5°C, G = 606 kg/m^2-s; x_{ave} = 0.39)

Inputs	Equations	Results
Dimensional Parameters and Properties		
d_{TS} = 0.1 mm w_{TS} = 0.2 mm	$D = \dfrac{4 \times w_{TS} \times d_{TS}}{2 \cdot (w_{TS} + d_{TS})}$	D = 133×10^{-6} m
	$AR = \dfrac{w_{TS}}{d_{TS}}$	AR = 2
T_{ave} = 60.4°C	$\rho_L = f(T = T_{ave}, x = 0)$ $\mu_L = f(T = T_{ave}, x = 0)$	ρ_L = 1051 kg/m^3 μ_L = 1.23×10^{-4} kg/m-s
x = 0.39	$\rho_V = f(T = T_{ave}, x = 0)$ $\mu_V = f(T = T_{ave}, x = 0)$	ρ_V = 88 kg/m^3 μ_V = 1.4×10^{-5} kg/m-s
	$\beta = \dfrac{x \cdot \rho_L}{x \cdot \rho_L + (1-x) \cdot \rho_V}$	β = 0.88
	$\alpha = 0.833 \times \beta$	α = 0.74

Table D-1 continued …

Inputs	Equations	Results
Slug Frictional Pressure Drop		
G = 606 kg/m^2-s x = 0.39	$j_L = \dfrac{(1-x)G}{\rho_L}$	j_L = 0.35 m/s
ρ_L = 1051 kg/m^3 ρ_V = 88 kg/m^3	$j_V = \dfrac{x \cdot G}{\rho_V}$	j_V = 2.7 m/s
	$U_{slug} = j_L + j_V$	U_{slug} = 3.05 m/s
D = 133×10^{-6} m μ_L = 1.23×10^{-4} kg/m-s	$\mathrm{Re}_{slug} = \dfrac{\rho_L \cdot U_{slug} \cdot D}{\mu_L}$ Since, the flow is in transition region:	Re_{slug} = 3.5×10^3
AR = 2 Re_{CL} = 2000	$f \cdot Re = 4 \times 24 \left(1 - 1.3553 \cdot \frac{1}{AR} + 1.9467 \cdot \left(\frac{1}{AR}\right)^2 - 1.7012 \cdot \left(\frac{1}{AR}\right)^3 + 0.9564 \cdot \left(\frac{1}{AR}\right)^4 - 0.2537 \cdot \left(\frac{1}{AR}\right)^5 \right)$	$f(Re_{CL})$ = 0.031
Re_{CU} = 4000	$f = \dfrac{0.3164}{Re^{0.25}} \cdot \left[1.0875 - 0.1125 \cdot \left(\frac{1}{AR}\right) \right]$	$f(Re_{CU})$ = 0.041

Table D-1 continued …

Inputs	Equations	Results
	$$f_{slug} = \exp\left[\left(\frac{\ln(\mathrm{Re}_{slug}) - \ln(\mathrm{Re}_{CL})}{\ln(\mathrm{Re}_{CU}) - \ln(\mathrm{Re}_{CL})}\right) \times \left(\ln(f(\mathrm{Re}_{CU})) - \ln(f(\mathrm{Re}_{CL}))\right) + \ln(f(\mathrm{Re}_{CL}))\right]$$ $$\left(\frac{dP}{dx}\right)_{slug} = \frac{1}{2} \cdot f_{slug} \cdot \frac{\rho_L \cdot U_{slug}^{2}}{D}$$	$f_{slug} = 0.039$ $\left(\frac{dP}{dx}\right)_{slug} = 1.42$ MPa/m
<u>Determination of Film/Bubble Section Pressure Drop</u>		
$AR = 2$ $d_{TS} = 0.1$ mm $w_{TS} = 0.2$ mm $\alpha = 0.74$	Following set of equations is solved iteratively: $$AR = \frac{w_B}{d_B}$$ $$\alpha = \left(1 - \frac{l_{slug}}{l_{slug} + l_{bubble}}\right) \cdot \frac{w_B \cdot d_B}{w_{TS} \cdot d_{TS}}$$ $$\delta_{ave} = \frac{1}{2} \cdot \left[\frac{(w_{TS} - w_B) \cdot d_{TS} + (d_{TS} - d_B) \cdot w_{TS}}{w_{TS} + d_{TS}}\right]$$ $$D_{Bubble} = \frac{4 \times w_B \cdot d_B}{2 \cdot (w_B + d_B)}$$	$w_B = 182$ µm $d_B = 91$ µm $l_{slug} = 0.29$ mm $l_{bubble} = 2.32$ mm $\delta_{ave} = 6$ µm $D_{Bubble} = 121$ µm

Table D-1 continued …

Inputs	Equations	Results
$\mu_L = 1.23\times10^{-4}$ kg/m-s	$U_{interface} = \left(\frac{dP}{dx}\right)_{f/b}\left(\frac{D_{bubble}}{2} - \delta_{ave}\right)\frac{\delta_{ave}}{2\cdot\mu_L}$	$U_{interface} = 0.201$ m/s
	$U_{film} = \frac{1}{4\mu_L}\left(\frac{dP}{dx}\right)_{f/b}\left[\left(\frac{1}{2}\right)D_{bubble} - \left(\frac{4}{3}\right)\delta_{ave}\right]\delta_{ave}$	$U_{film} = 0.097$ m/s
	$U_{slug} = U_{bubble}\left(\frac{w_B\cdot d_B}{w_{TS}\cdot d_{TS}}\right) + U_{film}\cdot\left(1 - \frac{w_B\cdot d_B}{w_{TS}\cdot d_{TS}}\right)$	$U_{bubble} = 3.66$ m/s
$U_{slug} = 3.047$ m/s	$\frac{G\cdot(1-x)}{\rho_L} = U_{slug}\cdot\left(\frac{l_{slug}}{l_{slug}+l_{bubble}}\right) + U_{film}\cdot\left(1 - \frac{w_B\cdot d_B}{w_{TS}\cdot d_{TS}}\right)\cdot\left(1 - \frac{l_{slug}}{l_{slug}+l_{bubble}}\right)$	
$\rho_V = 88$ kg/m^3 $\mu_V = 1.4\times10^{-5}$ kg/m-s	$\mathrm{Re}_{Bubble} = \frac{\rho_V\cdot\left(U_{bubble} - U_{interface}\right)\cdot D_{Bubble}}{\mu_V}$ Since the flow is in transition region:	$Re_{bubble} = 2.6\times10^3$
$Re_{CL} = 2000$ $Re_{CU} = 4000$ $f(Re_{CL}) = 0.03111$ $f(Re_{CU}) = 0.04103$	$f_{bubble} = \exp\left[\left(\frac{\ln(\mathrm{Re}_{bubble}) - \ln(\mathrm{Re}_{CL})}{\ln(\mathrm{Re}_{CU}) - \ln(\mathrm{Re}_{CL})}\right)\times\left(\ln\left(f(\mathrm{Re}_{CU})\right) - \ln\left(f(\mathrm{Re}_{CL})\right)\right) + \ln\left(f(\mathrm{Re}_{CL})\right)\right]$	$f_{bubble} = 0.035$

Table D-1 continued …

Inputs	Equations	Results
	$\left(\frac{dP}{dx}\right)_{f/b} = \frac{1}{2}\cdot f_{bubble}\cdot\frac{\rho_V\cdot\left(U_{bubble}-U_{interface}\right)^2}{D_{Bubble}}$	$\left(\frac{dP}{dx}\right)_{f/b}$ = 151 kPa/m
<u>Total Pressure Drop</u>		
l_{slug} = 0.29 mm l_{bubble} = 2.32 mm L_{tube} = 0.04 m $\left(\frac{dP}{dx}\right)_{f/b}$ = 151 kPa/m $\left(\frac{dP}{dx}\right)_{slug}$ = 1.42 MPa/m	$\Delta P_{fric,only} = L_{tube}\cdot\left[\left(\frac{dp}{dx}\right)_{f/b}\cdot\left(1-\frac{l_{slug}}{l_{slug}+l_{bubble}}\right)+\left(\frac{dp}{dx}\right)_{slug}\cdot\left(\frac{l_{slug}}{l_{slug}+l_{bubble}}\right)\right]$	$\Delta P_{fric,only}$ = 11.6 kPa
ρ_L = 1051 kg/m^3 U_{film} = 0.097 m/s U_{bubble} = 3.66 m/s w_B = 182 μm d_B = 91 μm	$\dot{m}_{transition} = \rho_L\cdot\left(w_{TS}\cdot d_{TS}-w_B\cdot d_B\right)\cdot\left(U_{bubble}-U_{film}\right)$	$\dot{m}_{transition}$ = 1.3×10^{-5} kg/s

Table D-1 continued …

Inputs	Equations	Results
d_{TS} = 0.1 mm w_{TS} = 0.2 mm U_{slug} = 3.05 m/s	$\Delta P_{transition} = \frac{\dot{m}_{transition} \cdot \left(U_{slug} - U_{film}\right)}{w_{TS} \cdot d_{TS}}$	$\Delta P_{transition}$ = 1.893 kPa
D = 133×10^{-6} m AR = 2 x = 0.39 ρ_L = 1051 kg/m^3 ρ_V = 88 kg/m^3 Re_{slug} = 3.5×10^{-3} $\Delta P_{fric,\exp}$ = 47.6 kPa	$N_{UC} \cdot \frac{D}{L_{tube}} = \left(2.8 \cdot e^{0.4 \cdot AR}\right) \cdot Re_{slug}{}^{-0.35} \cdot \left(\frac{1-x}{x}\right)^{0.46} \cdot \left(\frac{\rho_g}{\rho_l}\right)^{0.868}$ $\Delta P_{fric,model} = N_{UC} \cdot \Delta P_{transition} + \Delta P_{firc,only}$ $Error_{\Delta P} = \frac{\left\|\Delta P_{fric.\mathrm{mod}\,el} - \Delta P_{fric.\exp}\right\|}{\Delta P_{fric.\exp}} \times 100$	N_{UC} = 15.4 $\Delta P_{fric,model}$ = 40.7 kPa $Error_{\Delta P}$ = 14.43 %
Heat Transfer Model		
AR = 2	$Nu_l = 8.235\left(\begin{array}{l} 1 - 2.0421 \cdot \left(\frac{1}{AR}\right) + 3.0853 \cdot \left(\frac{1}{AR}\right)^2 - 2.4765 \cdot \left(\frac{1}{AR}\right)^3 \\ \qquad + 1.5078 \cdot \left(\frac{1}{AR}\right)^4 - 0.1861 \cdot \left(\frac{1}{AR}\right)^5 \end{array}\right)$	Nu_l = 4.126

Table D-1 continued …

Inputs	Equations	Results
$Re_{slug} = 3.5\times10^3$ $f_{slug} = 0.039$ $Pr_L = 3.17$ $Nu_0 = 6.3$	$Nu_{lc} = Nu_l$ $Nu_{slug}^{10} = Nu_l^{10} + \left[\frac{e^{\left(2200-\mathrm{Re}_{slug}\right)/365}}{Nu_{lc}^2} + \left(Nu_0 + \frac{0.079\cdot \mathrm{Re}_{slug}\cdot\sqrt{\frac{f_{slug}}{8}}\cdot \mathrm{Pr}_L}{\left(1+\mathrm{Pr}_L^{4/5}\right)^{5/6}} \right)^{-2} \right]^{-5}$	$Nu_{slug} = 17.91$
$T_{ave} = 60.4^{o}$C	$k_L = f\left(T = T_{ave}, x = 0\right)$	$k_L = 0.06452$ W/m-K
$D = 133\times10^{-6}$ m $x = 0.39$	$h_{slug} = Nu_{slug}\cdot\frac{k_l}{D}$	$h_{slug} = 8.6$ kW/m^2-K
δ_{ave} = 5.99 µm (from the ΔP model presented above) $D_{ref} = 160$ µm	$\frac{\delta_0}{\delta_{ave}} = 1 - 0.25\cdot e^{\left(-2.82\cdot\frac{D}{D_{ref}}\right)}\cdot\left(\frac{x}{1-x}\right)^{0.424}$	δ_0 = 5.87 µm
$h_{fg} = 138.6$ kJ/kg $\rho_L = 1051$ kg/m^3 $U_{bubble} = 3.657$ m/s	$h_{film} = \left(\delta_{ave} - \delta_0\right)\cdot\frac{2\cdot\rho_L\cdot h_{fg}\cdot U_{bubble}}{\left(T - T_{wall}\right)\cdot l_{bubble}}$	h_{film} = 24 .0 kW/m^2-K
$T_{wall} = 58.1^{o}$C $l_{slug} = 0.29$ mm $l_{bubble} = 2.32$ mm	$h_{refg,model} = h_{slug}\cdot\left(\frac{l_{slug}}{l_{slug}+l_{bubble}}\right) + h_{film}\cdot\left(1 - \frac{l_{slug}}{l_{slug}+l_{bubble}}\right)$	$h_{refg,model}$ = 22.3 kW/m^2-K

Table D-1 continued …

Inputs	Equations	Results
$h_{refg,\exp} = 21.7$ kW/m^2-K	$Error_{h_{refg}} = \frac{\left\| h_{refg,model} - h_{refg,\exp} \right\|}{h_{refg,\exp}} \times 100$	$Error_{h_{refg}} = 2.8$ %

REFERENCES

Agarwal, A. and S. Garimella (2006), "Modeling of Pressure Drop During Condensation in Circular and Non-Circular Microchannels," *Proceedings of the IMECE 2006: International Mechanical Engineering Congress and Exposition*, Chicago, Illinois, pp. IMECE2006-14672.

Akers, W. W., H. A. Deans and O. K. Crosser (1959), "Condensation Heat Transfer within Horizontal Tubes," *Chemical Engineering Progress Symposium Series* Vol. 55(29) pp. 171-176.

Armand, A. A. (1946), "The Resistance During the Movement of a Two-Phase System in Horizontal Pipes," *Izv. Vses. Teplotekh. Inst.* Vol. 1 pp. 16–23 (AERE-Lib/Trans 828).

Baird, J. R., D. F. Fletcher and B. S. Haynes (2003), "Local Condensation Heat Transfer Rates in Fine Passages," *International Journal of Heat and Mass Transfer* Vol. 46(23) pp. 4453-4466.

Bandhauer, T. M., A. Agarwal and S. Garimella (2006), "Measurement and Modeling of Condensation Heat Transfer Coefficients in Circular Microchannels," *Journal of Heat Transfer, Transactions of ASME* Vol. 128(October) pp. 1050-1059.

Barnea, D., Y. Luninski and Y. Taitel (1983), "Flow Pattern in Horizontal and Vertical Two Phase Flow in Small Diameter Tubes," *Canadian Journal of Chemical Engineering* Vol. 61(5) pp. 617-620.

Baroczy, C. J. (1965), "Correlation of Liquid Fraction in Two Phase Flow with Applications to Liquid Metals," *Chemical Engineering Progress Symposium Series* Vol. 61(57) pp. 179 -191.

Baroczy, C. J. (1966), "Systematic Correlation for Two-Phase Pressure Drop," *Chemical Engineering Progress Symposium Series* Vol. 62(64) pp. 232-249.

Baroczy, C. J. and V. D. Sanders (1961), "Pressure Drop for Flowing Vapors Condensing in Straight Horizontal Tube," *ASME Meeting WA-257, Nov 26-Dec 1 1961*, American Society of Mechanical Engineers (ASME), New York, NY, United States, p. 16.

Beattie, D. R. H. and P. B. Whalley (1982), "A Simple Two-Phase Frictional Pressure Drop Calculation Method," *International Journal of Multiphase Flow* Vol. 8(1) pp. 83-87.

Bhatti, M. S. and R. K. Shah (1987). Turbulent and Transitions Flow Convective Heat Transfer in Ducts. *Handbook of Single-Phase Convective Heat Transfer*. S. Kakaç, R. K. Shah and W. Aung. New York, NY, Wiley.

Breber, G., J. W. Palen and J. Taborek (1980), "Prediction of Horizontal Tubeside Condensation of Pure Components Using Flow Regime Criteria," *Journal of Heat Transfer, Transactions ASME* Vol. 102(3) pp. 471-476.

Carey, V. P. (1992). *Liquid Vapor Phase Change Phenomena*. 1992 Ed., Hemisphere Publishing Corporation.

Carpenter, F. G. and A. P. Colburn (1951), "The Effect of Vapor Velocity on Condensation inside Tubes," *ASME Proceedings of the General Discussion of Heat Transfer* pp. 20-26.

Cavallini, A., G. Censi, D. Del Col, L. Doretti, G. A. Longo and L. Rossetto (2002), "Condensation of Halogenated Refrigerants inside Smooth Tubes," *HVAC and R Research* Vol. 8(4) pp. 429-451.

Cavallini, A., D. Del Col, L. Doretti, M. Matkovic, L. Rossetto and C. Zilio (2005), "Condensation Heat Transfer and Pressure Gradient inside Multiport Minichannels," *Heat Transfer Engineering* Vol. 26(3) pp. 45-55.

Celata, G. P. (2004), "Single-Phase Heat Transfer and Fluid Flow in Micropipes," *Heat Transfer Engineering* Vol. 25(3) pp. 13-22.

Chato, J. C. (1962), "Laminar Condensation inside Horizontal and Inclined Tubes," *ASHRAE Journal* Vol. 4(2) pp. 52-60.

Chen, I. Y., K.-S. Yang, Y.-J. Chang and C.-C. Wang (2001), "Two-Phase Pressure Drop of Air-Water and R-410a in Small Horizontal Tubes," *International Journal of Multiphase Flow* Vol. 27(7) pp. 1293-1299.

Chen, S. L., F. M. Gerner and C. L. Tien (1987), "General Film Condensation Correlations," *Experimental Heat Transfer* Vol. 1(2) pp. 93-107.

Chen, Y. and P. Cheng (2005), "Condensation of Steam in Silicon Microchannels," *International Communications in Heat and Mass Transfer* Vol. 32(1-2) pp. 175-183.

Chisholm, D. (1967), "A Theoretical Basis for the Lockhart-Martinelli Correlation for Two-Phase Flow," *International Journal of Heat and Mass Transfer* Vol. 10(12) pp. 1767-1778.

Chisholm, D. (1973), "Pressure Gradients Due to Friction During the Flow of Evaporating Two-Phase Mixtures in Smooth Tubes and Channels," *International Journal of Heat and Mass Transfer* Vol. 16(2) pp. 347-358.

Christenson, T. (2005). *Email Communication Dated August 19th 2005*. A. Agarwal. Atlanta.

Chung, P. M.-Y. and M. Kawaji (2004), "The Effect of Channel Diameter on Adiabatic Two-Phase Flow Characteristics in Microchannels," *International Journal of Multiphase Flow* Vol. 30(7-8) pp. 735-761.

Chung, P. M.-Y., M. Kawaji, A. Kawahara and Y. Shibata (2004), "Two-Phase Flow through Square and Circular Microchannels---Effects of Channel Geometry," *Journal of Fluids Engineering* Vol. 126(4) pp. 546-552.

Churchill, S. W. (1977a), "Comprehensive Correlating Equations for Heat, Mass and Momentum Transfer in Fully Developed Flow in Smooth Tubes," *Industrial & Engineering Chemistry, Fundamentals* Vol. 16(1) pp. 109-116.

Churchill, S. W. (1977b), "Friction-Factor Equations Spans All Fluid-Flow Regimes," *Chemical Engineering Progress* Vol. 84(24) pp. 91 - 92.

Churchill, S. W. and H. H. S. Chu (1975), "Correlating Equations for Laminar and Turbulent Free Convection from a Horizontal Cylinder," *International Journal of Heat and Mass Transfer* Vol. 18(9) pp. 1049-1053.

Colebrook, C. F. (1939), "Turbulent Flow in Pipes, with Particular Reference to the Transition between the Smooth and Rough Pipe Laws," *Journal of the Institute of Civil Engineers* Vol. 11 pp. 133-156.

Coleman, J. W. and S. Garimella (1999), "Characterization of Two-Phase Flow Patterns in Small Diameter Round and Rectangular Tubes," *International Journal of Heat and Mass Transfer* Vol. 42(15) pp. 2869-2881.

Coleman, J. W. and S. Garimella (2000a), "Two-Phase Flow Regime Transitions in Microchannel Tubes: The Effect of Hydraulic Diameter," *American Society of Mechanical Engineers, Heat Transfer Division*, Orlando, FL, American Society of Mechanical Engineers, pp. 71-83.

Coleman, J. W. and S. Garimella (2000b), "Visualization of Two-Phase Refrigerant Flow During Phase Change," *Proceedings of the 34th National Heat Transfer Conference*, Pittsburgh, PA, ASME

Coleman, J. W. and S. Garimella (2003), "Two-Phase Flow Regimes in Round, Square and Rectangular Tubes During Condensation of Refrigerant R134a," *International Journal of Refrigeration* Vol. 26(1) pp. 117-128.

Cornwell, K. and P. A. Kew (1993). Boiling in Small Parallel Channels. *Energy Efficiency in Process Technology*. P. A. Pilavachi. New York, Elsevier pp. 624-638.

Damianides, C. A. and J. W. Westwater (1988), "Two-Phase Flow Patterns in a Compact Heat Exchanger and in Small Tubes," *Second UK National Conference on Heat Transfer (2 vols)*, Glasgow, Scotland, pp. 1257-1268.

Dobson, M. K. and J. C. Chato (1998), "Condensation in Smooth Horizontal Tubes," *Journal of Heat Transfer, Transactions ASME* Vol. 120(1) pp. 193-213.

Dukler, A. E. and M. G. Hubbard (1975), "A Model for Gas-Liquid Slug Flow in Horizontal and near Horizontal Tubes," *Industrial Engineering and Chemical Fundamentals* Vol. 14(4) pp. 337-347.

Dukler, A. E., M. Wicks III and R. G. Cleveland (1964), "Frictional Pressure Drop in Two-Phase Flow," *A.I.Ch.E. Journal* Vol. 10(1) pp. 38-51.

El Hajal, J., J. R. Thome and A. Cavallini (2003), "Condensation in Horizontal Tubes, Part 1: Two-Phase Flow Pattern Map," *International Journal of Heat and Mass Transfer* Vol. 46(18) pp. 3349-3363.

Feng, Z. and A. Serizawa (1999), "Visualization of Two-Phase Flow Patterns in an Ultra-Small Tube," *Proceedings of the 18th Multiphase Flow Symposium of Japan*, Suita, Osaka, Japan, pp. 33-36.

Friedel, L. (1979), "Improved Frictional Pressure Drop Correlations for Horizontal and Vertical Two-Phase Pipe Flow," *3 R International* Vol. 18(7) pp. 485-491.

Fukano, T., A. Kariyasaki and M. Kagawa (1989), "Flow Patterns and Pressure Drop in Isothermal Gas-Liquid Concurrent Flow in a Horizontal Capillary Tube," *Proceedings of the 1989 ANS National Heat Transfer Conference*, Philadelphia, Pennsylvania, pp. 153-161.

Fukano, T., A. Kariyasaki and M. Kagawa (1991), "Characteristics of Time Varying Void Fraction in Isothermal Air-Water Concurrent Flow in a Horizontal Capillary Tube," *Proceedings of the 3rd ASME/JSME Thermal Engineering Joint Conference Part 2 (of 5), Mar 17-22 1991*, Reno, NV, USA, Publ by ASME, New York, NY, USA, pp. 127-134.

Galbiati, L. and P. Andreini (1992), "Flow Pattern Transition for Vertical Downward Two-Phase Flow in Capillary Tubes. Inlet Mixing Effects," *International Communications in Heat and Mass Transfer* Vol. 19(6) pp. 791-799.

Garimella, S. (2004), "Condensation Flow Mechanisms in Microchannels: Basis for Pressure Drop and Heat Transfer Models," *Heat Transfer Engineering* Vol. 25(3) pp. 104-116.

Garimella, S., A. Agarwal and J. W. Coleman (2003a), "Two-Phase Pressure Drops in the Annular Flow Regime in Circular Microchannels," *21st IIR International Congress of Refrigeration*, Washington, D.C., International Institute of Refrigeration

Garimella, S., A. Agarwal and J. D. Killion (2005), "Condensation Pressure Drop in Circular Microchannels," *Heat Transfer Engineering* Vol. 26(3) pp. 1-8.

Garimella, S. and T. M. Bandhauer (2001), "Measurement of Condensation Heat Transfer Coefficients in Microchannel Tubes," *2001 ASME International Mechanical Engineering Congress and Exposition*, New York, NY, United States, American Society of Mechanical Engineers, pp. 243-249.

Garimella, S., J. D. Killion and J. W. Coleman (2002), "An Experimentally Validated Model for Two-Phase Pressure Drop in the Intermittent Flow Regime for Circular Microchannels," *Transactions of the ASME. Journal of Fluids Engineering* Vol. 124(1) pp. 205 -214.

Garimella, S., J. D. Killion and J. W. Coleman (2003b), "An Experimentally Validated Model for Two-Phase Pressure Drop in the Intermittent Flow Regime for Noncircular Microchannels," *Transactions of the ASME. Journal of Fluids Engineering* Vol. 125(5) pp. 887-894.

Garimella, S. V. and V. Singhal (2004), "Single-Phase Flow and Heat Transport and Pumping Considerations in Microchannel Heat Sinks," *Heat Transfer Engineering* Vol. 25(1).

Garimella, S. V. and C. B. Sobhan (2003). Transport in Microchannels - a Critical Review. *Annual Review of Heat Transfer*, Vol. 13.

Ghiaasiaan, S. M. and S. I. Abdel-Khalik (2001). Two-Phase Flow in Microchannels. *Advances in Heat Transfer*, Academic Press, Vol. 34 pp. 145-244.

Hewitt, G. F. (1984), "Two-Phase Flow through Orifices, Valves, Bends and Other Singularities," *Proceedings of the 9th Lecture Series on Two-Phase Flow*, Norwegian Institute of Technology, Trondheim, p. 163.

Hewitt, G. F., G. L. Shires and T. R. Bott (1993). *Process Heat Transfer*. 1993 Ed. Ann Arbor, MI, CRC Press, Inc.

Ide, H., H. Matsumura, Y. Tanaka and T. Fukano (1997), "Flow Patterns and Frictional Pressure Drop in Gas-Liquid Two-Phase Flow in Vertical Capillary Channels with Rectangular Cross Section," *Nippon Kikai Gakkai Ronbunshu, B Hen/Transactions of the Japan Society of Mechanical Engineers, Part B* Vol. 63(606) pp. 452-460.

Idelchik, I. E. (1986). *Handbook of Hydraulic Resistance*. 2 Ed., Hemisphere Publishing Corporation.

Incropera, F. P. and D. P. Dewitt (1996). *Fundamentals of Heat and Mass Transfer*. Fourth Ed., John Wiley & Sons.

Jung, D. S. and R. Radermacher (1989), "Prediction of Pressure Drop During Horizontal Annular Flow Boiling of Pure and Mixed Refrigerants," *International Journal of Heat and Mass Transfer* Vol. 32(12) pp. 2435-2446.

Kandlikar, S., S. Garimella, D. Li, S. Colin and M. R. King (2005). *Heat Transfer and Fluid Flow in Minichannels and Microchannels*. 1st Ed., Elsevier Science.

Kattan, N., J. R. Thome and D. Favrat (1998a), "Flow Boiling in Horizontal Tubes: Part 1 - Development of a Diabatic Two-Phase Flow Pattern Map," *Journal of Heat Transfer, Transactions ASME* Vol. 120(1) pp. 140-147.

Kattan, N., J. R. Thome and D. Favrat (1998b), "Flow Boiling in Horizontal Tubes: Part 2 - New Heat Transfer Data for Five Refrigerants," *Journal of Heat Transfer, Transactions ASME* Vol. 120(1) pp. 148-155.

Kattan, N., J. R. Thome and D. Favrat (1998c), "Flow Boiling in Horizontal Tubes: Part 3 - Development of a New Heat Transfer Model Based on Flow Pattern," *Journal of Heat Transfer, Transactions ASME* Vol. 120(1) pp. 156-165.

Kawahara, A., P. M.-Y. Chung and M. Kawaji (2002), "Investigation of Two-Phase Flow Pattern, Void Fraction and Pressure Drop in a Microchannel," *International Journal of Multiphase Flow* Vol. 28(9) pp. 1411-1435.

Kawahara, A., M. Sadatomi, K. Okayama, M. Kawaji and P. M.-Y. Chung (2005), "Effects of Channel Diameter and Liquid Properties on Void Fraction in Adiabatic Two-Phase Flow through Microchannels," *Heat Transfer Engineering* Vol. 26(3) pp. 13-19.

Klein, S. A. (2006), "Engineering Equation Solver," Ver: Academic Commercial V7.697-3D,

Kosky, P. G. and F. W. Staub (1971), "Local Condensing Heat Transfer Coefficients in the Annular Flow Regime," *AIChE Journal* Vol. 17(5) pp. 1037-1043.

Kureta, M., T. Kobayashi, K. Mishima and H. Nishihara (1998), "Pressure Drop and Heat Transfer for Flow-Boiling of Water in Small-Diameter Tubes," *JSME International Journal, Series B* Vol. 41(4) pp. 871-879.

Lee, H. J. and S. Y. Lee (2001), "Pressure Drop Correlations for Two-Phase Flow within Horizontal Rectangular Channels with Small Heights," *International Journal of Multiphase flow* Vol. 27(5) pp. 783-796.

Liu, D. and S. V. Garimella (2004), "Investigation of Liquid Flow in Microchannels," *AIAA Journal of Thermophysics and Heat Transfer* Vol. 18(1).

Lockhart, R. W. and R. C. Martinelli (1949), "Proposed Correlation of Data for Isothermal Two-Phase, Two-Component Flow in Pipes," *Chemical Engineering Progress* Vol. 45(1) pp. 39-45.

Mandhane, J. M., G. A. Gregory and K. Aziz (1974), "A Flow Pattern Map for Gas-Liquid Flow in Horizontal Pipes," *International Journal of Multiphase Flow* Vol. 1(4) pp. 537-553.

Mishima, K. and T. Hibiki (1996), "Some Characteristics of Air-Water Two-Phase Flow in Small Diameter Vertical Tubes," *International Journal of Multiphase Flow* Vol. 22(4) pp. 703 - 712.

Mishima, K. and T. Hibiki (1998), "Development of High-Frame-Rate Neutron Radiography and Quantitative Measurement Method for Multiphase Flow Research," *Nuclear Engineering and Design* Vol. 184(2-3) pp. 183-201.

Mishima, K., T. Hibiki and H. Nishihara (1997), "Visualization and Measurement of Two-Phase Flow by Using Neutron Radiography," *Nuclear Engineering and Design* Vol. 175(1-2) pp. 25-35.

Mishima, K. and M. Ishii (1984), "Flow Regime Transition Criteria for Upward Two-Phase Flow in Vertical Tubes," *International Journal of Heat and Mass Transfer* Vol. 27(5) pp. 723-737.

Moser, K. W., R. L. Webb and B. Na (1998), "A New Equivalent Reynolds Number Model for Condensation in Smooth Tubes," *Transactions of ASME, Journal of Heat Transfer* Vol. 120(2) pp. 410 - 417.

Munson, B. R., D. F. Young and T. H. Okiishi (2002). *Fundamentals of Fluid Mechanics*. 4th Ed. New York, John Wiley & Sons, Inc.

Myers, G. E. (1998). Separation of Variables. *Analytical Methods in Conduction Heat Transfer*. G. E. Myers, AMCHT Publications pp. 54-85.

Powers, D. J. (1999). The Heat Equation. *Boundary Value Problems*. D. J. Powers, Harcourt Academic Press pp. 134-208.

Rouhani, S. Z. and E. Axelsson (1970), "Calculation of Void Volume Fraction in the Subcooled and Quality Boiling Regions," *International Journal of Heat and Mass Transfer* Vol. 13(2) pp. 383-393.

Sardesai, R. G., R. G. Owen and D. J. Pulling (1981), "Flow Regimes for Condensation of a Vapour inside a Horizontal Tube," *Chemical Engineering Science* Vol. 36(7) pp. 1173-1180.

Serizawa, A. and Z. Feng (2004). Two-Phase Fluid Flow. *Heat Transfer and Fluid Flow in Microchannels*. G. P. Celata. New York, NY, Begell House, Vol. 1 pp. 91-117.

Serizawa, A., Z. Feng and Z. Kawara (2002), "Two-Phase Flow in Microchannels," *Experimental Thermal and Fluid Science* Vol. 26(6-7) pp. 703-714.

Shah, M. M. (1976), "New Correlation for Heat Transfer During Boiling Flow through Pipes.," *Proc of Annu Meet, Jun 27-Jul 1 1976* Vol. 82 pat 2 pp. 66-86.

Shah, M. M. (1979), "A General Correlation for Heat Transfer During Film Condensation inside Pipes," *International Journal of Heat and Mass Transfer* Vol. 22(4) pp. 547-556.

Shah, R. K. and M. S. Bhatti (1987). Laminar Convective Heat Transfer in Ducts. *Handbook of Single-Phase Convective Heat Transfer*. S. Kakaç, R. K. Shah and W. Aung. New York, NY, Wiley.

Sobhan, C. B. and S. V. Garimella (2001), "A Comparative Analysis of Studies on Heat Transfer and Fluid Flow in Microchannels," *Microscale Thermophysical Engineering* Vol. 5(4) pp. 293-311.

Soliman, H. M. (1982), "On the Annular-to-Wavy Flow Pattern Transition During Condensation inside Horizontal Tubes," *Canadian Journal of Chemical Engineering* Vol. 60(4) pp. 475-481.

Soliman, H. M. (1986), "Mist-Annular Transition During Condensation and Its Influence on the Heat Transfer Mechanism," *International Journal of Multiphase Flow* Vol. 12(2) pp. 277-288.

Soliman, H. M., J. R. Schuster and P. J. Berenson (1968), "A General Heat Transfer Correlation for Annular Flow Condensation," *Transactions of ASME, Journal of Heat Transfer* Vol. 90(2) pp. 267-276.

Souza, A. L., J. C. Chato, J. P. Wattelet and B. R. Christoffersen (1993), "Pressure Drop During Two-Phase Flow of Pure Refrigerants and Refrigerant-Oil Mixtures in Horizontal Smooth Tubes," *29th National Heat Transfer Conference, Aug 8-11 1993*, Atlanta, GA, USA, Publ by ASME, New York, NY, USA, pp. 35-41.

Streeter, V. L. and E. B. Wylie (1981). *Fluid Mechanics*. First SI Metric Ed., McGraw-Hill Ryerson Ltd.

Sun, G., G. F. Hewitt and V. V. Wadekar (2004), "A Heat Transfer Model for Slug Flow in a Horizontal Tube," *International Journal of Heat and Mass Transfer* Vol. 47(12-13) pp. 2807-2816.

Suo, M. and P. Griffith (1964), "Two-Phase Flow in Capillary Tubes," *Journal of Basic Engineering* Vol. 86 pp. 576-582.

Tabatabai, A. and A. Faghri (2001), "A New Two-Phase Flow Map and Transition Boundary Accounting for Surface Tension Effects in Horizontal Miniature and Micro Tubes," *Journal of Heat Transfer* Vol. 123(5) pp. 958-968.

Taitel, Y. and A. E. Dukler (1976), "A Model for Predicting Flow Regime Transitions in Horizontal and near Horizontal Gas-Liquid Flow," *AIChE Journal* Vol. 22(1) pp. 47-55.

Tandon, T. N., H. K. Varma and C. P. Gupta (1982), "New Flow Regimes Map for Condensation inside Horizontal Tubes," *Journal of Heat Transfer* Vol. 104(4) pp. 763-768.

Taylor, B. N. and C. E. Kuyatt (1994). Guidelines for Evaluating and Expressing the Uncertainty of Nist Measurement Results. National Institute of Standards and Technology, Washington, DC, USA, 15 p.

Thome, J. R., J. El Hajal and A. Cavallini (2003), "Condensation in Horizontal Tubes, Part 2: New Heat Transfer Model Based on Flow Regimes," *International Journal of Heat and Mass Transfer* Vol. 46(18) pp. 3365-3387.

Tran, T. N., M.-C. Chyu, M. W. Wambsganss and D. M. France (2000), "Two-Phase Pressure Drop of Refrigerants During Flow Boiling in Small Channels: An Experimental Investigation and Correlation Development," *International Journal of Multiphase Flow* Vol. 26(11) pp. 1739-1754.

Traviss, D. P. and W. M. Rohsenow (1973), "Flow Regimes in Horizontal Two-Phase Flow with Condensation," *ASHRAE Transactions* Vol. 79(Part 2) pp. 31-39.

Traviss, D. P., W. M. Rohsenow and A. B. Baron (1973), "Forced-Convection Condensation inside Tubes: A Heat Transfer Equation for Condenser Design," *ASHRAE Transactions* Vol. 79(1) pp. 157-165.

Triplett, K. A., S. M. Ghiaasiaan, S. I. Abdel-Khalik, A. LeMouel and B. N. McCord (1999a), "Gas-Liquid Two-Phase Flow in Microchannels. Part 2: Void Fraction and Pressure Drop," *International Journal of Multiphase Flow* Vol. 25(3) pp. 395-410.

Triplett, K. A., S. M. Ghiaasiaan, S. I. Abdel-Khalik and D. L. Sadowski (1999b), "Gas-Liquid Two-Phase Flow in Microchannels. Part 1: Two-Phase Flow Patterns," *International Journal of Multiphase Flow* Vol. 25(3) pp. 377-394.

Tuckerman, D. B. and R. F. W. Pease (1981), "High-Performance Heat Sinking for Vlsi," *IEEE Electron. Device Lett.* Vol. 2 pp. 126-129.

Tuckerman, D. B. and R. F. W. Pease (1982), "Ultrahigh Thermal Conductance Microstructures for Cooling Integrated Circuits," *32nd Electronics Components Conf.*, IEEE, EIA, CHMT, pp. 145-149.

Ungar, E. K. and J. D. Cornwell (1992), "Two-Phase Pressure Drop of Ammonia in Small Diameter Horizontal Tubes," *AIAA paper 92-3891*

Wambsganss, M. W., J. A. Jendrzejczyk and D. M. France (1991), "Two-Phase Flow Patterns and Transitions in a Small, Horizontal, Rectangular Channel," *International Journal of Multiphase Flow* Vol. 17(3) pp. 327-342.

Wambsganss, M. W., J. A. Jendrzejczyk and D. M. France (1994), "Determination and Characteristics of the Transition to Two-Phase Slug Flow in Small Horizontal Channels," *Journal of Fluids Engineering, Transactions of the ASME* Vol. 116(1) pp. 140-146.

Wang, C.-C., C.-S. Chiang and D.-C. Lu (1997), "Visual Observation of Two-Phase Flow Pattern of R-22, R-134a, and R-407c in a 6.5-Mm Smooth Tube," *Experimental Thermal and Fluid Science* Vol. 15(4) pp. 395-405.

Wang, H. S. and J. W. Rose (2004), "Film Condensation in Horizontal Triangular Section Microchannels: A Theoretical Model," *Proceedings of the Second International Conference on Microchannels and Minichannels (ICMM2004), Jun 17-19 2004*, Rochester, NY, United States, American Society of Mechanical Engineers, New York, NY 10016-5990, United States, pp. 661-666.

Wang, H. S., J. W. Rose and H. Honda (2004), "A Theoretical Model of Film Condensation in Square Section Horizontal Microchannels," *Chemical Engineering Research and Design* Vol. 82(4) pp. 430-434.

Webb, R. L. and K. Ermis (2001), "Effect of Hydraulic Diameter on Condensation of R-134a in Flat, Extruded Aluminum Tubes," *Journal of Enhanced Heat Transfer* Vol. 8(2) pp. 77-90.

Wilson, M. J., T. A. Newell, J. C. Chato and C. A. Infante Ferreira (2003), "Refrigerant Charge, Pressure Drop, and Condensation Heat Transfer in Flattened Tubes," *International Journal of Refrigeration* Vol. 26(4) pp. 442-451.

Wu, H. Y. and P. Cheng (2005), "Condensation Flow Patterns in Silicon Microchannels," *International Journal of Heat and Mass Transfer* Vol. 48(11) pp. 2186-2197.

Wu, P. Y. and W. A. Little (1983), "Measurement of Friction Factor for the Flow of Gases in Very Fine Channels Used for Micro Miniature Joule Thompson Refrigerators," *Cryogenics* Vol. 23 pp. 273-277.

Wu, P. Y. and W. A. Little (1984), "Measurement of the Heat Transfer Characteristics of Gas Flow in Fine Channel Heat Exchangers for Micro Miniature Refrigerators," *Cryogenics* Vol. 24 pp. 415-420.

Xu, B., K. T. Ooi, N. T. Wong and W. K. Choi (2000), "Experimental Investigation of Flow Friction for Liquid Flow in Microchannels," *International Communications in Heat and Mass Transfer* Vol. 27(8) pp. 1165-1176.

Yan, Y.-Y. and T.-F. Lin (1999), "Condensation Heat Transfer and Pressure Drop of Refrigerant R-134a in a Small Pipe," *International Journal of Heat and Mass Transfer* Vol. 42(4) pp. 697-708.

Yang, C.-Y. and C.-C. Shieh (2001), "Flow Pattern of Air-Water and Two-Phase R-134a in Small Circular Tubes," *International Journal of Multiphase Flow* Vol. 27(7) pp. 1163-1177.

Yang, C.-Y. and R. L. Webb (1996a), "Condensation of R-12 in Small Hydraulic Diameter Extruded Aluminum Tubes with and without Micro-Fins," *International Journal of Heat and Mass Transfer* Vol. 39(4) pp. 791-800.

Yang, C.-Y. and R. L. Webb (1996b), "Friction Pressure Drop of R-12 in Small Hydraulic Diameter Extruded Aluminum Tubes with and without Micro-Fins," *International Journal of Heat and Mass Transfer* Vol. 39(4) pp. 801-809.

Yang, C.-Y. and R. L. Webb (1997), "Predictive Model for Condensation in Small Hydraulic Diameter Tubes Having Axial Micro-Fins," *Journal of Heat Transfer, Transactions ASME* Vol. 119(4) pp. 776-782.

Zhang, M. and R. L. Webb (2001), "Correlation of Two-Phase Friction for Refrigerants in Small-Diameter Tubes," *Experimental Thermal and Fluid Science* Vol. 25(3-4) pp. 131-139.

Zhao, T. S. and Q. C. Bi (2001a), "Co-Current Air-Water Two-Phase Flow Patterns in Vertical Triangular Microchannels," *International Journal of Multiphase Flow* Vol. 27(5) pp. 765-782.

Zhao, T. S. and Q. C. Bi (2001b), "Pressure Drop Characteristics of Gas-Liquid Two-Phase Flow in Vertical Miniature Triangular Channels," *International Journal of Heat and Mass Transfer* Vol. 44(13) pp. 2523-2534.